Master Thesis

Implementation of continuous time quantum Monte Carlo solvers for the infinite dimensional Hubbard model at half filling

Julian Stobbe

Institut für Theoretische Physik
Johann Wolfgang Goethe-Universität
Frankfurt am Main Monday 26$^{\text{th}}$ March, 2018

Eidesstattliche Erklärung nach § 30 (12) Ordnung für den Bachelor- und dem Masterstudiengang

Hiermit erkläre ich, dass ich die Arbeit selbstständig und ohne Benutzung anderer als der angegebenen Quellen und Hilfsmittel verfasst habe. Alle Stellen der Arbeit, die wörtlich oder sinngemäss aus Veröffentlichungen oder aus anderen fremden Texten entnommen wurden, sind von mir als solche kenntlich gemacht worden. Ferner erkläre ich, dass die Arbeit nicht — auch nicht auszugsweise — für eine andere Prüfung verwendet wurde.

Frankfurt, den

CONTENTS

LIST OF FIGURES

LIST OF ALGORITHMS

HUBBARD MODEL

1.1 INTRODUCTION

The full description of realistic interacting systems with computable solutions has been of interest since the advent of quantum mechanics. While it is easy to write down a Hamiltonian with all contributing interactions, solutions to the Schrödinger equation already fail for the simple electron coulomb repulsion due to the large amount of particles and quadratic scaling in the number of equations. With this problem in mind approximations and effective models have been developed in order to explain effects like the quantum hall effect, the Mott insulating phase or type II superconductivity as emergent behavior without having to solve the full system of $\sim 10^{23}$ coupled differential equations.

In the past great progress has been made for systems with weakly to moderately correlated electrons expedited by the success of density functional theory. Strongly correlated electrons systems however have proven to be more problematic. One indication of this shortcoming is the band gap problem [103]. Model systems can be beneficial in describing exactly this behavior by giving up the ab initio nature. In this thesis I will consider the Hubbard model on the hypercubic and Bethe lattice in different regions of interaction strengths. The dynamical mean field approximation method, that is able to find the Mott transition in this model system, has been implemented for the Bethe and hypercubic lattice for this thesis. Within the DMFT approximation there is the need to solve the fully interacting problem on one (or at most a few) lattice sites. Commonly used methods are exact diagonalization (ED), iterated perturbation theory (IPT), discrete and continuous time quantum Monte Carlo (HF-QMC and CTQMC) and renormalization group methods. I have implemented IPT and two different CTQMC solvers. The perturbation theory solver allows easy access to the most important features of the phase diagram, since it can be written as a set of algebraic equations. CTQMC solvers are then used to refine the results obtained from IPT. While very accurate, Monte Carlo solvers tend to be inefficient near phase transitions. Due to this fact a complementary solver could be based and renormalization group methods.

In chapter 1 there will be a short discussion of the Hubbard model, traditional mean field methods and the Mott transition.

In chapter 2 we will discuss the mathematical basics for Monte Carlo methods along some tools for statistical evaluation. There will also be a discussion of essential auxiliary algorithms for the accumulation and computation of statistics.

Chapter 3 gives a short overview of the Green's function formalism, functional integral formalism, diagrammatic perturbation theory and quasi particles.

In Chapter 4 the dynamical mean field theory is derived and the quantum Monte Carlo solvers are introduced.

In Chapters 5 and 6 implementation details and results are discussed.

1.2   HUBBARD MODEL

We will only consider solid state systems with negligible relativistic contributions and consequently no spin dependent potentials in this thesis. These systems are described by the well-known Hamiltonian consisting of N_e electron contributions at positions r_i with masses m_i and N_n ions at R_k with masses M_k:

$$
\hat{H} = -\underbrace{\sum_i^{N_e} \frac{\hbar^2}{2m_i} \nabla_{r_i}^2 + \frac{1}{2} \sum_{i \neq j} V_{e-e}(\hat{r}_i, \hat{r}_j)}_{\hat{T}_e + \hat{V}_{e-e}}
$$

$$
-\underbrace{\sum_k^{N_n} \frac{\hbar^2}{2M_k} \nabla_{R_k}^2 + \frac{1}{2} \sum_{k \neq l} V_{n-n}(\hat{R}_k, \hat{R}_l)}_{\hat{T}_n + \hat{V}_{n-n}}
$$

$$
+\underbrace{\sum_i^{N_e} \sum_k^{N_n} V_{e-n}(\hat{r}_i, \hat{R}_k)}_{\hat{V}_{e-n}}
\tag{1.2.1}
$$

Even though we use a non-relativistic formulation which neglects for example the important effects of spin orbit coupling, this is already impossible to solve directly. In order to be able to proceed further, it is often assumed that the wave functions of ions and electrons decouple. This is known as Born-Oppenheimer approximation.

$$
\psi_{\text{total}}\left(\{r_i\}; \{R_k\}\right) = \psi_e\left(\{r_i\}; \{R_k\}\right) \times \psi_{\text{ion}}\left(\{R_k\}\right)
\tag{1.2.2}
$$

It follows that we can decouple the electronic Hamiltonian $\hat{H}_{el} = \hat{T}_e + \hat{V}_{e-e} + \hat{V}_{e-n}$ from the lattice Hamiltonian. In this context the lattice potential will often be called external potential V_{ext}. Since the solution of the electronic problem in an external potential is still infeasible, it is necessary to find additional approximations. There are several well established methods which provide insight into solid state phenomena. Hartree Fock (HF) approximation introduces an effective static mean field of electrons to avoid explicit electron-electron interactions. However correlations stemming from coulomb interactions are not captured.

Density functional theory (DFT) improves upon HF by taking exchange and correlation effects into account. The basis for DFT are the Hohenberg-Kohn theorems, which state that there exists a one-to-one mapping between the ground state electron density and the external potential: The external potential can be written as a functional of the electron density. This external potential provides the ground state energy if and only if (iff) the argument is the ground state energy. Since part of this functional, the so called exchange correlation functional is in practice approximated and almost certainly unobtainable in general, DFT remains an approximation and is unable to fully capture effects that stem from strong interaction between electrons[1]. Usual approximations for the exchange correlation term such as local density approximation (LDA) or generalized gradient approximations (GGA) tend to underestimate localization terms and as a result over-stabilize the metallic phase [31]. They

---

1 This is only true for the original form relying on the Hohenberg-Kohn theorem. Extensions such as DFT+U or DFT+DMFT incorporate these interactions — sometimes at the expense of a controllable error. This becomes especially apparent in the mostly intractable double counting term.

also result in the so called band gap problem since they produce smooth exchange correlation functionals [28, 118] (see also sec. 3.7).

Model Hamiltonians, in contrast to ab initio methods, can not only offer another picture of phenomena such as the Mott insulating phase but also contribute a more systematic justification for certain questions within DFT such as the physical meaning of Kohn-Sham eigenvalues [28]. The combination of both methods have the problem of double counting certain contributions [31]. They do however allow to introduce specific effects (such as Coulomb correlations) into ab initio methods, see for example DFT+DMFT.

We will now map the electronic Hamiltonian onto the Hubbard model that will then be used through out this thesis. This model explicitly retains two interactions, kinetic energy and electron repulsion. To rewrite $\hat{H}_{el}$ in second quantization we use the transformation identities from $1, 2, \ldots$ -particle Hilbert spaces to the Fock space (for a derivation see chapter 1 [70]):

$$\hat{O}_1 = \sum_{\alpha\beta} \langle\alpha|\,\hat{o}\,|\beta\rangle\, a_\alpha^\dagger a_\beta \tag{1.2.3}$$

$$\hat{O}_2 = \sum_{\alpha\beta\gamma\delta} \langle\alpha\beta|\,\hat{o}\,|\gamma\delta\rangle\, a_\alpha^\dagger a_\beta^\dagger a_\delta a_\gamma \tag{1.2.4}$$

$$\ldots$$

a_α and $a_\alpha^\dagger$ can be either fermionic (denoted by $c_\alpha, c_\alpha^\dagger$) or bosonic ($b_\alpha, b_\alpha^\dagger$) annihilation and creation operators for the state α with the usual (anti) commutator relations.

$$\left[a_\alpha, a_\beta^\dagger\right]_\zeta = a_\alpha a_\beta^\dagger - \zeta a_\beta^\dagger a_\alpha = \delta_{\alpha,\beta} \tag{1.2.5}$$

$$\left[a_\alpha, a_\beta\right]_\zeta = \left[a_\alpha^\dagger, a_\beta^\dagger\right]_\zeta = 0 \tag{1.2.6}$$

$$n_\alpha = a_\beta^\dagger a_\alpha \tag{1.2.7}$$

$$\zeta = \begin{cases} +1 & \text{bosons} \\ -1 & \text{fermions} \end{cases} \tag{1.2.8}$$

We will later use coherent states as basis for the Fock space where the basis states are defined as the eigenstates of the annihilation operator.

$$\hat{a}_\alpha\,|\phi\rangle = \phi_\alpha\,|\phi\rangle = \phi_\alpha \exp\left[\sum_\alpha \phi_\alpha \hat{a}_\alpha^\dagger\right]|0\rangle \tag{1.2.9}$$

$$\hat{a}_\alpha^\dagger\,|\phi\rangle = \zeta\frac{\partial}{\partial\phi_\alpha}\,|\phi\rangle \tag{1.2.10}$$

$$1 = \int \prod_\alpha \frac{d\phi_\alpha^\star d\phi_\alpha}{\mathcal{N}} \exp\left[-\sum_\alpha \phi_\alpha^\star \phi_\alpha\right]|\phi\rangle\langle\phi| \tag{1.2.11}$$

$$\text{Tr}\left[\hat{O}\right] = \int \prod_\alpha \frac{d\phi_\alpha^\star d\phi_\alpha}{\mathcal{N}} \exp\left[-\sum_\alpha \phi_\alpha^\star \phi_\alpha\right]\langle\zeta\phi|\,\hat{O}\,|\phi\rangle \tag{1.2.12}$$

In order to fulfill the fermionic commutator relations (eq. 1.2.5) it is necessary for the eigenvalues of $a^\dagger$ to anti-commute i.e. $\phi_\alpha \phi_\alpha^\dagger = -\phi_\alpha^\dagger \phi_\alpha$. This property is provided by elements of the exterior algebra over complex numbers usually called Grassmann numbers. We will not need any details except the fact that derivatives of Grassmann variables also anti commute with other Grassmann variables (and derivatives of

Grassmann numbers). Surprisingly, the resulting completeness, trace and Gauss integral formulas are almost equivalent between bosons and fermions up to factors of ζ and different normalization constants.

The periodicity of the lattice with lattice vectors R results in periodic eigenfunctions called as Bloch functions $\phi_{\alpha,k}$. We use α as the band, k as wave vector and i as the site index[2]. The Bloch basis is related to the localized (around ions at R_j) Wannier basis φ_α for N ions:

$$\phi_{\alpha k}(r) = e^{ik \cdot R} u_{\alpha k}(r), \qquad u_{\alpha k}(r + R) = u_{\alpha k}(r) \tag{1.2.13}$$

$$\varphi_{\alpha i}(r) = \frac{1}{\sqrt{N}} \sum_k \phi_{\alpha k}(r - R_i) \tag{1.2.14}$$

The Wannier basis can be used as the local basis with eq. 1.2.3 for the kinetic term and eq. 1.2.4 for two particle potentials, resulting in the generalized tight binding Hamiltonian.

$$H = \sum_{\substack{\alpha\beta \\ ij \\ \sigma}} t_{ij}^{\alpha\beta} c_{\alpha i\sigma}^\dagger c_{\beta j\sigma'} + \frac{1}{2} \sum_{\substack{\alpha\beta\gamma\delta \\ ijkl \\ \sigma\sigma'}} U_{\alpha\beta\gamma\delta}^{ijkl} c_{\alpha i\sigma}^\dagger c_{\beta j\sigma'}^\dagger c_{\gamma k\sigma'} c_{\delta l\sigma} \tag{1.2.15}$$

$$t_{ij}^{\alpha\beta} = \langle \varphi_{\alpha i\sigma} | \hat{T}_e + \hat{V}_{e-n} | \varphi_{\beta j\sigma} \rangle = \int d^3 r \, \varphi_{\alpha i}^\star(r) \left(\hat{T}_e(r) + \hat{V}_{e-n}(r) \right) \varphi_{\beta j}(r) \tag{1.2.16}$$

$$U_{\alpha\beta\gamma\delta}^{ijkl} = \int d^3r \, d^3r' \, \varphi_{\alpha i}^\star(r) \varphi_{\beta j}^\star(r') \hat{V}_{e-e}(r,r') \varphi_{\gamma k}(r') \varphi_{\delta l}(r) \tag{1.2.17}$$

The Wannier functions are assumed to be localized enough to be eigenfunctions of the one particle Hamiltonian $\hat{T}_e + \hat{V}_{e-n}$ [39]. This means the hopping matrix $t_{ij}^{\alpha\beta}$ contains the energies without electron-electron interactions and hopping between bands is forbidden.

$$t_{ij}^{\alpha\beta} = \delta_{\alpha,\beta} \frac{1}{N} \sum_k e^{ik(R_i - R_j)} \epsilon_{\alpha k} \tag{1.2.18}$$

These energies could be computed using DFT or the tight binding approximation (only nearest neighbor hopping).

The overlap integral $U_{\alpha\beta\gamma\delta}^{ijkl}$ still contains the full interaction. In the Hubbard model it is assumed to be completely local and only density-density terms contribute:

$$U_{\alpha\beta\gamma\delta}^{ijkl} = U_{\alpha\beta\gamma\delta} \delta_{i,j} \delta_{j,k} \delta_{k,l} \delta_{\alpha,\gamma} \delta_{\beta,\delta} \tag{1.2.19}$$

From that we finally get the Hubbard Hamiltonian

$$H = \sum_{ij\alpha\sigma} t_{ij}^\alpha c_{i\alpha\sigma}^\dagger c_{j\alpha\sigma} + \frac{1}{2} \sum_{i\alpha\beta\sigma\sigma'} U_{\alpha\beta} \, n_{i\alpha\sigma} n_{i\beta\sigma'} \tag{1.2.20}$$

We will later use the single band Hubbard model with $U_{\alpha\beta} = \delta_{\alpha,\beta} U_{\alpha\beta}$. This is justified when the Fermi surface falls inside a single band and the other bands are separated by a large energy gap [39]. In this case U becomes a scalar and all band indices (due to the Pauli principle also the spin sums) can be omitted. Additionally hopping is often restricted to next neighbors: $t_{ij} = t$ iff i and j are neighbors, the $i = j$

---

2 Bloch functions solve the Hubbard Hamiltonian in the non-interacting case $U = 0$
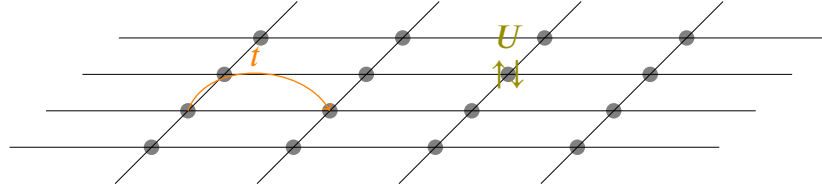
Figure 1.1: Lattice Model with hopping t and interaction U

contributions are split off as μ. The result is the most simple form of the Hubbard model.

$$H = -t \sum_{\langle ij \rangle \sigma} c_{i\sigma}^\dagger c_{j\sigma} - \mu \sum_{i\sigma} n_{i\sigma} + U \sum_i n_{i\uparrow} n_{i\downarrow} \qquad (1.2.21)$$

Non overlapping bands with only one band contributing at the Fermi level will obviously not model realistic band structures. Also only s-wave symmetries are well represented despite the otherwise realistic lattice model. However, kinetic and Coulomb energy as well as the Pauli exclusion are captured within this model.
A typical graphical illustration of these kind of lattice models is the two dimensional cartoon in fig. 1.1. Despite of these somewhat crude approximations few analytic results are available. For one dimension with nearest neighbor and next nearest neighbor interactions on square lattices there are analytic solutions using the Bethe ansatz [19, 86, 91, 39]. But even in two dimensions one has to consider limiting cases in order to extract results (see [30] for ground state at $U \to 0$).
We will later use the limit of infinite coordination number (neighbors) as this can be treated analytically with certain electronic configurations on the Bethe lattice. Despite these approximations, the Hubbard model still captures the competition of itinerancy due to the kinetic energy and localization due to the Coulomb term with the important transition to the Mott insulating phase. The interesting physics stem exactly from this competition. In the limiting cases of one dominating force approximations are easy:

Delocalization: $U \ll t$: We can neglect the second term of the Hubbard Hamiltonian. Fourier transformation and restriction to next nearest neighbor hopping results in the usual tight binding solution: $H \approx \sum_k \epsilon_k c_k^\dagger c_k$. For instance the $1D$ chain with spacing a has the solution $\epsilon_k = \epsilon_0 + 2t \cos(ka)$. The behavior only depends on the number of electrons per atom (odd — metallic, even — insulating). This is the case that is well described by Hartree Fock.

Localization: $U \gg t$: We use $H \approx \epsilon_0 \sum_{i\sigma} n_{i\sigma} + \frac{U}{2} \sum_i n_{i\uparrow} n_{i\downarrow}$, so that the energies for $0, 1, 2$ electrons at one site are 0, ϵ_0, $2\epsilon_0 + U$. Consider the configuration of all ions having exactly one electron, now the energy difference to another configuration is $\Delta E = 0 + (2\epsilon_0 + U) - 2(\epsilon_0) = U$. So for large enough U the system becomes insulating. This is the Mott insulating phase which can not be obtained by band structure calculations alone.

One of the main goals will be to find this Mott transition for the T-U phase diagram.

1.3   PROPERTIES OF THE HUBBARD HAMILTONIAN

It is worth inspecting the limiting cases of the Hubbard model one the square lattice in more detail. We first introduce the particle-hole symmetric Hamiltonian of the Hubbard model by partitioning the lattice into two sub-lattices in such a way, that every site of lattice A only has neighbors of lattice B: A particle hole transformation
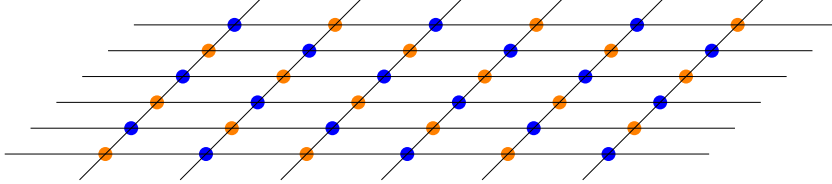
Figure 1.2: Bipartite square lattice in two dimensions

$d_{i\sigma}^{\dagger} = (-1)^i c_{i\sigma}$, see chapter 4 [101], introduces only a shift in the chemical potential $\mu \to \mu + \frac{U}{2}$ but leaves the other terms in the Hamiltonian unchanged if no next nearest neighbor hopping is considered. This means one can directly relate anti-ferromagnetic and ferromagnetic states

$$H = -t \sum_{\langle ij \rangle \sigma} c_{i\sigma}^{\dagger} c_{j\sigma} - \mu \sum_{i\sigma} n_{i\sigma} + U \sum_{i} \left(n_{i\uparrow} - \frac{1}{2} \right) \left(n_{i\downarrow} - \frac{1}{2} \right) \tag{1.3.1}$$

The density transforms as function of the chemical potential: $n(\mu) = 2 - n(-\mu), \Delta m(\mu) = \Delta m(-\mu)$ which leads to $\rho = 1$ at half filling ($\mu = 0$). This is a particularly important property for the interaction expansion algorithm, that will be introduced later[3]. It also implies that the phase diagram is symmetric around $\mu = 0$.

We will first look at the atomic limit. The Hamiltonian is easily solved analytically since the lattice characteristic is completely contained in the hopping term and one only needs to solve a single particle problem.

$$H_{\mathrm{AL}} = U \sum_{i} \left(n_{i\uparrow} - \frac{1}{2} \right) \left(n_{i\downarrow} - \frac{1}{2} \right) - \mu \sum_{i\sigma} n_{i\sigma} \tag{1.3.2}$$

The eigenstates with corresponding eigenvalues for eq. 1.3.2 are: $\frac{U}{4}, |0\rangle$; $-\frac{U}{4} - \mu, |\uparrow\rangle$; $\frac{U}{4} - \mu, |\downarrow\rangle$; $-\frac{U}{4} - 2\mu, |\uparrow\downarrow\rangle$. Since we have the explicit form of the Hamiltonian available we now choose some basis in order to calculate quantities.

$$\hat{c}_{\uparrow} \doteq \begin{pmatrix} 0 & 1 & 0 & 0 \\ 0 & 0 & 0 & 0 \\ 0 & 0 & 0 & 1 \\ 0 & 0 & 0 & 0 \end{pmatrix}, \qquad \hat{c}_{\downarrow} \doteq \begin{pmatrix} 0 & 0 & 1 & 0 \\ 0 & 0 & 0 & 1 \\ 0 & 0 & 0 & 0 \\ 0 & 0 & 0 & 0 \end{pmatrix}$$

We immediately obtain the partition function:

$$Z = \mathrm{Tr}\, e^{-\beta H_{\mathrm{AL}}} = e^{-\beta \frac{U}{4}} + 2 e^{-\beta \left(\frac{U}{4} + \mu \right)} + e^{-\beta \left(\frac{U}{4} - 2\mu \right)} \tag{1.3.3}$$

---

3 In this special case there are algorithms without a sign problem available, since the particle-hole transformation relates $U \leftrightarrow -U$ and we can avoid expanding in $(-U)^2$.

Note that we could also use the non particle hole symmetric partition function. This will however not change the observables:

$$Z = \text{Tr}\, e^{-\beta H} = 1 + 2e^{-\beta(\mu)} + e^{-\beta(U-2\mu)} \tag{1.3.4}$$

$$n = \langle n_\uparrow + n_\downarrow \rangle = \frac{2}{Z} \left(e^{\beta\left(\frac{U}{4}+\mu\right)} + e^{-\beta\left(\frac{U}{4}-2\mu\right)} \right) \tag{1.3.5}$$

$$\Delta n = \left\langle \left(n_\uparrow + n_\downarrow\right)^2 \right\rangle = n - 2D \tag{1.3.6}$$

Δn is called local moment and D double occupancy. The local moment is exactly then equal to 1, when the average occupancy of the site is 1. Density and local moments are plotted as a function of the chemical potential in fig. 1.3.

We see that $n \approx 1$ for $-U/2 < \mu < U/2$. This behavior becomes more pronounced
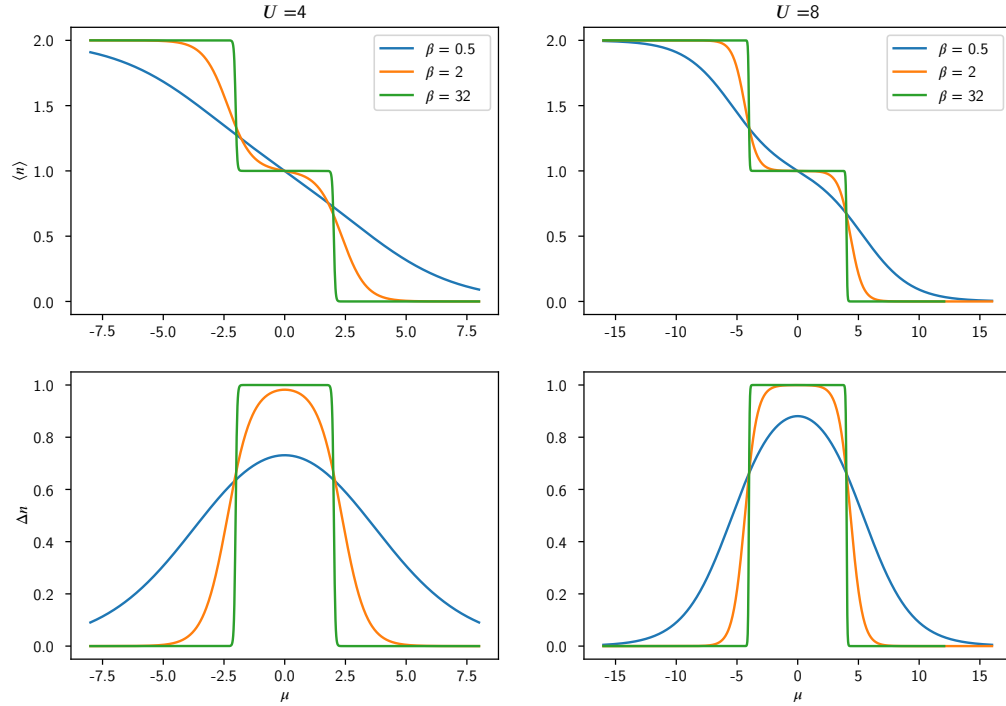
Figure 1.3: Density and local moment in the atomic limit

for increasing U or β[4]. This energy gap that is required to add a second electron to a site is known as "Mott insulating gap"[5].

An increase in the kinetic energy term will eventually result in a breakdown of the Mott insulating behavior, similar to an increase in temperature. This insulating behavior is distinct from the band insulating phases since it stems purely from electron-electron interaction instead of interactions with the periodic potential, lattice deformations or impurities [50]. It is however a well-known and often encountered phenomenon in materials with strong electron interactions such as transition metal oxides.

---

4 The Python code which generates these plots can be found along the rest of the implementations for this Thesis at [121]

5 One can verify this energy gap by considering the compressibility and noting that $\partial\rho/\partial\mu = 0$ for $-U/2 < \mu < U/2$.
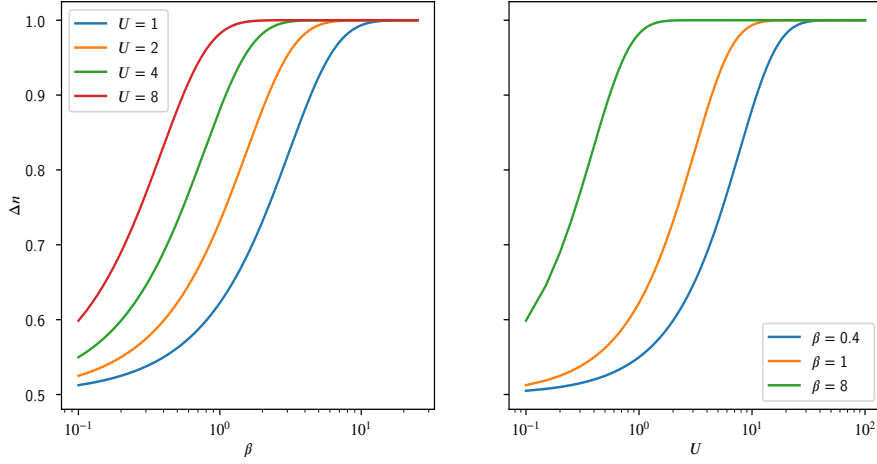
Figure 1.4: Local moment as function of U and β at half filling ($\mu = 0$).

We will later focus on the Green's function formulation of many body interactions. For the sake of completeness, we will discuss the limiting cases from this point of view here already. An introduction is given in the third chapter. It is more convenient to choose the normal instead of particle hole symmetric eigenstates here and later shift the chemical potential to $U/2$.

$$G_{ij\sigma}(\tau) = -\delta_{ij}\frac{1}{Z}\,\mathrm{Tr}\left[e^{-(\beta-\tau)H}c_\sigma e^{-H\tau}c_\sigma^\dagger\right]$$

$$G_{ij,\uparrow} = -\delta_{ij}\frac{1}{Z}\left[e^{\mu\tau} + e^{\beta\mu-\tau(U-\mu)}\right]$$

As expected this is neither site nor spin dependent. The behavior of the imaginary times Green's function is plotted in fig. 1.5.

We can compute the Matsubara Green's function for spin up in the Lehmann rep-
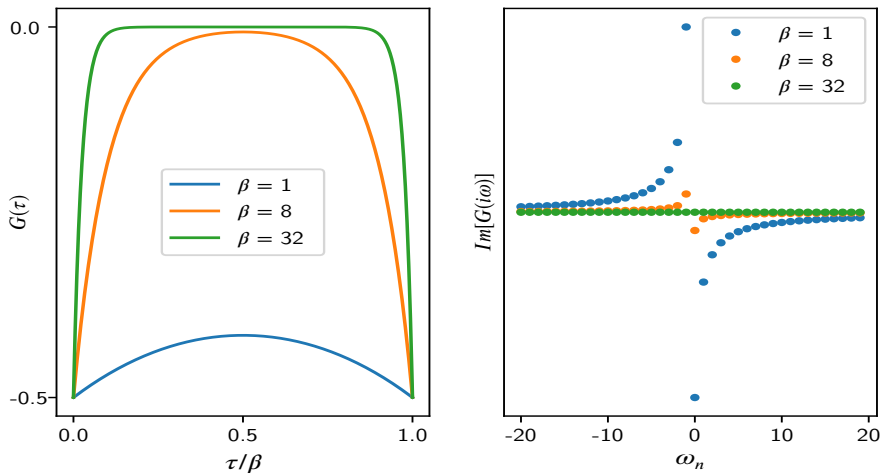
Figure 1.5: Imaginary time and Matsubara Green's function at $\mu = U/2$

resentation (see eq. 3.4.7).

$$G_\uparrow(k, k', i\omega_n) = \sum_{ij} \int_0^\beta e^{ikr_i - ik'r_j} e^{i\omega_n \tau} G_{ij,\uparrow}(\tau) \, d\tau$$

$$= -\sum_{ij} \int_0^\beta e^{ikr_i - ik'r_j} \delta_{ij} \frac{e^{i\omega_n \tau}}{Z} \left[e^{\mu\tau} + e^{\beta\mu - \tau(U-\mu)} \right] d\tau$$

$$= \delta(k - k') \left(\frac{1 + e^{\beta\mu}}{i\omega_n + \mu} + \frac{e^{\beta\mu} + e^{-\beta(U-2\mu)}}{i\omega_n + \mu - U} \right)$$

In fig. 1.5 we can see that the imaginary time Green's function is mostly featureless. The Matsubara Green's function is spin and k independent. The result is actually quite general as discussed in the third chapter.

$$G_\sigma^R(i\omega_n) = \frac{1 - n_{-\sigma}}{i\omega_n + \mu + i\eta} + \frac{n_{-\sigma}}{i\omega_n + \mu - U + i\eta}$$

$$\rightarrow \frac{1}{\omega + \mu + i\eta - \Sigma_\sigma^{\text{AL}}(\omega)} \tag{1.3.7}$$

$$\Sigma_\sigma^{\text{AL}}(\omega) = U n_{-\sigma} + U^2 \frac{n_{-\sigma}(1 - n_{-\sigma})}{\omega + \mu + i\eta - U(1 - n_{-\sigma})} \tag{1.3.8}$$

We now consider the half filling case $\mu = U/2$ and use eq. 1.3.4

$$G_\sigma^R(\omega) = \frac{1}{2} \left(\frac{1}{\omega + i\eta + U/2} + \frac{1}{\omega + i\eta - U/2} \right) \tag{1.3.9}$$

$$= \frac{1}{\omega + i\eta - \frac{U^2}{4(\omega + i\eta)}} \tag{1.3.10}$$

$$\Sigma_\sigma^{\text{AL}}(\omega) = \frac{U}{2} + U^2 \frac{G_{0,\sigma}(\omega)}{4} \tag{1.3.11}$$

With $G_{0,\sigma}(\omega)$ being the free Green's function.

The spectral function (to be discussed at the end of chapter three) can be obtained as the analytic continuation of the retarded Green's function $A(r, r', \omega) = -\frac{1}{\pi} \Im\{G^R(r, r', \omega)\}$.

$$A(\omega) = \delta(\omega + \mu) + 2\delta(\omega + \mu - U) \tag{1.3.12}$$

One can directly read off the self energy $\Sigma(\omega)$ from the retarded Green's function in eq. 1.3.10. We can see that $\Sigma(\omega)$ exhibits a singularity at $\omega = 0$ at half filling, which turns out to be a general feature of the Mott transition [65, 50].

In fig. 1.6 both the spectral function and the self energy are plotted as functions of ω. Usually one obtains the density of states from the spectral function as the trace over the position or momentum degree of freedom: $n(\omega) = \frac{1}{V} \text{Tr}_{\alpha,\alpha'} A(\alpha, \alpha', \omega)$. Since we have a purely local limit, the spectral function directly corresponds to the available density of states and we deduce that the system is insulating as there is no spectral weight at the Fermi surface.

We will now discuss the other limiting case of the Hubbard model, where $U = 0$. In this non-interacting limit the number operator does not commute with the Hamiltonian.

$$H_0 = -t \sum_{\langle ij \rangle \sigma} \left(c_{i\sigma}^\dagger c_{j\sigma} + c_{j\sigma}^\dagger c_{i\sigma} \right) \tag{1.3.13}$$
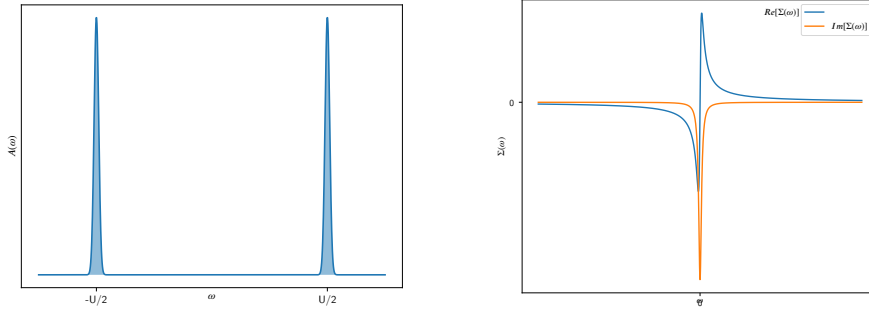
Figure 1.6: Spectral function in the atomic limit, delta peaks are broadened ($\eta \approx 0.2$), left. Self energy, ω singularity broadened ($\eta \approx 0.2$), right

The basis is readily found anyway by considering $N_\sigma = \sum_i n_{i\sigma}$. We use the occupa-
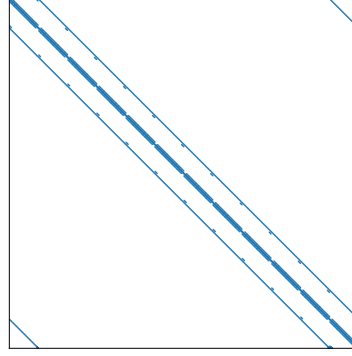
Figure 1.7: Matrix structure for the tight binding Hamiltonian on a 4 dimensional simple cubic lattice with periodic boundary conditions in real space. Even though this is sparse, hermitian and self similar, the Fourier basis expansion is more efficient even for complex lattice geometries.

tion number of each site, so that the Hamiltonian is a superposition of neighboring states. Consider for example a linear chain with periodic boundary conditions

$$H \left|100\cdots\right\rangle = -\mu \left|100\cdots\right\rangle - t \left|0100\cdots\right\rangle - t \left|00\cdots01\right\rangle$$

The Hamiltonian can then be explicitly constructed by setting $H_{ij} = -t$ if i and j are neighbors. In principal this allows for a straightforward solution by exact diagonalization of arbitrary hopping and lattice structures since the matrix structure resembles that of the usual finite difference approximation of the kinetic energy (see fig. 1.7). However the lattice must be large enough to suppress finite size effects and the Hamiltonian matrix is usually too large to diagonalize directly. One therefore uses the periodicity of the problem by transformation into momentum space which yields the well-known tight binding solutions. In our case we use the simple cubic lattice and rescaled hopping $t \to t/\sqrt{2 \cdot \text{dimension}}$. The reason for this the rescaling will be discussed in the fourth chapter. The corresponding Green's
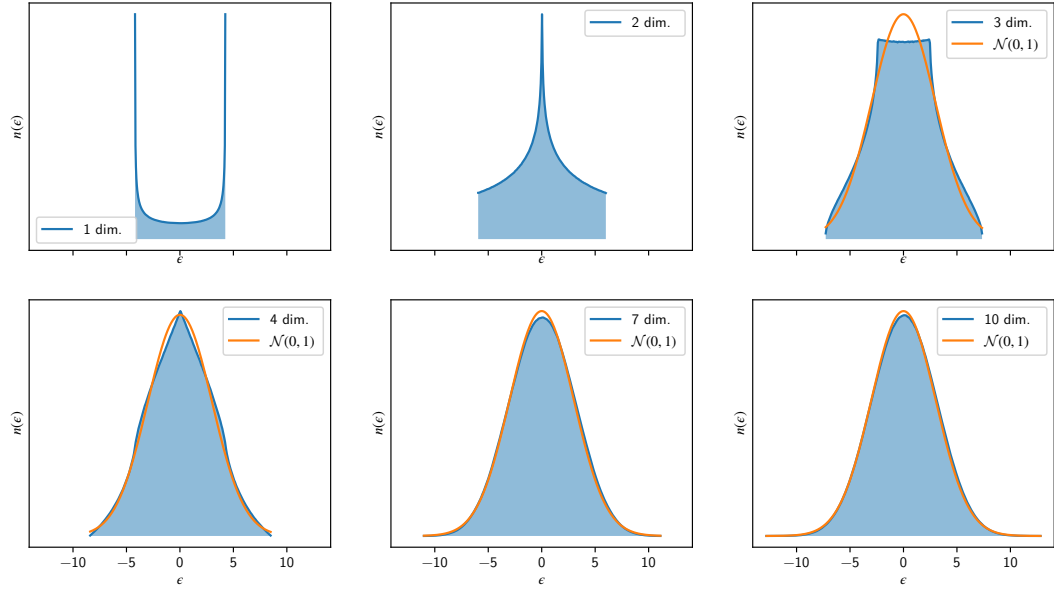
Figure 1.8: DOS for different dimensions on a hypercubic lattice with dispersion $\epsilon_0(k) = -2t^\star \sum_d^D \cos(k_d a)$. The bandwidth is only finite for $D < \infty$.

function for this system can be obtained from the dispersion.

$$G_{0,\sigma}(k, i\omega_n) = \frac{1}{i\omega_n + \mu - \epsilon_0(k)} \qquad (1.3.14)$$

Having obtained results for $t \ll U$ and $U \ll t$, we know that a phase transition between metallic and insulating phase must occur in the intermediary region (in reference to the Mott insulating phase, band insulation can of course be obtained in the tight binding approximation).

fig. 1.9 and fig. 1.10 show the general properties of this transition at half filling (the meaning of the bandwidth parameter will be discussed in sec. 4). In this thesis we do not consider the behavior away from half filling because the quantum Monte Carlo algorithms exhibit a so called sign problem (see sec. 2.8), depending on the chemical potential. We will discuss methods to work around this problem at half filling. Other values of the chemical potential however require more care. In fig. 1.9 and fig. 1.10 we can see the structure of the phase transition as obtained by second order perturbation theory. The first order phase transition line as well as the exact borders of the coexistence region can not be obtained by this simple method. We will discuss this solver and the phase diagram obtained by it in sec. 6

1.4 MEAN FIELD APPROXIMATION

Before introducing the dynamical mean field approximation, it is useful to look at traditional mean field approximations. The central assumption is, that fluctuations around the average of observables are small.

$$a_\alpha^\dagger a_\beta \approx \left(\left\langle a_\alpha^\dagger a_\beta \right\rangle + \delta \right) \cdot \mathbb{1} \qquad (1.4.1)$$
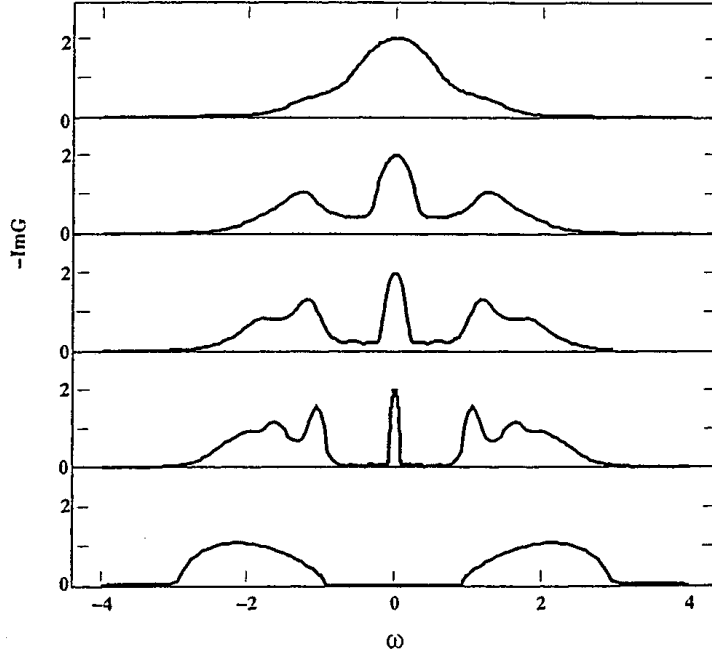
Figure 1.9: Spectral density at $T = 0$ and half bandwidth D, computed with iterated perturbation theory for $U/D = 1, 2, 2.5, 3, 4$ top to bottom, from sec. VII. B [51]. For $U/D = 4$ The system is in a insulating phase (since there is no spectral weight at the Fermi surface. Details will be discussed in sec. 3)
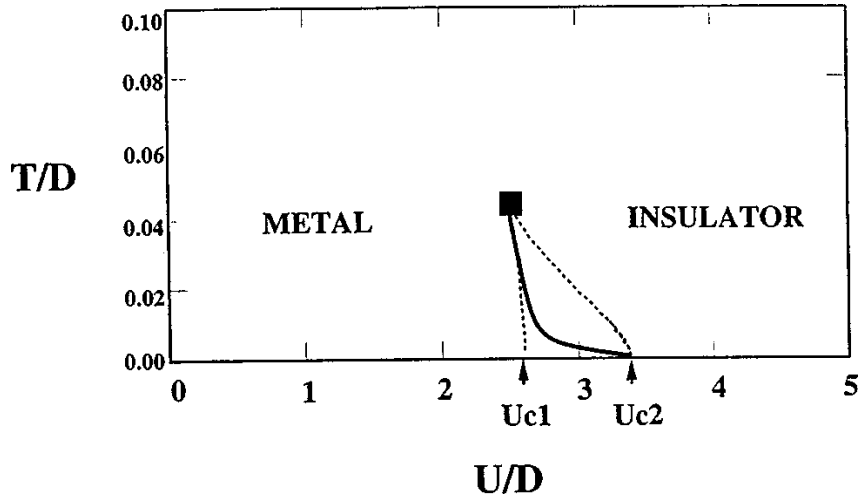
Figure 1.10: Phase diagram of $d = \infty$ Hubbard model at half filling with half bandwidth D. The dotted lines $U_{c1}(T), U_{c2}(T)$ mark the crossover region from metal to insulating phase while the solid line marks the first order transition line $U_c(T)$, see sec. VII. B [51].

$$\Rightarrow O_1 O_2 = \left(O_1 - \langle O_1 \rangle\right)\left(O_2 - \langle O_2 \rangle\right)$$
$$+ \langle O_1 \rangle O_2 + O_1 \langle O_2 \rangle - \langle O_1 \rangle \langle O_2 \rangle \tag{1.4.2}$$
$$\approx \langle O_1 \rangle O_2 + O_1 \langle O_2 \rangle - \langle O_1 \rangle \langle O_2 \rangle \tag{1.4.3}$$

With the δ small enough so δ^2 can be neglected. O_1, O_2 are operators written in terms of creation and annihilation operators. The averages are unknown parameters, eq. 1.4.3 is a recipe for the construction of the mean field Hamiltonian from which these parameters can then be obtained. A possible way to construct so called self consistency equations for the mean field parameters are the calculation of average densities with respect to the mean field Hamiltonian (that is itself a function of these parameters).

$$\langle \cdots \rangle_{\mathrm{MF}} = \frac{\mathrm{Tr}\left(e^{-\beta H_{\mathrm{MF}}}\cdots\right)}{\mathrm{Tr}\left(e^{-\beta H_{\mathrm{MF}}}\right)} \tag{1.4.4}$$

$$\left\langle a_\alpha^\dagger a_\beta \right\rangle_{\mathrm{MF}}^{(n)} = \left\langle a_\alpha^\dagger a_\beta \right\rangle_{\mathrm{MF}}^{(n-1)} \tag{1.4.5}$$

n is the iteration of the self consistency cycle. The first method of this kind was introduced by Pierre Weiss in 1907 [130] in order to describe phase transitions in ferromagnetic materials. Later, the Hartree Fock method provided a way to include the full quantum mechanical exchange terms between electrons which arise from the Pauli principle.

An alternative name for Hartree Fock is "self consistent field method" due to the structure of the algorithm: In order to find an effective mean field Hamiltonian, one usually first Legendre transforms to some order parameter (e.g. magnetization $m = \langle s_i \rangle$) and then minimizes the free energy with respect to spatial changes under the constraint of physical behavior (i.e. normalization, correct orbitals). This leads to a set of equations that are solved iteratively. One usually starts with the free Hamiltonian H_0, solves the set of generalized eigenproblems which results in an improved solution for the equations. In case the method relies on the Ritz variational principle (eq. 1.4.6) the solution is guaranteed to be an upper bound. [61]

$$\frac{\langle \Psi | H | \Psi \rangle}{\langle \Psi | \Psi \rangle} \geq \langle \Psi_o | H | \Psi_0 \rangle = E_0 \tag{1.4.6}$$

However convergence is not guaranteed and in many modern algorithms the convergence criteria are hard to determine (improvements can be made with quasi newton methods, see sec. 5). There are however many analytically well defined bounds such as the spectral radius of the discretized Hamiltonian. Dynamic mean field theory tries to capitalize on the computationally inexpensive structure of this procedure while improving upon the static nature of the mean field. As a toy example we consider the Ising model (at each lattice point in D dimensions sits one classical spin which either points up or down) on the hypercubic lattice, meaning the coordination number is $z = 2D$. Any spin at position i has the Hamiltonian with an external magnetic field h:

$$H = -J \sum_{\langle i,j \rangle} s_i s_j \tag{1.4.7}$$

$$H_i = -s_i \left[\sum_{j=1}^{z} J s_j + h \right] \tag{1.4.8}$$

$$= -s_i \left[z J m + h \right] - J \left[J \sum_{j=1}^{z} (s_j - m) \right]$$

$$\overset{\text{eq. 1.4.1}}{\approx} -s_i \left[z J m + h \right] \tag{1.4.9}$$

The self consistency equation is obtained by computing the average spin:

$$m = \langle s_i \rangle = \frac{\text{Tr} \left[s_i \exp\{\beta s_i (z J m + h)\} \right]}{\text{Tr} \left[\exp\{\beta s_i (z J m + h)\} \right]}$$

$$= \tanh \left(\beta z J m + \beta h \right) \tag{1.4.10}$$

This is an ordinary (non-linear) equation that can be solved numerically. For more sophisticated mean field theories, these equations become much more complicated (in the sense of the mathematical objects involved) and so do the solution methods. We can see in eq. 1.4.8 that the approximation becomes exact if we define a renormalized $J \to \frac{J^\star}{z}$ and let $z \to \infty$, so that the number of dimensions approaches infinity as well.

$$\lim_{z \to \infty} \sum_{j=1}^{z} \frac{J^\star}{z} s_j = J^\star \langle m \rangle \tag{1.4.11}$$

This observation will be instrumental in the derivation of the dynamical mean field approximation.

Usually the self consistency equations for the HF method are obtained by minimizing the free energy. Nonetheless the prescription from eq. 1.4.3 can be used to obtain an effective Hamiltonian.

$$H_{\text{HF}} = \epsilon_k + \sum_{k'\sigma'} \left[\mathcal{N} V(0) + \zeta \delta_{\sigma,\sigma'} V(k - k') \right] n_{k'\sigma'} \tag{1.4.12}$$

The second term is the background charge which is usually canceled out by the ionic charge, V is the Fourier transformed potential [24]. We will encounter this Hamiltonian again when discussing the self energy. This will enable us to find the similarities and advantages of DMFT over traditional mean field theories with HF as prime example[6].

---

6 Even though DFT is in principle exact, the often employed LDA/GGA approximation for the exchange correlation functional does lead to similar problems as HF in our case. We will not consider extended versions of both methods here.

MONTE CARLO SAMPLING

2.1 PROBABILITY THEORY

Definitions and theorems presented in this section are adapted from [33, 119, 137], a pedagogically valuable introduction to stochastic processes can be found here [42, 127]. This chapter is not intended as an introduction to probability theory but as an overview of definitions and theorems that will be used later. It is necessary to be rather general in our notation since we will later not only employ Markov chains in complicated state spaces but also use these mathematical tools to obtain error bounds for our simulation results. We start by setting up the general concepts of randomness and sampling.

Definition 1 (Random Variable) We call $X : \Omega \to S$ a S-valued random variable if it is a $\mathcal{F}$-measurable function from a probability space $(\Omega, \mathcal{F}, P)$ [1] to some measurable space $(S, \mathcal{S})$.

Ω is called sample space, members of $\mathcal{F}$ are events and $\omega \in \Omega$ are the outcomes or realizations, $P(E)$ is the probability of an event $E \in \mathcal{F}$. The random variable X is a function of possible outcomes $X(\omega)$. It can be proven that X uniquely induces a measure (in the following μ_X) on $\mathcal{S}$ [33]. The probability of a random variable X taking a specific value $x \in S$ will also be written as $P(X = x)$.

As an example for the definitions above, lets consider a number of n coin tosses where we assign 0 to heads and 1 to tails. We want to compute the sum over all tosses. This is encoded in the previous definitions by setting $\Omega = \{0, 1\}^n$ and $X : \Omega \to \mathbb{R}$ with $X(\omega_1, \cdots \omega_n) = \omega_1 + \cdots + \omega_n$ and therefore $S = \{0, \dots, n\}$.

The probability distribution of X for a set of events B is given as:

Definition 2 (Probability Distribution)

$$\mu_X(B) = P(X \in B) = P(X^{-1}(B)), \ B \in \mathcal{S} \tag{2.1.1}$$

The distribution of X is sometimes also called law of X. In case X is continuously distributed and real valued, we can also uniquely define the (cumulative) distribution function (CDF) as:

Definition 3 (cumulative distribution function)

$$F_X(x) = P(X \leq x) = \mu_X((-\infty, x]) = \int_{-\infty}^{x} \rho_X(s) \, \mathrm{d}s \tag{2.1.2}$$

With $\rho_X(s)$ being the probability density function (see eq. 2.1.7).

We call two events $E_1, E_2 \in \Omega$ independent iff the joint probability $P(E_1 \cap E_2)$ of two events E_1 and E_2 both occurring, factors into

$$P(E_1 \cap E_2) = P(E_1)P(E_2) \tag{2.1.3}$$

---

1 measurable space $(\Omega, \mathcal{F})$ with probability measure P over sample space (open set) Ω with a σ-algebra $\mathcal{F}$ (called events).
The probability measure $P \colon \mathcal{F} \to [0, 1]$, $P(\Omega) = 1$, σ-additive [33].

we will also use the following shorthand notation for joint probabilities

$$P(E_1, E_2, \dots) = P(E_1 \cap E_2 \cap \dots) \tag{2.1.4}$$

The conditional probability of E_1 given that E_2 occurred is written as:

Definition 4 (Conditional probability)

$$P(E_1|E_2) = \frac{P(E_1, E_2)}{P(E_2)} \tag{2.1.5}$$

Furthermore we will need Bayes' theorem:

$$P(E_1|E_2) = \frac{P(E_2|E_1)P(E_1)}{P(E_2)} \tag{2.1.6}$$

We will later mostly deal with probability density functions (PDF). A PDF ρ_X for a random variable X and $B \in \mathcal{S}$ connects both measures μ_X and P and provides a transition to Lebesgue integration. The formal derivation which employs the Radon-Nikodym theorem (this is also needed for the derivation of expectation values) can be found for example here [119, 137].

$$P(X \in B) = \int_B \rho_X(x)\, d\mu_X(x) \qquad \Rightarrow \int_\Omega \rho_X(\omega)\, dP(\omega) = \mathbb{1} \tag{2.1.7}$$

Although this is not guaranteed in general, we will assume existence of the PDF for all following random variables. The notation in eq. 2.1.8 will be used whenever we want to indicate that a random variable was drawn according to some PDF ρ_X:

$$X \sim \rho_X \tag{2.1.8}$$

Lastly, we also need the definitions of expected value and variance for a measurable function g.

Definition 5 (Expected value)

$$\mathbb{E}_{\rho_X}[g(X)] = \int_\Omega g(X(\omega))\, dP(\omega) = \int_S g(x)\rho_X(x)\, d\mu_X(x) \tag{2.1.9}$$

Note that μ_X is not transformed by g. This very useful fact (sometimes known as law of the unconscious statistician) sadly does not translate to higher moments. Choosing $g(X) \equiv X$ provides the usual definition of the expected value. The expectation value provides two different unique ways of describing the distribution of a random variable. We can redefine the CDF from eq. 2.1.2 using the indicator function $\mathbb{1}$.

$$F_X(x) = \mathbb{E}_{\rho_X}\left[\mathbb{1}_{\{X \le x\}}(x)\right] \tag{2.1.10}$$

$$\mathbb{1}_S(x) = \begin{cases} 1 & x \in S \\ 0 & x \notin S \end{cases} \tag{2.1.11}$$

An important property of multiple random variables is the covariance. It gives a measure for the dependence of two random variables on each other, i.e. the expected common deviation from their respective expected value.

Definition 6 (Covariance)

$$\text{Cov}[X, Y] = \mathbb{E}[(X - \mathbb{E}[X])(Y - \mathbb{E}[Y])] \tag{2.1.12}$$

Independent random variables have a covariance of 0 ($\mathbb{E}[X, Y] = \mathbb{E}[X]\mathbb{E}[Y]$). In the context of Monte Carlo sampling the covariance of samples at different sample steps, called autocorrelation, is an often used measure for the quality of the samples. This is done because large covariance between two samples implies low information gain. The variance is a measure for the spread of the distribution

Definition 7 (Variance)

$$\text{Var}[X] = \text{Cov}[X, X] = \mathbb{E}[(X - \mathbb{E}[X])^2] \tag{2.1.13}$$
$$= \mathbb{E}[X^2] - \mathbb{E}[X]^2, \quad \text{if } \mathbb{E}[X^2] < \infty$$

Unlike the expected value, the variance is not linear. Variance and covariance are related in the following way for any $c_i, c_j \in \mathbb{R}$:

$$\text{Var}\left[\sum_i c_i X_i\right] = \sum_i c_i^2 \text{Var}\left[X_i\right] + 2 \sum_{i<j} c_i c_j \text{Cov}\left[X_i, X_j\right] \tag{2.1.14}$$

The expected value is the same as first raw moment/first cumulant and the variance is equal to the second central moment and the second cumulant. For data analysis it is useful to define higher moments around m

$$\mu_n = \int_S (x - c)^n \rho_X(x) \, \mathrm{d}\mu_X(x) \tag{2.1.15}$$

When calculating moments for statistical data one has to bear in mind, that higher moments tend to be less numerically stable. This is due to the fact that the larger exponents amplify statistical and numerical uncertainty. However, higher moments are sometimes needed anyway in order to characterize a sampled distribution. For example one may want to compare a sampled distribution to a normal distribution for which all cumulants of order 3 and higher are zero.
The third central moment is called *skewness*. It gives a measure for the lack of symmetry of the distribution. This implies, that the third moment is zero for a symmetric distribution such as the normal distribution. The skewness will sometimes be used as an indication for data sufficiency: When the distribution of sample data is expected to converge according to the central limit theorem, one can check whether or not cumulants above the second order vanish[2].
In preparation for the functional formulation of many body theory we introduce characteristic and moment generating functions. These are associated with a PDF and provide an alternative way of characterizing the random variable. The uniqueness of the characteristic function is immediately clear as it is the Fourier transform of the PDF.

Definition 8 (Characteristic function) Let $k \in \mathbb{R}$ and X be some random variable

$$\varphi_X(k) = \mathbb{E}\left[e^{-ikX}\right] = \int e^{ikx} \rho_X(x) \, \mathrm{d}\mu(x) \tag{2.1.16}$$

---

2 This is one of the most convenient normality tests and sufficient for this thesis.

$$= \sum_{n=1}^{\infty} \frac{(ik)^n}{n!} \mathbb{E}\left[X^n\right] \qquad (2.1.17)$$

The inverse transformation of the characteristic function provides access to the PDF if the characteristic function is known. This is useful since the characteristic function is often easier to deal with than the PDF (especially since we will use a transformation of the random variable, i.e. $X \to f(X)$, in many applications during the rest of this thesis). Closely related to characteristic functions are the moment generating functions:

Definition 9 (Moment generating function) Let $t \in \mathbb{R}$ and X be some random variable

$$M_X(t) = \mathbb{E}\left[e^{tX}\right] \qquad (2.1.18)$$

The name stems from the fact that central moments can be calculated as derivatives of $M_x(t)$.

$$m_n = \mathbb{E}[X^n] = \left.\frac{\mathrm{d}^n M_x(t)}{\mathrm{d}t^n}\right|_{t=0} = (-i)^n \left.\frac{\mathrm{d}^n \varphi_X(k)}{\mathrm{d}k^n}\right|_{k=0}$$

$$\mathrm{Var}[X] = \left.\frac{\mathrm{d}^2 M_x(t)}{\mathrm{d}t^2}\right|_{t=0} - \left(\left.\frac{\mathrm{d}M_x(t)}{\mathrm{d}t}\right|_{t=0}\right)^2$$

$$= \left.\frac{\mathrm{d}^2 H_X(t)}{\mathrm{d}t^2}\right|_{t=0}$$

Where we introduced $H_X(t)$ as the logarithm of the moment generating function. This is called cumulant-generating function.

$$H_X(t) = \log\left(M_X(t)\right) \qquad (2.1.19)$$

Cumulants and moments can be written in terms of each other using Faà di Bruno's formula. This provides an interesting analog in real numbers, to the relationship between connected and complete sums over Feynman diagrams. Faà di Bruno's formula for normal distributed random variables corresponds to Wicks theorem for the computation of Gaussian moments [52, 40].
The (cumulant) moment generating functions will later (see sec. 3.1) be extended to generating functionals for (connected) Green's functions. Since cumulants generalize the concept of covariance (for example $\kappa_{X+Y}(t) = \kappa_X(t) + \kappa_Y(t)$ for independent variables), they provide an intuitive way of describing higher order correlations of many particle states.
In our present case of real numbers we can write down the characteristic function for the real and the multivariate complex Gaussian distribution as a motivation for the construction of generating functionals (for proofs see [5]). First let $X \sim \mathcal{N}(\mu, \sigma^2)$, then by definition

$$\rho_X = \frac{1}{\sqrt{2\pi\sigma^2}} \exp\left[-\frac{(x-\mu)^2}{2\sigma^2}\right]$$

$$\varphi_X(k) = \int_{-\infty}^{\infty} \frac{1}{\sqrt{2\pi\sigma^2}} \exp\left[i\mu k - \frac{(x-\mu)^2}{2\sigma^2}\right] \mathrm{d}x$$

$$= \exp\left[i\mu k - \frac{\sigma^2 k^2}{2}\right]$$

$$H_X(t) = \mu t + \frac{\sigma^2 t^2}{2}$$

From the last line we can immediately see the aforementioned fact, that only the two first cumulants of the normal distribution are non-vanishing (because higher derivatives are zero). The generalization to multivariate distributions is straight forward.Let X be an n-dimensional random variable with $\mathbb{E}[X] = (\mathbb{E}[X_1], \dots, \mathbb{E}[X_n]) = \mu$ and $\Sigma = \mathbb{E}[(X - \mu)(X - \mu)^T]$.

$$\rho_X(x) = \frac{1}{\sqrt{\det(2\pi\Sigma)}} e^{-(x-\mu)^T\Sigma^{-1}(x-\mu)}$$

$$\varphi_X(J) = \exp\left[iJ^T\mu - \frac{J^T\Sigma J}{2}\right]$$

In the context of free scalar fields in quantum field theory J, will take the role of an external field and Σ^{-1} that of the Green's function.

The moment generating function is closely related to the characteristic function of a distribution, but does not always exist.

$$M_x(it) \hat{=} \phi_X(k) \tag{2.1.20}$$

This shift between imaginary and real valued variables of generating functions will find an analog version in many body generating functionals by the use of the Wick rotation.

Before considering statistical samples of distributions, it is worth making some remarks regarding the notation. For most examples in the rest of this chapter we will use $\Omega \subset \mathbb{R}^n$ but later on we will require the random variables to be elements of more general sets. These sets can be products of different kinds of subsets. For example countable and finite ones, such as spins — or uncountable, infinite ones, such as time variables. In the context of physical quantities, especially quantum mechanics, S (see definition for S-valued random variables eq. 1) will often be called configuration-space. $C \in S$ is then called configuration. In preparation for our later uses of this, we take a look at an example for S and C. A sample from a system with three free parameters site index i, Ising-spin direction up or down and temperature τ for the system, will be written in the following way:

$$C = \left(4, \uparrow, \frac{\beta}{2}\right) \tag{2.1.21}$$

$$S = \{(i, \sigma, \tau) \mid i \in \mathbb{N}, \sigma \in \{\uparrow, \downarrow\}, \tau \in [0, \beta)\}, \quad \beta \in \mathbb{R} \tag{2.1.22}$$

This is an example of a configuration a sampler in sec. 4 might draw using the Metropolis Hastings algorithm.

We will use a symbolic notation to indicate the integration over this set with measure μ_C

$$\int dC = \int_S d\mu_C \tag{2.1.23}$$

Note that this is not necessarily well defined in the Lebesgue sense, rigorous justification will usually depend on the actual structure of the state-space. We will mostly deal with discrete Markov processes but do not consider the symmetry aspects of the group for the underlying model. In case one is interested in preservation

of gauge symmetries during numerical calculations, the choice of the measure requires more considerations. For example in lattice gauge theories, the Haar measure is used to preserve $SU(N)$ symmetry [49]. However, for our purpose it is sufficient to assume existence of all integrals. This means that the formal integral $\int dC$ will in practice be computed by sums or products for discrete variables and Lebesgue integrals for continuous ones. For example eq. 2.1.21 will be assumed to have the form $\int_\Omega dC = \sum_i \sum_\sigma \int_0^\beta d\tau$.

We will now introduce Birkhoff's ergodic theorem and then consider sampling methods based on this central assumption. The ergodic theorem states that time and phase space average of systems exist and are equal almost everywhere for so called ergodic systems. In other words, ergodic systems "forget" about their initial distribution over time[3]. Let $(\Omega, \mathcal{F}, P)$ be a probability space and $T : \Omega \to \Omega$ a measure preserving transformation, $\mathcal{T}$ the σ-algebra of T invariant sets, then for every $f \in L^1(P)$

$$\lim_{n \to \infty} \frac{1}{n} \sum_{i=0}^{n-1} f(T^i x) = \mathbb{E}[f \mid \mathcal{T}] \tag{2.1.24}$$

$$= \frac{1}{\mu(X)} \int f \, \mathrm{d}C = \overline{f} \tag{2.1.25}$$

The second equality is also called space average of f. It additionally requires T to be an ergodic transformation (i.e. $\forall E \in \mathcal{F}$ with $T^{-1}(E) = E : P(E) = 0 \vee P(E) = 1$). In case of Markov chains we will find more precise conditions that imply ergodicity. We will however assume without proof that all transformations and functions in this thesis fulfill the necessary requirements.

2.2 DATA SAMPLES

Usually we only have access to a subset $\Omega_{\text{sample}} \subsetneq \Omega$ of the full state space which is called sample of this population. Since we will deal with limited amount of data generated by numerical algorithms it is worth discussing some details. We first introduce some notations to shorten the following discussions. Let X_i be independent identically distributed (i.i.d.) random variables. The sample mean (or arithmetic mean) for some sample size N will be written as:

$$\bar{x}_N = \frac{1}{N} \sum_{i=1}^{N} x_i \tag{2.2.1}$$

Even though the sample mean is formally the same as the expected value over Ω_{sample}, we will use a different notation to emphasize the use of sample data (for example from MC simulations).

$$\mathbb{E}[X] = \lim_{N \to \infty} \bar{x}_N \tag{2.2.2}$$

Definition 10 (Estimator bias) We call a formula for the approximation for a function of random variables an *estimator* of the true value. The difference between the expected value of an estimator and the true value is called bias of that estimator. An estimator with zero bias is called unbiased estimator.

---

3 This is a very crude formulation the ergodic theorem, an in-depth discussion can be found here [128]

Finding unbiased estimators with good efficiency (small variance) can be important for large simulations, but in-depth discussion will be omitted here (see [84] for more details). We will however touch again on this subject later, with the introduction of jackknife analysis and other resampling methods. The sample mean is an unbiased estimator of the expected value, which can be proved using the linearity of the expected value.

$$\mathbb{E}_{\rho_X}[\bar{X}] = \mathbb{E}_{\rho_X}\left[\frac{1}{N}\sum_{i=1}^{N}x_i\right] = \frac{1}{N}\sum_{i=1}^{N}\mathbb{E}_{\rho_X}[x_i] \qquad (2.2.3)$$

When talking about sample populations we will employ another notation for the expected value. In case an estimator for the expected value was used, we will denote this with a subscript. For example with $_{MC}$ for Monte Carlo estimates. When the context permits it (especially when using $\rho \equiv \mathcal{U}(0,1)$) or the distribution is unknown, the index for the probability distribution is also omitted.

$$\langle X \rangle_\rho = \langle \bar{X} \rangle_\rho = \int x \, \rho_X(x) \, \mathrm{d}x \qquad (2.2.4)$$

While the sample mean is an unbiased estimator for the population mean as shown before, variance σ_x^2 and sample variance $\hat{\sigma}_{\bar{X}}^2$ do differ. We rewrite eq. 2.1.13 in our new notation. Even though the formula for the variance in eq. 2.2.5 is often used in analytic calculations, it is numerically unstable and requires all samples to be stored at the same time. This is impossible even for rather small simulations. Fortunately, there are algorithms available to circumvent these problems (see sec. 5.7).

$$\sigma_X^2 = \int (x - \langle x \rangle)^2 \, \rho_X(x) \, \mathrm{d}x = \langle X^2 \rangle - \langle X \rangle^2 \qquad (2.2.5)$$

$$\hat{\sigma}_X^2 = \frac{1}{N-1}\sum_{i=1}^{N}\left(x_i - \bar{x}\right)^2 \qquad (2.2.6)$$

This is again an unbiased estimator for the true variance, i.e.

$$\mathbb{E}\left[\hat{\sigma}_{\bar{X}}^2\right] = \sigma_x^2 \qquad (2.2.7)$$

The unbiased estimator of the covariance called sample covariance follows directly:

$$\hat{\sigma}_{\bar{X}\bar{Y}} = \frac{1}{N-1}\sum_{i=1}^{N}\left(x_i - \bar{X}\right)\left(y_i - \bar{Y}\right) \qquad (2.2.8)$$

In order to be able to compare the amount of dependence between two variables with different units, a better measure is the normalized covariance known as Pearson correlation function which takes values in [-1, 1].

$$\rho_{XY} = \frac{\mathrm{Cov}[X,Y]}{\sqrt{\mathrm{Var}[X]\mathrm{Var}[Y]}} \qquad (2.2.9)$$

Although hugely beneficial when dealing with sample data (due to the possibility for bootstrap algorithms and hypothesis testing), the Pearson correlation is to cum-

bersome for physics applications. Here we will use another measure that will later be generalized to Green's functions

$$C_{XY}(n, m) = \langle X_n Y_m \rangle \tag{2.2.10}$$

Note that the intuitive choice of an estimator $\hat{\rho}_{XY} = \hat{\sigma}_{\bar{X}\bar{Y}}\left(\hat{\sigma}_{\bar{X}}^2 \hat{\sigma}_{\bar{Y}}^2\right)^{-1/2}$ is biased[4]!

We will introduce stochastic processes later in this chapter. These can have changing mean and variance over time. In order to describe correlations between samples from these processes, we define the cross-covariance and cross-correlation functions[5]. They are equivalent to variance and correlation at equal times. Let X_n, Y_n be samples distributed according to ρ_X, ρ_Y:

$$\sigma_{XY}(m) = \mathbb{E}\left[\left(X_n - \mathbb{E}\left[X\right]\right)\left(Y_{n+m} - \mathbb{E}\left[Y\right]\right)\right]$$
$$= \mathbb{E}\left[X_n Y_{n+m}\right] - \mathbb{E}\left[X_n\right]\mathbb{E}\left[Y_{n+m}\right] \tag{2.2.11}$$

$$\rho_{XY}(m) = \mathbb{E}\left[\left(X_n - \mathbb{E}\left[X\right]\right)\left(Y_{n+m} - \mathbb{E}\left[Y\right]\right)\right] / \sqrt{\mathrm{Var}[X]\mathrm{Var}[Y]} \tag{2.2.12}$$

In case $Y = X$ these are called autocovariance and autocorrelation (as a shorthand this is often denoted $\rho_X(m) = \rho_{XX}(m)$). They reduce to the normal covariance and correlation, if $m \equiv 0$.

From this follows the interpretation of the autocorrelation distance (later called autocorrelation time since m becomes the time variable): assuming a process is designed in such a way that correlations between different samples are monotonically decreasing, then there exists an autocorrelation length m' which marks a threshold after which the correlation of two random variables $X_i, X_{i+m'}$ becomes negligible. In fact, the increase of autocorrelation becomes the main limiting factor beside the sign problem in the efficiency of Monte Carlo algorithms.

We can redefine the sample variance in terms of the autocorrelation time τ_X (see [54] for details).

$$\sigma_{\bar{X}}^2 = \frac{\mathrm{Var}[X]}{N}\left(1 + 2\tau_X\right) \tag{2.2.13}$$

$$\tau_X = \frac{1}{2\,N\,\mathrm{Var}[X]}\sum_{i>j}\left(x_i x_j - \langle x_i \rangle \langle x_j \rangle\right) \tag{2.2.14}$$

$$= \sum_{n=1}^{N}\left(1 - \frac{n}{N-1}\right)\frac{\rho_X(n)}{\mathrm{Var}[X]} \tag{2.2.15}$$

Comparison with eq. 2.1.14 shows that the autocorrelation time contains information about the covariance of measurements at different steps. Notice that we need access to all samples at once to compute the naive formula above. This becomes unfeasible in realistic simulations. We will discuss suitable approximations in sec. 2.7.1 and corresponding algorithms in sec. 5.7.

2.3   PSEUDO RANDOM NUMBERS

Computers are deterministic Turing machines and can therefore not generate true randomness without the use of an external device. Monte Carlo applications re-

---

4 As discussed by [84], there is a complicated unbiased estimator in terms of the hypergeometric function available.

5 In the literature these terms are often used interchangeably. This is problematic since one has a closed form unbiased estimator, the other does not.

quire special care in the selection of algorithms for the generation of pseudo random number because a very large uncorrelated number of them is needed. These correlations are dangerous as results obtained from them may be systematically wrong even though the usual diagnostics fail (see discussion at the end of this chapter). In the following we will formalize the notion of pseudo random numbers and discuss common strategies to obtain such numbers.

A function $f(x)$ is called *one way function* if it is computable in polynomial time and for all probabilistic polynomial time algorithms a (pseudo) inversion (i.e. find x' with $f(x') = f(x)$) only succeeds with negligible probability.

It can be proven that the existence of true one-way functions implies not only the existence of polynomial time pseudo random generators but also corresponding cryptographic algorithms (see chapter 9 of [8]). From their existence would also follow that $\mathbb{P} \neq \mathbb{NP}$ [6]. It is thus a reasonable conjecture to assume the existence of these functions.

An often used example for one way functions is the modulo (remainder after division) operation which illustrates many of the techniques and possible shortcomings of more complicated methods. A well known property from number theory, proven by C. F. Gauss in 1801 in article 57 of "Disquisitiones Arithmeticae", is the existence of primitive roots modulo some integer of prime numbers. One defines the primitive root b modulo n in the following way.

$$b^i \equiv j \quad (\text{mod } n), \qquad 1 \leq i \leq n \tag{2.3.1}$$

The remainders j are by definition a permutation of all integer numbers from 1 to n in a conjectured unpredictable order[7]. Since the modulo operation restricts invertibility of the computation of j, $f(n, i) = j$ is a one-way-function.

There are two common uses of the formula above: The first one is the Diffie–Hellman key exchange which provides the link to cryptography[8].

The second one is the generation of a string of n pseudo random numbers j. Pseudo number generating algorithms of this type are called linear congruential generators (LCG).

$$X_{n+1} = aX_n + b \quad (\text{mod } n) \tag{2.3.2}$$

X_0 is called seed and usually set from the current time stamp or another rapidly changing external value. Iterative application constructs a characteristic polynomial with monomials according to eq. 2.3.1 which inherit properties such as period length from primitive roots [79]. Realistic algorithms often include non-linearities to obfuscate the generation process more. But this does not guarantee to increase "randomness" despite the cost of additional computation time [79]. A reasonable compromise is for example the well tested "Mersenne prime twister" or "lagged Fibonacci generator".

Even though unpredictable, the generated pseudo random numbers will in some sense be correlated due to common generation process. This is especially true in

---

6 One can proof this by showing that $\mathbb{P} = \mathbb{NP}$ implies non-existence of one-way functions. A great non-technical explanation was given by by R. Impagliazzo [66].

7 There is no algorithm available to find a primitive root, but they tend to be quite dense. If n has at least one primitive root it can be proven to have exactly $\phi(\phi(n))$, ϕ is Euler's totient function. See chapter 8 [26].

8 Two people each compute f with common values for b and n, but secret i and i'. Clever computation provides a common key that no man-in-the-middle is able to compute. See [53] for a full discussion of this algorithm.

high dimensions and programs utilizing multiple processors, where the limiting factor of a finite period becomes quickly noticeable. The reason for this is the sequential nature of the generation algorithm. This can for example be visualized by constructing n-dimensional vectors and setting the components to $X_i, \dots, X_{i+n}$. One can then imagine these vectors as points in a high dimensional space and plot planes along certain axis. This has been done in fig. 2.1. One can clearly see some sort of correlation between these "random" points. This shows that certain areas
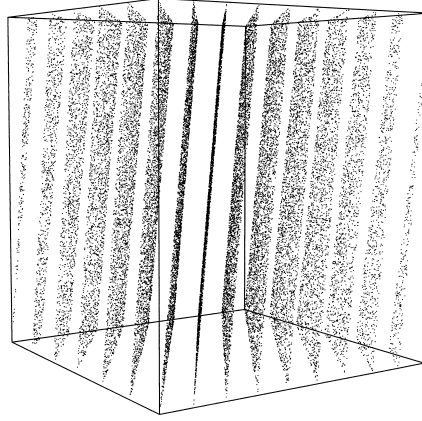
Figure 2.1: Correlated pseudo random numbers along hyper planes, generated using a LCG, taken from [63].

of space may never be reached by a chain of pseudo random numbers which can change the result of simulations drastically. There is no mathematically justifiable best strategy available in these cases. However there are some established software suites such as Diehard [112] or TestU01 [82] that are designed to test pseudo random number generators (PRNGs) for known shortcomings. They do not only bring some mathematically rigorous tests but also contain Monte Carlo methods which are tested for consistency across multiple PRNGs. This is an important test every Monte Carlo program should undergo at some point. More examples of problems with pseudo random numbers and possible solutions are discussed in [63]. Often algorithms provide some control parameter for the maximal length of a cycle, this value should be tweaked and the consistency of the result checked. When using multiple CPUs, the use of PRNGs becomes more difficult since the seed or the algorithm itself may introduce additional correlations.

The central requirement for the algorithm which uses the PRNG is to *play fair*, this means the results should be independent of hardware and operating system. The naive approach of having every thread (thread and process are interchangeable in this context) handle its own seed is also known as random seeding. This obviously violates our constraint since some compiler optimizations or hardware configurations may lead to the same seed [9]. This will result in completely correlated samples which in turn change the resulting observables. Note that even when different seeds are chosen, the fact that all generators posses the same period, correlations are still possible. There are two prevailing strategies for the distribution of random numbers over multiple threads in use: leapfrog and sequential splitting [13].

Let T be the number of threads and X_i the i-th pseudo random number for some

---

9 This is true for single instruction multiple data architectures (SIMD), similar problems arise with all other architectures as well [6].
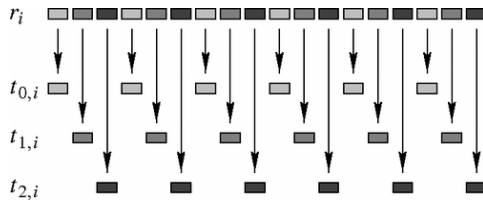
Figure 2.2: Leapfrog scheme for three streams [13]
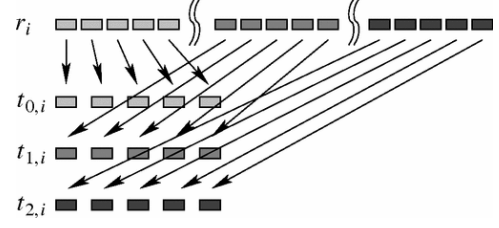
Figure 2.3: Block splitting scheme for three streams [13]

seed X_0. Then leapfrog assigns the j-th number for thread k as $X_{T \cdot j+k}$. Sequential splitting assigns $X_{M \cdot k+j}$ where $j < M$ has to be enforced. The second method needs the ability of the PRNG to jump ahead in the stream, leapfrog's efficiency is improved by this as well. Most modern algorithms provide this feature.

There are many libraries available that provide a collection of PRNGs together with transformation (sec. 2.5.1) and distribution algorithms. They usually return a uniformly distributed floating point number in $[0, 1)$ which then has to be transformed in order to obtain the desired distribution.

For this project I decided to use Tina's Random Number Generator Library [13] due to its modern C++ design and tested behavior in solid state Monte Carlo programs. All PRNG algorithms contained in this package were tested for consistency on the Ising model using the Wolff algorithm by the developer.

2.4 MONTE CARLO INTRODUCTION

Monte Carlo (MC) methods play a central role for the simulation of complex processes in the fields of numerical mathematics, economics and physics. The most distinct advantage over other, more specialized, approaches is the brute force character of MC methods. They do assume almost nothing about the underlying numerical or physical structure of the problem and are therefore especially well suited in cases where either no fast specialized algorithms are available or where an unbiased comparison is needed.

The common structure of all MC algorithms is the estimation of parameters by stochastic sampling. One well known example is the evaluation of high dimensional integrals where MC sampling converges as $1/\sqrt{N}$ with the number of samples, while traditional integration methods have exponentially larger runtime in the number of dimensions. Below we will discuss this example in more detail since other, more complex problems can be mapped to it. Lets start by restricting our probability space to a subset of $\mathbb{R}^D$

$$f : \Omega \to \mathbb{R}, \qquad \Omega \subset \mathbb{R}^D$$

We want to evaluate the integral

$$I(f) = \int_\Omega f(x)\, \mathrm{d}\mu \qquad (2.4.1)$$

Consider the simple trapezoidal rule. The computational complexity scales exponentially with the dimension of Ω. The simplest estimation for eq. 2.4.1 with $D = 1, \Omega = [a, b]$ and equal spacing h is:

$$I(f) = I_{\text{trapezoidal}}(f) + \mathcal{O}(h^2)$$

$$= \frac{h}{2} \left(f(a) + f(b) + \sum_{a < x_i < b} 2 f(x_i) \right) \tag{2.4.2}$$

One can obtain a multi-dimensional version of this method by slicing the D-dimension domain in to $m \times D - 1$ dimensional regions. Doing this recursively and applying the one-dimensional method for $D = 1$, then for every slice of $D = 2$ and so on, one arrives at a runtime of $\mathcal{O}(C^D)$, where C is the runtime for the method in 1D.
For the trapezoidal rule eq. 2.4.2 this reads with $\Omega = [a, b] \times [c, d]$ and equal spacing h in both dimension

$$I_{\text{trap}}(f) = \frac{h^2}{4} \left(4 \sum_{\substack{x_j > c \\ x_j < d}}^{\substack{x_j < d \\ x_i < b}} \sum_{x_i > a}^{x_i < b} f(x_i, x_j) + 2 \sum_{x_i > a}^{x_i < b} f(x_i, d) + \cdots \right)$$

This runtime estimate also holds for more sophisticated methods such as newton quadrature. Since the error of numerical integration methods is bounded by the m-th derivative $\propto f^{(m)}$, additional problems may occur for oscillatory functions.
Monte Carlo integration is motivated by the observation that for some continuously distributed random variable X over Ω, with a probability density function ρ_X, integrations can be expressed by drawing samples $x_i \sim \rho_X$ and computing the expected value of finding them inside the integration area. We can rewrite eq. 2.4.1 as an expected value, we require $\rho(x) > 0 \ \ \forall g(x) \neq 0$:

$$\int_\Omega g(x) \, \mathrm{d}\mu = \int_\Omega \frac{g(x)}{\rho(x)} \rho(x) \, \mathrm{d}\mu \stackrel{\text{eq. 2.1.9}}{=} \mathbb{E}_\rho \left[\frac{g(x)}{\rho(x)} \right] \tag{2.4.3}$$

$$\Rightarrow I(f) = \mathbb{E}_\rho[f(x)] \tag{2.4.4}$$

The error and convergence of this method can be obtained with use of the central limit theorem (CLT). Let X_i i.i.d. random variables with $X_i \sim \rho$:

$$\bar{f}_N = \frac{1}{N} \sum_{i=1}^{N} f(x_i) \tag{2.4.5}$$

then

$$\lim_{N \to \infty} P \left(a \leq \frac{I(f) - \bar{f}_N}{\sqrt{\frac{\sigma_f^2}{N}}} \leq b \right) \stackrel{CLT}{=} \Phi(b) - \Phi(a) \tag{2.4.6}$$

where $\Phi(x) = \frac{1}{\sqrt{2\pi}} \int_{-\infty}^{x} e^{-\frac{t^2}{2}} \, \mathrm{d}t$ is the cumulative distribution function of the normal distribution. This implies the convergence of $\bar{f}_N$ and provides us with an estimation of eq. 2.4.4.
It is still assumed that $\Omega = [a, b]^D$. We will later discuss methods to find (x_i) so that $f(x_i)$ i.i.d. (for example inversion sampling). Inserting the estimator (eq. 2.4.5) and integral (eq. 2.4.1) into the CLT, we obtain

$$\left| \frac{1}{N} \sum_{i=1}^{N} f(x_i) - I(f) \right| = \sqrt{\frac{\sigma_f^2}{N}} \left| \frac{\frac{1}{N} \sum_{i=1}^{N} f(x_i) - N \cdot I(f)}{\sqrt{\sigma_f^2 N}} \right| = \sqrt{\frac{\sigma_f^2}{N}} |\zeta| \tag{2.4.7}$$

with $\sigma_f^2 = \int_\Omega (f(x) - I)^2 \rho(x) \, d\mu$ and $\zeta \sim \mathcal{N}(0, 1)$. This shows that the convergence ratio is $\mathcal{O}(\frac{1}{\sqrt{N}})$, which does not explicitly depend on D! Independence on the dimension of Ω is the single most important property of Monte Carlo methods, since most other methods can not be used in high dimensional state spaces. The rate of convergence for the variance is however not guaranteed to be bounded. Although there are variance reduction schemes available which will be discussed in sec. 2.5, they can break down when dealing with fermionic many particle interactions. This is known as the sign problem (see sec. 2.8).

2.5 SAMPLING METHODS

Sampling methods are an important tool in cases where a full distribution function is not known as an analytic function or the state space is very large and full computation of the distribution is impossible. Both cases are present in many body particle physics for which the Hilbert space grows exponentially with the number of particles and the full interacting wave function is unknown. In order to simplify the discussion of sampling methods, we narrow the definition to real valued, continuous random variables and functions for now.

Let $f : \mathbb{R} \to \mathbb{R}$ be a probability distribution. We want to generate samples from that distribution so that a

Figure 2.4: ζ as argument of the pseudo inverse (in this case equivalent to the normal inverse).

histogram of all samples will give a reasonable estimation of f (see MC convergence in the previous section). There are different methods available in order to sample $x_i \sim f$ which differ in convergence performance depending on the form of f and have varying requirements.

2.5.1 *Inversion Sampling*

Let ζ be some real valued random variable. Note that $\forall x : f(x) \geq 0$ implies that the CDF $F_X(x) = \int_{-\infty}^x f(z) \, dz$ is monotonic ($x \sim \rho_X$). We first define the pseudo inverse of $F_X(x)$ by using the fact that the cumulative distribution function $F_X(x) = P(X \leq x)$ is monotonic and right continuous:

$$F_X^{\leftarrow}(x) = \inf\{ z \mid F_X(z) \geq x \} \tag{2.5.1}$$

One can easily check that this meets the requirements of a pseudo inverse in eq. 2.5.3. Now we choose $\zeta \sim U(0, 1)$ so that:

$$F_\zeta(x) = x \tag{2.5.2}$$

$$\Rightarrow P(F_X^{\leftarrow}(\zeta) \leq x) = P(\zeta \leq F_X(x)) = F_X(x) \tag{2.5.3}$$

with $\zeta \sim f(U)$. See also fig. 2.4.

This results in an easy algorithm (alg. 1) for the estimation of the distribution $F_f(x)$ which will serve as a prototype for the more sophisticated methods below. It is pos-

---

input : Solver for $x = F_X^{\leftarrow}(\zeta)$, U (0,1), N
output: Array x of length N with samples

1 Reserve array x of length N
2 $i = 0$
3 **while** $i < N$:
4   Draw $\zeta \sim U(0, 1)$
5   Solve $x[i] = F_X^{\leftarrow}(\zeta)$
6      $i = i + 1$
7 **return** x

Algorithm 1: Inversion Sampling

---

sible to extend this method to $x \in \mathbb{R}^n$.

In fig. 2.5 and fig. 2.6 the result for the inversion sampling algorithm implemented in Python is shown [10]. Comparing the results for 100 and 2000 samples we can estimate that data sufficiency is achieved at around 500 samples with this method. The $\frac{1}{\sqrt{N}}$ convergence bound is plotted for comparison. The inversion sampling algorithm provides an efficient way of transforming a "well behaved" distribution to a more complicated one. This is actually a very common problem since most libraries for the generation of pseudo random numbers only generate uniformly distributed random variables. The most widely used application for this is the Box-Muller algorithm which computes Gaussian distributed variables from uniform samples. Although inversion sampling is very efficient compared to the next methods, it relies on the fact that the pseudo inverse can be constructed. We will now look at methods that get around this problem.

2.5.2   *Rejection Sampling*

The first attempt of an improved method will be rejection sampling.

Let $f \colon \mathbb{R}^n \to \mathbb{R}$ be some measurable function with measure μ, that is analytically unknown and hard to sample from directly. Choose some *envelop density* $\tilde{f} \colon \mathbb{R}^n \to \mathbb{R}$ and factor $c \in \mathbb{R}$ so that $\forall x \in \mathbb{R}^n : c\tilde{f}(x) \geq \mu(f(x))$. We don't require f to be positive or even real valued. Its measure can be used to obtain a positive function and the renormalization can be absorbed into c. To obtain a sample from $\tilde{f}$ one could use algorithm alg. 1. The efficiency of this algorithm obviously depends on the discrepancy of f and $\tilde{f}$ and can therefore be estimated by c. Proof of this method is left to the literature, e.g. [54].

We will later use Monte Carlo methods for complex valued functions. Of course $\mathbb{C} \sim \mathbb{R}^2$ guarantees correctness but there are some subtleties nonetheless. For details see [38].

While this method is stated for continuous distributions, it is of course easily adapted to discrete distributions using the Dirac or discrete measure. We can see from fig. 2.9 that the target distribution is less accurately approximated than through inversion sampling for equal runtime. The reason is the lower effective sample size, because

---

10 The code for all sampling algorithms is available at `https://github.com/Atomtomate/MSC_Thesis`
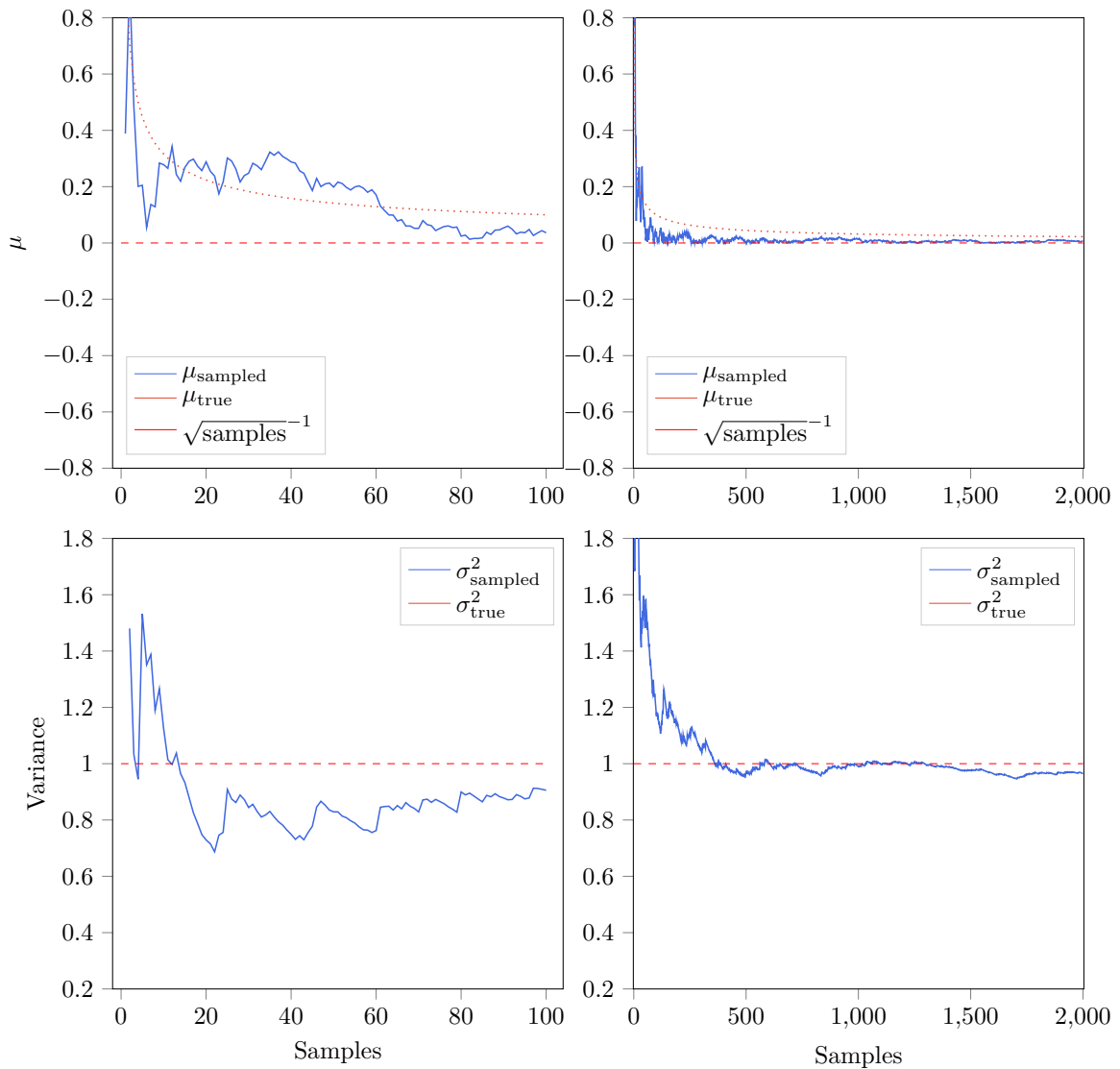
Figure 2.5: Inversion sampling of normal distribution
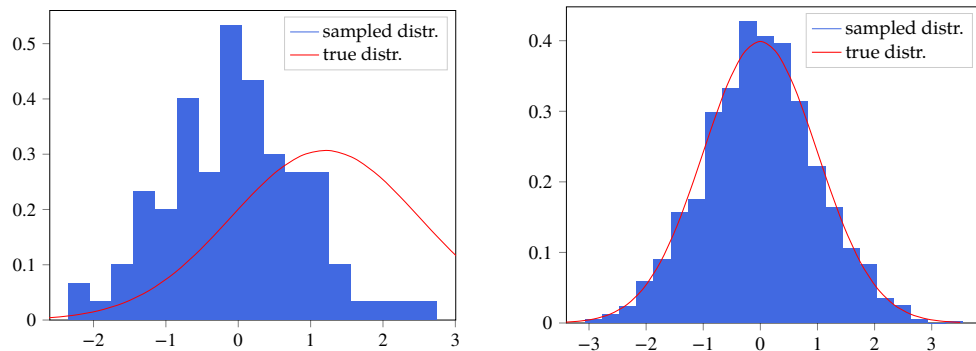
Figure 2.6: Sampled standard normal distribution using inversion sampling 100 and 2000 samples.

we reject some of the samples. One can improve rejection sampling by changing the envelop distribution whenever a sample is rejected. This is done by setting the envelop distribution to the true value $f(x)$ at this point of the now piecewise defined
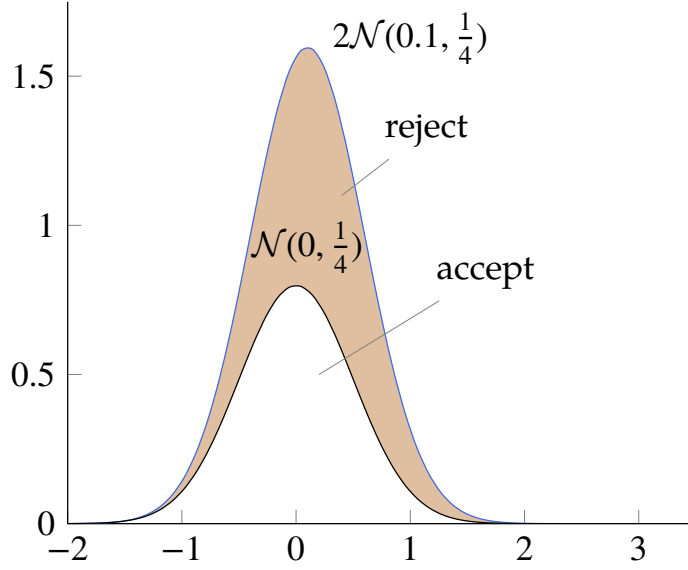
Figure 2.7: Slightly shifted normal distribution with $c = 2$ scaling as envelope distribution for another Normal distribution

input : PDFs $\tilde{f}, U(0,1)$; a function f, factor c
output: Array x of length N with samples

1 reserve array f_{sample} of length N
2 $i = 0$
3 **while** $i < N$**:**
4   Draw $x_i \sim \tilde{f}$
5   Draw $\zeta \sim U(0, c \cdot \tilde{f}(x_i))$
6   **if** $\zeta < \mu(f(x))$**:**
7          $f_{sample}[i] \leftarrow x$
8          $i = i + 1$
9 **return** f_{sample}

Algorithm 2: Rejection Sampling

envelope distribution. Using this method the rejection rate is reduced with every rejected sample. We will however not use this improvement here since the implications for the autocorrelation times when using the Metropolis algorithm are quite complicated to track. Because we only use the simple version the next method is strictly better than rejection sampling.

2.5.3   *Importance Sampling*

Sometimes the following class of algorithms are also called variance reduction methods. This connects our previous considerations in sec. 2.4 to the sampling methods we have used so far. It is clear that we need to require $f(x) > 0$ for all sampling methods to work. We can however transform any L^1 function into a probability distribution by setting $\rho_f = \frac{1}{Z} |f(x)|$ with appropriate normalization Z and by tracking
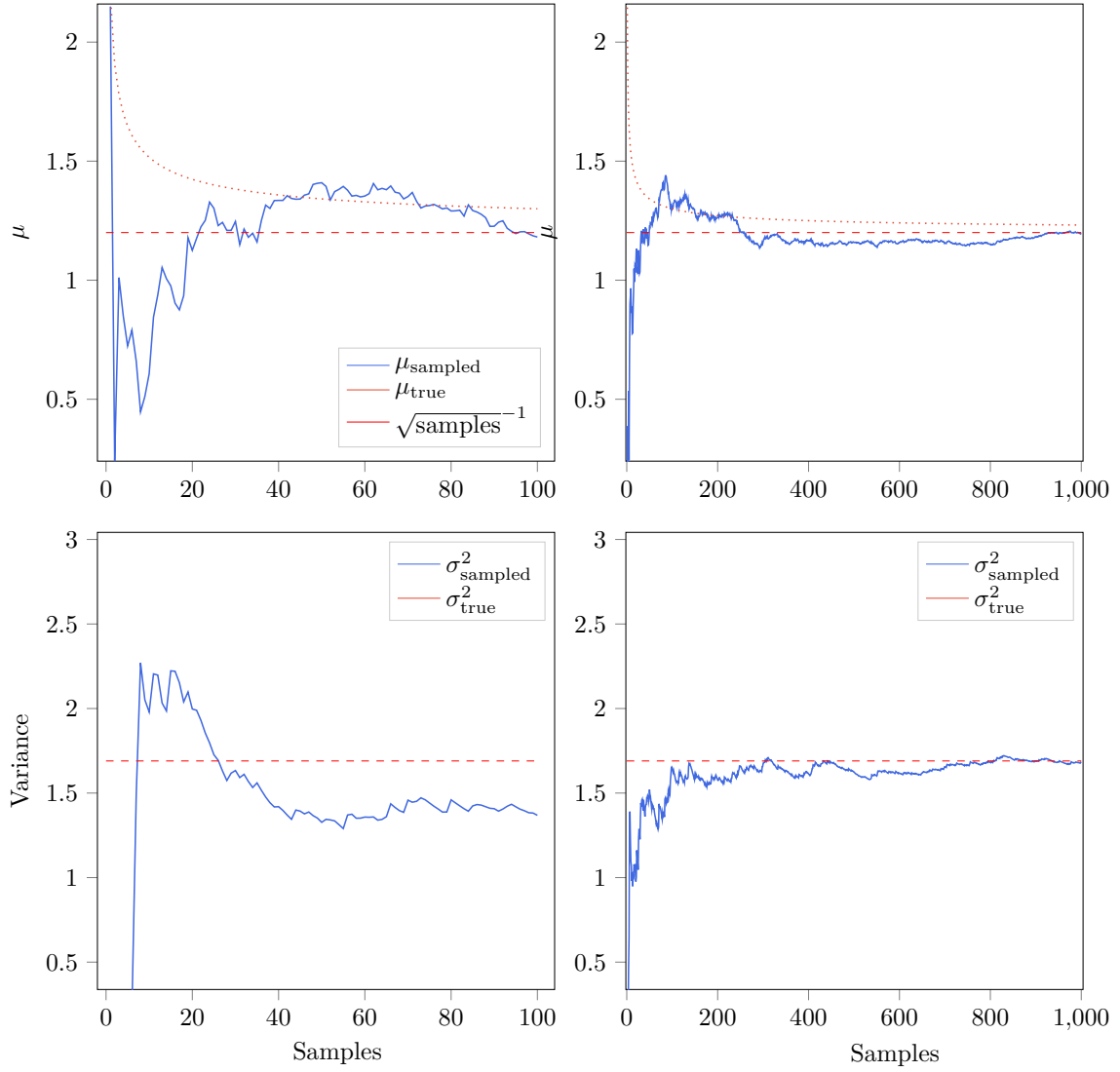
Figure 2.8: Rejection sampling for 100 and 1000 samples. $\mathcal{N}(1.2, 1.3)$ as true and $5.2 \cdot \mathcal{N}(1.2, 2.5)$ as envelope distribution.

the actual sign of each sample and accumulating the absolute value of f as well as that of the sign.

$$\frac{1}{N} \sum_i^N x_i \longrightarrow \frac{1}{\sum_i^N \text{sign}(x_i)} \sum_i^N \text{sign}(x_i)|x_i|$$

As before (see also sign problem, sec. 2.8) this is especially problematic for oscillating functions. In quantum mechanics a change of basis can sometimes improve the sign problem, we will find an example later for the continuous time CTQMC algorithm. While importance sampling is often used due to its simplicity, it is problematic for skewed distributions which are badly approximated by the envelope distribution $\tilde{\rho}(x)$. This becomes especially important in high dimensions, when the volume is concentrated near the surface. Since high dimensional integrals are exactly the domain of MC integrations it is important to find a solution to this problem.

Similarly to eq. 2.4.3 it is possible to introduce another distribution $\tilde{\rho}$ in order to
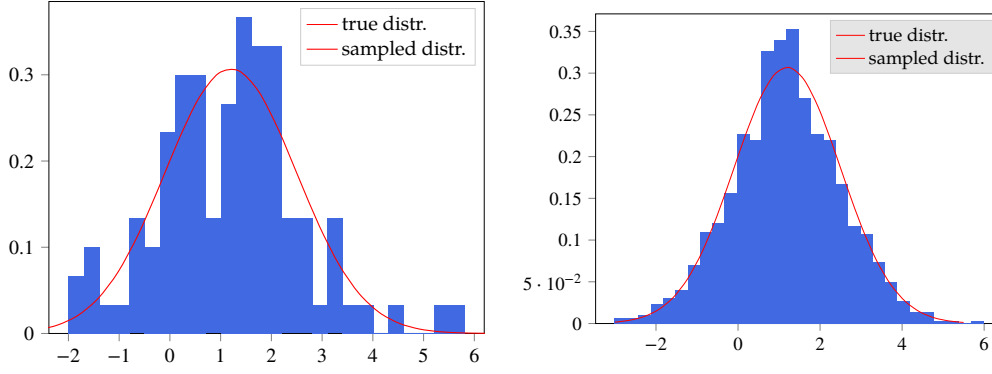
Figure 2.9: Sampled distribution with 100 and 1000 samples, using rejection sampling.

weigh samples. Note that we use notations for configurations here but it may be more intuitive for now to think of $\Omega = \mathbb{R}^n$ and different configurations $C \in S$ as samples $x_1, x_2, \ldots, x_N$. Then all integrals have well defined Lebesgue measure and the convergence of a sample set $|S| = N$ becomes the usual $\lim_{N \to \infty}$ for N samples.

$$\mathbf{E}_\rho[f] = \int f(C)\rho(C) \ \mathrm{d}C = \int f(C)\tilde{\rho}(C)\frac{\rho(C)}{\tilde{\rho}(C)} \ \mathrm{d}C \qquad (2.5.4)$$

$$= \mathbf{E}_{\tilde{\rho}}\left[f\frac{\rho}{\tilde{\rho}}\right] \qquad (2.5.5)$$

There are two main reasons why we did we not immediately choose $\tilde{\rho}$ as an envelope distribution instead of $\rho(x)$: We do not necessarily have access to a sampling mechanism for ρ and while inversion sampling can provide a method for transformations it is not guaranteed to be feasible. Evaluation of the expectation of $f\frac{\rho}{\tilde{\rho}}$ amounts to only some function evaluations and can easily be offset by faster sampling. An even more important reason is that we can compute the normalization constant Z for ρ during the sampling process. In preparation for the application in statistical physics we already use the same symbol as for the partition function.

$$1 = \frac{1}{Z}\int \rho(C)\,\mathrm{d}C = \frac{1}{Z}\int \tilde{\rho}\,\frac{\rho}{\tilde{\rho}}\,\mathrm{d}C = \frac{1}{Z}\mathbf{E}_{\tilde{\rho}}\left[\frac{\rho}{\tilde{\rho}}\right]$$

This property is essential since naive computation of Z involves a similar integral to the original one, which is precisely the problem this algorithm was supposed to alleviate in the first place. The fraction $\rho(C)/\tilde{\rho}(C)$ is called weight w_C of configuration C with probability p_C

$$w_C = \frac{\rho(C)}{\tilde{\rho}(C)} \qquad (2.5.6)$$

$$p_C = \frac{w_C}{Z} \qquad (2.5.7)$$

Putting everything together we get a very useful estimator for the expected value of a function f for some sample set $S \subset \Omega$

$$I(f) = \mathbf{E}_{\rho}[f] = \frac{\int_{\Omega} w_C f(C) \tilde{\rho}(C) \, dC}{\int_{\Omega} \rho(C) \, dC} \tag{2.5.8}$$

$$\approx \langle f \rangle_{\rho} = \frac{\sum\limits_{C \in S} w_C f(C)}{\sum\limits_{C \in S} w_C} = \sum\limits_{C \in S} p_C f(C) \tag{2.5.9}$$

In case the weights are not all positive because they were not sampled from a probability distribution, there is still a way to make this calculation work by defining $s(c)$ as the sign of the configuration:

$$\frac{\sum\limits_{C \in S} w_C f(C)}{\sum\limits_{C \in S} w_C} = \frac{\sum\limits_{C \in S} \text{sign}(C) |w_C| f(C)}{\sum\limits_{C \in S} \text{sign}(C) |w_C|} \tag{2.5.10}$$

From the general expression for the variance estimator (eq. 2.2.6) follows the estimator for the variance in terms of the weights

$$\text{Var}[f] \approx \frac{1}{N-1} \frac{\left\langle \left(w_C f(C) - w_C \langle f \rangle \right)^2 \right\rangle}{\langle w_C \rangle^2} \tag{2.5.11}$$

$$= \sum\limits_{C \in S} w_C^2 (f(C) - \langle f \rangle)^2 \tag{2.5.12}$$

In order to verify the results one can chose from a large number of statistical methods. It is not worth going into much detail here since the dominant factor in our case will be correlations and estimators for the confidence intervals of importance sampled observables do not generally carry over to the Metropolis algorithm in the next section [2].

We can however immediately observe that there is only an effective number of samples contributing to the overall average. This is a good estimator for data sufficiency and quality of the proposal distribution. The choice of a good estimator for the effective sample size is an art that requires a lot of experience with Monte Carlo simulations. Generally there are three formulas used when no specific details of the simulation are known [2, 54]:

$$n_{\text{eff},1} = \frac{N \langle w \rangle^2}{\langle w^2 \rangle} \tag{2.5.13}$$

$$\approx \frac{N}{\langle w \rangle_{\rho}} \tag{2.5.14}$$

$$n_{\text{eff},2} = \frac{N}{1 + cv^2(w)} \tag{2.5.15}$$

$$cv^2(w) = \sqrt{\frac{1}{N-1} \sum\limits_{C} \left(w_C - \langle w \rangle \right)^2}$$

The effective sample size is a better measure for the quality of the simulation than the variance of the expected value, because skewed weights may lead to a low sample variance around a skewed sample mean. The concept of effective sample sizes

```
input  : functions f̃, f;
output: Array f_sample of length N with samples and normalization Z

1  reserve array f_sample of length N
2  Z = i = 0
3  while i < N:
4      Draw x_i ~ f̃
5      w_i = f(x_i)/f̃(x_i)
6      f_sample[i] = w_i · x_i
7      Z = Z + w_i
8      i = i + 1
9  return f_sample, Z
```

Algorithm 3: Importance Sampling

can however be generalized to variance and skewness (a derivation can be found in chapter 9 of [2]):

$$n_{\text{eff},\sigma} = \frac{\left(\sum_C w_C^2\right)^2}{\sum_C w_C^4} \tag{2.5.16}$$

$$n_{\text{eff},\gamma} = \frac{\left(\sum_C w_C^2\right)^3}{\left(\sum_C w_C^3\right)^2} \tag{2.5.17}$$

The form of eq. 2.5.9 is especially useful due to its similar form to many particle expectation values. We now have a method for sampling which does not require us to know the normalization of the distribution. The drawbacks so far are:

proposal distribution   We need to have at least some knowledge about our desired distribution. This can turn out to be a severe limitation for simulations of many particle wave functions since their form is generally unknown and the algorithm does not adapt with more knowledge of the target distribution.

curse of dimensionality All direct sampling methods suffer from the so called curse of dimensionality: With increasing dimension of $\mathbb{R}^n$ the shell region of sub-manifolds contribute more to the overall volume. But the methods above sample uniformly over regions. In other words, relative distances become increasingly indistinguishable in high dimensions [2].

2.6 MARKOV CHAIN MONTE CARLO

Proofs and derivations for the statements in this section can be found here: [127, 4] In the previous chapter we have discussed independent samples of distributions. We have improved the sampling from skewed distributions before using importance sampling. This assumed existence of not only an envelope/proposal distribution ρ but also a second distribution $\tilde{\rho}$. Since we often don't know the form of ρ, it may be the exact many particle wave function or similarly unobtainable functions, our approximation $\tilde{\rho}$ will be very crude when trying to define it explicitly. This is the
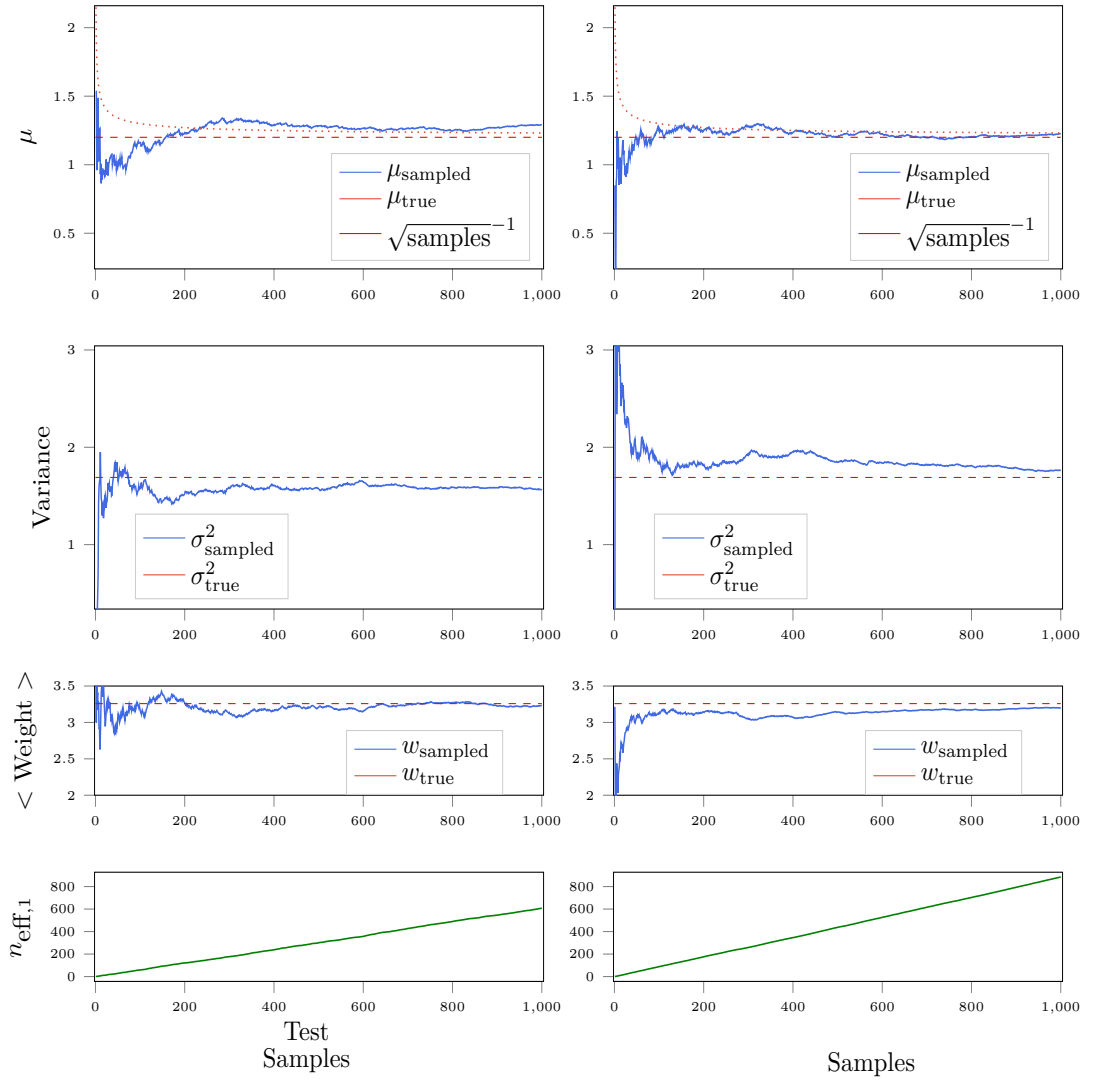
Figure 2.10: Importance sampling for 1000 samples with envelope distribution $\mathcal{N}(2.5, 1.5)$ and $\mathcal{N}(1.5, 1.3)$ as proposal distributions.
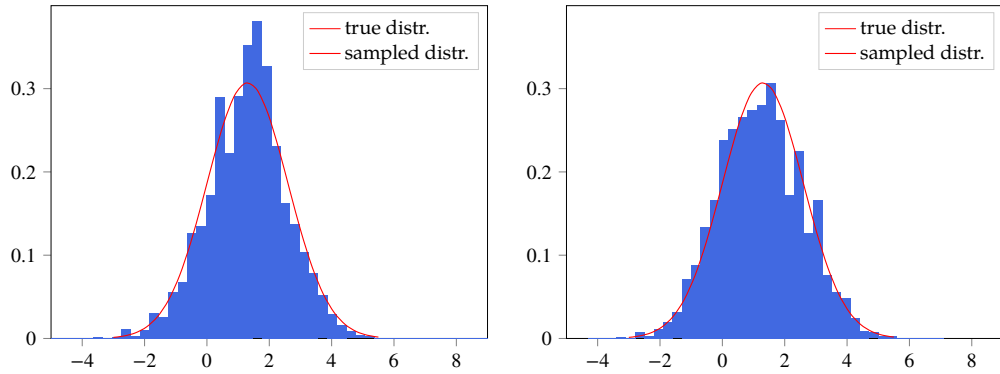
Figure 2.11: Sampled distributions using importance sampling for 1000 samples with envelope distribution $\mathcal{N}(2.5, 1.5)$ and $\mathcal{N}(1.5, 1.3)$ as proposal distributions.

field of application for Markov chains which "converge" against a limiting distribution, while providing computationally cheap samples. They belong in the domain of stochastic processes where one defines a series of variables over a common domain. Stochastic processes are widely used in physics. For example the Lagevin equation in non-equilibrium thermodynamics is related to Brownian motion (Wiener process) and the Fokker-Planck equation to the Ornstein-Uhlenbeck process.

A Markov chain is a chain of possible transitions which only depend on the last state. Still using def. 1, let Ω be countable and $C_i \in S$.

Definition 11 (Markov Chain) We call a sequence of discrete random variables $(X_n) = X_1, X_2, \dots$ a Markov chain if the Markov condition is fulfilled:

$$P(X_j = C_{n+1} | X_n = C_n, \dots, X_1 = C_1) = P(X_{n+1} = C_{n+1} | X_n = C_n) = P_{n,n+1} \qquad (2.6.1)$$

Since all conditional probabilities only depend on two random variables, they can be written in matrix form as indicated above.

Definition 12 (Homogeneous transition matrix) P_{ij} is called transition matrix or stochastic matrix and satisfies $P_{ij} \geq 0$, for $i, j \in S$ and $\sum_{j \in S} P_{ij} = 1$.
The Markov chain is called *homogeneous* in case $P_{i\,i+1} = P_{0\,1}$ for all $0 < i < n$.

It is possible to extend this definition to continuous random variables. In short, the continuous Markov process is a stochastic process that only depends on the time difference (not the absolute times) in the homogeneous case. Even though we will encounter continuous processes later, a derivation is left to the literature [127] From def. 12 follows, that

$$P(X_n = C_n, \dots, X_0 = C_0) \stackrel{def\ 11}{=} P_{n-1\,n} \cdots P_{0\,1} P(X_0 = C_0)$$

It is obvious that the initial state $\rho_i = P(X_0 = C_i)$, $C_i \in S$ has an influence on the overall behavior of the Markov chain. In the following, two shorthand notations will be used to indicate which initial state (i.e. initial distribution) was used ($\rho = (\rho_1, \cdots)$ is a row vector here).

$$P_i(\cdot) = P(\cdot)P(X_0 = C_i) \qquad (2.6.2)$$
$$P(\cdot) = P_\rho(\cdot) \qquad (2.6.3)$$

It is easy to see that a transition probability from the starting distribution $P(X_0 = i)$ in n steps to state j is the n-th power of the transition matrix.

$$\left[P^n\right]_{ij} = P_i(X_n = C_j) \qquad (2.6.4)$$
$$\left[\rho P^n\right]_j = P(X_n = C_j) \qquad (2.6.5)$$

The statement follows by induction from the observation:

$$P(X_1 = C_j) = \sum_{i \in S} \rho_i(X_1 = C_j | X_0 = C_i) = \sum_{i \in S} \rho_i P_{ij}$$
$$P_i(X_2 = C_j) = \sum_{k \in S} P_i(X_2 = C_j, X_1 = C_k) = \sum_{k \in S} P_{ik} P_{kj} = [P^2]_{ij}$$
$$P(X_2 = C_j) = \sum_{i \in S} P_i(X_2 = C_j) = \sum_{i,k \in S} \rho_i P_{ik} P_{kj} = [\rho P^2]_j$$

From this follows a special case of the Chapman-Kolmogorov equation:

$$[\boldsymbol{P}^{n+m}]_{ij} = \sum_{k \in S} [\boldsymbol{P}^{n}]_{ik}[\boldsymbol{P}^{m}]_{kj} \tag{2.6.6}$$

In order to connect our previous sampling algorithms with Markov chains we first need three definitions. Left eigenvectors of the transition matrix P are called *invariant (or stationary) measure* for P.

$$\sum_{i \in S} w_i P_{ij} = w_j, \qquad i, j \in S, \quad 0 \leq w_j < \infty \tag{2.6.7}$$

If the invariant measure is also normalized it is called *stationary distribution*. It is usually denoted by $\pi = \left(\pi_C\right)_{C \in S}$

$$\sum_{C \in S} \pi_C = 1 \tag{2.6.8}$$

This can of course be obtained from eq. 2.6.7, although using the unnormalized w_C in place of π_C is often more preferable (see detailed balance in eq. 2.6.16).

$$\pi_C = \frac{w_C}{\sum_{\tilde{C} \in S} w_{\tilde{C}}} \tag{2.6.9}$$

Using the stationary distribution π as the initial distribution we can rewrite eq. 2.6.7 and eq. 2.6.4:

$$P_\pi(X_n = C) = \pi_C \tag{2.6.10}$$

So the distribution of X_n is independent of n. A Markov chain is called *aperiodic irreducible* if

$$\forall\, C_i, C_j, C_k \in S\, \exists\, n \geq 1\, : $$
$$P_i(X_n = C_k) > 0, \quad P_j(X_n = C_k) > 0 \tag{2.6.11}$$

Notice that any state must be reachable from any other state in just one transition, otherwise the the Markov chain would be periodic irreducible, this case will not be needed here. For some arguments about Markov chains, the set of visits in state C as v_C will be used:

$$v_C(n) = \{n \in \mathbb{N}_{>0}\, :\, X_n = C\} \tag{2.6.12}$$
$$m_C = \mathbb{E}[\min_n\{v_C(n)\}] \tag{2.6.13}$$

A state $C \in S$ is called *recurrent* if the return probability tends towards one, transient otherwise. It is called *(positive) recurrent* if in addition the mean return time is finite. This property splits the states into equivalence classes in which any state is reachable from each other state (see [127] p. 39 ff.).

It can be proven that each recurrent class has exactly one invariant measure ($\Rightarrow$ exactly one stationary distribution) which is uniquely determined up to a constant factor. The most useful property for our algorithms will be the convergence theorem for Markov chains (for a proof see [127] p. 52). Any aperiodic irreducible

Markov chain that possess a stationary distribution π will for any initial distribution converge against π. In this case π is also called equilibrium distribution.

$$P(X_n \in A) \rightarrow \sum_{C \in A} \pi_C \quad \forall\, A \subset S \tag{2.6.14}$$

Since the probability converges for any initial distribution the subscript is omitted here. However, for numerical implementations it is worth keeping in mind that the rate of convergence will depend on the choice of the initial distribution.

We can illustrate stationary distributions by imagining the possible configurations as nodes V on a graph $\mathcal{G} = (V, E)$ and the transition probabilities as edge weights $f(E)$ [11]. In each iteration of the Markov process updates the edge weights according to P (see eq. 2.6.4) and the Markov chain "visits" configuration C in iteration n if $X_n = C$. Now the stationary probability is the average number of visits to a node (compare eq. 2.6.12) in the limit $n \rightarrow \infty$.

$$\pi_C = \lim_{n \to \infty} \frac{|v_c(n)|}{n}$$

This is a restatement of the ergodic theorem.

We can now use the strong condition of reversibility in order to ensure the above requirements for Markov Chains with exactly one stationary distribution. A distribution π is *reversible* with regard to the transition probabilities P if:

$$\pi_i P_{ij} = \pi_j P_{ji}, \quad \forall\, i, j \in S \tag{2.6.15}$$

One can immediately see that any reversible distribution must also be a stationary distribution by comparison with eq. 2.6.9. Reversibility is also known as *detailed balance* condition when rearranged (the normalization constants cancel out in the fraction):

$$\frac{P_{ij}}{P_{ji}} = \frac{\pi_j}{\pi_i} = \frac{w_j}{w_i} \tag{2.6.16}$$

Both conditions obviously also imply eq. 2.6.11 and therefore guaranty convergence in the sense of eq. 2.6.14. Note that the converse is not true, i.e. the existence of a distribution fulfilling detailed balance is a stronger condition than aperiodic irreducibility.

The detailed balance condition is useful in the same way the weights were for importance sampling, since the state space may be very large or even unknown and computation of the normalization can be numerically unfeasible.

2.6.1 *Metropolis-Hastings Algorithm*

We have seen that an aperiodic, irreducible Markov chains will converge against a unique stationary distribution π in case π exists. The central observation for the first Markov chain Monte Carlo algorithm is eq. 2.6.16. While not a necessary condition for the existence of a stationary distribution it is easy to verify, which makes it the most practical condition.

We will use the rejection sampling method (see sec. 2.5.2) but instead of using independent samples, they will be drawn according to a Markov process (X_n). This

---

[11] the PageRank algorithm for the early version of Google search used this model, here websites are represented by nodes and hyper links are edges

means we can choose some function $Q(C_j|C_i) = Q_{ij}$ that is proportional to the distribution P we want to approximate. While these samples are correlated (which means that we gain less information per sample), there are several advantages to the Markov chain sampling: In contrast to direct sampling methods there is no need for a well suited envelope distribution. This problem is transferred to the much easier task of finding suitable proposals for the next step, because this is a local instead of a global problem. Markov chain Monte Carlo will always produce samples contrary to rejection sampling[12] and due to eq. 2.6.16 do not require the knowledge of the normalization like importance sampling.

The most important risk of Markov Chain Monte Carlo (MCMC) is the possibility of getting trapped in a small subregion of space. While the Metropolis-Hastings algorithm does not offer any mitigation for this, there are mathematical tools available to minimize this problem (see data analysis sec. 2.7). One can also chose more sophisticated proposal algorithms. This leads to the popular Gibbs sampler, suited for highly skewed distributions in high dimensional spaces, and Hybrid Monte Carlo methods, that provide adaptive step size exploration according to knowledge about the underlying physics, which are popular in finance simulations and lattice gauge theories respectively. They can however require a lot of additional function evaluations and may in fact be slower than more crude methods with more samples [54].

We will now write down the Metropolis-Hastings algorithm, which implements the basic idea of MCMC sampling. To stay consistent with our previous notation we call the weights w_C (only countable state spaces are considered in this section). $f(C) = \pi_C = \frac{1}{Z} \cdot w_C, \; Z \in \mathbb{R}$.

We split the the transition probability into a *proposal distribution Q* and a *acceptance rate R*.

$$f(C_j|C_i) = R(C_j|C_i)Q(C_j|C_i) \tag{2.6.17}$$
$$\Leftrightarrow P_{ij} = R_{ij}Q_{ij}$$

The proportionality constant $\frac{1}{Z}$ is absorbed into the right hand side. This is possible since the choice of R and Q is free as long as Q is a probability distribution. Using detailed balance ($\pi_i w_{ij} = \pi_j w_{ji}$, eq. 2.6.16) we can rewrite this to

$$\frac{R_{ij}}{R_{ji}} = \frac{w_j}{w_i}\frac{Q_{ji}}{Q_{ij}} \tag{2.6.18}$$

Our goal is the construction of a transition matrix Q_{ij} so that detailed balance for Q holds and the equilibrium distribution for Q is π. In order to see why the proposal distribution Q constructs the correct stationary distribution we write down the resulting transition matrix P using eq. 2.6.17.

$$P_{ij} = \begin{cases} R_{ij}Q_{ij} & i \neq j, R_{ij} < 1 \\ Q_{ij} & i \neq j, R_{ij} \geq 1 \\ 1 - \sum_{i \neq j} P_{ij} & i = j \end{cases} \tag{2.6.19}$$

In each step the Metropolis algorithm we propose a transition from C_i to C_j. If accepted, the new initial state will be C_j, otherwise C_i. In both cases a sample is

---

12 However the rejection rate for a transition to a new configuration can be very high, leading to correlated samples.

---

input : Q, initial state C_0, $U(0, 1)$, burn-in steps j, skip steps k
output: Array x of length N with samples

1 reserve array f_{sample} of length $(N - j)/k$
2 $i = 1$
3 $x_0 = C_0$
4 **while** $i < N$:
5      $C_a = x_{i-1}$
6   Draw $\zeta \sim U(0, 1)$
7   Draw $C_b \sim Q_{ab}$
8      $R_{ab} = \min\left(1, \frac{w_b}{w_a}\frac{Q_{ba}}{Q_{ab}}\right)$
9   **if** $R_{ab} < \zeta$:
10          $x_i = C_b$
11   **else**:
12          $x_i = C_a$
13   **if** $i \geq j$ *and* $i - j\%k == 0$:
14          $f_{sample}[\frac{i-j}{k}] = x_i$
15 **return** f_{sample}

Algorithm 4: Metropolis Hastings

returned which is then used as the next initial state.

The choice for Q can influence the convergence properties: conservative proposals with high acceptance rate will lead to slow exploration of the state space while the opposite choice will lead to a high rejection rate and therefore slow convergence as well [13]. The good value for the acceptance ratio is quoted to be 0.234 (e.g. [113, 15]), this is of course purely heuristic but demonstrates that in the absence of quantitative estimators for multiple problematic behaviors (see below), there is often no other orientation.

Deliberately aiming for a low acceptance rate may appear unintuitive. However taking into consideration that samples in MCMC are correlated, the rejection nearby steps may actually be a good way of reducing autocorrelation times and therefore achieving a higher *effective* sample size (we have already observed this in the case of importance sampling). We will later (sec. 2.7) find an estimator for the autocorrelation of samples which should decrease once the stationary distribution is reached.

One last remark can be made about the skewness of the estimators for a bad starting position. Since the initial distribution will be different from the equilibrium distribution, it is necessary to disregard the first results in order to not take the convergence towards the equilibrium into account. This is known as burn-in period.

For MCMC methods to work, we do not only require detailed balance (which implies aperiodic irreducibility) but also ergodicity (aperiodicity and positive recurrence). In case of finite Markov chains, detailed balance is equivalent to ergodicity[14].A quasi-segmentation into recurrent classes (that means taking out a few transitions would split one class into several) can lead to the simulation staying in one region for the whole simulation and therefore yielding skewed results for observables. This problem clearly depends on the initial configuration ρ_0, so a possible

---

13 There is an optimal choice, here $Q_{ij} = P(C_j)$ which assumes the knowledge of of the unknown parameter
14 This follows directly from the definition of the mean return time

indicator can be obtained by running the simulation with different ρ_0 and comparing convergence. Because the proposal distribution is chosen for the application at hand, it may also be possible to give an argument for ergodicity from the construction. In practice one has to test convergence against known results and observe the behavior of the program over many runs.

To substantiate this, we consider a simple example how segmentation may show up during simulation. Initially the observables will change rapidly while the probabilities converge according to eq. 2.6.14. After some time equilibrium is reached, i.e. the expected value of our observable fluctuates around some value. Subsequently there is a sudden change in the average value before it again converges.

This is obviously problematic since we have no way of predicting this kind of behavior from the numerical data. One can use trace-plots, a history of observables at each step, to spot such a jump in observables. But generally it is quite hard to predict such a behavior since the simulation behaves completely the same to one of a smaller sample space.

It sill remains to show that we can solve integrals of the type eq. 2.5.9. To this end we use the form eq. 2.6.9, let $S \subset S_{\text{full}}$ with S the space of sampled states and S_{full} the full sample space.

$$I(f) = \frac{\sum\limits_{C \in S} w_C f(C)}{\sum\limits_{C \in S} w_C} \approx \frac{\sum\limits_{C \in S} w_C f(C)}{Z} = \sum_{C \in S} \pi_C f(C) \tag{2.6.20}$$

Even though the metropolis algorithm improves upon direct sampling, especially in high dimensions, we have identified three drawbacks above:

local changes   The changes in configurations are local which becomes especially important near phase transitions and the correlation length between sites in real space diverges.

effective rate   While the samples are not rejected directly, changes in configurations are. This may lead to a significantly lower effective sample size than direct sampling methods. This can also be expressed as long autocorrelation times in regions of low density.

convergence   Depending on the starting distribution, the first samples of the Markov chain will be unusable because the stationary distribution has not yet been reached. It is possible to find heuristics for the number of steps one should skip (see sec. 2.7) but this makes naive parallelization inefficient, because the number of unusable samples grows proportionally to the number of Markov chains used.

These problems have been subject to research and there are mitigations especially for the problem of local changes and rejection rate available. Cluster algorithms introduce the possibility to change whole groups of configurations and add new transitions since configurations that were previously only connected through a large number of steps are now adjacent (e.g. in the 2D Ising model a group of n spins flips at once instead of each one after another). Examples for cluster algorithms are the Swendsen-Wang or the Wolff-Algorithm which is presented for the Ising model in alg. 5.

Usually one will employ MCMC methods for more sophisticated models, so it is

---

input : Grid with N_I Ising spins G, $U(0, 1)$, Temperature $K = \beta J$
output: Array f_{sample} of length N_I with grids

1   reserve array f_{sample} of length $N \cdot |G|$
2   $i = 1$
3   **while** $i < N$:
4   Draw site-index $s_i \sim \lfloor U(0, N_I) \rfloor$
5   Initialize list of neighbor indices NB_L
6   Initialize list of cluster member indices CL_L
7      $CL_l.push(G[S_i])$
8   **while** NB_L *not empty*:
9         $NB = pop(NB_L)$
10   **if** $G[NB].spin == G[s_i].spin$:
11   Draw $\zeta \sim U(0, 1)$
12   **if** $e^{-2K} > \zeta$:
13              $CL_L.push(NB)$
14   push neighbors NB in NB_L
15   **foreach** *site* $\in CL_L$ **do**
16        $G[site].spin = \text{flip}\left(G[site].spin\right)$
17      $f_{sample}[i] = G$
18 **return** f_{sample}

Algorithm 5: Wolff Algorithm

instructional to have a look at the central argument one has to give when adapting a Metropolis-like algorithm. As explained above, detailed balance (eq. 2.6.16) is a sufficient condition and quite easy to check. Let $1 - \tilde{P}$ for now be the undefined probability of a site k not being added to the cluster from site l. Since every bond has the same probability to exist, the probability to be in configuration i or j with n or m unconnected bonds (a neighbor outside the cluster) is proportional to $\left(1 - \tilde{P}\right)^n$ and $\left(1 - \tilde{P}\right)^m$.
We write eq. 2.6.18 as:

$$e^{\beta\left(E_j - E_i\right)} \overset{!}{=} \frac{R_{ij}}{R_{ji}} = \frac{\left(1 - \tilde{P}\right)^n Q_{ij}}{\left(1 - \tilde{P}\right)^m Q_{ji}} \tag{2.6.21}$$

$$\Rightarrow \frac{Q_{ij}}{Q_{ji}} = \left[\left(1 - \tilde{P}\right) e^{2\beta J}\right]^{m-n} \overset{!}{=} 1 \tag{2.6.22}$$

This condition is required from detailed balance (eq. 2.6.16).

$$\Rightarrow \tilde{P} = 1 - e^{-2\beta J} \tag{2.6.23}$$

Ergodicity is obviously fulfilled since the cluster can take any shape.
Another possible improvement for better exploration of the state space is simulated annealing. Here an (artificial) temperature is introduced and lowered during simulation. The adaptation for the Wolff algorithm is straight forward using K as the parameter. Moves are then rejected more likely with lower temperature. To prevent getting stuck in local optima an alternative to simulated annealing is the attachment of a kinetic energy term to the acceptance ratio. This is related to the aforementioned hybrid MCMC, for example if the acceptance rate is modified to

$$R = \min\left(1, \frac{\exp(-H(p',q'))}{-H(p',q')}\right).$$

However these methods neither guarantee more connections between semi disconnected recurrent class, nor do they yield any control parameter for the quantification of this behavior.

2.7 DATA ANALYSIS

Previously we have discussed methods to obtain samples from an (partially) unknown distribution. But auxiliary properties such as data sufficiency, precision and accuracy are just as important to make measurements meaningful. The probabilities of data samples acquired from Monte Carlo simulations are assumed to converge according to eq. 2.6.14. While this holds for arbitrarily long simulations we still need tools to test the quality of finite time simulation results. The main concerns are:

data sufficiency   Since we do not know the true observables such as the sample mean, we need additional parameters to quantify the convergence behavior. This also includes error estimates for the measurements.

equilibrium   Especially near phase transitions, long range order will prohibit the simulation from reaching the equilibrium distribution when we are using local changes in configurations. Before the stationary distribution is reached, the sample mean will not fluctuate around the true mean since all samples lie within a subset of the full phase space. The equilibration time can also dramatically depend on the starting configuration, structure of the state space or even pseudo number random seeds. It is important to note that the following measures for data quality will be incorrect when the simulation has not reached equilibrium yet.

correlations   The variance in Monte Carlo simulations decays with $1/\sqrt{N}$ according to the central limit theorem. This does however assume uncorrelated samples as correlations reduce the amount of new information we obtain from each new sample. Additionally, correlations can introduce non monotonic convergence as discussed before. We will dedicate the rest of the section to this problem.

2.7.1   *Blocking analysis*

Blocking or binning analysis provides the easiest method for the estimation of the correlation time. The data samples are collected in bins of different sizes. The change of variance in relation to the bin size provides an extrapolation method for the true variance and therefore autocorrelation. Using eq. 2.1.14 and assuming independence, we can write the variance of sample mean as:

$$\mathrm{Var}[\bar{X}] = \mathrm{Var}\left[\frac{1}{N}\sum_{i=1}^{N} X_i\right] = \mathrm{Var}\left[\frac{1}{N_{\mathrm{blocks}}} \sum_{j=1}^{N_{\mathrm{blocks}}} \frac{N_{\mathrm{blocks}}}{N} \sum_{i\in\mathrm{Block}_j}^{N} X_i\right]$$

$$\approx \mathrm{Var}\left[\frac{1}{N_{\mathrm{blocks}}} \sum_{j=1}^{N_{\mathrm{blocks}}} \bar{X}_j\right] \tag{2.7.1}$$

$$\approx \frac{1}{N_{\text{blocks}}^2} \sum_{j=1}^{N_{\text{blocks}}} \text{Var}\left[\bar{X}_j\right] \tag{2.7.2}$$

$$\approx \frac{1}{N_{\text{blocks}}} Var\left[\bar{X}_1\right] \approx \frac{1}{N_{\text{blocks}}\left(N_{\text{blocks}} - 1\right)} \sum_{j=1}^{N_{\text{blocks}}} \left(\bar{X}_j - \bar{X}\right)^2 \tag{2.7.3}$$

We have used several approximations: eq. 2.7.1 assumes sufficiently large blocks to estimate the expected value correctly. Next we assume statistical independence in eq. 2.7.2. This is the key in estimating correlations, since our result will change with block size and the ensuing change in covariance can be extrapolated. Finally we assumed equal variance for all blocks and use the standard unbiased variance estimator. In order to find the appropriate block size it is useful to define the ratio between block variance and true variance as a measurement for the statistical independence between blocks.

$$R_X = \frac{N}{N_{\text{blocks}}} \frac{\text{Var}\left[\bar{X}_1\right]}{\text{Var}\left[X\right]} \tag{2.7.4}$$

In the limit of independent blocks the ratio reduces to $R_X \sim \frac{N}{N_{\text{blocks}}}$. This means R_X increases up to a certain threshold and decreases linearly in N_{blocks} after that. The rate at this turning point will be called $R_X^\star$ and the corresponding block size $N_{\text{blocks}}^\star$. With this definition and eq. 2.7.3 we obtain the following estimation for the true variance.

$$\text{Var}\left[\bar{X}\right] = R_X \frac{\text{Var}\left[X\right]}{N} \tag{2.7.5}$$

$$\overset{\text{eq. 2.2.13}}{\Rightarrow} \tau_X = \frac{1}{2}\left(R_X^\star - 1\right) \tag{2.7.6}$$

Note that one has to compute the autocorrelation time for all observables separately. The most important advantage about this definition is its space efficiency, since it can be implemented using only $\mathcal{O}\left(\log(N_{\text{blocks}})\right)$ variables [3]. This is necessary since saving the complete time series would be impossible and further approximations are undesirable due to the importance of this parameter.
We derive this algorithm in the following. Let X_i with $1 \leq i \leq N$ be our samples, then the bins are defined as

$$S_i^{(l)} = \sum_{k=l \cdot i}^{(l+1) \cdot i} X_i, \quad 0 \leq l \leq \log_2\left(\frac{N}{N_{\text{blocks}}}\right) \tag{2.7.7}$$

So for a bin size of two, the first two adjacent measurements are summed up into $S_1^{(1)}$, after four measurements the resulting two bins are summed up into $S_1^{(2)}$ and so on, see fig. 2.12 for an illustration. By setting $Z_i = S_i^{(l)}/2^l$ one obtains $\frac{N}{2^l}$ independent identically distributed random variables with finite mean. The $S_i^{(l-1)}$ bins are disregarded after $S_j^{(l)}$ has been computed. We are now also in the position to estimate the number of samples needed for the computation of observables:
Assuming finite variance, this can be used as indication for data sufficiency since the Z_I should be Gaussian distributed according to the CLT. Too few data samples result in a skewed or too narrow/wide distribution. One can measure the normalized skewness z_3 and kurtosis (a measure for the heaviness of the tail) z_4 and compare
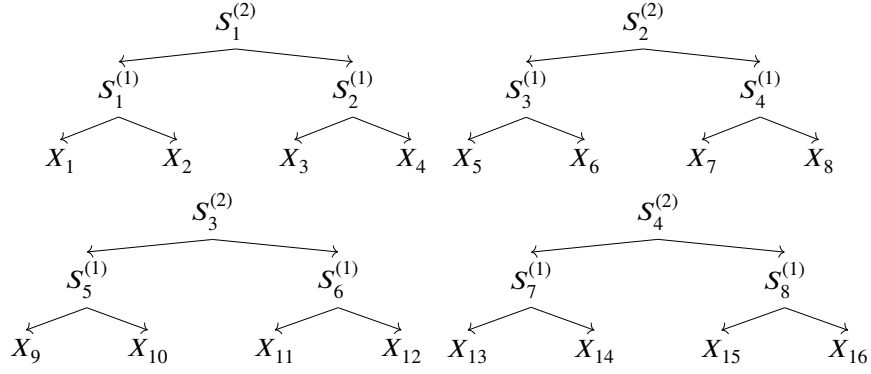
Figure 2.12: Logarithmic binning for Blocking Analysis

the results to that of a Gaussian distribution, for which $z_3 = z_4 = 0$ (see discussion of cumulants above). Sufficient similarity then implies uncorrelated measurements.

$$z_3 = \frac{\sum_{i=1}^{N_{\text{blocks}}} \left(\bar{X}_i - \langle X \rangle\right)^3}{\left(N_{blocks} - 1\right) \hat{\sigma}_{\bar{X}}^3} \qquad (2.7.8)$$

$$z_4 = \frac{\sum_{i=1}^{N_{\text{blocks}}} \left(\bar{X}_i - \langle X \rangle\right)^4}{\left(N_{\text{blocks}} - 1\right) \hat{\sigma}_{\bar{X}}^4} - 3 \qquad (2.7.9)$$

Note the -3 in our definition of z_4. This is a convenient choice here since we always want to compare to normal distributions, but inconsistent to some literature.

We will not look into unbiased estimators for these values, since they are only used as a rough estimation for the sufficiency of our sample data (see [62] for more details about unbiased estimators of kurtosis and skewness). In the implementation of this thesis I used the formulas derived in [111] and for one-pass algorithms [102, 133]. For the standard runs, after the convergence behavior has been determined, the built in features of the boost library proofed sufficient.

With the blocking analysis and z_3, z_4 estimations, we have quantified correlations and data sufficiency. We can however not predict whether we have reached equilibrium or are stuck within a region! It is therefore crucial to vary the initial configuration even during tests of the software and observe the convergence behavior in detail.

2.7.2 *Resampling Methods*

After having obtained methods for the estimation of observables and their error one is usually interested in confidence and bias in these variables. Even more importantly, this is connected to the error estimation of functions over the sample spaces with one or more sampled random variables $g(\langle X_1 \rangle, \langle X_2 \rangle, \cdots)$. Resampling approximates the distribution of the estimator for g from which not only confidence and bias but also a lot of other statistics can be obtained. This is of course an essential feature that production level software should be able to compute, however for this work the quantum Monte Carlo algorithms as well as numerical problems and their solutions are the primary focus[15]. The results obtained in this thesis are well known

---

15 An overview of the bootstrapping method, its relation to the Jackknife and maximum likelihood methods as well as efficient algorithms for parameter estimation and hypothesis testing can be found in [36].

and serve as check for the proof of concept implementation. For that reason we will only sketch two prominent examples of resampling methods, block bootstrap and jackknife analysis, briefly.

The general idea is to simulate the data generation from a known distribution by sampling from the samples obtained from the previously described sampling precesses. Let's call the distribution of the real data P and that of the bootstrap $\hat{P}$. We write a parameter of P as θ and its estimate as $\hat{\theta}$. The Bootstrap versions are usually denoted by a star $\theta^\star, \hat{\theta}^\star$.

The following line of argument may be reminiscent of the maximum likelihood (ML) method but especially for Monte Carlo algorithms, ML methods often fall short due to intractable analytical calculations. They also require a lot of theoretical footwork (see for example SEM algorithms [32]).

In order to derive the block bootstrap method we reuse the block construction from above (eq. 2.7.7) but vary the process of generating the blocks. Instead of selecting consecutive samples, the index i is permuted so that $X_i \rightarrow X_{\pi(i)}$. Using the indicator function we write:

$$\hat{P}\left(\hat{\theta} \in S\right) = \frac{1}{N_{\text{blocks}}} \sum_{k=1}^{N_{\text{blocks}}} \mathbb{1}_S\left\{\hat{\theta}_k^\star\right\}, \qquad \theta_k^\star = g\left(S_k^{(l)}\right) \tag{2.7.10}$$

$$\hat{\theta}_{[\cdot]}^\star = \frac{1}{N_{\text{blocks}}} \sum_{k=1}^{N_{\text{blocks}}} \hat{\theta}_k^\star \tag{2.7.11}$$

This yields the variance estimator and confidence intervals $[g_l, g_u]$

$$\hat{\sigma}_{\text{boot}}^2\left(\hat{\theta}\right) = \frac{1}{N_{\text{blocks}} - 1} \sum_{k=1}^{N_{\text{blocks}}} \left(\hat{\theta}_k^\star - \hat{\theta}_{[\cdot]}^\star\right)^2 = \frac{N_{\text{blocks}}}{N_{\text{blocks}} - 1} \hat{\sigma}^2\left[\hat{\theta}\right] \tag{2.7.12}$$

Using appropriate definitions for $X_k^\star$ (e.g. $X_k^\star = \frac{\hat{\theta}_k^\star - \hat{\theta}}{\hat{\sigma}_{boot}[\hat{\theta}]}$ for the t-interval) in eq. 2.7.10 it is now possible to obtain usual confidence interval estimates.

The popular Jackknife analysis is a special case of the bootstrap analysis. Instead of using a permutation of the indices, resampling is achieved by leaving out one block at a time

$$\hat{X}_{[i]} = \frac{1}{N_{\text{blocks}} - 1} \sum_{j \neq i} S_j^{(l)} \tag{2.7.13}$$

Mean and variance can be computed similarly to eq. 2.7.11 and eq. 2.7.12 above. However, the Jackknife linearizes the estimation of parameters (see [36, 54] or [93] for a derivation) which results in corresponding underestimation of non linear contributions.

2.8 SIGN PROBLEM

As mentioned above, there is well known problem for fermionic MC simulations which can prevent convergence of the sample variance. Due to the fact that the interchange of fermions in a system changes the sign of the wave function according to the Pauli principle, the weights w_C, which we want to interpret as probability weights, can become negative (see eq. 2.5.9) or for certain algorithms even complex. This can be remedied by decomposing w_C into phase and amplitude, as we have

done for example in the importance sampling algorithm, $w_C = s(c)|w_C|$. This allows us to rewrite eq. 2.5.9:

$$\langle f \rangle_w \approx \frac{\sum\limits_C w_C f(C)}{\sum\limits_{C \in S} w_C} = \frac{\sum\limits_C s(c)|w_C|f(C)}{\sum\limits_C s(c)|w_C|} \bigg/ \frac{\sum\limits_C |w_C|}{\sum\limits_C |w_C|} \tag{2.8.1}$$

$$= \frac{\langle fs \rangle_{|w|}}{\langle s \rangle_{|w|}} \tag{2.8.2}$$

Let Z_f, Z_b be the fermionic/bosonic partition function and $\Delta f = f_f - f_b$ the difference between free energies. Then positive and negative contributions to the partition function may cancel each other out in the denominator of eq. 2.8.2, while all contributions to the bosonic partition function are positive [88, 29].

$$\langle s \rangle_{|w|} \propto \frac{Z_f}{Z_b} = e^{-\beta V \Delta f} \tag{2.8.3}$$

$$\Rightarrow \frac{\Delta \langle s \rangle}{\langle s \rangle} = \frac{\sqrt{\langle s^2 \rangle - \langle s \rangle^2}}{\sqrt{N} \langle s \rangle} \propto \frac{e^{\beta V \Delta f}}{\sqrt{N}} \tag{2.8.4}$$

There has been a shift of negative signs proposed using cluster algorithms, which improves the effective sample rate $N \to N'$ [29]. We will discuss another method, employing the particle hole symmetrization from the last chapter, for the CT-INT algorithm later.

GREEN'S FUNCTION FORMALISM

3.1 PATH INTEGRAL FORMALISM

The goal of this section is the reformulation of the Hubbard model in terms of the path integral formalism. This will provide the mathematical tools from quantum field theories and allow us to define the DMFT approximation.

We will need a brief overview of the important steps for the derivation of the path integral formalism, since they appear again in the derivation of the DMFT approximation. Details are found in the literature [104, 129, 70]. A full derivation specialized to the path integral formalism with references to all mathematical details can be found here [78]. Central for the formulation of functional path integrals as well as the first numerical algorithms (namely discrete time quantum Monte Carlo), is the Baker–Campbell–Hausdorff formula [37].

Consider some Lie algebra g of a Lie group G. Let $A, B, C \in g$ and $\exp : g \to G$ be the exponential map[1]. The first few terms are (we omit the proof as well as the closed form solution here):

$$
\begin{aligned}
\exp(A)\exp(B) = \exp\Big(A + B + \frac{1}{2}[A,B] \\
+ \frac{1}{12}[A,[A,B]] + \frac{1}{12}[B,[B,A]] \\
- \frac{1}{24}[B,[A,[A,B]]] \pm \cdots\Big)
\end{aligned}
\tag{3.1.1}
$$

There are two corollaries that we will frequently use, the Lie-Trotter product formula [123] (eq. 3.1.3) and the Suzuki-Trotter expansion (formally proved by the Zassenhaus formula eq. 3.1.2).

$$
e^{\lambda(A+B)} = e^{\lambda A} e^{\lambda B} e^{-\frac{\lambda^2}{2}[A,B]} e^{\frac{\lambda^3}{3}[B,[A,B]]+\frac{\lambda^3}{6}[A,[A,B]]} \cdots
\tag{3.1.2}
$$

$$
\Rightarrow e^{\lambda(A+B)} = \lim_{n\to\infty}\left(e^{\frac{\lambda A}{n}} e^{\frac{\lambda B}{n}}\right)^n
\tag{3.1.3}
$$

$$
= \lim_{n\to\infty}\left(e^{\frac{\lambda A}{2n}} e^{\frac{\lambda B}{n}} e^{\frac{\lambda A}{2n}}\right)^n
\tag{3.1.4}
$$

We start with the matrix element for the time evolution operator U in some initial state x_i at time t_i and final state x_f at time t_f. By dividing the time interval into segments of equal length it becomes possible to use eq. 3.1.3 with $\lambda = \frac{t_f - t_i}{N}$. Repeated use of the closure relations for momentum and position states

$$
\mathbb{1} = \int \frac{d^3 p_n}{(2\pi\hbar)^3}\, |p_n\rangle\langle p_n| = \int d^3 x_n\, |x_n\rangle\langle x_n|
\tag{3.1.5}
$$

---

1 since we will deal with a matrix Lie group, the formula $\exp(A) = \sum_{n=0}^{\infty}\frac{A^n}{n!}$ holds

will enable us to get rid of all operators in favor of integrable variables. It is sufficient for us to consider Hamiltonians of the form eq. 1.2.1 or in short

$$H = \frac{\hat{p}^2}{2m} + V(\hat{x}) \tag{3.1.6}$$

Additional care has to be taken, since the order of momentum and position operators may not appear in a suitable order. We omit a detailed discussion here[2]. The heuristic argument is enough in this context.

An operator $\hat{O}(\hat{x}, \hat{p})$ is said to have normal form if all $\hat{p}$ are to the left of all $\hat{x}$. This is also the order at which we will truncate the trotter expansion. Normal order is denoted by colons: $:\hat{O}:$.

$$K(x_i, \tau_f; x_i, \tau_i) = \langle x_f | e^{-\hat{H}\frac{i}{\hbar}(\tau_i - \tau_i)} | x_i \rangle = \langle x_f | : e^{-\hat{H}\frac{i}{\hbar}(\tau_i - \tau_i)} : | x_i \rangle + \mathcal{O}(\lambda^2)$$

$$= \langle x_f | : e^{-\hat{H}\frac{i\lambda}{\hbar}} \cdots e^{-\hat{H}\frac{i\lambda}{\hbar}} : | x_i \rangle + \mathcal{O}(\lambda^2)$$

$$= \langle x_f | : e^{-\hat{H}\frac{\lambda}{\hbar}} \cdots e^{-\hat{H}\frac{\lambda}{\hbar}} : | x_i \rangle + \mathcal{O}(\lambda^2) \tag{3.1.7}$$

We also used a special case of the Wick rotation at this point and replace $t = -i\tau \Rightarrow \lambda \to -i\lambda$. The resulting path integral is often called euclidean path integral (since for full quantum field theories this is a shift from Minkowski to euclidean space). As a result the exponents become real valued and the imaginary time evolution operator, as well as time evolved operators, are no longer unitary!

$$\hat{O}^\dagger(\tau) = e^{H\tau}\hat{O}^\dagger e^{-H\tau} \neq \left(\hat{O}^\dagger(\tau)\right)^\dagger = e^{-H\tau}\hat{O}^\dagger e^{H\tau} \tag{3.1.8}$$

For every time slice (i.e. between t_n and t_{n+1} for all n) we enter unity operators in form of momentum eigenstates to the left and position eigenstates to the right of the exponential.

$$\langle x_{x+1} | p_n \rangle \langle p_n | e^{-\hat{H}\frac{i\lambda}{\hbar}} | x_n \rangle = \langle p_n | e^{-\hat{H}(\hat{x},\hat{p})\frac{i}{\hbar}} | x_n \rangle$$

$$\overset{\text{eq. 3.1.6}}{=} \exp\left[-\frac{\lambda}{\hbar}\left(\frac{p_n^2}{2m} - ip_n\frac{x_{n+1} - x_n}{\lambda} - V(x_n)\right) + \mathcal{O}(\lambda)\right] \tag{3.1.9}$$

The propagator contains N factors of eq. 3.1.9. Using the Trotter expansion this results in a sum over N terms in the exponent where one has to take care to define x_1 and x_N.

The asymmetry of the products stems from the fact, that the endpoints for x are fixed. When deriving the partition function in the same way, this problem is avoided by a closed path (i.e. $x_n = x_0$).

---

2 In order to shorten the derivation we use a formulation that may have an ill defined measure (no sigma additivity) for potentials without a lower bound [27]. K. Itô remedied this in 1967 for certain "well behaved" potentials [68, 77]. Out later use for numerical simulations relies on the time slicing approach, which also does not suffer from this problem [22]

We now formally replace sums by integrals and the difference by a derivative. The propagator then reads:

$$K(x_f, \tau_f; x_i, \tau_i) = \lim_{N \to \infty} \left[\prod_{n=1}^{N} \int_{-\infty}^{\infty} \mathrm{d}^3 x_n \right] \left[\prod_{n=0}^{N} \int_{-\infty}^{\infty} \frac{\mathrm{d}^3 p_n}{(2\pi\hbar)^3} \right]$$
$$\times e^{-\frac{\lambda}{\hbar} \int \mathrm{d}\tau \left(\frac{p_n^2(\tau)}{2m} - i p_n(\tau) \left(\frac{\mathrm{d}x_n(\tau)}{\mathrm{d}\tau} \right) + V(x_n(\tau)) \right)} \tag{3.1.10}$$

Only Gaussian integrals appear in the momentum integration, so it can be carried out immediately.

$$= \lim_{N \to \infty} \left[\prod_{n=1}^{N} C_n \int \mathrm{d}^3 x_n \right] e^{-\frac{1}{\hbar} \int \mathrm{d}\tau \left(\frac{m}{2} \left(\frac{\mathrm{d}x_n(\tau)}{\mathrm{d}\tau} \right)^2 - V(x_n(\tau)) \right)}$$

The infinite product of integrals, including the normalization factor, is denoted by $\int \mathcal{D}$. For our purposes this is not a measure but just a formal abbreviation.

$$= \int_{(x_i, \tau_i)}^{(x_f, \tau_f)} \mathcal{D}[x(\tau)] \, e^{-\frac{1}{\hbar} S_E[x(\tau), \dot{x}(\tau)]} \tag{3.1.11}$$

$$= \int_{(x_i, \tau_i)}^{(x_f, \tau_f)} \mathcal{D}[x(\tau)] \frac{\mathcal{D}[p(\tau)]}{2\pi\hbar} e^{-\frac{1}{\hbar} A[x,p]} \tag{3.1.12}$$

S_E is called euclidean action of the system. This is the Wick rotated Minkowski action of the system. At this point the subscript can be dropped since we only work in Euclidean space in this thesis.

$$S[x(\tau), \dot{x}(\tau)] = \int_{\tau_i}^{\tau_f} \mathrm{d}\tau \mathcal{L}_E[x(\tau), \dot{x}(\tau)]$$

$$A[x, p] = \int_{\tau_i}^{\tau_f} \mathrm{d}\tau \left(p(\tau) \dot{x}(\tau) - H[p(\tau), \dot{x}(\tau), \tau] \right)$$

$$\mathcal{L}_E = -\mathcal{L}_M(\tau = it) = \frac{m}{2} \left(\frac{dx(\tau)}{d\tau} \right)^2 - V(x(\tau))$$

The usual interpretation of the path integral uses a similar structure to the Boltzmann weights. Instead of assigning each configuration in phase space the weight $\exp(-E/k_B T)$, the path integral factor $e^{-\frac{1}{\hbar} A[x,p]}$ is the weight of one configuration in "path phase space", see fig. 3.1. This space additionally contains all possible histories of the particle due to eq. 3.1.9, which are then "summed up". One can immediately see that the classical path (i.e. fulfilling the Euler-Lagrange equations) receives the only contribution in the classical limit $\hbar \to 0$.

This interpretation also provides us with the application of path integrals we will later use. Every possible diagonal matrix element of the time evolution operator at imaginary time $\tau_f - \tau_f = \beta\hbar$ (see eq. 3.1.7) is a contribution to the partition function of the system. In case of our simple Hamiltonian eq. 3.1.6, the partition function can be rewritten in the following way:

$$Z = \mathrm{Tr} \left[e^{-\beta H} \right] = \int_{-\infty}^{\infty} \mathrm{d}^3 x_i K(\beta, x_i; 0, x_i) \tag{3.1.13}$$

$$= \int_{x(\beta)=x(0)} \mathcal{D}[x(\tau)] \, e^{-S[x(\tau)]} \tag{3.1.14}$$

$$S[x(\tau), \dot{x}(\tau)] = \int_0^\beta d\tau \mathcal{L}[x(\tau), \dot{x}(\tau)]$$

To further abbreviate the notation, we choose natural units, i.e. $c = \hbar = k_B = 1$.

For many body systems there is a straightforward generalization using the symmetrized product over all states. But since the Hubbard model is formulated in second quantization, it will be easier to transition to the coherent state path integral first and then write down our final version of the partition function. The steps for the derivation of the coherent state path integral are similar to eq. 3.1.1 to eq. 3.1.14, where the field ϕ and the conjugate field $\phi^\star$ take the roles of position and momentum states. Unity and trace formulas from eq. 3.1.15 and eq. 3.1.18 replace the previous version. ψ and $\overline{\psi}$ denote bosonic fields or Grassmann fields and their complex conjugate depending on the context. This also means that the integral symbol is a formal replacement and one has to insert measure and integral type (i.e. Lebesgue or Berezin) depending on the actual field.
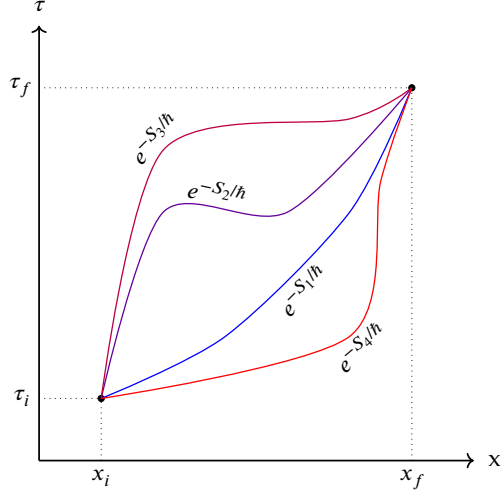
Figure 3.1: Paths contributing to the propagator

$$\mathbb{1} = \int \prod_\alpha d\psi_\alpha^\star \, d\psi_\alpha e^{-\sum_\alpha \psi_\alpha^\star \psi_\alpha} |\psi\rangle \langle \psi| \tag{3.1.15}$$

Grassmann fields will be denoted with ξ and bosonic field with ϕ.
There is a very useful generalization of the Gaussian integral identities which will be used later.

$$\int \prod_\alpha d\xi_\alpha^\star \, d\xi_\alpha \exp\left(-\sum_{\alpha\beta} \xi_\alpha^\star M_{\alpha\beta}\xi_\beta + J_\alpha^\star \xi_\alpha + \xi_\alpha^\star J_\alpha\right)$$

$$= \det(M) \, e^{\sum_{\alpha\beta} J_\alpha^\star \left[M^{-1}\right]_{\alpha\beta} J_\beta} \tag{3.1.16}$$

$$\int \prod_\alpha d\phi_\alpha^\star \, d\phi_\alpha \exp\left(-\frac{1}{2}\sum_{\alpha\beta} \phi_\alpha^\star M_{\alpha\beta}\phi_\beta + J_\alpha\phi_\alpha\right)$$

$$= \sqrt{\frac{(2\pi)^n}{\det(M)}} e^{\frac{1}{2}\sum_{\alpha\beta} J_\alpha \left[M^{-1}\right]_{\alpha\beta} J_\beta} \tag{3.1.17}$$

The definition of the partition function is also similar to the previous derivation.

$$Z = \text{Tr}\left[e^{-\beta(H-\mu N)}\right] = \int_{\psi_\alpha(\beta)=\zeta\psi_\alpha(0)} \mathcal{D}\left[\overline{\psi}_\alpha(\tau)\psi_\alpha(\tau)\right] e^{-A\left[\overline{\psi}_\alpha, \psi_\alpha\right]} \tag{3.1.18}$$

$$A\left[\overline{\psi}_\alpha, \psi_\alpha\right] = \int_0^\beta d\tau \left[\sum_\alpha \overline{\psi}_\alpha(\tau)\left(\frac{\partial}{\partial \tau} - \mu\right)\psi_\alpha(\tau) + H\left(\overline{\psi}_\alpha(\tau), \psi_\alpha(\tau)\right)\right] \tag{3.1.19}$$

$$\int \mathcal{D}[\overline{\psi}, \psi] \cdots = \lim_{N \to \infty} \int_{-\infty}^{\infty} \prod_{n=1}^{N} \prod_{\alpha} \frac{\mathrm{d}\overline{\psi}_{\alpha,n} \, \mathrm{d}\psi_{\alpha,n}}{\mathcal{N}} \cdots \qquad (3.1.20)$$

This new representation of the partition function looks more complicated than the original trace. However the Trotter expansion provides a natural discretization that may be better controllable than truncation errors in the trace. There have been many algorithms developed around this, we will discuss three of these in depth in the next chapter.

A particularly useful property of functional integrals is their natural time ordering property. For example, consider two operators O_1, O_2 depending on different times $\tau_1 < \tau_2$:

$$\int_{\psi_\alpha(\beta) = \zeta \psi_\alpha(0)} \mathcal{D}[\overline{\psi}, \psi] \, e^{-A[\overline{\psi}, \psi]} O_1(\psi_\alpha(\tau_1)) O_2(\overline{\psi}_\beta(\tau_2))$$

The operators are projected to the nearest imaginary time slice which orders them in this case as $\tau_1 < \tau_2$.

$$= \lim_{N \to \infty} \left[\prod_{n=1}^{N} \int \cdots \right] \cdots \langle \psi_{\alpha,i} | O_1(\psi_\alpha) e^{-\frac{\epsilon}{\hbar} H_0} | \psi_{\alpha,i-1} \rangle \cdots \langle \psi_{\alpha,j} | T \left[O_2(\overline{\psi}_\beta) e^{-\frac{\epsilon}{\hbar} H_0} \right] | \psi_{\alpha,j-1} \rangle$$

$$= \left\langle T_\zeta \left[O_1(\psi_\alpha(\tau_1)) O_2(\overline{\psi}_\beta(\tau_2)) \right] \right\rangle \cdots$$

Where we defined the time ordering operator T_ζ in this case for imaginary time. Time ordering for real time operators is defined equivalently[3].

Definition 13 (Time ordering operator)

$$T_\zeta \left[\psi(\tau_1) \overline{\psi}(\tau_2) \right] = \begin{cases} \psi(\tau_1) \overline{\psi}(\tau_2) & \text{if } \tau_1 > \tau_2 \\ \zeta \overline{\psi}(\tau_2) \psi(\tau_1) & \text{if } \tau_1 < \tau_2 \end{cases} \qquad (3.1.21)$$

This implicit time ordering property of the path integral will often be used but not denoted explicitly. For example in eq. 3.5.8, functional derivatives retain this property but the time ordering operator is not written out explicitly.

3.2 GREEN'S FUNCTIONS

In this section we will discuss some aspects of the Green's function formalism which will help us to treat the action systematically $A[\overline{\psi}, \psi]$. Let L be some linear differential operator, the Green's function is defined as

$$LG(x, s) = \delta(x - s) \qquad (3.2.1)$$

Convolution with some function f and use of the linearity of L gives:

$$\int LG(x, s) f(s) \, \mathrm{d}s = \int \delta(x - s) f(s) \, \mathrm{d}s$$

$$L \left[\int G(x, s) f(s) \, \mathrm{d}s \right] = f(x)$$

$$L u(x) = f(x), \qquad u(x) := \int G(x, s) f(s) \, \mathrm{d}s \qquad (3.2.2)$$

---

3 It is unnecessary to distinguish between Wick time ordering and real time ordering here.

So the knowledge of the Green's function provides a solution for the inhomogeneous differential equation in eq. 3.2.2.

There are different methods for the (approximate) construction of Green's functions such as Laplace transforms or results from Fredholm theory. For example if L has a complete set of eigenfunctions then we can explicitly construct the form of G:

$$L\psi_n = \lambda_n \psi_n$$

$$G(x, y) = \sum_n \frac{\psi_n^{\dagger}(x)\psi_n(y)}{\lambda_n} \tag{3.2.3}$$

In many particle physics the definition above is extended to capture correlation effects between multiple particles. The original definition only covers the special case of the free scalar field. One can check the validity in this case by considering the definition of the time evolution operator [4].

$$L\Psi(r,t) = V(r,t)\Psi(r,t), \qquad L = i\hbar\frac{\partial}{\partial t} + \frac{\hbar^2}{2m}\nabla^2$$

$$LG(r,t;r',t') = \delta(r-r')\delta(t-t')$$

We can identify the same structure as in the definition of the Greens function in eq. 3.2.2. The only generalization are additional dimensions and the Heaviside function is used to ensure causality.

$$\Psi(r,t)\Theta(t-t') = \Theta(t-t')\int dr'\, G(r,t;r',t')\Psi(r',t') \tag{3.2.4}$$

$$= \langle r|\,\Theta(t-t')U(t,t')\,|\Psi(t')\rangle$$

$$= \int dr'\left[\langle r|\,\Theta(t-t')e^{-\frac{i}{\hbar}\int_t^{t'} H(s)\,ds}\,|r'\rangle\langle r'\,|\,\Psi(t')\rangle\right] \tag{3.2.5}$$

Comparison of the first and third line yields the definition of the quantum mechanical retarded (since we enforced $t > t'$) Green's function. This operator can be can be understood as the operator for causal forward propagation of a state in time. The advanced Green's function is defined accordingly and equivalently propagates a state back in time.

$$G^R(r,t;r',t') = \Theta(t-t')\langle r|\,e^{-\frac{i}{\hbar}\int_t^{t'} H(s)\,ds}\,|r'\rangle = \Theta(t-t')K(r,t;r',t') \tag{3.2.6}$$

$$= -i\Theta(t-t')\left\langle\left[\Psi(r,t),\Psi^{\dagger}(r',t')\right]_{\zeta}\right\rangle \tag{3.2.7}$$

$$G^A(r,t;r',t') = i\Theta(t'-t)\left\langle\left[\Psi(r,t),\Psi^{\dagger}(r',t')\right]_{\zeta}\right\rangle \tag{3.2.8}$$

$$G(r,t;r',t') = -i\left\langle T_{\zeta}\left[\Psi(r,t)\Psi^{\dagger}(r',t')\right]\right\rangle \tag{3.2.9}$$

In addition to retarded and advanced, we will also need the time ordered Green's function. It arises naturally from the path integral formalism. The relationship between retarded, advanced and time ordered Green's function will become more apparent when discussing the spectral representation especially the pole structure (see fig. 3.2). This makes extraction of the (physically relevant) retarded Green's function possible.

---

4 A complete introduction with examples and additional explanations can be found here [98].

A useful representation is obtained by viewing the Green's function as a Fredholm kernel. This can be done in the context of many particle physics by expansion of the Hamiltonian into energy eigenstates $|n\rangle$ ($\phi_n(r) = \langle r \,|\, n \rangle$) using eq. 3.2.3. The result is a version of the so called Lehmann spectral representation (a more usable version will be introduced later).

$$G(r, r', E) = \sum_n \frac{\phi_n(r)\phi_n^\star(r')}{E - E_n} \qquad (3.2.10)$$

In this representation one can clearly see the role as propagation from position r' at time t' to position r at time t.

By comparison of eq. 3.5.17 and eq. 3.2.2 we can identify the Green's function for the free Hamiltonian as

$$\left(\frac{\partial}{\partial \tau} + \epsilon_\alpha - \mu \right) G_0(\alpha, \tau; \alpha', \tau') = \delta(\alpha - \alpha')\delta(\tau - \tau') \qquad (3.2.11)$$

with $\epsilon_\alpha = \delta_{\alpha\alpha'} \langle \alpha | \, H \, | \alpha' \rangle$.

In general many particle systems this notion may be expressed as expected valued of the annihilation and subsequently creation of a state or vice versa. This is not a Green's function in the previous sense, but a meaningful generalization of the Green's function for free Hamiltonians to interacting ones.

Looking back at the previous section it is also convenient to choose the time ordered Green's function as our main definition, since we want to incorporate the natural time ordering property of the path integral formalism. The main drawback of the time ordered Green's function is a branch cut along the real axis of the argument. Using the advanced and retarded functions and establishing a connection between all three will allow us to get around this problem.

Following are the definitions of generalized n-particle imaginary and real time Green's functions. All additional operations for path integral or normal statistical averages are hidden by the bracket notation. Whenever it is unclear from the context, subscripts will denote the actual computation of the average.

The zero temperature Green's function is defined as a ground state expectation value while the finite temperature Green's function is a thermal expectation value e.g. in the grand canonical ensemble[5].

$$\langle \cdots \rangle_{T=0} = \langle \Psi_0 | \cdots | \Psi_0 \rangle \qquad (3.2.12)$$

$$\langle \cdots \rangle_{T>0} = \frac{1}{Z} Tr \left(T \left[e^{-\beta(\hat{H} - \mu\hat{N})} \cdots \right] \right) \qquad (3.2.13)$$

We can again state the trace in terms of the functional integral formulation:

$$= \frac{\int \mathcal{D}\left[\overline{\psi}, \psi \right] \cdots e^{-A\left[\overline{\psi}, \psi \right]}}{\int \mathcal{D}\left[\overline{\psi}, \psi \right] e^{-A\left[\overline{\psi}, \psi \right]}} \qquad (3.2.14)$$

Both representation provide physically relevant information. The real time Green's function describes the response of a system while the imaginary time Green's function encodes thermal properties.

---

5 I decided not to use different notation for thermal and zero temperature Green's function since the distinction is clear from the context everywhere through out this thesis.

Definition 14 (Many particle Green's function)

$$G^{(n)}(\alpha_1 t_1, \ldots, \alpha_n t_n; \alpha_1' t_1', \ldots, \alpha_n' t_n')$$

$$= (-i)^n \left\langle T_\zeta \left[a_{\alpha_1}(t_1) \cdots a_{\alpha_n}(t_n) a_{\alpha_n'}^\dagger(t_n') \cdots a_{\alpha_1'}^\dagger(t_1') \right] \right\rangle \qquad (3.2.15)$$

$$G^{(n)}(\alpha_1 \tau_1, \ldots, \alpha_n \tau_n; \alpha_1' \tau_1', \ldots, \alpha_n' \tau_n')$$

$$= \left\langle T_\zeta \left[a_{\alpha_1}(\tau_1) \cdots a_{\alpha_n}(\tau_n) a_{\alpha_n'}^\dagger(\tau_n') \cdots a_{\alpha_1'}^\dagger(\tau_1') \right] \right\rangle \qquad (3.2.16)$$

For example we can write down the average in terms of the functional integral formulation of the partition function:

$$= \frac{\int \mathcal{D}[\overline{\psi}, \psi]\, e^{-A[\psi, \psi]} \psi_{\alpha_1}(\tau_1) \cdots \psi_{\alpha_n}(\tau_n) \overline{\psi}_{\alpha_n'}(\tau_n') \cdots \overline{\psi}_{\alpha_1'}(\tau_1')}{\int \mathcal{D}[\overline{\psi}, \psi]\, e^{-A[\overline{\psi}, \psi]}} \qquad (3.2.17)$$

Note that for the imaginary time Green's function, there is no factor of $(-1)^n$ as some authors tend to choose. This choice is not consistent throughout the literature and only results in a few differences in signs (none of which are of physical relevance). As before, the time ordering operator permutes the creation and annihilation operators so they are ordered with descending time left to right. This results in an overall sign change of $\zeta^{|inv(\pi)|}$, i.e. an uneven number of inversions leads to a factor of -1 for fermions.

From the representation of $n-$particle operators in Fock-Space (eq. 1.2.3, eq. 1.2.4, etc.) it is clear that the Green's functions give another representation for the expected value of observables[6]. This connection to observables is (together with the spectral representation and their relation to response functions) central to the effectiveness of the Green's function formalism. For example the representation of a one-body operator is given as:

$$\left\langle \hat{O}^{(1)}(t) \right\rangle = i\zeta \sum_{\alpha\alpha'} \langle \alpha | \hat{O} | \alpha' \rangle\, G(\alpha t; \alpha' t') \qquad (3.2.18)$$

$$= \zeta \sum_{\alpha\alpha'} \langle \alpha | \hat{O} | \alpha' \rangle\, G(\alpha \tau; \alpha' \tau') \qquad (3.2.19)$$

We will use this, for example, to find the kinetic energy of the system.

3.3   SPECTRAL REPRESENTATION

Often it is justified to assume that the Green's function only depends on state and time differences[7].

$$G(r_1, t_1; r_2, t_2) = G(r, t; 0, 0), \qquad t = t_1 - t_2, r = r_1 - r_2$$

This allows simplification by Fourier transformations after writing the field operators in momentum space ($\psi(r) = V^{-1/2} \sum_k e^{ikr} a_k$):

$$G(k, \omega) = \frac{1}{(2\pi)^4} \int d\omega \int d^3k\, e^{i(kr - \omega t)}\, G(k, \omega)$$

---

6 We need to set $t_1 = \cdots = t_n = t$ and $t_1' = \cdots t_n' = t + \eta$ so the time ordering operator T_ζ shifts all creation and annihilation operators into place.

7 e.g. translational symmetry in thermal equilibrium or generally time independent Hamiltonians.

$$= \left\langle T_\zeta \left[a_k(t)\, a_k^\dagger(0) \right] \right\rangle \tag{3.3.1}$$

We proceed without translational invariance for now and use the definition of the real time ordered Green's function (eq. 3.2.15) at $T = 0$.

One inserts field operators connecting N particle ground states (since we are evaluating at $T = 0$) with $N + 1$ and $N - 1$ particle states. The overlap to the ground state is given as $\sum_n \langle \psi_0 | \psi(r) | \psi_n^{N+1} \rangle$ (for details to this derivation see chapter 2 [70]).

We will also use the Fourier transform of the Heaviside function. The integral is not convergent but a Cauchy principal value can be extracted. This is also often called regularization of the step function.

$$\int_{-\infty}^{\infty} dt\, \Theta(t) e^{-it(\omega - \omega_0)} = \lim_{\eta \to 0^\pm} \frac{1}{\omega - \omega_0 \pm i\eta} \tag{3.3.2}$$

The limit is often omitted in the following because η is understood to be a small regularization parameter that is physically not attainable since $T = 0$ will never be reached.

There is also a more formal way of retaining this shift in form of the resolvent operator (compare eq. 3.2.11) [78].

$$G^{R/A}(\alpha, \alpha', \omega) = \langle \alpha | \left[(\omega \pm i\eta)\mathbb{1} - H \right]^{-1} | \alpha' \rangle = \langle \alpha | \sum_{n=0}^{\infty} \frac{H^n}{z^{n+1}} | \alpha' \rangle \tag{3.3.3}$$

Especially the formulation as a Neumann series gives rigorous justification for the Dyson series. There is however no straightforward extension of the resolvent formulation to the time ordered Green's function.

Using eq. 3.3.2 as well as the momentum representation from eq. 3.3.1 we can write down an expression from which the poles of the Green's function in momentum space can be explicitly seen.

$$\begin{aligned}
G(r_1, t; r_2, 0) = {}& \Theta(t) \langle \psi_0 | \psi(r_1, t_1) \psi^\dagger(r_2, t_2) | \psi_0 \rangle \\
& + \zeta \Theta(-t) \langle \psi_0 | \psi^\dagger(r_2, t_2) \psi(r_1, t_1) | \psi_0 \rangle \\
& \vdots
\end{aligned}$$

$$G(k, \omega) = \sum_n \left[\frac{|\langle \psi_n^{N+1} | a_k^\dagger | \psi_0 \rangle|^2}{\omega - \omega_n^{N+1} + i\eta} - \zeta \frac{|\langle \psi_n^{N-1} | a_k | \psi_0 \rangle|^2}{\omega + \omega_n^{N-1} - i\eta} \right] \tag{3.3.4}$$

With $\omega_n^{N\pm1} = E_n^{N\pm1} - E_0 \mp \mu = E_N^{n\pm1} - E_0^{n\pm1}$ since the chemical potential $\mu^{N\pm1} \approx \mu^N$ for large systems and μ is approximately the energy to add or remove a particle to the ground state (for $T \to 0$).

This is the Lehmann representation corresponding to the expansion in Eigenfunctions (using eq. 3.2.3 and eq. 3.2.10). We can also identify the retarded and advanced Green's functions by different sign choices for $i\eta$ (both $+$ for advanced, $-$ for retarded). The choice of sign before the imaginary shift of the poles is consistent with the time ordered Green's function we are using.

When calculating the analytic continuation, the time ordered Green's function can present mathematical obstacles because the path cannot easily be closed in the upper or lower plane as a semi circle (a prerequisite for Jordan's lemma). We can immediately see this problem in fig. 3.2.

From the spectral representation and the pole structure in fig. 3.2 we can see that re-
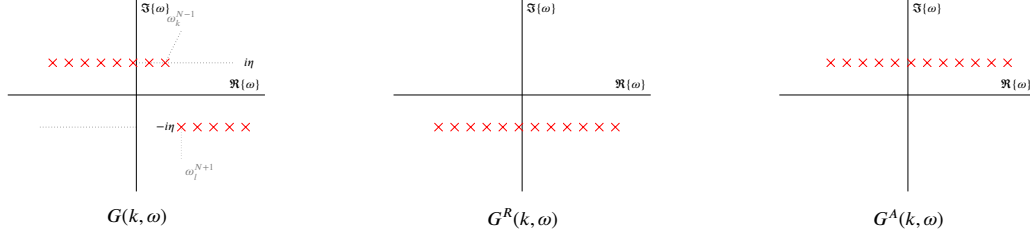
Figure 3.2: spectral Green's function poles with energies measured relative to the chemical potential: $\omega_n^{N\pm1} = \epsilon_n^{N\pm1} \pm \mu$

tarded, advanced and time ordered Green's functions are connected in the following way:

$$\left[G^R(k,\omega)\right]^\star = G^A(k,\omega) \tag{3.3.5}$$

$$G(k,\omega) = \Theta(\omega - \mu)G^R(k,\omega) + \Theta(\mu - \omega)G^A(k,\omega) \tag{3.3.6}$$

Another observation is, that the spacing between poles depends on the energy levels of the system. This motivates the introduction of the spectral weight function $A(,\omega)$ as a parametrization of the pole structure.

The spectral function will later be of importance as it provides analytical checks for numerical properties of the continuous time quantum Monte Carlo (CT-QMC) methods as well as a connection to experimentally accessible observables.

We first need the Sokhotski–Plemelj theorem for a representation of the fractions of eq. 3.3.4.

$$\lim_{\eta \to 0^+} \int_a^b \frac{f(\omega)}{\omega \pm i\eta} \, d\omega = \mp i\pi f(0) + \mathcal{P} \int_a^b \frac{f(\omega)}{\omega} \, d\omega \tag{3.3.7}$$

In our case $f(\omega) = \delta(\omega - \omega_n^{N+1})$ and $f(\omega) = \delta(\omega - \omega_n^{N-1})$ will allow us to define:

$$G(k,\omega) = \int_{-\infty}^{\infty} \frac{d\omega'}{2\pi} \frac{A(k,\omega')}{\omega - \omega' + \text{sign}(\omega)i\eta} \tag{3.3.8}$$

$$A(k,\omega) = \Theta(\omega) \underbrace{\sum_n |\langle \psi_n^{N+1}| a_k^\dagger |\psi_0\rangle|^2 2\pi\delta(\omega - \omega_n^{N+1})}_{A^+(k,\omega)}$$

$$- \zeta\Theta(-\omega) \underbrace{\sum_n |\langle \psi_n^{N-1}| a_k |\psi_0\rangle|^2 2\pi\delta(\omega - \omega_n^{N-1})}_{A^-(k,-\omega)} \tag{3.3.9}$$

As mentioned before, the spectral function is not only of interest from the numerical point of view but also because it is experimentally accessible through emission spectroscopy such as ARPES [90]. This can be seen from eq. 3.3.9: $A(k,\omega)$ is proportional to the probability density of an excitation with momentum k and energy ω (since $\omega_{n(k)}^{N\pm1} = \epsilon_{n(k)}^{N\pm1} \pm \mu$) [138]. In order to measure the occupied/available states, one shoots a particle with a large enough momentum into a $N-$particle system in its ground state. That system then emits one particle. The momentum of particles emitted in this way, can be measured as the overlap of the ground state (which absorbed the momentum) and the $N-1$ particle state [108]. The cross section is exactly

the $A^-(k,\omega)$ amplitude [8].

We will now discuss some properties of the Green's function to be used later during the development of the DMFT algorithms. Using the Sokhotski–Plemelj formula again (eq. 3.3.7), we can obtain a special case of the Kramers-Kronig relations. We first notice by direct application of eq. 3.3.7, that the imaginary part of the real frequency Green's function is (up to a factor) identical to the spectral function. This is also essential for the extraction of this function from simulations. Moreover it also means that real and imaginary part of Green's functions are not independent.

$$\mathfrak{I}\{G(k,\omega)\} = -\frac{\text{sign}(\omega)}{2} A(k,\omega) \tag{3.3.10}$$

$$\mathfrak{R}\{G(k,\omega)\} = \mathcal{P}\int_{-\infty}^{\infty} \frac{d\omega'}{2\pi} \frac{A(k,\omega')}{\omega-\omega'} = \mathcal{P}\int_{-\infty}^{\infty} \frac{d\omega'}{\pi} \frac{\text{sign}(\omega')\mathfrak{I}\{G(k,\omega')\}}{\omega-\omega'} \tag{3.3.11}$$

We can deduce that the spectral function contains the same information as the Green's function.

Two additional observations will provide conditions for the measured observables. The first one is the sum rule for the spectral function:

$$\begin{aligned}
1 &= \langle\psi_0| \left[a_k, a_k^\dagger\right] |\psi_0\rangle \\
&= \sum_n |\langle\psi_n^{N+1}| a_k^\dagger |\psi_0\rangle|^2 - \zeta \sum_n |\langle\psi_n^{N-1}| a_k |\psi_0\rangle|^2 \\
&= \int_{-\infty}^{\infty} \frac{d\omega}{2\pi} A(k,\omega) \tag{3.3.12}
\end{aligned}$$

Testing for this property provides not only a "sanity check" (i.e. if this fails, something went wrong) for simulations but also a constrained that can be used to obtain better numerical precision when computing $A(\omega)$ from $G(\omega)$ (see maximum entropy method in sec. 5).

From the sum rule follows the second important property of the Green's function: The behavior for large ω, i.e. the tail of the Green's function. See also sec. 5 for uses of this property.

$$\lim_{\omega\to\infty} G(k,\omega) \sim \lim_{\omega\to\infty} \int_{-\infty}^{\infty} \frac{d\omega'}{2\pi} \frac{A(k,\omega')}{\omega} = \frac{1}{\omega} \tag{3.3.13}$$

The asymptotic tail will be used to speed up simulations and reduce noise in the measurements.

For free fermions without spin, the $T=0$ Green's function ($H_0 = \sum_k \epsilon_k c_k^\dagger c_k$) can be evaluated immediately. We call the ground state energy $E_0 = \sum_{|k|<k_f} \epsilon_k$

$$|E_0\rangle = \prod_{|k|<k_f} c_k^\dagger |0\rangle$$

$$\Rightarrow |E_n^{N+1}\rangle = c_k^\dagger |E_0\rangle \Rightarrow c_k |E_0\rangle = |E_n^{N-1}\rangle \qquad \text{if } |k| < k_\text{f}$$
$$0 \qquad\qquad\qquad \text{otherwise}$$

---

8 See for example chapter 5 [70] and [43] for details about the underlying (γ, p) and $(e, e'p)$ reactions and measurement details.

Since ϵ_k is the energy needed to add a particle, we have $\omega_n^{N\pm1} = \pm(\epsilon_k - \mu)$. Evaluation of eq. 3.3.4 with these states gives:

$$G_0^\sigma(k,\omega) = \int \frac{d\omega'}{2\pi} \frac{2\pi\delta(\omega' - \epsilon_{k,\sigma} - \mu)}{\omega - \omega'}$$

$$= \frac{1}{\omega - \epsilon_{k,\sigma} + \mu + \text{sign}(\omega)i\eta} \tag{3.3.14}$$

This result can of course also be obtained by Fourier transformation and subsequent use of the residue theorem from eq. 3.2.11.

Comparison to fig. 3.2 shows that the free Green's function only has two poles, in the lower right and upper left quadrant. This allows for an easy application of the residue theorem by closing the path in a semi circle in the lower plane (Jordan's lemma takes care of the half circle contribution) for the retarded Green's function and in the upper half for the advanced Green's function.

$$\Rightarrow G_0^R(k,t) = -i\Theta(+t)e^{-it(\epsilon_k - \mu)} \tag{3.3.15}$$

$$G_0^A(k,t) = i\Theta(-t)e^{-it(\epsilon_k - \mu)} \tag{3.3.16}$$

A complete discussion can be found for example here [138, 70].

3.4 FINITE TEMPERATURE

While the frequency formulation has already proven useful from the numerical as well the experimental standpoint, we have only considered the case of $T = 0$. It turns out that going to finite temperatures is even more advantageous for numerical computations as we obtain a natural discretization that can be used for simulations. For finite temperatures, the imaginary time Green's functions is the natural choice. One can obtain very similar results for the spectral function as in the case of zero temperature with similar derivations.

$$A(k,\omega) = \frac{1}{Z}\sum_{n,m} |\langle E_n | a_k^\dagger | E_m \rangle|^2 e^{-\beta(E_m - \mu N_m)} \left(1 - e^{-\beta\omega}\right)$$

$$\times 2\pi\delta(E_n - E_m - \mu - \omega) \tag{3.4.1}$$

There is however an important distinction for the frequency representation: The finite temperatures Green's function is (anti) periodic, which can be seen using the cyclic permutation property of the trace operation[9].

$$G_{\alpha\alpha'}(\tau - \beta) = \frac{1}{Z}\text{Tr}\left(e^{-\beta H}T_\zeta\left[a_\alpha(\tau)a_{\alpha'}^\dagger(\beta)\right]\right)$$

$$= \zeta\frac{1}{Z}\text{Tr}\left(e^{-\beta H}T_\zeta\left[a_{\alpha'}^\dagger(\beta)a_\alpha(\tau)\right]\right)$$

$$= \zeta\frac{1}{Z}\text{Tr}\left(e^{-\beta H}e^{\beta H}a_{\alpha'}^\dagger(0)e^{-\beta H}a_\alpha(\tau)\right)$$

$$= \zeta\frac{1}{Z}\text{Tr}\left(e^{-\beta H}a_\alpha(\tau)a_{\alpha'}^\dagger(0)\right)$$

$$= \zeta G_{\alpha\alpha'}(\tau), \qquad 0 < \tau < \beta \tag{3.4.2}$$

---

9 $Tr(ABC) = Tr(CAB) = Tr(BCA)$

We have again assumed a time independent Hamiltonian and used the property that operators inside the trace operation can be cyclically permuted.

Due to the finite interval of τ, the Fourier transform is discrete (we use that the Green's function only depends on the difference in imaginary time in our case).

$$G_{\alpha\alpha'}(\tau) = \frac{1}{\beta} \sum_{n=-\infty}^{\infty} e^{-i\frac{\tau}{\beta}\pi n} G_n^{\alpha\alpha'}$$

$$\omega_n = \begin{cases} \frac{2\pi n}{\beta} & \text{fermions} \\ \frac{2\pi(n+1)}{\beta} & \text{bosons} \end{cases} \tag{3.4.3}$$

Using the periodic boundary conditions and noting that $e^{i\beta\omega_n} = \zeta$ with the Matsubara frequencies ω_n, we obtain the later most often used representation of the Green's function.

$$G_{\alpha\alpha'}(\tau) = \frac{1}{\beta} \sum_{n=-\infty}^{\infty} e^{-i\omega_n\tau} G_{\alpha\alpha'}(i\omega_n) \tag{3.4.4}$$

$$G_{\alpha\alpha'}(i\omega_n) = \int_0^\beta e^{i\omega_n\tau} G_{\alpha\alpha'}(\tau)\, \mathrm{d}\tau \tag{3.4.5}$$

We can write down a similar expression to eq. 3.3.9 but this brings up a problem: There are two frequency representations which need to be connected. The discrete representation in terms of imaginary Matsubara frequencies and the continuous one in real frequencies from before.

$$G_{\alpha\alpha'}(\omega) = \frac{1}{Z} \sum_{m,n} \langle E_n | a_\alpha | E_m \rangle \langle E_m | a_{\alpha'}^\dagger | E_n \rangle$$

$$\times \left[\frac{e^{-\beta E_n}}{\omega - E_m + E_n + i\eta} - \zeta \frac{e^{-\beta E_m}}{\omega - E_m + E_n - i\eta} \right] \tag{3.4.6}$$

In cases of the retarded and advanced Green's function the usual signs of both $+i\eta$ or both $-i\eta$ replace the alternating sign of the time ordered η above. Using translational symmetry we can write down the familiar form of the thermal Green's function in terms of the spectral function.

$$G(k - k', i\omega_n) = \frac{1}{Z} \sum_{m,l} \frac{\langle E_l | a_k | E_m \rangle \langle E_m | a_{k'}^\dagger | E_l \rangle}{i\omega_n - E_m + E_l} \left(e^{-\beta E_l} - \zeta e^{-\beta E_m} \right) \tag{3.4.7}$$

$$= -\int_{-\infty}^{\infty} \frac{\mathrm{d}\omega}{2\pi} \frac{A(k - k', \omega)}{i\omega_n - \omega} \tag{3.4.8}$$

In fact both representations can be connected by analytic continuation $i\omega_n \to z$. One however must verify the choice of integration limits in the finite temperature Fourier transform (see chapter 3 [11], chapter 5 [70]). It is unnecessary to repeat the details here, however it is worth noting that special care must be taken which path in the complex plane one chooses. This is due to the aforementioned branch cut (as a result of a continuum of poles at ω_n) on the real axis of z in the time ordered Green's function. The formula for spectral weight is also affected by this (see eq. 3.4.1).

Again omitting analogous derivations, we also write down the Kramers-Kronig relations for finite temperatures. They are useful for consistency checks of simulations,

because the whole Green's function is obtained from simulations, but imaginary and real part are related analytically:

$$\Im\{G(k,\omega)\} = -\frac{1}{2}\tanh\left(\frac{\beta\omega}{2}\right)^{-\zeta}A(k,\omega) \tag{3.4.9}$$

$$\Re\{G(k,\omega)\} = \mathcal{P}\int_{-\infty}^{\infty}\frac{d\omega'}{2\pi}\frac{A(k,\omega')}{\omega-\omega'}$$

$$= \mathcal{P}\int_{-\infty}^{\infty}\frac{d\omega'}{\pi}\frac{\text{sign}(\omega')\Im\{G(k,\omega')\}}{\omega-\omega'} \tag{3.4.10}$$

This finally provides us with the relationship between time ordered, retarded and advanced Green's function at finite temperatures.

$$G(k,\omega) = (1+\zeta n(\omega+\mu))\,G^R(k,\omega) - \zeta n(\mu-\omega)G^A(k,\omega) \tag{3.4.11}$$

During the development of simulation programs it is useful to check results for known analytic properties of the measured Green's functions. The Kramers-Kronig relations gave a first check and the β periodicity will also be used frequently. There are three more useful properties that are easily verifiable.
The diagonal fermionic Green's function exhibits a discontinuity at the origin of the complex plane, that provides the first of these identities.

$$\lim_{\tau\searrow 0}\left[G_{\alpha\alpha'}(\tau)-G_{\alpha\alpha'}(-\tau)\right] = \lim_{\tau\searrow 0}\frac{1}{Z}\text{Tr}\left(e^{-(\beta H-\mu N)}T_\zeta\left[c_\alpha(\tau)c_{\alpha'}^\dagger(0)-c_\alpha(-\tau)c_{\alpha'}^\dagger(0)\right]\right)$$

$$= \lim_{\tau\searrow 0}\frac{1}{Z}\text{Tr}\left(e^{-(\beta H-\mu N)}\left[c_\alpha(\tau)c_{\alpha'}^\dagger(0)+c_{\alpha'}^\dagger(0)c_\alpha(-\tau)\right]\right)$$

$$= \frac{1}{Z}\text{Tr}\left(e^{-(\beta H-\mu N)}\left[c_\alpha c_{\alpha'}^\dagger+c_{\alpha'}^\dagger c_\alpha\right]\right) \tag{3.4.12}$$

$$= \left\langle\{c_\alpha,c_{\alpha'}^\dagger\}\right\rangle \overset{\text{eq. 1.2.5}}{=} \delta_{\alpha\alpha'} \tag{3.4.13}$$

The second property can also be used to reduce storage space for Green's functions in multi band simulations, we will use that the imaginary time evolution is not unitary:

$$\left[G_{\alpha\alpha'}(\tau)\right]^\dagger = \frac{1}{Z}\text{Tr}\left\{\left(e^{-\beta H}e^{\tau H}c_\alpha^\dagger(0)e^{-\tau H}c_{\alpha'}(0)\right)\right\}^\dagger$$

$$= \frac{1}{Z}\text{Tr}\left(c_{\alpha'}^\dagger(0)e^{-\tau H}c_\alpha(0)e^{\tau H}e^{-\beta H}\right)$$

$$= \frac{1}{Z}\text{Tr}\left(e^{-\beta H}e^{\tau H}c_{\alpha'}^\dagger(0)e^{-\tau H}c_\alpha(0)\right)$$

$$= G_{\alpha'\alpha}(\tau) \tag{3.4.14}$$

This implies that the diagonal Green's function is real valued which in turn implies (by one of the basic properties of Fourier transforms) that $\left[G_{\alpha\alpha}(\omega)\right]^\dagger = G_{\alpha\alpha}(-\omega)$. Indeed there is a more general version for Matsubara Green's functions:

$$\left[G_{\alpha\alpha'}(i\omega_n)\right]^\dagger = \int_0^\beta e^{-i\omega_n\tau}\left[G_{\alpha\alpha'}(\tau)\right]^\dagger d\tau$$

$$\overset{\text{eq. 3.4.14}}{=}\int_0^\beta e^{-i\omega_n\tau}G_{\alpha'\alpha}(\tau)\,d\tau$$

$$= G_{\alpha'\alpha}(i\omega_n) \tag{3.4.15}$$

So for the diagonal translational invariant Green's function, there is again a simplification because only positive Matsubara frequencies have to be stored.

Lastly we look one more time at the free Green's function as an example. Using eq. 3.5.9 with the appropriate zero potential Hamiltonian H_0, one can derive an expression for the free Green's function[10] as function of the bosonic or fermionic distribution n_α.

$$G_{0,\alpha\alpha'}(\tau) = \delta_{\alpha\alpha'} e^{-(\epsilon_\alpha - \mu)\tau} \left[\Theta(\tau - \eta)(1 - \zeta n_\alpha) + \zeta\Theta(\tau + \eta)\right] \tag{3.4.16}$$

$$n_\alpha = \frac{1}{e^{\beta(\epsilon_\alpha - \mu)} - \zeta} \tag{3.4.17}$$

We obtain the Matsubara representation by inserting eq. 3.4.16 into eq. 3.4.5

$$G_{0,\alpha\alpha'}(i\omega_n) = \delta_{\alpha\alpha'} \int_0^\beta e^{i\omega_n\tau} e^{-(\epsilon_\alpha - \mu)\tau}(1 + \zeta n_\alpha)\, d\tau$$

$$= \frac{\delta_{\alpha\alpha'}}{i\omega_n - \epsilon_\alpha + \mu} \tag{3.4.18}$$

Comparing both frequency representations of the free propagator (eq. 3.3.14 and eq. 3.4.18) one can again verify the connection between Matsubara and real frequency representation.

We have now several analytic properties available which should be considered during implementations simulation algorithms:

Sum Rule (eq. 3.3.12)   This should be used after analytic continuation to verify the spectral function

HF Tail (eq. 3.3.13)   The knowledge about the analytic form of the high frequency tail can be used to suppress noise, for example in the CT-HYB solver and to improve precision of Fourier transformations.

periodicity (eq. 3.4.2)   This property is used in many derivations and serves as a check for $\tau \to \beta$

Kramer Kronig Rel. (eq. 3.4.10)   After having measured the Green's function numerically or after analytic continuation, the Kramer Kronig relations should be verified

Hermitian (eq. 3.4.15)   This property can be used for the diagonal Green's function to reduce the storage requirements and speed up mathematical operations. This is due to the fact that only real *or* imaginary part have to be stored and all operations can be done on pure floating point variables.

3.5 FEYNMAN DIAGRAMS

In this section a very brief overview over diagrammatic perturbation theory is given. This is necessary because the class of continuous time quantum Monte Carlo methods expands in orders of these diagrams. We limit all definitions to the case we need

---

10 One separately considers particle ($G_0^{\alpha\alpha'}(1 - n_a)$) and particle hole ($G_0^{\alpha\alpha'} n_\alpha$) states chapter 5 [70].
For brevity we evaluate our abbreviated derivation under the canonical ensemble.

for the derivation of the dynamical mean field approximation in the next chapter. Full derivations and proofs can be found for example in [70, 104, 129].

A useful tool for the systematic construction of Green's functions and their perturbative expansions are generating functionals. As mentioned before, these resemble generalized characteristic functions (see eq. 2.1.16), in that they generate all possible correlation functions (which are generalized to Green's functions now). We let some external source J act for a limited amount of time T_S such that $T_S \ll t_f - t_i$.

$$Z\left[\overline{J}_\alpha, J_\alpha\right] = \int \mathcal{D}\left[\overline{\psi}_\alpha, \psi_\alpha\right] e^{-A\left[\overline{\psi}_\alpha, \psi_\alpha\right]} \times e^{-\sum_\alpha \int_0^\beta d\tau \left[\overline{J}_\alpha(\tau)\psi_\alpha(\tau) + \overline{\psi}_\alpha(\tau)J_\alpha(\tau)\right]}$$
$$= \left\langle e^{-\langle J, \psi \rangle} \right\rangle \tag{3.5.1}$$

Where the generalized inner product was defined as

$$\langle J, \psi \rangle = \sum_\gamma \int_0^\beta d\tau' \left(\overline{\psi}_\alpha(\tau')J_\alpha(\tau') + \overline{J}_\alpha(\tau')\psi_\alpha(\tau') \right) \tag{3.5.2}$$

Depending on the number of fields in the underlying model, the generating functional and number of external fields may change. They can have Grassmann or complex scalar behavior for fermionic and bosonic field respectively. In preparation for the rest of this section we define the generating functionals for unconnected and connected diagrams (which will be be introduced later).

The normalized partition functional $G\left[\overline{J}, J\right]$ can be viewed as functional generalizations of the moment generating functions (eq. 2.1.16), because correlation functions can be expressed as its derivatives. Connected and unconnected correlation functions are related through similar formulas as moments and cumulants. W is called effective potential, it is a generalization of the cumulant generating function. The role of W and its Legendre transform Γ, the effective action, will be discussed in the remaining part of this chapter.

The following definitions can be extended by choosing more general source terms, however this definition will be sufficient for my thesis.

$$G[\overline{J}_\alpha, J_\alpha] = \frac{1}{Z} Z\left[\overline{J}_\alpha, J_\alpha\right] \tag{3.5.3}$$

$$W[\overline{J}_\alpha, J_\alpha] = \ln\left(G[\overline{J}_\alpha, J_\alpha]\right) \tag{3.5.4}$$

$$\Gamma\left[\overline{\psi}_\alpha, \psi_\alpha\right] = -W[\overline{J}_\alpha, J_\alpha] - \langle J, \psi \rangle \tag{3.5.5}$$

One can express expectation values of the fields ψ and $\overline{\psi}$ (the correlation functions) as functional derivatives. This is done similarly to the moment trick for the n-th moment of Gaussian integrals.

$$\psi_\alpha e^{-\langle J, \psi \rangle} \leftrightarrow \left(\frac{\delta}{\delta J_\alpha} \right) \tag{3.5.6}$$

From that we obtain:

$$G^{(1)}(\alpha_1 \tau_1; \alpha_2 \tau_2) = \left\langle T_\zeta \left[\psi_{\alpha_1}(\tau_1) \overline{\psi}_{\alpha_2}(\tau_2) \right] \right\rangle \tag{3.5.7}$$

$$= \zeta \frac{\delta^2 G[\overline{J}, J]}{\delta \overline{J}_{\alpha_2}(\tau_2) \delta J_{\alpha_1}(\tau_1)} \Bigg|_{J=\overline{J}=0} \tag{3.5.8}$$

This method is central to diagrammatic perturbation theory as the above and similar generating functionals can be used in conjunction with Wick's theorem to systematically generate Feynman diagrams. Each functional derivative generates an additional field operator inside the resulting expectation value and fixes the argument which can be used to generate n-body (connected) Green's functions.

$$G^{(n)}(\alpha_1\tau_1,\ldots,\alpha_n\tau_n;\alpha_1'\tau_1',\ldots,\alpha_n'\tau_n') = \frac{1}{\zeta^n}\frac{\delta^{2n}G[\overline{J},J]}{\delta\overline{J}_{\alpha_1}(\tau_1)\cdots\overline{J}_{\alpha_n}(\tau_n)J_{\alpha_n'}(\tau_n')\cdots J_{\alpha_1'}(\tau_1')}\bigg|_{J=\overline{J}=0} \quad (3.5.9)$$

$$G_c^{(n)}(\alpha_1\tau_1,\ldots,\alpha_n\tau_n;\alpha_1'\tau_1',\ldots,\alpha_n'\tau_n') = \zeta^n\frac{\delta^{2n}W[\overline{J},J]}{\delta\overline{J}_{\alpha_1}(\tau_1)\cdots\overline{J}_{\alpha_n}(\tau_n)J_{\alpha_n'}(\tau_n')\cdots J_{\alpha_1'}(\tau_1')}\bigg|_{J=\overline{J}=0}$$

$$(3.5.10)$$

The functional derivatives provide an intuitive method to fix external states and times for propagators.

We can simplify calculations by introducing Feynman diagrams to represent propagators and interactions. Creation (field) operators for a state α at time τ are represented by an outgoing arrow originating at a point labeled τ. Annihilation operators are defined in the same way with an incoming arrow. Equal times are connected at a single point.

This means propagation of a state from time τ_2 to τ_1 is written as follows:

$$\alpha_2\tau_2 \longrightarrow \alpha_1\tau_1 \quad = \delta_{\alpha_1\alpha_2}G(\alpha_1\tau_1;\alpha_2\tau_2) \quad (3.5.11)$$

An interaction due to a potential V at time τ is first written according to eq. 1.2.4.

$$V(a^\dagger(\tau),a(\tau)) = \sum_{\alpha\beta\gamma\delta}\langle\alpha\beta|\,v\,|\gamma\delta\rangle\,a_\alpha^\dagger(\tau)a_\beta^\dagger(\tau)a_\gamma(\tau)a_\delta(\tau) \quad (3.5.12)$$

This is graphically represented by vertex connections at equal times with a dashed line:

$$= \langle\alpha\beta|\,v\,|\gamma\delta\rangle$$

$$(3.5.13)$$

There are so called Feynman rules, governing the possible diagrams and pre-factors (see [1, 70] for a full derivation). Even though diagrammatic methods will be used quite a lot, a detailed introduction exceeds the scope of this thesis.

We can however do an expansion of a general interaction and look at the resulting Feynman diagrams. In the next chapter, we will use a specific model and describe a method to obtain a simple type of diagrams numerically.

Let $\hat{H} = \hat{H}_0 + \lambda\hat{V}$ such that $H_0\,|\epsilon_k\rangle = \epsilon_k\,|\epsilon_k\rangle$ is exactly solvable and V a small perturbation λ.

We write the usual Dyson series in imaginary time as

$$U_{\text{int}}(\tau) = T_\zeta\exp\left[-\int_0^\tau V(\tau')\,d\tau'\right] \quad (3.5.14)$$

$$\frac{Z}{Z_0} = \frac{\text{Tr}\left(e^{-\beta(H_0-\mu N)}U_{\text{int}}(\beta)\right)}{\text{Tr}\left(e^{-\beta H_0-\mu N}\right)}$$
$$\equiv \langle U_{\text{int}}(\beta)\rangle_0 \tag{3.5.15}$$

Explicit expansion yields:

$$= \sum_{n=0}^{\infty} \frac{(-1)^n}{n!} \int_0^{\beta} \mathrm{d}\tau_1 \cdots \mathrm{d}\tau_n \left\langle V(a_{\alpha_1}^{\dagger}(\tau_1),\cdots a_{\alpha_k}(\tau_1))\cdots V(a_{\alpha_1}^{\dagger}(\tau_n)\cdots a_{\alpha_k}(\tau_n))\cdots\right\rangle_0 \tag{3.5.16}$$

$$Z_0 = \int \mathcal{D}[\overline{\psi},\psi] \exp\left[-\sum_{\alpha}\int_0^{\beta}\overline{\psi}_{\alpha}(\tau)\underbrace{\left(\frac{\partial}{\partial\tau}+\epsilon_{\alpha}-\mu\right)}_{\left(G_0^{\alpha\alpha'}(\tau)\right)^{-1}}\psi_{\alpha}(\tau)\right]\mathrm{d}\tau \tag{3.5.17}$$

An expanded form of the imaginary times Green's function follows immediately.

$$\Rightarrow G^{(n)}(\alpha_1\tau_1\cdots\alpha_1'\tau_1') = \frac{\left\langle T_{\zeta}\left[U_{\text{int}}(\beta)a_{\alpha_1}(\tau_1)\cdots a_{\alpha_1'}^{\dagger}(\tau_1')\right]\right\rangle_0}{\langle U_{\text{int}}(\tau)\rangle_0} \tag{3.5.18}$$

The notation $\langle\cdot\rangle_0$ stands for the average with respect to a zero potential Hamiltonian H_0 with partition function Z_0. This identity is especially useful since Z_0 is only a shift in the grand canonical potential:

$$-\frac{1}{\beta}\ln\left(\frac{Z}{Z_0}\right) = \Omega - \Omega_0 = -\frac{1}{\beta}W\left[\overline{J},J\right] = -\frac{1}{\beta}\ln\left(\langle U_{\text{int}}(\tau)\rangle\right) \tag{3.5.19}$$

As a consequence of the linked cluster theorem $\Omega-\Omega_0$ is identical to the sum over all connected vacuum diagrams (no external legs), so $W[\overline{J},J]$ generates all contributing terms. An often quoted hand-waving argument for the vanishing contribution of unconnected diagrams is, that they are already included in lower order diagrams, i.e. one unconnected n-point diagram can be written as sum of $k,l,\cdots$-point diagrams so that $k+l+\cdots = n$, see also correspondence of moments and cumulants.
The last important ingredient for the diagrammatic perturbation theory is the Wick's theorem[11]. This formula allows the expression of expected values of creation and annihilation operators under the free Hamiltonian as sum over free Green's functions.
Note that in the non symmetry breaking case, the number of creation and annihilation operators must be the same for $\langle\cdots\rangle_0$, under the constraint of a quadratic Hamiltonian. A pair of creation and annihilation operator is called contraction in this case, often the possible contractions are denoted by brackets in the following way:

$$\left\langle a_{\alpha_1}^?(\tau_1)a_{\alpha_2}^?(\tau_2)\cdots a_{\alpha_n}^?(\tau_n)\right\rangle_0 = \sum_{\pi\in K}\prod_{i=1}^{n}\zeta^{sgn(\pi)}\left\langle a_{\alpha_{\pi(1)}}(\tau_{\pi(1)})a_{\alpha_{\pi(2)}}^{\dagger}(\tau_{\pi(2)})\right\rangle_0$$
$$\cdots\left\langle a_{\alpha_{\pi(n-1)}}(\tau_{\pi(n-1)})a_{\alpha_{\pi(n)}}^{\dagger}(\tau_{\pi(n)})\right\rangle_0 \tag{3.5.20}$$

---

11 In the context of random variables a similar result is known as Isserlis' theorem for Gaussian moments. This further verifies the connection between moments, cumulants and Green's functions [67, 135].

With $K \in S_n$ [12] such that no permutations with two creation/annihilation operators occur. The minus sign for fermions can be obtained by counting the number of times, lines cross each other. For example:

$$\left\langle a_{\alpha_1}(\tau_1) a_{\alpha_2}(\tau_2) a^\dagger_{\alpha_3}(\tau_3) a^\dagger_{\alpha_4}(\tau_4) \right\rangle_0 = \zeta \delta_{\alpha_1 \alpha_3} G_0^{\alpha_1 \alpha_3}(\tau_1 - \tau_3) \delta_{\alpha_1 \alpha_4} G_0^{\alpha_1 \alpha_4}(\tau_1 - \tau_4)$$
$$+ \delta_{\alpha_2 \alpha_3} G_0^{\alpha_2 \alpha_3}(\tau_2 - \tau_3) \delta_{\alpha_2 \alpha_4} G_0^{\alpha_2 \alpha_4}(\tau_2 - \tau_4)$$

We can now expand eq. 3.5.16 using Feynman diagrams. The first order diagrams for eq. 3.5.16 of a two body potential are (zero-th order is of course the free propagator):

$$V(a^\dagger(\tau), a(\tau)) = \frac{1}{2} \sum_{\alpha\beta\gamma\delta} \langle \alpha\beta | \hat{v} | \gamma\delta \rangle \, a^\dagger_\alpha(\tau) a^\dagger_\beta(\tau) a_\gamma(\tau) a_\delta(\tau)$$

$$\left[\frac{Z}{Z_0} \right]_{n=1} = -\frac{1}{2} \int_0^\beta \mathrm{d}\tau \sum_{\alpha\beta\gamma\delta} \langle \alpha\beta | \hat{v} | \gamma\delta \rangle \left\langle a^\dagger_\alpha(\tau) a^\dagger_\beta(\tau) a_\gamma(\tau) a_\delta(\tau) \right\rangle_0$$

$$= -\frac{1}{2} \int_0^\beta \mathrm{d}\tau \sum_{\alpha\beta} \left[(\langle \alpha\beta | \hat{v} | \alpha\beta \rangle + \zeta \langle \alpha\beta | \hat{v} | \beta\alpha \rangle) \underbrace{G_0^{\alpha\alpha}(0)}_{=n_\alpha} G_0^{\beta\beta}(0) \right] \quad (3.5.21)$$

$$= \frac{1}{2} \bigcirc^{\alpha}{}^{\tau} \text{-----} \bigcirc^{\beta} + \zeta \frac{1}{2} \overset{\tau}{\underset{}{\bigcirc\!\!\!\!\bigcirc}} \quad (3.5.22)$$

Ignoring all mathematical pitfalls, we imagine reordering all diagrams of Z into two groups: the unconnected part is pulled into one bracket in front of the sum over all connected diagrams. The unconnected contributions are the vacuum contributions which cancel of with Z_0 in the denominator.

It is also common to sum up isomorphic diagrams and omit labels. This changes the weight of each diagram according to some symmetry factor $1/\overline{S}_n$ and the number of possible permutations $2^n n!$. Only topologically different diagrams describe distinct physical processes. We will therefore mostly use unlabeled diagrams, derivations for the pre-factors relating them to labeled ones can be found in the literature [70, 104, 129]

3.6 DYSON EQUATION

We have stated before, that only connected diagrams contribute to the shift in the grand canonical potential. One can classify these once more by checking whether or not cutting one propagator results in two diagrams of lower order. Diagrams for which such a cut does not result in two of lower order are called one particle irreducible (1PI). For example diagram eq. 3.6.2 is one particle reducible while eq. 3.6.1 is not.

$$(3.6.1)$$

$$\text{(3.6.2)}$$

There is an important formal way to group these diagrams. We will assume a free scalar field for now (i.e. $Z\left[\bar{J}, J\right] \rightarrow Z[J]$) in order to shorten the following argument[13]. No symmetry breaking is assumed in the following calculations. For a derivation of the symmetry breaking case see chapter 2 [76].

$$\sum_{\alpha_0} \int d\tau_0 \frac{\delta^2 W[J]}{\delta J_{\alpha_1}(\tau_1) \delta J_{\alpha_0}(\tau_0)} \frac{\delta^2 \Gamma[\psi, \psi]}{\delta \psi_{\alpha_0}(\tau_0) \delta \psi_{\alpha_2}(\tau_2)} \qquad (3.6.3)$$

$$= \sum_{\alpha_0} \int d\tau_0 \left[\frac{\delta \psi_{\alpha_1}(\tau_1)}{\delta J_{\alpha_0}}\right] \cdot \left[-\frac{\delta J_{\alpha_2}(\tau_2)}{\delta \psi_{\alpha_2}}(\tau_2)\right] \qquad (3.6.4)$$

$$= -\frac{\delta \psi_{\alpha_1}(\tau_1)}{\delta \psi_{\alpha_2}(\tau_2)} = -\delta_{\alpha_1 \alpha_2} \delta(\tau_2 - \tau_1) \qquad (3.6.5)$$

$$\Leftrightarrow \quad \underset{\alpha_2}{\overset{\Gamma \qquad G}{\longrightarrow \bigotimes \longrightarrow \bigotimes \overset{\alpha_1}{\longrightarrow}}} = -\delta_{\alpha_1 \alpha_2} \delta(\tau_1 - \tau_2) \qquad (3.6.6)$$

$$\Rightarrow \quad \Gamma^{(1)}(\alpha_1 \tau_1; \alpha_2 \tau_2) = -G_C^{-1}(\alpha_1 \tau_1; \alpha_2 \tau_2) \qquad (3.6.7)$$

This means the connected one particle Green's function is the inverse operator of the two point vertex function.

We have seen that each functional derivative with respect to external field or source results in an additional leg of Green's function and vertex function respectively. Diagrammatically this can be expressed be attaching a leg to the Γ blob in the first case and another leg with a Γ blob in the second. Successive differentiation and use of eq. 3.6.6 with a shorthand notation $(i) \rightarrow (\alpha_i \tau_i)$ and $\oint_{i \cdots j} \rightarrow \sum_{\alpha_i \cdots \alpha_j} \int_0^\beta d\tau_i \cdots d\tau_j$ yields (we again need to assume the non symmetry breaking case):

$$\text{(3.6.8)}$$

$$\Leftrightarrow G_C^{(2)}(5, 6; 5'6') = -\oint_{1 \cdots 4} G_C^{(1)}(5; 1) G_C^{(1)}(6; 2) \Gamma(1, 2; 3, 4) G_C^{(1)}(3; 5') G_C^{(1)}(4; 6') \quad (3.6.9)$$

This identity can be extended to higher order Green's functions [70].

There are two implications: Connected Green's functions can be constructed as tree diagrams (i.e. no loops) using vertex functions, which is the reason for the name "effective action".

One can show that loops contribute with a factor of $1/\hbar$. So in the classical limit of $\hbar \rightarrow 0$, loops should no longer be present and the effective action converges against the classical action[14] [70, 20].

The fact that Γ can be interpreted as action, can also be seen by setting the external

---

13 The extension to fermionic fields can be obtained by using the functional chain rule to introduce external field $\bar{J}$ and write their derivatives as second derivatives of the effective action.

14 In fact, loop expansion to first order gives $\Gamma[\psi] = A[\psi] + \frac{1}{2l} \operatorname{Tr} \log \frac{\delta^2 A[\psi]}{\delta \psi^2}$

fields to zero (i.e. the field are stationary points of Γ).

The second property is the fact that the vertex function must be 1PI: Imagine cutting a single propagator inside Γ in eq. 3.6.8. If Γ would not be 1PI, this would result in the left hand side to be disconnected (which it is not by definition). Therefore $\Gamma[\overline{\psi}, \psi]$ is also sometimes called generating function for 1PI diagrams.

We now define the self energy Σ as difference between the effective action of the interacting Hamiltonian and that of a free one.

The subscript $_C$ will be dropped where the context permits it. In addition the following identities are true in momentum space, so we can drop the corresponding arguments as well.

Definition 15 (Self Energy)

$$\Sigma(1; 2) = \Gamma(1; 2) - \Gamma_0(1; 2) \tag{3.6.10}$$

The self energy will be central to the DMFT algorithm so it is worth stating some properties which justify its interpretation as effective potential. Σ again only contains 1PI diagrams. But in contrast to $\Gamma^{(2)}$ does not expand into in a tree like structure. With the use of the inverse (eq. 3.6.6) we can now find the Dyson equation:

$$G^{-1} = G_0^{-1} + \Sigma \tag{3.6.11}$$

One often rewrites this by multiplying with $\frac{G_0^{-1}}{G_C^{-1}}$, or G_0 from the left and G from the right to obtain two alternative forms. Even though this simplified notation might suggest otherwise, we are still dealing with operators.

$$G = \left[G_0^{-1} - \Sigma\right]^{-1} \tag{3.6.12}$$

$$= G_0 - G_0 \Sigma G = G_0 - G_0 \Sigma G_0 + G_0 \Sigma G_0 \Sigma G_0 \pm \cdots \tag{3.6.13}$$

 (3.6.14)

 (3.6.15)

$$= \cdots \tag{3.6.16}$$

We will later often use the Dyson equation in Matsubara representation. It then reads:

$$G(k, i\omega_n) \overset{\text{eq. 3.4.18}}{=} \frac{1}{i\omega_n - \epsilon_k + \mu - \Sigma(k, i\omega_n)} \tag{3.6.17}$$

We introduced a double line for the full propagator that includes all self energy contributions. This is also called dressed propagator. From the last expression, the role of the self energy as effective one-body potential becomes clear, since it is the only term that changes in comparison to G_0.

We have also seen that the pole structure of the Green's function is related to the features of the quasi particle spectrum. Properties such as the effective mass or density of states will later be directly calculated as derivatives of Σ. This will later be used to obtain results from DMFT calculations.

For a more general proof of the effective action (tree diagram) hierarchy one can use the Dyson Schwinger equation with the connected Green's functions [104].
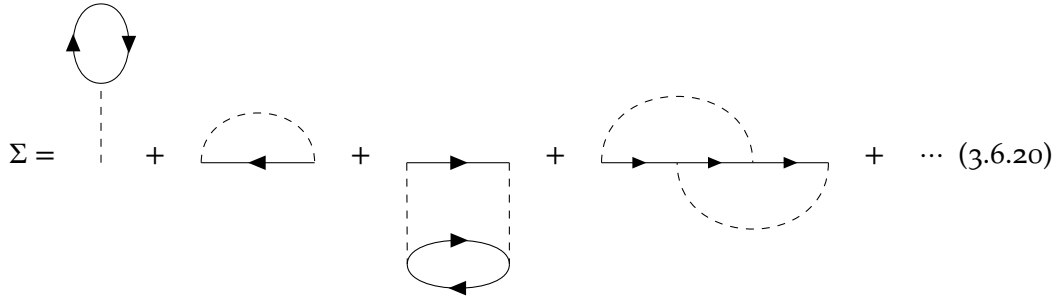
By comparison of the resolvent representation (eq. 3.3.3) for a free and an interaction system, one can obtain the Lippmann Schwinger equation.

$$G^{R/A}(z) = \left[(z \pm i\eta)\mathbb{1} - H_0 - V\right]^{-1} \tag{3.6.18}$$

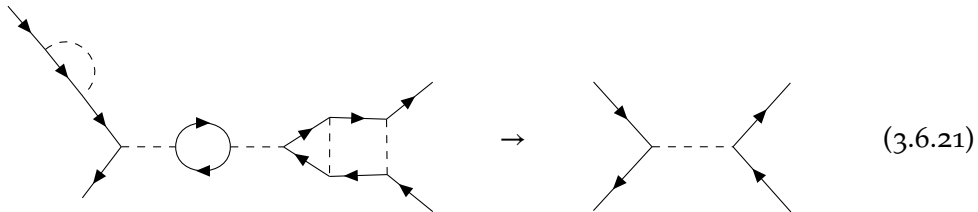$$= \left[\left[G_0^{R/A}(z)\right]^{-1} - V\right]^{-1} \tag{3.6.19}$$

Subsequently comparing eq. 3.6.11 and eq. 3.6.19 again confirms the role of Σ as an effective potential.

Before moving on quasi particles, we take a closer look at the diagrammatic expansion of the self energy. One of the solvers will use this expansion. Let's write down the first few contributions of the self energy. Separating the contributions for Hartree-Fock mean field is instructive in order to differentiate dynamical mean field theory.

$$\Sigma = \quad + \quad + \quad + \quad + \quad \cdots \tag{3.6.20}$$

We can now distinguish diagrams with and without self energy interactions quite easily as we only need to look for contributions, i.e. sub graphs with two amputated outer propagator legs. Replacing all self energy insertions by propagators and replacing vertex parts (two fermion legs, one interaction leg) by corners ("bare vertices"), we can obtain a skeleton diagram[15].

$$\rightarrow \tag{3.6.21}$$

Through substitution of free propagators by full ones, we obtain so called dressed skeleton diagrams. This turns out to be a useful grouping for the derivation of the dynamical mean field theory. The well known Hartree Fock method can be expressed in dressed skeleton diagrams as well:

$$\Sigma_{HF} = \quad + \quad \tag{3.6.22}$$

---

15 Not all contributions have to be replaced. A diagram that is its own skeleton diagram is called irreducible [116].

Since we did not fully develop the diagrammatic rules, the calculation of these diagrams is left to the literature [24, 80].

But even without explicit calculation we can make an important observation which empathizes the distinction between DMFT and HF approximations: The Hartree and Fock like contributions are given in eq. 3.6.23 and eq. 3.6.24, the outer legs are amputated as usual. Outer momenta and frequencies are fixed by the external free propagators.

$k', i\omega_n', \sigma'$

$$= -\sum_{k,n,\sigma'} \langle kk' | v | kk' \rangle G_0^{\sigma'}(k', i\omega_n') e^{i\omega_n'\eta}$$

$$0,0$$

$$= \langle kk' | v | kk' \rangle n_{HF}(k) \tag{3.6.23}$$

$k - k', i\omega_n - i\omega_n'$

$$= \zeta \sum_{k,n,\sigma'} \delta_{\sigma,\sigma'} \langle kk' | v | k'k \rangle \delta_{\sigma,\sigma'} G_0^{\sigma'}(k', i\omega_n') e^{i\omega_n'\eta}$$

$k', i\omega_n', \sigma'$

$$= \zeta \langle kk' | v | k'k \rangle n_{HF}(k) \tag{3.6.24}$$

$$\Rightarrow \Sigma_{HF}(k, i\omega_n) = \Sigma_{HF}(k) \tag{3.6.25}$$

$$= \left(\langle kk' | v | kk' \rangle + \zeta \langle kk' | v | k'k \rangle \right) n_{HF}(k) \tag{3.6.26}$$

$$= \frac{1}{V} \left(v(0) + \zeta v(k - k') \right) n_{HF}(k) \tag{3.6.27}$$

The last line shows again (by comparison to eq. 1.4.12) that the self energy is the correction to the energy of the free system. We also used that:

$$\frac{1}{\beta} \sum_{\omega_n} G_{HF}(k, i\omega_n) e^{i\omega_n\eta} = -\frac{\zeta}{e^{\epsilon_k - \mu + \Sigma_{HF}(k)}} = -\zeta n_{HF}(k) \tag{3.6.28}$$

This is a self consistency equation as introduced in eq. 1.4.5 since the distribution function $n_{\mathrm{HF}}(k)$ is a function of the self energy that again determines the electron distribution.

It also now becomes obvious why the bare propagators in eq. 3.6.23 and eq. 3.6.24 should be replaced by the full HF Green's function (see eq. 3.6.22): Iterative calculation of the self consistency equation will introduce more HF-like contributions[16]. The most important feature of the self energy in HF approximation for us is the independence of $i\omega_n$. The DMFT approximation will be in a certain sense complimentary, since it will be independent of k but retain full frequency dependence.

An expansion into skeleton diagrams is often formalized in the definition of the Luttinger-Ward functional. Similar to the the definition of the self energy in eq. 3.6.10, the difference between an effective action of interacting and non-interacting systems is used. However, this time one uses the 2PI effective action obtained from Legendre

---

16 In order to speed up convergence or even make it possible at all, one normally does not start with the free propagator but some more sophisticated guess.

transformation of the effective potential using a (assumed) convex Green's function as source [109, 105]

$$\Gamma[G] = \left[-W[J] - \oint_{\alpha,\beta} J_{\alpha,\beta} G(\beta,\alpha)\right]\bigg|_{J=J[G]} \qquad (3.6.29)$$

$\Gamma[G]$ is called Baym-Kadanoff functional. The second term on the right side is usually abbreviated as tr(JG).

Now the Luttinger-Ward function is defined as the difference between interacting and non-interacting 2PI effective action:

$$\Phi[G] = \Gamma[G] - \Gamma_0[G] \qquad (3.6.30)$$

$$= \Gamma[G] - \text{tr}\log(-G) - \text{tr}\left((G_0^{-1} - G^{-1})G\right) \qquad (3.6.31)$$

Φ is the sum over all closed 2PI skeleton diagrams [106].

The usefulness stems from the relation to the grand canonical potential [14, 89] as well as the ability to generate irreducible functions from derivatives with respect to the full Green's function [81].

$$\Omega = \text{Tr}\log(-G) + \text{Tr}(\Sigma G) + \Phi[G] \qquad (3.6.32)$$

$$\Sigma_{\text{skeleton}}[G] = \frac{1}{T}\frac{\delta\Phi[G]}{\delta G} \qquad (3.6.33)$$

$$\Sigma_{ij} = \Sigma_{\text{skeleton}}[G] \qquad (3.6.34)$$

There are two important properties that are needed for the use of the Luttinger-Ward functional in DMFT [105]:

$$\Phi[G] = 0, \text{ if } U = 0 \qquad (3.6.35)$$

$$\Phi[G] \quad \text{universal} \qquad (3.6.36)$$

Universality means that Φ is the same for two Hubbard systems with identical U, regardless of the parameter t_{ij}. This will be central to the application in DMFT.

3.7 QUASI PARTICLES

With the introduction of the spectral function we have already seen that the pole structure of Green's functions can also be represented by the experimentally measurable spectral weight function. Its features give rise to the concept of quasi particles. These particles are a collection of many excitations that behave collectively as one particle would.

The Green's function for free fermions without spin has exactly two poles. This results in the corresponding spectral function having two delta peaks. The introduction of interactions will broaden the delta peak due to more excitation poles (see also discussion of the Green's function for the Hubbard model in the first chapter). However, the sum of them can still result in a peak of the spectral function and the overall excitation may retain some characteristics of a particle. This can be seen more formally by looking at the propagation of an excitation with energy k over some time t:

$$iG(k,t) = i\int_{-\infty}^{\infty}\frac{d\omega}{2\pi}e^{i\omega t}G(k,\omega)$$

$$= i \int_{-\infty}^{0} \frac{d\omega}{2\pi} e^{i\omega t} G^{A}(k,\omega) + i \int_{0}^{\infty} \frac{d\omega}{2\pi} e^{i\omega t} G^{R}(k,\omega) \tag{3.7.1}$$

One again has to carefully consider the integration path. Because the time ordered Green's function is not analytic everywhere one has to use the retarded and advanced propagator and choose the contour accordingly [90, 80].

Let's assume one pole at $\xi_k - i\gamma_k$ with residue Z_k. After applying the residue theorem we obtain:

$$= Z_k e^{-t(\xi_k + i\gamma_k)} + \int_{-i\infty}^{0} \frac{d\omega}{2\pi} e^{-i\omega t} \left[G^{A}(k,\omega) - G^{R}(k,\omega) \right] \tag{3.7.2}$$

The remaining integral can be approximated if the real part of the pole is much larger than the imaginary one. It measures the background noise of the quasi particle weight Z_k

$$\approx Z_k e^{-t(\xi_k + i\gamma_k)} \quad \text{if } \gamma_k \ll \xi_k \tag{3.7.3}$$

The corresponding spectral function will have a sharp peak at ξ_k with height proportional to Z_k/γ_k and width proportional to γ_k. Since the quasi particle lifetime is inversely proportional to the width of the collective excitation, it is useful to define the quasi particle lifetime as $\tau_k = \frac{1}{\gamma_k}$. Z_k can for example be measured by Compton
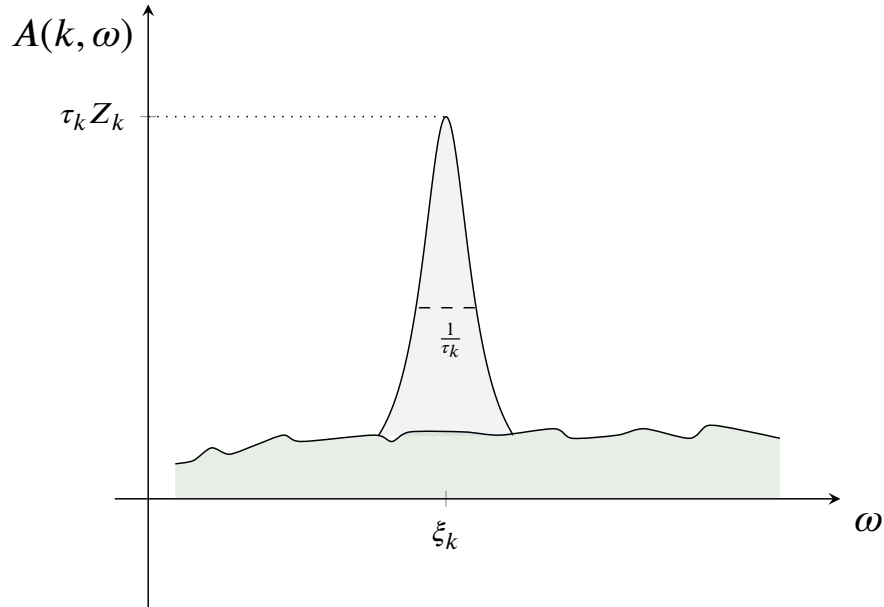

Figure 3.3: Spectral function example

scattering as it is proportional to the distribution function at the Fermi level [90].

In practice, the spectral weight will be expressed in terms of the self energy. One does however need to make certain approximations as the analytic continuation for arbitrary poles is not possible. Expansion around the Fermi energy (i.e. self energy around $\omega = 0$) gives a simplified formula for the retarded Green's function [24, 44, 100]:

$$G^{R}(k,\omega) = \frac{Z_k}{\omega - \xi_k + i\tau_k} \tag{3.7.4}$$

Using the Kramers-Kronig relations and Dyson equation, a useful representation of the spectral function in terms of the self energy can be found. It has the a Lorentzian shape.

$$A(k, \omega) = \frac{1}{\pi} \frac{-\Im\{\Sigma^R(k, \omega)\}}{\left(\omega - \epsilon_k + \mu - \Re\{\Sigma^R(k, \omega)\}\right)^2 + \left(\Im\{\Sigma^R(k, \omega)\}\right)^2} \tag{3.7.5}$$

This form is plotted in fig. 3.3. We can also see here that the imaginary part of the self energy needs to be negative, since the spectral function is always positive.
The quasi particle lifetime can be approximated in the vicinity of the Fermi surface:

$$\tau_k = -\frac{Z_k}{\gamma_k} \approx -[\Im\{\Sigma(k, \omega)\}]^{-1} \tag{3.7.6}$$

$$Z_k = \left[1 - \frac{\partial}{\partial \omega}\Re\{\Sigma(k, \omega)\}\bigg|_{\omega=0}\right]^{-1} \tag{3.7.7}$$

In some cases it is possible to neglect the finite life time of quasi particles. This approximation is known as Fermi liquid theory, a sufficient condition for its validity is [70, 97, 24]:

$$\lim_{k \to k_f} \lim_{\omega \to 0} -2\Im\{\Sigma(k, \omega)\} = 0 \tag{3.7.8}$$

Dynamic mean field theory is known to predict Fermi liquid behavior at low temperatures except for half filling in the Mott insulating region [9]. Our calculations will not be in real frequencies which means that the above formula for the quasi particle weight can only be applied to the analytic continuation of the results. There is however a numerically more stable method (see section III.A [9])[17].

$$\frac{\partial}{\partial \omega}\Re\{\Sigma(\omega)\}\bigg|_{\omega=0} = \int \frac{d\omega}{\pi} \frac{\Sigma(\omega)}{\omega^2} \approx \frac{\Im\{\Sigma(\omega_n)\}}{\omega_n}\bigg|_{\omega_n=\omega_0} \tag{3.7.9}$$

We can therefore deduce the broadening of the quasi particle peak from the imaginary part of the self energy. In practice, the value at $T = 0$ is extrapolated by computing eq. 3.7.9 from a few samples at low temperatures. Because the self energy is an even function the expansion around $\omega = 0$ is best fitted with an according polynomial

$$\Im\Sigma(\omega) \approx \omega^2 + \omega^4 + \cdots$$

For the estimation in this thesis I obtained reasonable results for a fourth order polynomial, fitted to the lowest six samples of the self energy.
The most important observation of this section is that HF approximations are frequency independent. Therefore $Z_k \equiv 1$ and according to the sum rule no peaks can appear, which means no quasi particles can be defined. This gives a hint, why standard HF fails to predict the Mott insulating phase. Standard DFT with LDA or GGA approximations for the exchange correlation term fail as well, due to the band gap problem [28, 118]. It stems from the fact that there is no discontinuity in the potential for both approximations:

$$\lim_{\delta \to 0} \Delta_{xc} = \lim_{\delta \to 0} \left[\frac{\delta E_{xc}}{\delta n}\bigg|_{N+\delta} - \frac{\delta E_{xc}}{\delta n}\bigg|_{N-\delta}\right]$$

---

17 The k dependence is omitted, since we will be using the DMFT approximation

$$\overset{\text{LDA,GGA}}{=} 0$$

The dynamical mean field approximation does introduce a frequency dependence, at the cost of the k dependence and being a first principle method.

DYNAMIC MEAN FIELD THEORY

In this chapter we will introduce the dynamical mean field theory (DMFT) as an approximative solution method for the Hubbard model. DMFT becomes exact in infinite spacial dimensions. This means the coordination number can be used as a control parameter for the quality of the approximation. Even though the number of spacial dimensions is fixed at three, the coordination number can become quite large especially when next nearest neighbor interactions are introduced.

We will later find, that the central approximation can be reformulated as k independence of the self energy.

$$\Sigma(k, \omega) \to \Sigma(\omega) \tag{4.0.1}$$

4.1 DERIVATION

The central realization that led to the development of DMFT came from Metzner and Vollhardt in 1989 [95]:

In the noninteracting limit of the single band Hubbard model on the hypercubic lattice with lattice constant a and dimension D, the energy reduces to the pure kinetic energy term (see discussion following eq. 1.2.21):

$$\epsilon_k = 2t \sum_{d=1}^{D} \cos(k_d a)$$

One can define the contribution of the kinetic energy for one dimension as a random variable. Thus the total energy is given as a sum over D i.i.d. random variables X_d with mean 0 and variance $2t^2$, because X_d can take values in the interval $[-2t, 2t]$ and is symmetric.

$$X_d = 2t \cos(k_d a)$$

Since we assume $U \to 0$ for now, the density of states is that of free electrons on a lattice with N sites:

$$\rho(\omega) = A_0(\omega) = \frac{1}{N} \sum_k \delta(\omega - \epsilon_k) \tag{4.1.1}$$

Following the argument from [95] we assume k to be randomly distributed and transform it using the cosine function. Now ϵ_k is the sum over i.i.d. random variables with finite expected value and variance, so that we can use the CLT to obtain a Gaussian density of states[1].

$$\rho(\omega) \xrightarrow{D \ll 1} \frac{1}{2t\sqrt{\pi D}} \cdot e^{-\left(\frac{\omega}{2t\sqrt{D}}\right)^2} \tag{4.1.2}$$

In order for the DOS to be finite in this limit, the hopping strength obviously needs to be rescaled. A more intuitive reason for this rescaling is, that the kinetic energy

---

1 The CLT is applicable for finite D as shown in appendix sec. A.

has to be of the same order of magnitude as the interaction strength U in order to allow for meaningful results away from the atomic limit.

$$t \to \frac{t^\star}{\sqrt{z}} = \frac{t^\star}{\sqrt{2D}} = \text{const} \tag{4.1.3}$$

The resulting approximate DOS for large dimension is a normal distribution.

$$\rho(\omega) \xrightarrow{D \ll 1} \frac{1}{t^\star \sqrt{2\pi}} e^{-\frac{1}{2}\left(\frac{\omega}{t^\star}\right)^2} \tag{4.1.4}$$

One can see this convergence quite easily by comparison of the plots for the tight binding DOS with increasing dimensions (see also fig. 1.8). Notice that we scaled
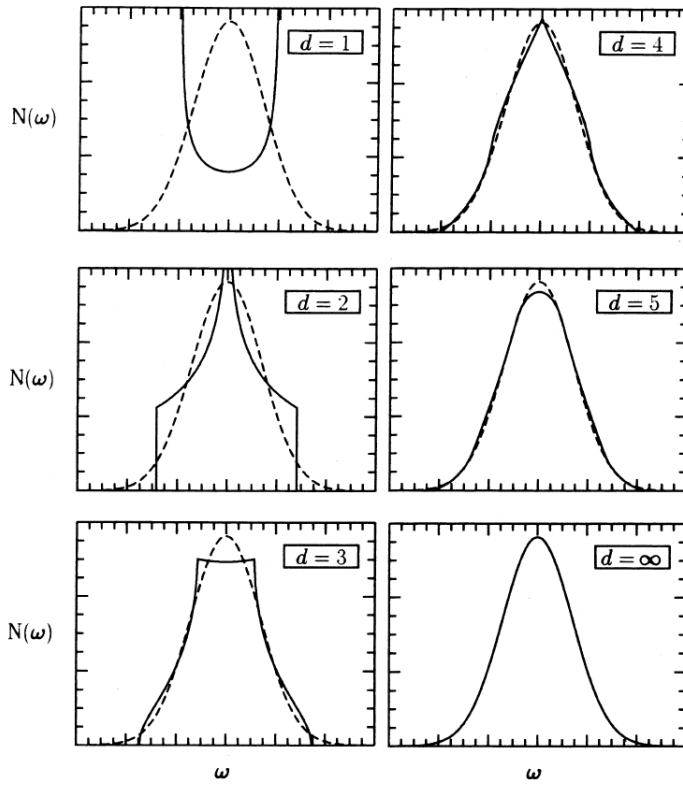
Figure 4.1: Tight binding DOS for increasing dimensions. Taken from [125], here $N(\omega)$ instead of $\rho(\omega)$

with $1/\sqrt{z}$ instead of $1/z$ for the Weiss mean field theory (see eq. 1.4.11). While the "classical" renormalization is not unphysical, it does results in $E_{\text{kin}} = 0$ and is therefore an unusable approximation [126], as can be seen directly from the Hubbard Hamiltonian (eq. 1.2.21).

$$H = -\frac{t^\star}{\sqrt{z}} \sum_{\langle ij \rangle \sigma} c^\dagger_{i\sigma} c_{j\sigma} + \epsilon_0 \sum_{i\sigma} n_{i\sigma} + U \sum_i n_{i\uparrow} n_{i\downarrow} \tag{4.1.5}$$

This "non-classical" scaling allows for competition between kinetic and on-site terms. We will now discuss the implications of infinite dimensions in terms of the diagrammatic expansion. After that we will use the cavity construction to obtain the self

consistency equations for the dynamical mean field theory. Lastly, the Anderson impurity model (AIM) is introduced and by comparison of the effective action in infinite dimensions, we obtain a much simpler picture of the dynamical mean field approach for the Hubbard model.

4.2 PERTURBATION THEORY IN INFINITE DIMENSIONS

As discussed in the previous chapter, we can represent the kinetic energy at $T = 0$ by the free Green's function:

$$\langle \hat{T} \rangle_0 = - \left\langle t \sum_{\langle ij \rangle \sigma} c_{i\sigma}^\dagger c_{j\sigma} \right\rangle_0 \tag{4.2.1}$$

$$= -t \sum_{\langle ij \rangle \sigma} \left\langle c_{i\sigma}^\dagger c_{j\sigma} \right\rangle_0 \tag{4.2.2}$$

$$= -t \sum_{\langle ij \rangle \sigma} G_{0,ij}(-\eta) \tag{4.2.3}$$

Because $|G_{0,ij}(-\eta)|^2$ is the transition amplitude to a nearest neighbor, the non-interacting Green's function must scale proportional to $\frac{1}{\sqrt{z}}$

$$G_{0,ij}(-\eta) \overset{d \to \infty}{=} \mathcal{O}\left(\frac{1}{\sqrt{z}}\right) \tag{4.2.4}$$
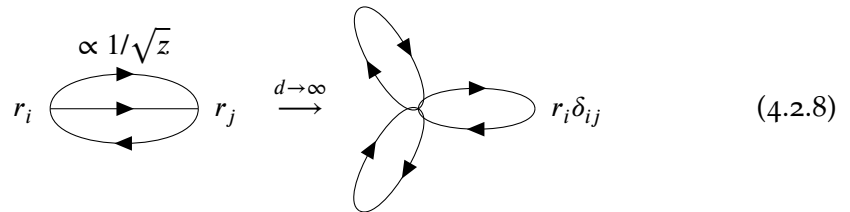
This property does not depend on the imaginary time of the system and must therefore also hold for other representations of the free propagator (the transformation to Matsubara frequencies is a linear operation). More specifically, it has been shown that the scaling of the Green's function[2] is [124, 94]:

$$G_{0,ij}(\tau) \overset{d \to \infty}{\propto} \mathcal{O}\left(t^{|i-j|}\right) = \mathcal{O}\left(d^{\frac{|i-j|}{2}}\right) \tag{4.2.5}$$

$$\propto \mathcal{O}\left(\frac{1}{\sqrt{z}}\right) \tag{4.2.6}$$

$$G_{0,ij}(i\omega_n) \overset{d \to \infty}{\propto} \mathcal{O}\left(\frac{1}{\sqrt{z}}\right) \tag{4.2.7}$$

Where we used the rescaled hopping from eq. 4.1.3. This scaling also leads to a collapse of diagrams for infinite dimensions. Tables for the collapse of the first three orders in the self energy are computed here [94]. For example the only proper second order self energy diagram collapses in the following way:

$$\tag{4.2.8}$$

---

[2] i, j are the lattice points, local $i = j$ and non local $i \neq j$, $| \cdot |$ is the Manhattan distance

This collapse of the propagators does result in a purely local self energy:

$$\lim_{d\to\infty} \Sigma(r_i, r_j, i\omega_n) = \delta_{ij}\Sigma(r_i, r_i, i\omega_n) \tag{4.2.9}$$

From this follows by Fourier transformation a momentum independent self energy

$$\lim_{d\to\infty} \Sigma(k, i\omega_n) = \Sigma(i\omega_n) \tag{4.2.10}$$

It is important to note, that the particles are not localized but only the transition between fixed lattice points i and j becomes negligible (since there are now infinitely many neighbors). This results in DMFT retaining the dynamics of non local electrons while providing mathematical simplifications.

Using the Dyson equation and assuming no symmetry breaking, the interaction Green's function without k-dependence now reads:

$$G(i\omega_n) = \frac{1}{N_k} \sum_k \left[i\omega_n + \mu - \epsilon_k - \Sigma(i\omega_n)\right]^{-1}$$

$$= \int \frac{\rho(\epsilon)}{i\omega_n + \mu - \epsilon - \Sigma(i\omega_n)} \, d\epsilon \tag{4.2.11}$$

The DOS $\rho(\epsilon)$ introduces the effects of the lattice.

Note that eq. 4.2.11 is a Hilbert transform:

$$H(f)(s) = \frac{1}{\pi} p.v. \int \frac{f(\tau)}{s - \tau} \, d\tau \tag{4.2.12}$$

It is also useful to define a reciprocal function [51]:

$$R[H(f)] = f^{-1}(H^{-1}(f)(s)) = s \tag{4.2.13}$$

This is important due to its well understood properties, many of which are useful in chemistry and physics [92, 87, 75, 134].

4.3 CAVITY CONSTRUCTION AND ANDERSON IMPURITY MODEL

The central idea for the so called cavity construction is the same that we already used for the simple Weiss mean field derivation (see eq. 1.4.8): We imagine one lattice point as separated from the rest and calculate the sum of interactions to and from it. This site is called impurity.

The impurity Hamiltonian is a single particle problem and can be solved exactly (at least numerically) with an internal interaction term U and one that stems from the exchange of particles with the bath V. This means one can obtain the full interacting Green's function and the corresponding self energy. For now we will assume an interacting bath, however we will map the effective action of the Hubbard model onto the Anderson impurity model in infinite dimensions with the following steps. For the derivation we will follow the steps of Ohkawa [69] and A. Georges et al. [51]. We will find that the self energy of the bath and the impurity must be equal thus making the bath interactions also implicitly dependent on U and V. Since the hybridization then changes the impurity Hamiltonian, the impurity problem has to be solved again, generating an updated self energy, thereby closing the mean field

self consistency loop.

Let $i = 0$ be the removed lattice point. We also use $\partial_\tau = \frac{\partial}{\partial \tau}$

$$A = A_{\text{lattice}} + A_{\text{cavity}} + A_{\text{hyb}} \tag{4.3.1}$$

$$A_{\text{lattice}} = \sum_{i \neq 0, \sigma} \int_0^\beta \left(c_{i\sigma}^\dagger(\tau) \left[\partial_\tau - \mu \right] c_{i\sigma}(\tau) - \sum_{\substack{i \neq 0, j \neq 0 \\ \sigma}} t_{ij} c_{i\sigma}^\dagger(\tau) c_{j\sigma}(\tau) + U \sum_{i \neq 0} n_{i,\uparrow}(\tau) n_{i,\downarrow}(\tau) \right) d\tau$$

$$A_{\text{cavity}} = \sum_{\sigma} \int_0^\beta \left(c_{0\sigma}^\dagger(\tau) \left[\partial_\tau - \mu \right] c_{0\sigma}(\tau) + U n_{0,\uparrow}(\tau) n_{0,\downarrow}(\tau) \right) d\tau$$

$$A_{\text{hyb}} = -\sum_{i,\sigma} \int_0^\beta \left(t_{i0} c_{i\sigma}^\dagger(\tau) c_{0\sigma}(\tau) + t_{0i} c_{0\sigma}^\dagger(\tau) c_{i\sigma}(\tau) \right) d\tau$$

We will now consider an effective action instead of the full one and argue that both resulting thermodynamic averages are equivalent under the DMFT approximation.

$$\langle O \rangle_{\text{full}} = \frac{1}{Z} \int \prod_i \mathcal{D}\left[c_{i\sigma}^\dagger \right] \mathcal{D}[c_{i\sigma}] \, O e^{-A}$$

Now the integration over the bath can be carried out. The remaining action of lattice site 0 is then called effective action.

$$\frac{1}{Z_{\text{eff}}} e^{-A_{\text{eff}}} = \frac{1}{Z_{\text{full}}} \int \prod_{i \neq 0, \sigma} \mathcal{D}\left[c_{i\sigma}^\dagger \right] \mathcal{D}[c_{i\sigma}] \, e^{-A}$$

$$\approx \frac{1}{Z_{\text{full}}} \int \prod_{i \neq 0, \sigma} \mathcal{D}\left[c_{i\sigma}^\dagger \right] \mathcal{D}[c_{i\sigma}] \, e^{-A_{\text{lattice}}[c_{i\neq 0\sigma}^\dagger, c_{i\neq 0\sigma}]} e^{-A_{\text{hyb}}[c_{i\sigma}^\dagger, c_{i\sigma}]} e^{-A_{\text{cavity}}[c_{0\sigma}^\dagger, c_{0\sigma}]}$$

$$= \frac{1}{Z_{\text{full}}} e^{-A_{\text{cavity}}} \int \prod_{i \neq 0, \sigma} \mathcal{D}\left[c_{i\sigma}^\dagger \right] \mathcal{D}[c_{i\sigma}] \, e^{-A_{\text{hyb}}} e^{-A_{\text{lattice}}} \tag{4.3.2}$$

$$= \frac{Z_{\text{lattice}}}{Z_{\text{full}}} e^{-A_{\text{cavity}}} \left\langle e^{-A_{\text{hyb}}} \right\rangle_{\text{lattice}} \tag{4.3.3}$$

$$\Rightarrow Z_{\text{eff}} = \frac{Z_{\text{full}}}{Z_{\text{lattice}}} \tag{4.3.4}$$

$$A_{\text{eff}} = A_{\text{cavity}} - \log \left[\left\langle e^{-A_{\text{hyb}}} \right\rangle_{\text{lattice}} \right] \tag{4.3.5}$$

We can pull the hybridization inside the expected value of the cavity action using this effective action. In order to apply the DMFT approximation we expand the hybridization action (eq. 4.3.2) and find the leading order of $\frac{1}{\sqrt{D}}$.

$$Z_{\text{eff}} = \int \mathcal{D}\left[c_{0\sigma}^\dagger \right] \mathcal{D}[c_{0\sigma}]$$

$$\times e^{-A_{\text{cavity}}} \left\langle \sum_{n=0}^\infty \frac{1}{n!} \prod_{m=1}^n \left[\int_0^\beta \sum_{i,\sigma} \left(t_{i0} c_{i\sigma}^\dagger(\tau_m) c_{0\sigma}(\tau_m) + t_{0i} c_{0\sigma}^\dagger(\tau_m) c_{i\sigma}(\tau_m) \right) d\tau_m \right] \right\rangle_{\text{lattice}}$$

$$= \int \mathcal{D}\left[c_{0\sigma}^\dagger \right] \mathcal{D}[c_{0\sigma}] \, e^{-A_{\text{cavity}}}$$

$$\times \left[1 - \int d\tau_1 \sum_{\sigma, i \neq 0} \left\langle t_{i0} c_{i\sigma}^\dagger(\tau_1) c_{0\sigma}(\tau_1) + t_{0i} c_{0\sigma}^\dagger(\tau_2) c_{i\sigma}(\tau_2) \right\rangle_{\text{lattice}} \right.$$

$$+ \frac{1}{2!} \int d\tau_1 \int d\tau_2 \sum_{\sigma, i, j \neq 0} \left\langle t_{i0} t_{j0} c_{i\sigma}^\dagger(\tau_1) c_{0\sigma}(\tau_1) c_{j\sigma}^\dagger(\tau_2) c_{0\sigma}(\tau_2) \right\rangle_{\text{lattice}}$$

$$+ \frac{1}{2!} \int d\tau_1 \int d\tau_2 \sum_{\sigma, i, j \neq 0} \left\langle t_{0i} t_{j0} c_{0\sigma}^\dagger(\tau_1) c_{i\sigma}(\tau_1) c_{j\sigma}^\dagger(\tau_2) c_{0\sigma}(\tau_2) \right\rangle_{\text{lattice}}$$

$$+ \frac{1}{2!} \int d\tau_1 \int d\tau_2 \sum_{\sigma, i, j \neq 0} \left\langle t_{i0} c_{i\sigma}^\dagger(\tau_1) c_{0\sigma}(\tau_1) t_{0j} c_{0\sigma}^\dagger(\tau_2) c_{j\sigma}(\tau_2) \right\rangle_{\text{lattice}}$$

$$+ \frac{1}{2!} \int d\tau_1 \int d\tau_2 \sum_{\sigma, i, j \neq 0} \left\langle t_{0i} c_{0\sigma}^\dagger(\tau_1) c_{i\sigma}(\tau_1) t_{0j} c_{0\sigma}^\dagger(\tau_2) c_{j\sigma}(\tau_2) \right\rangle_{\text{lattice}}$$

$$\left. + \mathcal{O}(t^3) \right] \tag{4.3.6}$$

$$= \int \mathcal{D}\left[c_{0\sigma}^\dagger \right] \mathcal{D}\left[c_{0\sigma} \right] e^{-A_{\text{cavity}}}$$

$$\times \left[1 + \int d\tau_1 \int d\tau_2 \sum_{\sigma} \left\langle c_{0\sigma}^\dagger(\tau_1) \sum_{i, j \neq 0} \left(t_{i0} t_{0j} c_{i\sigma}^\dagger(\tau_1) c_{j\sigma}(\tau_2) \right) c_{0\sigma}(\tau_2) \right\rangle_{\text{lattice}} \right] \tag{4.3.7}$$

The first order, as well as the first and fourth term of second order are equal to 0, because we do not consider symmetry breaking. The other two terms are the same as the number of creator annihilator permutations must be even. This also leads to all other odd terms of the perturbative expansion disappearing and only connected n-point Green's functions (see linked cluster theorem eq. 3.5.19) G^{cavity} contributing.

$$G_{\cdots}^{C,\text{lattice}}(\cdots) = \langle T[\cdots] \rangle_{\text{lattice}} \tag{4.3.8}$$

$$A_{\text{eff}} = A_{\text{cavity}} + \sum_{n=1}^{\infty} \sum_{i_1 \cdots i_n i_n' i_1'} \int_0^\beta d\tau_1 \cdots d\tau_n \, d\tau_n' \cdots d\tau_1'$$

$$\times J_{i_1}^\dagger(\tau_1) \cdots J_{i_n}^\dagger(\tau_n) J_{i_n'}(\tau_n') \cdots J_{i_1}(\tau_1') G_{i_1 \cdots i_1'}^{C,\text{lattice}}(\tau_1 \cdots \tau_1') \tag{4.3.9}$$

With the source term $J_{i_1}(\tau_1) = t_{i_1 0} c_{0\sigma}$ coupling to $c_{i\sigma}^\dagger$, this provides a generating functional for the connected Green's functions of the cavity Hamiltonian [51].
We can now use eq. 4.2.5 to find the contributing terms of $d \to \infty$. By considering all scaling contributions (the sums contribute a factor of d each, n point functions d^n) one can see that the nth term in the expansion scales as [51]:

$$A_{\text{eff}}^{(n)} = \mathcal{O}(d^{2-n}), \text{ for } n > 1 \tag{4.3.10}$$

This means only the $n = 2$ term contributes in the DMFT limit.

$$A_{\text{eff}} = A_{\text{cavity}} + \int_0^\beta d\tau_1 \int_0^\beta d\tau_2 \sum_{\sigma i j} c_{0\sigma}^\dagger t_{i0} t_{0j} G_{ij}^{C,\text{lattice}}(\tau_1 - \tau_2) \tag{4.3.11}$$

$$\Rightarrow \quad \mathcal{G}_{0\sigma}^{-1}(\tau_1 - \tau_2) = -\delta_{ij} \left(\partial_{\tau_1} - \mu \right) - \sum_{ij} t_{i0} t_{0j} G_{ij}^{C,\text{lattice}}(\tau_1 - \tau_2) \tag{4.3.12}$$

Here we defined the Weiss function $\mathcal{G}_{0\sigma}(\tau_1 - \tau_2)$, where the name was chosen in reference to the original mean field approach.
The self consistency equations relating the Weiss function to the lattice Green's func-

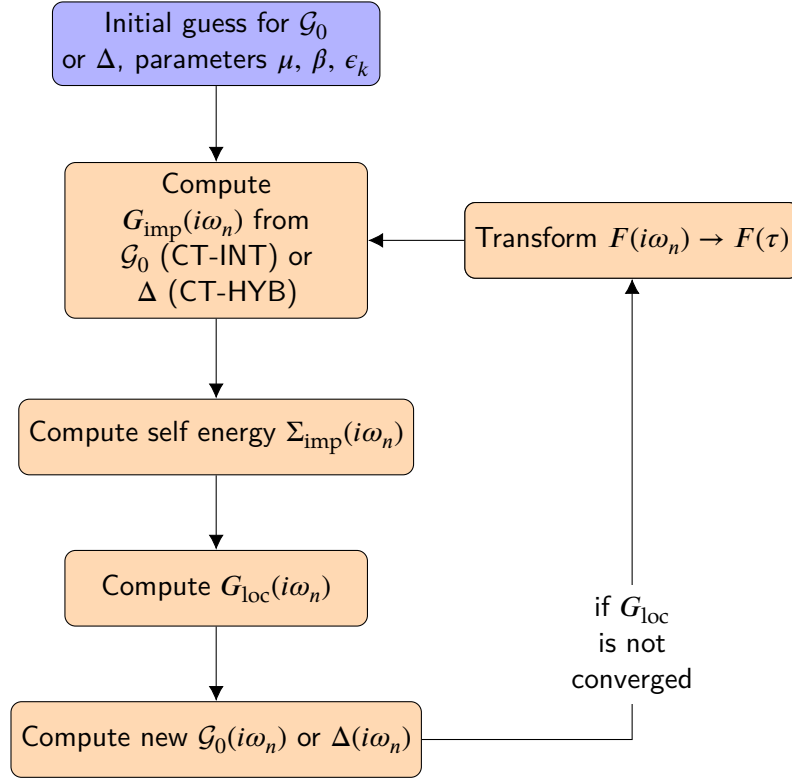tion are the DMFT equations that will be used later. Even though there is a relation

Figure 4.2: Program flow of the DMFT loop. The initial guess can be obtained from the non interacting DOS of the lattice.

between cavity and full Green's function known (see [51]), we will not make use of it. The mapping to the Anderson impurity model (derived in the rest of this section) will provide a more convenient formulation.

$$G_{ij}^{C,\text{lattice}} = G_{ij} - \frac{G_{i0}G_{0j}}{G_{00}} \tag{4.3.13}$$

Inserting eq. 4.3.13 into eq. 4.3.12 and using the Matsubara representation as well as Hilbert transform properties, one can show that:

$$\mathscr{G}_{0\sigma}^{-1}(i\omega_n) = \Sigma(i\omega_n) + \frac{1}{H(D(\epsilon))(i\omega_n + \mu - \Sigma(i\omega_n))} \tag{4.3.14}$$

While this is a feasible operation (see alg. 9), it does require additional effort and adds a layer of numerical evaluation which can otherwise be carried out analytically. In case of certain lattice types, such as the simple cubic one, it is possible to map the problem on a tree like lattice which allows the analytic evaluation of eq. 4.3.13 to an algebraic equation. We will derive this in sec. 4.4.

In any other case, as well as when using LDA+DMFT, one has to resort to the computationally more expensive k-space integration. However the general structure of the computation from fig. 4.2 does still hold.

The next steps now are to write down the Anderson impurity model. Let $\hat{d}_\alpha$ be the

annihilation operator of state α for the impurity and $\hat{c}_\alpha$ the annihilation operator for the bath.

$$
\begin{aligned}
H_{\text{AIM}} = \; & \underbrace{\oint_{\alpha\beta} \tilde{\epsilon}_{\alpha\beta} d_\alpha^\dagger d_\beta + \frac{1}{2} \oint_{\alpha\beta\gamma\delta} U_{\alpha\beta\gamma\delta} d_\alpha^\dagger d_\beta^\dagger d_\gamma d_\delta}_{H_{\text{loc}}} \\
& + \underbrace{\oint_{\alpha\mu\nu} \left(V_{\alpha\mu\nu}^\star c_{\mu\nu}^\dagger d_\alpha + h.c. \right)}_{H_{\text{hyb}}} + \underbrace{\oint_{\mu\nu} \epsilon_\mu c_{\mu\nu}^\dagger c_{\mu\nu}}_{H_{\text{bath}}}
\end{aligned}
\tag{4.3.15}
$$

We only consider a single impurity site and the same simplifications as during the derivation of the Hubbard model are applied. Also the quantum numbers are assumed to be discrete (we set $-\mu \equiv \tilde{\epsilon}_{\alpha\beta}$)

$$
\begin{aligned}
H_{\text{AIM}} = \; & \underbrace{-\mu(n_\uparrow + n_\downarrow) + U n_\uparrow n_\downarrow}_{H_{\text{loc}}} \\
& + \underbrace{\sum_{\alpha\sigma} \left(V_{\alpha\sigma} d_\sigma^\dagger c_{\alpha\sigma} + h.c. \right)}_{H_{\text{hyb}}} + \underbrace{\sum_{\alpha\sigma} \epsilon_\alpha c_{\alpha\sigma}^\dagger c_{\alpha\sigma}}_{H_{\text{bath}}}
\end{aligned}
\tag{4.3.16}
$$

Obviously the Hubbard model is a special case of the AIM. We can immediately recover it by fixing the impurity site at $i = 0$ and setting $\tilde{\epsilon}_{\alpha\beta} = t_{ij}$, $V_{\alpha\sigma} = t_{0j}$.

We can use the coherent state path integral formalism to find the action corresponding to this Hamiltonian (see eq. 3.1.15 to eq. 3.1.20). This will allow us to integrate out the bath and only work with the impurity effective action. The Grassmann fields for the impurity and bath action are denoted by a c and d subscript respectively (the following discussion has been adapted from [54]).

$$
Z = \int \prod_\alpha \mathcal{D}[\xi_{\alpha d}^\star] \, \mathcal{D}[\xi_{\alpha d}] \, \mathcal{D}[\xi_{\alpha c}^\star] \, \mathcal{D}[\xi_{\alpha c}] \, e^{-A[\xi_{\alpha d}^\star, \xi_{\alpha d}, \xi_{\alpha c}^\star, \xi_{\alpha c}]}
$$

$$
\begin{aligned}
A\left[\xi_{\alpha d}^\star, \xi_{\alpha d}, \xi_{\alpha c}^\star, \xi_{\alpha c}\right] = & \sum_\alpha \int d\tau \left[\xi_\alpha^\star \left(\partial_\tau - \mu \right) \xi_\alpha + H_{\text{AIM}}\left[\xi_{\alpha d}^\star(\tau), \xi_{\alpha d}(\tau), \xi_{\alpha c}^\star(\tau), \xi_{\alpha c}(\tau) \right] \right] \\
= & \sum_\alpha \int d\tau \Bigg[\xi_{id\sigma}^\star(\tau) \left(\partial_\tau - \mu \right) \xi_{id\sigma}(\tau) + H_{\text{loc}}\left[\xi_{id}^\star(\tau), \xi_{id}(\tau) \right] \\
& + \xi_{ic\sigma}^\star(\tau) \left(\partial_\tau - \mu + \epsilon_i \right) \xi_{ic\sigma}(\tau) \\
& + \xi_{ic\sigma}^\star(\tau) V_{i\sigma}^\star \xi_{id\sigma}(\tau) + \xi_{id\sigma}^\star(\tau) V_{i\sigma} \xi_{jc\sigma}(\tau) \Bigg]
\end{aligned}
$$

The first line of the equation above is the impurity action, the second line the bath action and the third line is the hybridization.

$$
\begin{aligned}
= & \sum_\alpha \int d\tau \Bigg[\xi_{id\sigma}^\star(\tau) \left(\partial_\tau - \mu \right) \xi_{id\sigma}(\tau) + H_{\text{loc}}\left[\xi_{id}^\star(\tau), \xi_{id}(\tau) \right] \\
& - \sum_j \xi_{ic\sigma}^\star(\tau) M_{ij} \xi_{jc\sigma}^\star(\tau) + \xi_{ic\sigma}^\star(\tau) J_{id\sigma}(\tau) + J_{id\sigma}^\star(\tau) \xi_{ic\sigma}(\tau) \Bigg]
\end{aligned}
$$

Here we introduced the following symbols:

$$J_{i\sigma}(\tau) = V_{i\sigma}\xi_{jc\sigma}(\tau)$$
$$M_{ij} = -\delta_{ij}\left(\partial_\tau + \mu - \epsilon_i\right)$$

This allows us to use eq. 3.1.16 in order to integrate out the bath into a constant factor. The constants and pre-factor of $\ln\left(\det(M)\right)$ can be computed exactly, but since they are absorbed into Z_{eff} later, they will be ignored here.

$$A_{\text{eff}} = A - \text{Tr}\left(\ln\left[\delta_{ij}\left(\partial_\tau - e_i + \mu\right)\right]\right)$$
$$= A - S_0 - \text{Tr}\left(\ln\left(G_{0,\sigma}^{-1}(i,j,\tau)\right)\right)$$

We denote the bath Green's function with $G_{0,\sigma}(\cdot)$

$$= \sum_{i\sigma}\int d\tau\left[\xi_{id\sigma}^\star(\tau)\left(\partial_\tau - \mu\right)\xi_{id\sigma}(\tau) + H_{\text{loc}}\left[\xi_{id}^\star(\tau),\xi_{id}(\tau)\right]\right]$$
$$+ \sum_{ij\sigma}\int d\tau\int d\tau' J_{id\sigma}^\star(\tau)\left[M^{-1}\right]_{ij}J_{jd\sigma}(\tau')$$
$$= \sum_{i\sigma}\int d\tau\left[\xi_{id\sigma}^\star(\tau)\left(\partial_\tau - \mu\right)\xi_{id\sigma}(\tau) + H_{\text{loc}}\left[\xi_{id}^\star(\tau),\xi_{id}(\tau)\right]\right]$$
$$+ \sum_{ij\sigma}\int d\tau\int d\tau' \xi_{id\sigma}^\star(\tau)\underbrace{\left[\Delta_\sigma(\tau - \tau')\right]_{ij}}_{=V_{i\sigma}^\star G_{0,\sigma}(i,j,\tau-\tau')V_{j\sigma}}\xi_{jd\sigma}(\tau')$$

We can now insert the simplified Hubbard model (eq. 1.2.21) as local Hamiltonian

$$A_{\text{eff}} = \sum_\sigma \int d\tau\int d\tau'\left[\xi_{d\sigma}^\star(\tau)\delta(\tau - \tau')\left(\partial_{\tau'} - \mu\right)\xi_{d\sigma}(\tau')\right.$$
$$+ \epsilon_0\xi_{d\sigma}^\star(\tau)\delta_\sigma(\tau - \tau')\xi_{d\sigma}(\tau') + \xi_{d\sigma}^\star(\tau)\Delta(\tau - \tau')\xi_{d\sigma}(\tau')$$
$$\left. + \delta(\tau - \tau')U n_\uparrow(\tau)n_\downarrow(\tau)\right]$$
$$= -\sum_\sigma \int_0^\beta d\tau\int_0^\beta d\tau' \xi_{d\sigma}^\star(\tau)\mathscr{G}_{0\sigma}^{-1}(\tau - \tau')\xi_{d\sigma}(\tau') + \int_0^\beta d\tau U n_\uparrow(\tau)n_\downarrow(\tau) \quad (4.3.17)$$

We identified the Weiss function by comparison with the cavity method as the Green's function generated by the effective action. An alternative representation in terms of the hybridization operator is later used for the hybridization expansion solver.

$$\widetilde{A}_{\text{eff}} = -\sum_\sigma \int_0^\beta\int_0^\beta d_\sigma^\dagger(\tau)\Delta_\sigma(\tau - \tau')d_\sigma(\tau')\,d\tau\,d\tau'$$
$$+ \int_0^\beta\left(U n_\uparrow(\tau)n_\downarrow(\tau) - \mu n_\uparrow(\tau) - \mu n_\downarrow(\tau)\right)d\tau \quad (4.3.18)$$

The hybridization operator Δ_σ can be written in terms of Matsubara frequencies:

$$\Delta_\sigma(\tau) = \sum_k |V_{k\sigma}|^2 G_{0,\sigma}(k,\tau - \tau') \quad (4.3.19)$$

$$\Delta_\sigma(i\omega_n) = \sum_k \frac{|V_{k\sigma}|^2}{i\omega_n - \epsilon_k + \mu} \tag{4.3.20}$$

$$\mathscr{G}_{0\,\sigma}(\tau - \tau') = \left[-\delta(\tau - \tau')\left(\partial_\tau - \mu\right) - \Delta_\sigma(\tau - \tau')\right]^{-1} \tag{4.3.21}$$

$$\mathscr{G}_{0\,\sigma}(i\omega_n) = \left[i\omega_n + \mu - \Delta_\sigma(i\omega_n)\right]^{-1} \tag{4.3.22}$$

$$= \left[i\omega_n + \mu - \sum_k \frac{|V_{k\sigma}|^2}{i\omega_n - \epsilon_k + \mu}\right]^{-1} \tag{4.3.23}$$

For the Hubbard model with impurity site $i = 0$ the hybridization reads:

$$\Delta_\sigma(i\omega_n) = \sum_{i,j \neq 0} t_{i0} t_{j0} G_0^{ij}(i\omega_n) \tag{4.3.24}$$

In order to obtain the relation between lattice and impurity Green's function one can
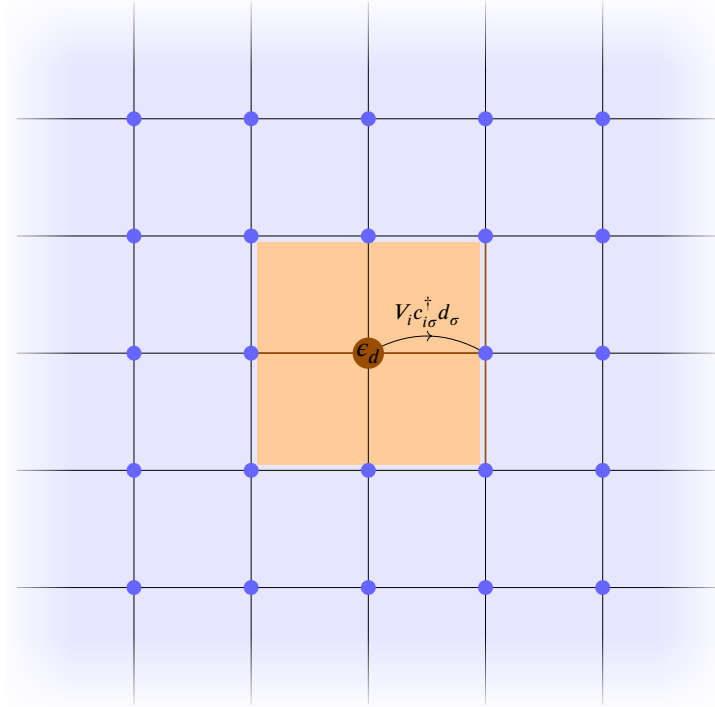
Figure 4.3: DMFT scheme on the AIM. The orange lattice point is solved exactly, the blue region is the bath with the impurity self energy, the orange region is the local problem connecting bath and impurity site.

also use the universality of the Luttinger-Ward functional [105]. The Hubbard model parameters are denoted as subscripts in the context of the functional construction.

$$\mathcal{G}_U[G_{t,0}^{-1}] = G_{t,U}$$

$$\hat{G}_U[\Sigma] = \mathcal{G}_U[\hat{G}_U^{-1}[\Sigma] + \Sigma]$$

Using the stationary point of the grand canonical potential in terms of the Luttinger-Ward functional, M. Potthoff derived the DMFT self consistency equations without the need for perturbative expansion [105]:

$$\hat{G}_U[\Sigma] = \frac{1}{G_{t,0}^{-1} - \Sigma}$$

$$\Rightarrow \quad G_{t',U}\Big|_{\text{local}} = \frac{1}{G_{t,0}^{-1} - \Sigma_{t',U}}\Big|_{\text{local}}$$

Because of $\Sigma_{ij} = \frac{\delta\Phi}{\delta G_{ij}}$ this can also be understood as the first order of an expansion for $\Phi = \sum_i \Phi_1[G_{ii}] + \sum_{\langle ij \rangle} \Phi_2[G_{ii}, G_{jj}, G_{ij}]$, where only Φ_1 is taken into account [81]. While the non-perturbative approach can be useful for related methods such as the self consistent cluster method, for the present case of single site DMFT, the perturbative derivation will be sufficient.

4.4 BETHE LATTICE

Since the hypercubic lattice does not retain the physical property of a finite bandwidth in infinite dimensions (see also fig. 4.1), it is useful to map the DOS onto a simpler lattice with similar properties and finite bandwidth. In practice one often chooses the Bethe lattice [18] which is a tree with degree z for every vertex. Even though this introduces very strong surface effects due to exponential increase in nodes per generation (see fig. 4.4), one gains the ability to do analytical calculations on such a graph which greatly reduce the computational cost of the DMFT loop [34]. In order to use the Bethe lattice, a relation between the original and the Bethe lattice needs to be established. In our case this will be done for the hopping parameter t_d, also the number of neighbors on the hypercubic lattice is set to be equal to the degree of the Bethe lattice. We restrict ourselves to nearest neighbor hopping here, even though there is a hierarchy for higher order hopping known[3]. In fact the DOS in the limit of $\lim_{K \to \infty}$ and next nearest neighbor hopping $t_{ij} = t$ can be computed exactly [35, 34, 51].

Figure 4.4: Bethe lattice up to fifth and third generation with $z = 3$ and $z = 5$. The branching ratio is $K = z - 1$

$$\lim_{K \to \infty} \rho_{NN}(\omega) = \lim_{K \to \infty} \frac{\sqrt{\omega^2 - 4t^2(K-1)/K}}{2\pi(t^2 - \omega^2/K)}$$

$$= \frac{\sqrt{4t^2 - \omega^2}}{2\pi t^2} \qquad (4.4.1)$$

In the following we will write U, β and the DOS in terms of the half-bandwidth D.

$$= \frac{2\sqrt{1 - \frac{\omega^2}{D^2}}}{\pi D}, \qquad |\omega| < D \qquad (4.4.2)$$

As mentioned before, in addition to the finite bandwidth DOS, the Hilbert transform and its reciprocal on the Bethe lattice (eq. 4.2.12 and eq. 4.2.13) also have a closed form solution.

$$H(\rho)(s) = \frac{s - \mathrm{sign}(\Im\{s\})\sqrt{s^2 - 4t^2}}{2t^2} \qquad (4.4.3)$$

$$R[H(\rho)(s)] = t^2 H(\rho)(s) + H^{-1}(\rho)$$

---

3 For example the next nearest neighbor tight binding hopping Hamiltonian for coordination number z : $\hat{H}_2 = \left(\hat{H}_1\right)^2 - z\mathbb{1}$ [34]
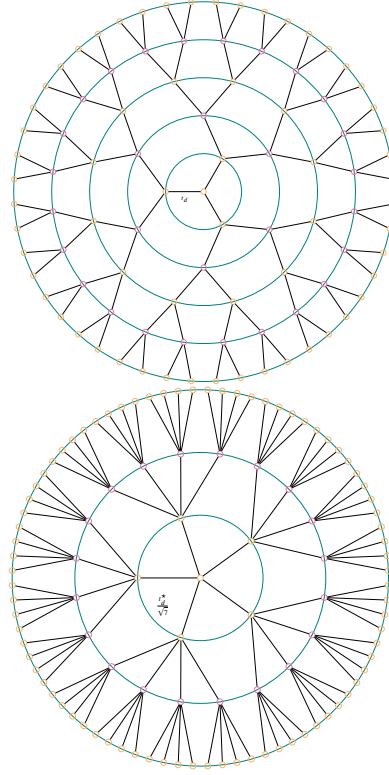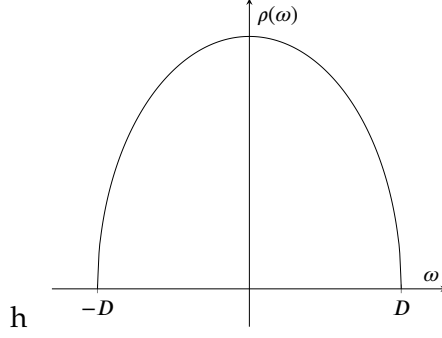
h

Figure 4.5: DOS for the Bethe lattice with bandwidth $2D$

Comparison with the original motivation for the introduction of the Hilbert transform yield a very useful relationship between the interacting and non interacting Green's function:

$$G(i\omega_n) = \frac{i\omega_n + \mu - \mathscr{G}_{0\sigma}^{-1}(i\omega_n)}{t^2} \tag{4.4.4}$$

$$= \frac{\Delta(i\omega_n)}{t^2} \tag{4.4.5}$$

This greatly reduces computational performance and numerical stability while retaining properties of some other lattice types.

The Hilbert transform of the Gaussian DOS (eq. 4.1.4) can also be obtained in closed form with $t = 1/\sqrt{2}$ as:

$$H(\rho_g)(s) = -i\,\text{sign}(\Im\{s\})\sqrt{\pi}e^{-s^2}\,\text{erfc}(-\,\text{sign}(\Im\{s\})is) \tag{4.4.6}$$

$\text{erfc}(x) = 1 - \text{erf}(x) = \frac{2}{\sqrt{\pi}}\int_x^\infty e^{-s^2}\,\mathrm{d}s$ is the complementary error function [4]. Bethe and hypercubic lattice at $T = 0$ have been shown to yield very similar results in the context of DMFT by R. Bulla [25]. Therefore all following calculations will be done using the Bethe lattice if not stated otherwise.

4.5 IMPURITY SOLVERS

We have now reduced the full lattice problem to an effective single site computation, in which the full lattice only enters through the bath interactions. There are several ways to obtain a solution for the impurity problem (i.e. obtain the impurity Green's function).

One possibility is exact diagonalization, that is finding a basis and solving the eigenvalue problem directly (at least for the lower energy states). For most problems in solid state physics this is unfeasible, since neither many body Hamiltonians nor systems approaching the thermodynamic limit are within the reach of computational possibility. The renormalization group method allows for very close inspection of phase transition but is only exact in this region of the phase diagram. Monte Carlo methods are computationally expensive in comparison to the above, especially when the sign problem is present, but offer an unbiased approach with few parameters that control convergence and precision. In this work I will focus on con-

---

4 In numerical calculations the (complementary) error function turned out to be unstable due to underflow errors. One can resort to the use of the Dawson or Faddeeva function instead. See also sec. 5

tinuous time quantum Monte Carlo. The name distinguishes these methods from the Hirsch-Fye algorithm, because instead of expansion of the action using Trotter approximation (eq. 3.1.3), one expands in terms of interaction vertices. Since we want to employ the Metropolis algorithm, we will have to identify appropriate weights and transition probabilities.

$$H = H_0 + H_1 \tag{4.5.1}$$

Let's introduce an auxiliary operator $A(\tau)$ which we use to rewrite the partition function.

$$A(\tau) = e^{\tau H} A e^{-\tau H} \tag{4.5.2}$$

$$Z = \text{Tr}\left(e^{-\beta H_0} A(\beta)\right) \tag{4.5.3}$$

$$e^{-\beta H_0} A(\tau) = e^{-\beta H_0}\left[e^{\tau H_0} e^{-\tau H}\right] = e^{-\beta H} \tag{4.5.4}$$

$$\partial_\tau A(\tau) = e^{\tau H_0}\left(H_0 - H\right) e^{-\beta H} = -e^{\tau H_0} H_1 e^{-\tau H_0} A(\tau)$$

$$= -H_1(\tau) A(\tau) \tag{4.5.5}$$

The boundary is $A(0) = \mathbb{1}$.

$$\Rightarrow \quad A(\beta) = T e^{-\int_0^\beta H_1(\tau) d\tau} \tag{4.5.6}$$

$$Z = \text{Tr}\left[e^{-\beta H_0} T\left[e^{-\int_0^\beta H_1(\tau) d\tau}\right]\right] \tag{4.5.7}$$

The exponential is then expanded to find the weight of a configuration:

$$Z = \sum_{n=0}^\infty \int_0^\beta \int_{\tau_1}^\beta \cdots \int_{\tau_{n-1}}^\beta \underbrace{\text{Tr}\left[e^{-(\beta-\tau_n)H_0}\left(-H_1\right)\cdots e^{-(\tau_2-\tau_1)H_0}\left(-H_1\right) e^{-\tau_1 H_0}\right] d\tau_n \cdots d\tau_1}_{w_C\, dC}$$

$$\tag{4.5.8}$$

$$C = \{\tau_1, \cdots \tau_n\}, \quad \tau_i < \tau_{i+1}, \quad \tau_i \in [0, \beta) \tag{4.5.9}$$

The three continuous time quantum Monte Carlo methods are obtained by choosing different decompositions of H_{AIM} for the single site impurity model.

$$H_{\text{AIM}} = H_{\text{loc}} + H_{\text{hyb}} + H_{\text{bath}} \tag{4.5.10}$$

$$H_{\text{loc}} = \underbrace{-\mu(n_\uparrow + n_\downarrow)}_{H_\mu} + \underbrace{U n_\uparrow n_\downarrow}_{H_U} \tag{4.5.11}$$

In order to employ Monte Carlo sampling, we recall that the expectation value needs to be in the form of eq. 2.5.9. Lets start with the usual grand canonical expectation value:

$$\langle O \rangle = \frac{\left\langle e^{-\beta(H-\mu N)} O\right\rangle}{Z}$$

$$= \frac{\text{Tr}\left[e^{-\beta(H-\mu N)} O\right]}{\text{Tr}\left[e^{-\beta(H-\mu N)}\right]}$$

This allows expansion of the exponentials perturbatively as a sum over weights. Theses are then identified as density matrices.

$$e^{-\beta(H-\mu N)} \sim \sum_C \rho_C$$

$$\Rightarrow \langle O \rangle \sim \frac{\sum_C \mathrm{Tr}\left[\rho_C O\right]}{\sum_C \mathrm{Tr}\left[\rho_C\right]}$$

$$= \sum_C \underbrace{\frac{\mathrm{Tr}\left[\rho_C\right]}{\sum_{C'} \mathrm{Tr}\left[\rho_{C'}\right]}}_{p_C} \underbrace{\frac{\mathrm{Tr}\left[\rho_C O\right]}{\mathrm{Tr}\left[\rho_C\right]}}_{w_C}$$

$$\Rightarrow \langle O \rangle_p = \sum_C p_C w_C$$

As proven in sec. 2.1, sampling with these probabilities provides an unbiased estimator for the expected value of the operator O. We will now look at algorithms which allow us to sample these weights within a Monte Carlo simulation, which in turn provides the estimated probabilities. The general strategy will be to transition between different perturbation orders k and calculate the sum over all diagrams Z_k contributing to this order.

$$Z = Z_0 + \cdots + Z_{k-1} + Z_k + Z_{k+1} + \cdots \tag{4.5.12}$$

This is made possible by a matrix identity that allows the computation of determinant ratios $\frac{Z_k}{Z_{k+1}}$, as well as the value of the new determinant, in $\mathcal{O}(k^2)$ operations. After every move, the measurement for the impurity Green's function as well as other observables can be computed from the stored matrix.

4.5.1 *Interaction Expansion — CT-INT*

We first discuss the continuous time interaction expansion method (CT-INT). This method is also called Weak Coupling approach [115]. Here we chose $H_1 = H_U$ (in reference to eq. 4.5.8) and use $\left(\mathrm{d}\tau\right)^n$ as a formal abbreviation of the n equal integral measures.

$$H_0 = H_{\mathrm{hyb}} + H_{\mathrm{bath}} - \mu(n_\uparrow + n_\downarrow) \tag{4.5.13}$$

$$H_1 = U n_\uparrow n_\downarrow \tag{4.5.14}$$

We will assume only one impurity site for this, the resulting algorithm is easily extended by adding the necessary indices to the density operators.

$$\mathrm{d}C\, w_C = (-U\,\mathrm{d}\tau)^n \frac{\mathrm{Tr}\left[e^{-\beta H_0}\right]}{\mathrm{Tr}\left[e^{-\beta H_0}\right]} \mathrm{Tr}\left[e^{-(\beta-\tau_n)H_0} n_\uparrow n_\downarrow e^{-(\tau_n-\tau_{n-1})H_0} \dots\right]$$

$$= (-U\,\mathrm{d}\tau)^n \frac{Z_0}{Z_0} \mathrm{Tr}\left[e^{-\beta H_0} e^{\tau_n H_0} n_\uparrow e^{-(\tau_n-\tau_n)H_0} n_\downarrow e^{-(\tau_n-\tau_{n-1})H_0} \dots\right] \tag{4.5.15}$$

Having inserted the necessary unity operators, we can use Wick's theorem to rewrite the trace. Note that only equal spin creation annihilation pairs survive

$$= (-U\,\mathrm{d}\tau)^n Z_0 \left\langle \cdots \overline{d_\uparrow^\dagger(\tau_j) d_\uparrow(\tau_j)} \cdots d_\uparrow^\dagger(\tau_i) d_\uparrow(\tau_i) \cdots \right\rangle_0$$

$$= (-U\,d\tau)^n Z_0 \prod_\sigma \det \left[\mathcal{G}_{0\sigma}(\tau_i - \tau_j)\right]$$

The brackets indicate the matrix of all vertex insertion times i, j. In case $i = j$ we use the $\mathcal{G}_{0\sigma}(0^+)$.

$$= (-U\,d\tau)^n Z_0 \prod_\sigma \det M_\sigma^{-1} \tag{4.5.16}$$

Where we identified:

$$\mathcal{G}_{0\sigma}(\tau) = \frac{1}{\mathrm{Tr}\{e^{-\beta H_0}\}} \mathrm{Tr}\left[e^{-\beta H_0} T\left(d(\tau)d^\dagger(0)\right)\right] \tag{4.5.17}$$

$$\left[M_\sigma^{-1}\right]_{ij} = \mathcal{G}_{0\sigma}(\tau_i - \tau_j) \tag{4.5.18}$$

This identity can be confirmed by comparison to our derivation of the Anderson impurity action (eq. 4.3.17). Following diagrams contribute at order $n = 1$ and $n = 2$, we use red color to indicate Ising spin up and blue color for down for the rest of this chapter.

From the expansion in eq. 4.5.16 we can immediately spot a potential sign problem in the paramagnetic phase where $\mathcal{G}_{0\uparrow} \equiv \mathcal{G}_{0\downarrow}$, since odd perturbation orders lead to negative weights [54].
There is however an adjustment to the Hamiltonian from F. Assaad and T. C. Lang that suppresses the sign problem at $\mu \approx U/2$ [10]: One introduces a shift to the ground state energy, that depends on an external Ising field to the density operator. Note that this extension is not always implied when talking about the interaction expansion. The procedure including this shift is closely related to the auxiliary field method introduced below. In fact we will discuss a prove for their equivalence in the context of this work, where we consider density-density interactions [54]. The resulting algorithm is however more closely related to the original CT-INT method.

$$U n_\uparrow n_\downarrow = \frac{U}{2} \sum_s \prod_\sigma \left(n_\sigma - \alpha_\sigma(s)\right) + \frac{U}{2}(n_\uparrow + n_\downarrow) + U\left[\left(\frac{1}{2} + \delta\right)^2 - \frac{1}{4}\right] \tag{4.5.19}$$

$$\alpha_\sigma(s) = \frac{1}{2} + \sigma s \left(\frac{1}{2} + \delta\right) \tag{4.5.20}$$

With δ sufficiently small and $s = \pm 1$.
The last term is a constant and can be absorbed into the partition function. The

second term is just a shift in the chemical potential, resembling the particle hole transformation from chapter 1:

$$\mu \to \mu - \frac{1}{2}U \tag{4.5.21}$$

$$\mathcal{G}_{0\sigma}^{-1}(i\omega_n) \to \mathcal{G}_{0\sigma}^{-1}(i\omega_n) - \frac{1}{2}U \tag{4.5.22}$$

Note that this shift applies to the whole DMFT loop, not just the sampling step! More importantly however, the sample space and weights change as well:

$$S = \{\tau_i \mid \tau_i \in [0,\beta)\} \to S = \{(\tau_i, s_i) \mid \tau_i \in [0,\beta), \, s_i \in \{-1,+1\}\} \tag{4.5.23}$$
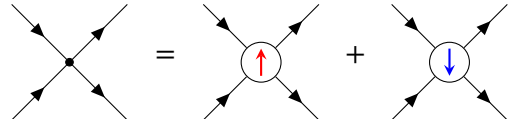
$$\left[M_\sigma^{-1}\right]_{ij} \to \left[M_\sigma^{-1}\right]_{ij} - \delta_{ij}\alpha_\sigma(s_i) \tag{4.5.24}$$

$$\mathrm{d}C\, w_C \to \tilde{Z}_0 \left(-\frac{U\,\mathrm{d}\tau}{2}\right)^n \det M_\uparrow^{-1} M_\downarrow^{-1} \tag{4.5.25}$$

For brevity we omitted all indices for impurity sites or different states. This transformation is not a full Hubbard-Stratonovich transformation, but due to the equivalence of CT-INT and CT-AUX for density-density interactions (see next section) we can use the same type of diagrams. The Hubbard-Stratonovich transformation introduces four fermion operators:

$$\exp\left[-U\left(n_\uparrow - \frac{1}{2}\right)\left(n_\downarrow - \frac{1}{2}\right)\right] = e^{-\frac{U}{4}} \sum_{s \in \{\pm 1\}} e^{-s\gamma(n_\uparrow - n_\downarrow)} \tag{4.5.26}$$

γ will be determined in the next section. The left hand side contains four fermion operators while the two particle density operator on the right hand side only couples to a classical Ising field. This can be written in form of diagrams:

$$\tag{4.5.27}$$

The role of the Ising dependent shift can be easily seen by writing down M^{-1} explicitly

$$M_{(n),\sigma}^{-1} = \begin{pmatrix} \mathcal{G}_{0\sigma}(0^+) - \alpha_\sigma(s) & \mathcal{G}_{0\sigma}(\tau_1 - \tau_2) & \cdots & \mathcal{G}_{0\sigma}(\tau_1 - \tau_n) \\ \mathcal{G}_{0\sigma}(\tau_2 - \tau_1) & \mathcal{G}_{0\sigma}(0^+) - \alpha_\sigma(s) & \cdots & \mathcal{G}_{0\sigma}(\tau_2 - \tau_n) \\ \vdots & \vdots & \ddots & \vdots \\ \mathcal{G}_{0\sigma}(\tau_n - \tau_1) & \mathcal{G}_{0\sigma}(\tau_n - \tau_2) & \cdots & \mathcal{G}_{0\sigma}(0^+) - \alpha_\sigma(s) \end{pmatrix} \tag{4.5.28}$$

We gain a better conditioned matrix as well as positive weights, but lose some performance [10]. This is not only due to the larger sample space but also the average perturbation order increases:

$$\langle n \rangle = -\beta U \left[\langle \hat{n}_\uparrow \hat{n}_\downarrow \rangle - \frac{1}{2}\langle \hat{n}_\uparrow + \hat{n}_\downarrow \rangle - \delta^2\right] \tag{4.5.29}$$

In practice it turned out to be sufficient to occasionally check for occurrence of negative weights due to numerical instabilities (from an ill conditioned M matrix) and increase δ until the sampled weights were all positive again. This is of course only

viable at half filling. A safe pick was $\delta \sim 0.001$ near half filling for $U \sim 2.5$, $\beta \sim 64$. The average perturbation order is proportional to the potential energy in case of the interaction expansion:

$$\langle n \rangle = -\beta E_{\text{pot}} + \frac{1}{2}\beta U \left\langle n_\uparrow + n_\downarrow \right\rangle \tag{4.5.30}$$

The kinetic energy can be obtained easily from the imaginary time Green's function:

$$E_{\text{kin}} = \frac{D^2}{2} \int_0^\beta \mathrm{d}\tau\, G(\tau) G(-\tau) \tag{4.5.31}$$

$$= \frac{\beta^2 D^2}{2} \sum_n G(i\omega_n) G(-i\omega_n) \tag{4.5.32}$$

4.5.2   CT-INT sampling and measurement

Due to the equivalence of CT-INT and CT-AUX in this thesis, we only write down the the sampling algorithm for CT-INT. The burn-in period is assumed to be taken care of by the accumulator object, which has to disregard the initial configurations. This is also the case for skipping of data points in order to reduce auto correlation. The Metropolis proposal rates $T(C \rightarrow C')$ and acceptance probabilities are in principal an almost free choice as explained before.

$$A(C \rightarrow C') = \min\{1, R(C \rightarrow C')\}$$

However, the simplest choice that still satisfies ergodicity is to draw insertion and removal proposal uniformly from their respective sample spaces. For the insertion we have to draw $\tau \in [0, \beta)$ and $s \in \{-1, 1\}$, for the removal $n \in |C|$.

$$T(n \rightarrow n+1) = \frac{1}{2\beta}, \qquad T(n+1 \rightarrow n) = \frac{1}{n+1} \tag{4.5.33}$$

$$R(n \rightarrow n+1) = \frac{\mathrm{d}C^{(n+1)}\, w_{C^{(n+1)}}\, T(n \rightarrow n+1)}{\mathrm{d}C^{(n)}\, w_{C^{(n)}}\, T(n+1 \rightarrow n)} \tag{4.5.34}$$

$$= \frac{-\beta U}{n+1} \prod_\sigma \frac{\det M_{(n+1),\sigma}^{-1}}{\det M_{(n),\sigma}^{-1}} \tag{4.5.35}$$

$$R(n+1 \rightarrow n) = \frac{1}{R(n \rightarrow n+1)} \tag{4.5.36}$$

The evaluation of the determinant looks unfeasible, but can in fact be done with only a couple of matrix multiplications as shown in sec. 5.1. In summary we have the following proposals: In order for this algorithm to work we need to store $M_{(n),\sigma}$,

Table 4.1: Proposals for the CT-INT solver which fulfill detailed balance

Proposal	Transition rate
Segment insertion	$\dfrac{-\beta U}{n+1} \prod_\sigma \dfrac{\det\left[M_\sigma^{(n+1)}\right]^{-1}}{\det\left[M_\sigma^{(n)}\right]^{-1}}$
Segment removal	$\dfrac{-n}{\beta U} \prod_\sigma \dfrac{\det\left[M_\sigma^{(n)}\right]^{-1}}{\det\left[M_\sigma^{(n+1)}\right]^{-1}}$

but since the algorithm provides us with the option to never use $M_{(n),\sigma}^{-1}$ explicitly, we do not even need the matrix inversion.

The sample algorithm is based on alg. 4. This is however only a single sampling step and the accumulation is done separately. The impurity Green's function for a

---

input : Weiss function $\mathscr{G}_{0\,\sigma}(\tau)$, Simulation parameters μ, β, U.
    Configuration $C^{(n)} = \{(\tau_1, s_1), \cdots (\tau_n, s_n)\}$, Matrix M_σ
output: Updated configuration C and M_σ

1   Draw $\zeta \sim U(0,1); \; \zeta' \sim U(0,1)$
2   **if** $\zeta < 0.5$:
3   Draw $s \sim 2 \cdot \lfloor U(0,1) \rfloor - 1$
4   Draw $\tau \sim U(0,\beta)$
5   **if** $n == 0$:
6   Set acceptance probability $R_{\text{insert}} = 1$
7   **else**:
8   Compute acceptance probability R using eq. 5.1.2
9   **if** $\zeta' < R$:
10   Set $\tilde{C}^{(n+1)} = C^{(n)} \cup \{(\tau, s)\}$
11   Update $M_{(n),\sigma} \to M_{(n+1),\sigma}$ using $\mathscr{G}_{0\,\sigma}(\tau)$ and eq. 5.1.6
12   **else**:
13   **if** $n == 0$:
14   **return** $\tilde{C}^0$
15   Draw $n' \sim U(0, n-1)$
16   Compute acceptance probability R using eq. 5.1.1
17   **if** $\zeta' < R$:
18   Set $\tilde{C}^{(n+1)} = C^{(n)} \backslash \{(\tau_{n'}, s_{n'})\}$
19   Update $M_{(n),\sigma} \to M_{(n-1),\sigma}$ using $\mathscr{G}_{0\,\sigma}(\tau)$ and eq. 5.1.7
20 **return** updated $\tilde{C}^{(n \pm l)}, M_{(l),\sigma}, l \in \{-1, 0, +1\}$

Algorithm 6: CT-INT sampling

---

single configuration can be obtained from eq. 4.5.15 by inserting $d^\dagger(0)$ and $d(\tau)$ and then using eq. 5.1.2 with Wick's theorem:

$$G_{C,\text{imp},\sigma}(\tau) = \frac{\left\langle T d(\tau) d^\dagger(0) \prod_i d_\sigma^\dagger(\tau_i) d_\sigma(\tau_i) \right\rangle_0}{\left\langle \prod_i d_\sigma^\dagger(\tau_i) d_\sigma(\tau_i) \right\rangle_0}$$

$$= \frac{\det M_{(n+1)}^{-1}}{\det M_{(n)}^{-1}}$$

$$= \mathscr{G}_{0\,\sigma}(\tau) - \sum_{ij} \mathscr{G}_{0\,\sigma}(\tau - \tau_i) \left[M_\sigma\right]_{ij} \mathscr{G}_{0\,\sigma}(\tau - \tau_j) \qquad (4.5.37)$$

Fourier transformation yields the measurement in Matsubara frequencies:

$$G_{C,\text{imp},\sigma}(i\omega_n) = \mathscr{G}_{0\,\sigma}(i\omega_n) - \beta^{-1} \left(\mathscr{G}_{0\,\sigma}(i\omega_n)\right)^2 \sum_{ij} e^{i\omega_n(\tau_i - \tau_j)} \left[M_\sigma\right]_{ij} \qquad (4.5.38)$$

These measurements can be done faster and more stable using a separate accumulation process (see sec. 5.3).

In order to obtain the full impurity Green's function, we use the usual Monte Carlo sign weighted sum

$$G_{\text{imp},\sigma}(\cdot) = \sum_{C \in S} \frac{w_C G_{C,\text{imp},\sigma}(\cdot)}{Z} \approx \frac{\sum_{C \in S_{MC}} \text{sign}_C |w_C| G_{C,\text{imp},\sigma}(\cdot)}{\sum_{C \in S_{MC}} \text{sign}_C |w_C|}$$

$$= \frac{\left\langle \text{sign} \cdot G_{\text{imp},\sigma}(\cdot) \right\rangle_{MC}}{\left\langle \text{sign} \right\rangle_{MC}} \tag{4.5.39}$$

$$C_{i,\sigma,\text{MC}} = \{(\tau_1, \dots, \tau_n, \left[M_\sigma\right]_{ij}, s_1, \dots, s_n)\} \tag{4.5.40}$$

4.5.3   Auxiliary Field — CT-AUX

The auxiliary field method is well known for its efficiency for large impurity cluster calculations, while still retaining an advantage over sign problem susceptible algorithms such as Hirsch-Fye or CT-INT [59].

However, we again consider only one impurity site for the derivation. The choice of H_1 is similar to CT-INT but we introduce an additional parameter K and employ the discrete Hubbard-Stratonovich transformation [64] during the derivation of the weights (compare eq. 4.5.15).

$$H_0 = H_{\text{hyb}} + H_{\text{bath}} - \mu(n_\uparrow + n_\downarrow) + \frac{1}{2}U\left(n_\uparrow + n_\downarrow\right) + \frac{K}{\beta} \tag{4.5.41}$$

$$H_1 = U n_\uparrow n_\downarrow - \frac{1}{2}U\left(n_\uparrow + n_\downarrow\right) - \frac{K}{\beta} \tag{4.5.42}$$

$$= \frac{K}{2\beta} \sum_{s \in \{+1,-1\}} e^{\gamma s(n_\uparrow - n_\downarrow)} = \frac{K}{2\beta} \sum_s \prod_\sigma \left(e^{\gamma s \sigma} - \left(e^{\gamma s \sigma} - 1\right) d_\sigma d_\sigma^\dagger\right) \tag{4.5.43}$$

$$K = \frac{\beta U}{2\cosh(\gamma) - 2} \tag{4.5.44}$$

Similar to the derivation of the weights for CT-INT it is now possible to evaluate the trace analytically. We decompose the original non-perturbed Hamiltonian into three commuting parts: $H_0 = \frac{K}{\beta} + \sum_{\sigma \in \{\uparrow,\downarrow\}} H_{\sigma,0}$

$$\mathrm{d}C\, w_C = \left(\frac{K\,\mathrm{d}\tau}{\beta}\right)^n e^{-K} Z_{\sigma,0} \left\langle \sum_s \prod_\sigma \left(\cdots e^{\gamma s_i \sigma} - \left(e^{\gamma s_i \sigma} - 1\right) d_\uparrow(\tau_i) d_\uparrow^\dagger(\tau_i) \cdots\right) \right\rangle_{\sigma,0}$$

Instead of summing over all Ising spins s, we once again extend the sample space. Also analog to before, the second term of H_1 is absorbed into the chemical potential so $\mu \to \mu - \frac{1}{2}U$ etc. The derivation of the trace factor is a bit more tedious this time and therefore left to the literature [51]

$$\cdot = \left(\frac{K\,\mathrm{d}\tau}{\beta}\right)^n e^{-K} Z_{\sigma,0} \prod_\sigma \text{Tr}\left[e^{-\beta H_{\sigma,0}}\right] \det N_\uparrow^{-1} N_\downarrow^{-1} \tag{4.5.45}$$

with

$$N_\sigma^{-1} = e^{\Gamma_\sigma} - \left[\mathscr{G}_{0\,\sigma}(\tau_i - \tau_j)\right]\left(e^{\Gamma_\sigma} - \mathbb{1}\right) \tag{4.5.46}$$

$$\left[e^{\Gamma_\sigma}\right]_{ij} = \delta_{ij} e^{\gamma \sigma s_i} \tag{4.5.47}$$

The matrix explicitly takes the following form:

$$N_\sigma^{-1} =$$

$$\begin{pmatrix} e^{\gamma\sigma s_1} - \mathscr{G}_{0\sigma}(0^+)\left(e^{\gamma\sigma s_1} - 1\right) & \mathscr{G}_{0\sigma}(\tau_1 - \tau_2)\left(e^{\gamma\sigma s_2} - 1\right) & \cdots & \mathscr{G}_{0\sigma}(\tau_1 - \tau_n)\left(e^{\gamma\sigma s_n} - 1\right) \\ \mathscr{G}_{0\sigma}(\tau_2 - \tau_1)\left(e^{\gamma\sigma s_1} - 1\right) & e^{\gamma\sigma s_2} - \mathscr{G}_{0\sigma}(0^+)\left(e^{\gamma\sigma s_2} - 1\right) & \cdots & \mathscr{G}_{0\sigma}(\tau_2 - \tau_n)\left(e^{\gamma\sigma s_n} - 1\right) \\ \vdots & \vdots & \ddots & \vdots \\ \mathscr{G}_{0\sigma}(\tau_n - \tau_1)\left(e^{\gamma\sigma s_1} - 1\right) & \mathscr{G}_{0\sigma}(\tau_n - \tau_2)\left(e^{\gamma\sigma s_2} - 1\right) & \cdots & e^{\gamma\sigma s_n} - \mathscr{G}_{0\sigma}(0^+)\left(e^{\gamma\sigma s_n} - 1\right) \end{pmatrix}$$

$$(4.5.48)$$

We again use $\mathscr{G}_{0\sigma}(0^+)$ for $i = j$.

In order to show the equivalence of CT-INT and CT-AUX we rewrite N_σ^{-1} in the following form [54]:

$$e^{\Gamma_\sigma} - \left[\mathscr{G}_{0\sigma}(\tau_i - \tau_j)\right]\left(e^{\Gamma_\sigma} - \mathbb{1}\right)$$

$$= \left(\left[\mathscr{G}_{0\sigma}(\tau_i - \tau_j)\right] - \frac{1}{2}\mathbb{1} - \left[\frac{1}{2}\mathbb{1} - \left(\mathbb{1} - e^{\Gamma_\sigma}\right)^{-1}\right]\right)\left(\mathbb{1} - e^{\Gamma_\sigma}\right)$$

The square bracket is a diagonal matrix with elements that can be evaluated to $\frac{\sigma s}{2\tanh(\gamma/2)}$ using $\sigma s = \pm 1$.

It follows that $\prod_\sigma \left(\mathbb{1} - e^{\Gamma_\sigma}\right) = -\frac{\beta U}{K}\mathbb{1}$

$$\Rightarrow \prod_\sigma \det\left(N_\sigma^{-1}\right) = \left(\frac{\beta U}{K}\right)^n \det\left(\left[\mathscr{G}_{0\sigma}(\tau_i - \tau_j)\right] - \frac{1}{2}\mathbb{1} - \frac{s\sigma}{2\tanh(\gamma/2)}\mathbb{1}\right)$$

$$\Rightarrow \frac{1}{2} + \delta = \frac{1}{2\tanh(\gamma/2)}$$

$$\Leftrightarrow K = \beta U\left[\left(\frac{1}{2} + \delta\right)^2 - \frac{1}{4}\right]$$

Note that we are still expanding in orders of U since $K \sim U$.

The average perturbation order for CT-AUX is therefore

$$\langle n \rangle = -\beta U\left[\langle \hat{n}_\uparrow \hat{n}_\downarrow \rangle - \frac{1}{2}\langle \hat{n}_\uparrow + \hat{n}_\downarrow \rangle\right] + K \qquad (4.5.49)$$

Since the CT-AUX methods requires more operations due to the exponential functions[5] the CT-INT method with Ising spin extension is preferable wherever these methods are equivalent.

4.5.4 *Hybridization Expansion — CT-HYB*

We can either express the effective action in terms of the Weiss Green's function eq. 4.3.17 or the hybridization function eq. 4.3.18. The strong coupling or hybridization expansion method expands in terms of the hybridization potential $V_{\alpha\sigma}$ instead of the interaction strength U [132].

However, the general idea for the derivation of this method is the same as before. We will again start with a suitable partition of the Hamiltonian

$$H_0 = H_{\text{loc}} + H_{\text{bath}} \qquad (4.5.50)$$

$$H_1 = H_{\text{hyb}} = H_1^{d^\dagger} + H_1^d \qquad (4.5.51)$$

---

5 In fact, this drawback can almost be completely neglected with proper optimization, since one can used cached values. However it still introduces unnecessary overhead.
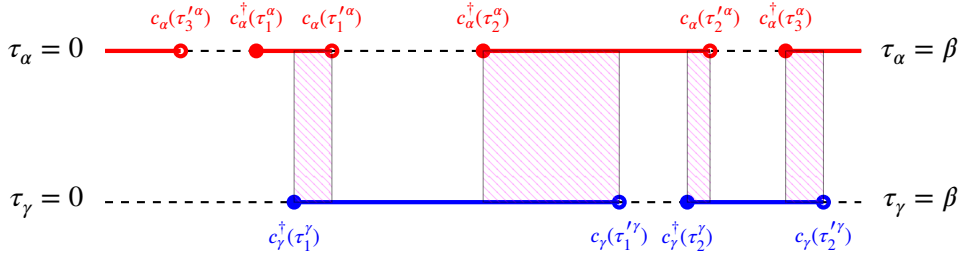
Figure 4.6: Overlap of segments for local trace computation. Line α has a permutation sign of -1 due to the last segment wrapping around.

$$= \sum_{\alpha,\sigma} V_{\alpha,\sigma} d^\dagger C_{\alpha,\sigma} + \sum_{\alpha,\sigma} V^\star_{\alpha,\sigma} c^\dagger_{\alpha,\sigma} d_\sigma \qquad (4.5.52)$$

We can use that $e^{-\tau H_0}$ does not flip the spin and therefore the number of creation operators for each configuration must be the same as the number of annihilation operators. This will be used in the second line. We start by writing eq. 4.5.8 explicitly with this choice of H_0 and H_1.

$$Z = \sum_{n=0}^{\infty} \int_0^\beta d\tau_1 \cdots \int_{\tau_n}^\beta d\tau_n \int_0^\beta d\tau'_1 \cdots \int_{\tau'_n}^\beta d\tau'_n$$
$$\times \mathrm{Tr}\left[e^{-\beta H_0} T H_1^d(\tau_n) H_1^{d^\dagger}(\tau'_n) \cdots H_1^d(\tau_1) H_1^{d^\dagger}(\tau'_1) \right]$$

One can now use that $[H_{\mathrm{bath}}, d] = [H_{\mathrm{loc}}, c] = 0$ to separate the traces over impurity and bath.

$$= Z_{\mathrm{bath}} \prod_\sigma \sum_{n_\sigma=0}^{\infty} \int_0^\beta d\tau_{1,\sigma} \cdots \int_{\tau_{n_\sigma-1,\sigma}}^\beta d\tau_{n_\sigma,\sigma} \int_0^\beta d\tau'_{1,\sigma} \cdots \int_{\tau'_{n_\sigma-1,\sigma}}^\beta d\tau'_{n_\sigma,\sigma}$$
$$\times \mathrm{Tr}_d\left[e^{-\beta H_{\mathrm{loc}}} T \prod_\sigma d_\sigma(\tau_{n_\sigma,\sigma}) d^\dagger_\sigma(\tau'_{n_\sigma,\sigma}) \cdots d_\sigma(\tau_{1,\sigma}) d^\dagger_\sigma(\tau'_{1,\sigma}) \right]$$
$$\times \frac{1}{Z_{\mathrm{bath}}} \mathrm{Tr}_c\left[e^{-\beta H_{\mathrm{bath}}} T \prod_\sigma \sum_{\alpha_1 \cdots \alpha_{n_\sigma}} \sum_{\alpha'_1 \cdots \alpha'_{n_\sigma}} V^\star_{\alpha_1,\sigma} V_{\alpha'_1,\sigma} \cdots c^\dagger_{\alpha_{n_\sigma},\sigma}(\tau_{n_\sigma,\sigma}) c_{\alpha'_{n_\sigma},\sigma}(\tau'_{n_\sigma,\sigma}) \cdots \right]$$

The trace over the bath Tr_c can be evaluated in the same manner as before and results in the determinant of a matrix. The impurity trace requires us to look at the eigenbasis of H_{loc}:

Creation and annihilation operators for the same spin $d_\sigma, d^\dagger_\sigma$ must alternate for the trace to contribute. This can be represented by two time lines $[0, \beta)$ with full segments for times during which the impurity is occupied and empty segments where it is not. This is called section picture [54]. While this is not the only way to treat this trace it is, sufficient for this thesis. These evaluations of the local trace are better suited for arbitrary local interactions, but are out of the scope of this thesis. The total length of segments for spin σ is called l_σ, the total length of all overlaps between

segments of different spin (or states in general) l_{overlap}. With these definitions one can write down the Monte Carlo weights:

$$dC\, w_C = (d\tau)^{2n_\sigma}(-1)^{\sum_\sigma s_\sigma} e^{\mu \sum_\sigma l_\sigma - U l_{\text{overlap}}} \times \det M_\sigma^{-1} \tag{4.5.53}$$

$$\left[M_\sigma^{-1}\right]_{ij} = \Delta_\sigma(\tau'_{i\sigma} - \tau_{j\sigma}) \tag{4.5.54}$$

$s_\sigma \in [0, 1]$ is equal to one iff a σ segment ends at $\tau'_\sigma < \tau_\sigma$ (since segments also follow the cyclic boundary conditions). An example for a segment configuration is given in fig. 4.6.

In contrast to the expansion in U, the $(-1)^{s_\uparrow + s_\downarrow}$ factor does not result in a "trivial" sign problem. In fact one can proof that both CT-INT and CT-HYB do not exhibit a sign problem at all for our application (half filling, density-density interactions), because the sign cancels with the determinant ratio, see chapter 8.7 [54]. For the hybridization expansion this can be explained using the fact that the hybridization function inherits the anti-symmetric property of the Green's function:

$$\Delta_\sigma(-\tau) = -\Delta_\sigma(\beta - \tau) \tag{4.5.55}$$

This follows from the time dependence only entering through the Green's function in eq. 4.3.19.

4.5.5   CT-HYB sampling and measurement

The proposal and acceptance probabilities follow similar to the CT-INT method. Proposed segments starting at τ can have a maximum length of

$$l_{\text{max}} = (\tau' - \tau) \qquad \text{mod } \beta \tag{4.5.56}$$

with τ' being the start of the next segment. In case there is no other segment, $l_{\text{max}} = \beta$.

We propose the insertion of a segment with random size $l_{\text{new}} \in (0, \beta]$, which changes the total overlap of segments between segments of σ and σ' by δ_{overlap}, with transition probabilities:

$$T(n_\sigma \to n_\sigma + 1) = \frac{d\tau}{\beta} \frac{d\tau}{l_{\text{max}}} \tag{4.5.57}$$

$$T(n_\sigma + 1 \to n_\sigma) = \frac{1}{n_\sigma + 1} \tag{4.5.58}$$

As before, we get the acceptance probabilities from the weight and proposal probabilities:

$$R(n \to n + 1) = \frac{dC^{(n+1)} w_{C^{(n+1)}} T(n_\sigma \to n_\sigma + 1)}{dC^{(n)} w_{C^{(n)}} T(n_\sigma + 1 \to n_\sigma)}$$

$$= \frac{\beta l_{\text{max}}}{n_\sigma + 1} e^{\mu l_{\text{new}} - U \delta_{\text{overlap}}} \frac{\det M_{(n_\sigma + 1),\sigma}^{-1}}{\det M_{(n_\sigma),\sigma}^{-1}} \tag{4.5.59}$$

$$R(n + 1 \to n) = 1/R(n \to n + 1) \tag{4.5.60}$$

The determinant ratio is again computed by using the fast update algorithm (eq. 5.1.8). However, one has to consider that completely empty and completely full lines (i.e.

segments of length β and no segment at all) are not sampled equally likely by only proposing the insertion of segments of random length. This should not be the case for an ergodic system. We therefore also need to allow for the insertion and removal of so called anti-segments. An insertion of an anti-segments amounts to a split of a segment, the removal of an anti-segment joins two segments together. This makes insertion and removal of anti-segments algorithmically equivalent to the operations on segments. The only special case we have to consider is an empty line which can either be encoded as a completely full or completely empty line.

The maximum length $l_{\max}$ for anti-segments starting at τ' is $\tau_j - \tau'$. τ_j is the the end of the segment which the anti-segment is splitting. Removal of an anti-segment at order $n_\sigma = 1$ leads to a full line that is conveniently encoded by $C\{(\tau, \tau)\}$. One usually also allows for a global shift of all segments. This is not required but reduces auto correlation times and overall "jitter" from high rejection rates. See table 4.2 for a list of all proposals including acceptance rates.

The measurement for the CT-HYB method requires a bit more work than the one
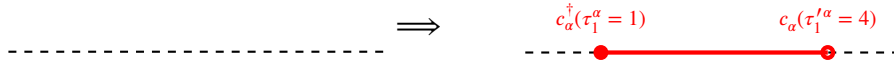

Figure 4.7: Segment insertion with uniformly drawn starting position from $[0, \beta)$, here $\tau_1^\alpha = 1$. Max length is $l_{\max} = \beta$, because no other segments are present. Length l_{new} is then uniformly drawn from $(0, \beta)$, here 3.
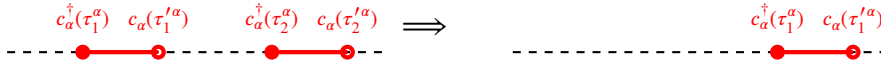

Figure 4.8: Segment removal. Segment is uniformly chosen (probability 1/2 in this example).
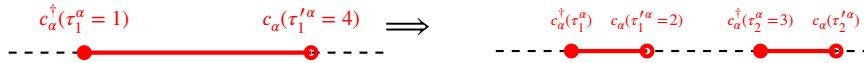

Figure 4.9: Anti segment insertion with uniformly drawn starting position from $[0, \beta)$, here $\tau_{1,\text{new}}^{\prime\alpha} = 2$, proposals which do not fall into an existing segment are rejected. The maximum length is $l_{\max} = \tau_{1,\text{old}}^{\prime\alpha} - \tau_{1,\text{new}}^{\prime\alpha} = 2$. Length l_{new} is then uniformly drawn from $(0, \beta)$, here 1.
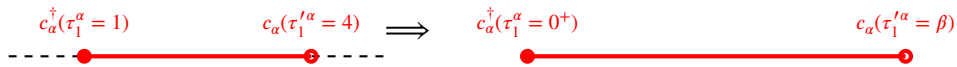Note that anti segments can also be inserted into full lines.

Figure 4.10: Anti segment removal. Segment is uniformly chosen (probability 1 in this example). The result is a full line (at expansion order 0).
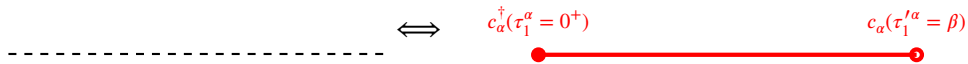

Figure 4.11: Empty to full line and vice versa. This is a decomposition of expansion order $n_\alpha = 0$.

for CT-INT. We will need the following generalized Dirac delta to capture the periodicity of the Green's function:

$$\delta(\tau, \tau') = \begin{cases} \delta(\tau - \tau') & \tau' \geq 0 \\ -\delta(t - \tau' - \beta) & \tau' < 0 \end{cases} \tag{4.5.61}$$

input : Hybridization function $\Delta_\sigma(\tau)$, Simulation parameters μ, β, U.

   Configuration $C_\sigma^{(n)} = \{ \left(\tau'_{1,\sigma}, \tau_{1,\sigma} \right), \cdots \left(\tau'_{n_\sigma,\sigma}, \tau_{n_\sigma,\sigma} \right) \}$, inverse expansion Matrix M^{-1}

output : Updated configuration C and M^{-1}

1 Draw $\zeta \sim U(0,1)$; $\zeta' \sim U(0,1)$; $\sigma \sim 2 \cdot \lfloor U(0,1) \rfloor - 1$

2 **if** $\zeta < 0.25$**:**

3   Draw $\tau'_\sigma \sim U(0,\beta)$

4   **if** τ'_σ not in segment and not in full line**:**

5   Draw $\tau_\sigma \sim U(0^+, l_{\max})$

6   Compute $R(n \rightarrow n+1)$ from eq. 4.5.59 and eq. 5.1.2

7   **if** $\zeta' < R$**:**

8   Insert segment $\left(\tau'_\sigma, \tau_\sigma \right)$

9   Update M_σ using $\Delta_\sigma(\tau)$ using eq. 5.1.6

10 **elif** $0.25 \leq \zeta < 0.5$**:**

11   **if** $n_\sigma > 0$**:**

12   Draw $n' \sim \lfloor U(0,n) \rfloor$

13   Compute $R(n+1 \rightarrow n)$ from eq. 4.5.60 and eq. 5.1.2

14   **if** $\zeta' < R$**:**

15   Remove segment n'

16   Update M_σ using $\Delta_\sigma(\tau)$ using eq. 5.1.7

17 **elif** $0.5 \leq \zeta < 0.75$**:**

18   Draw $\tau'_\sigma \sim U(0,\beta)$

19   **if** τ'_σ in segment or full line**:**

20   Draw $\tau_\sigma \sim U(0^+, l_{\max})$

21   Compute $R(n \rightarrow n+1)$ from eq. 4.5.59 and eq. 5.1.2

22   **if** $\zeta' < R$**:**

23   Split segment $\left(\tau'_{i,\sigma}, \tau_{i,\sigma} \right) \rightarrow \left(\tau'_{i,\sigma}, \tau'_\sigma \right), \left(\tau'_\sigma, \tau_{i,\sigma} \right)$

24   Update M_σ using $\Delta_\sigma(\tau)$ using eq. 5.1.6

25 **else:**

26   **if** $n_\sigma > 1$**:**

27   Draw $n' \sim \lfloor U(0,n) \rfloor$

28   Compute $R(n+1 \rightarrow n)$ from eq. 4.5.60 and eq. 5.1.2

29   **if** $\zeta' < R$**:**

30   Remove anti-segment n' (i.e. merge $\left(\tau'_i, \tau_i \right), \left(\tau'_{i+1}, \tau_{i+1} \right)$ to $\left(\tau'_i, \tau_{i+1} \right)$)

31   Update M_σ using $\Delta_\sigma(\tau)$ using eq. 5.1.7

32   **if** $n_\sigma == 1$ *and* $C \neq \{\tau_1, \tau_1\}$**:**

33   Compute $R(1 \rightarrow 0)$ from eq. 4.5.60 and eq. 5.1.2

34   **if** $\zeta' < R$**:**

35   Set full line

36 **return** updated $\tilde{C}^{(n\pm l)}$, $M_{(l)}^{-1}$, $l \in \{-1, 0, +1\}$

Algorithm 7: CT-HYB sampling using insertion and removal of segments and anti-segments.

Table 4.2: Proposals for the CT-HYB solver which fulfill detailed balance

Proposal	Transition rate
Segment insertion	$\left\| \dfrac{\det\left\{\left[\widetilde{M}_\sigma^{n_\sigma+1}\right]\right\}^{-1}}{\det\left\{\left[M_\sigma^{n_\sigma}\right]\right\}^{-1}} \right\| \dfrac{\beta l_{\max}}{k+1} e^{\mu l_{\text{new}} - U \Delta l_{\text{overlap}}}$
Segment removal	$\left\| \dfrac{\det\left\{\left[\widetilde{M}_\sigma^{n_\sigma}\right]\right\}^{-1}}{\det\left\{\left[M_\sigma^{n_\sigma+1}\right]\right\}^{-1}} \right\| \dfrac{\beta l}{k+1} e^{-\mu l_{\text{old}} + U \Delta l_{\text{overlap}}}$
Anti segment insertion	see segment insertion
Anti segment removal	see segment removal
Shift end-point	$\dfrac{\widetilde{M}_\sigma^{n_\sigma}}{M_\sigma^{n_\sigma}} \dfrac{\beta l_{\max}}{k+1} e^{\mu l_{\text{new}} - U \Delta l_{\text{overlap}}}$
Switch zero state	see insertion/removal

This allows to rewrite eq. 3.4.2 for the impurity Green's function as follows:

$$G_{\text{imp},\sigma}(\tau) = \int_0^\beta d\tau' \int_0^\beta d\tau'' \delta(\tau, \tau' - \tau'') G_{\text{imp},\sigma}(\tau' - \tau'') \tag{4.5.62}$$

$$= \frac{1}{Z_{\text{eff}}} \int_0^\beta d\tau' \int_0^\beta d\tau'' \delta(\tau, \tau' - \tau'') \left\langle T d(\tau') d^\dagger(\tau'') \right\rangle_{\text{eff}}$$

$$\overset{\text{eq. 4.3.18}}{=} \int_0^\beta d\tau' \int_0^\beta d\tau'' \delta(\tau, \tau' - \tau'') \frac{\delta Z_{\text{eff}}}{\delta \Delta_{\sigma'}(\tau'' - \tau')}$$

By explicit expansion of the partition function (as done in the derivation of the weights, see also [54]) and the definition of M (eq. 4.5.54), one can show the following form:

$$G_{C,\text{imp},\sigma}(\tau) \approx \int_0^\beta d\tau' \int_0^\beta d\tau'' \delta(\tau, \tau' - \tau'') \frac{1}{\det\left(M_C^{-1}\right)} \frac{\partial \det\left(M_C^{-1}\right)}{\partial \Delta_{\sigma'}(\tau'' - \tau')}$$

We can now use Jacobi's formula[6] eq. 4.5.54 and $\frac{\delta \Delta_\sigma(\tau)}{\delta \Delta_{\sigma'}(\tau')} = \delta(\tau - \tau')\delta_{\sigma\sigma'}$ to obtain the measurement formula in imaginary and Matsubara representation:

$$= \int_0^\beta d\tau' \int_0^\beta d\tau'' \delta(\tau, \tau' - \tau'') \delta(\tau_{n_i} - \tau'_{n_j} - (\tau' - \tau'')) \delta_{\sigma\sigma'} \frac{\det\left(M_{\sigma'}^{-1}\right)}{\det\left(M_\sigma^{-1}\right)} M_\sigma$$

$$= -\frac{1}{\beta} \delta(\tau, \tau_{n_i} - \tau'_{n_j}) [M]_{ij}$$

$$\Rightarrow G_{\text{imp},\sigma}(\tau) \approx \left\langle -\frac{1}{\beta} \sum_{ij} \delta(\tau, \tau_{n_i} - \tau'_{n_j}) [M]_{ij} \right\rangle_{MC} \tag{4.5.63}$$

$$G_{\text{imp},\sigma}(i\omega_n) \approx \left\langle -\frac{1}{\beta} \sum_{ij} e^{i\omega_n(\tau_i - \tau'_j)} [M]_{ij} \right\rangle_{MC} \tag{4.5.64}$$

Note that the measurement formula does not involve the convolution with another Green's function as in the case of CT-INT and CT-AUX. This means that the tail is not guaranteed to follow the $\sim \frac{1}{\omega_n}$ constraint (see eq. 3.3.13). One can however

---

6 We use a special case here since the derivative is with regards to a component of an invertible matrix: $\frac{\partial \det A}{\partial A_{ij}} = A^{-1} \det A$
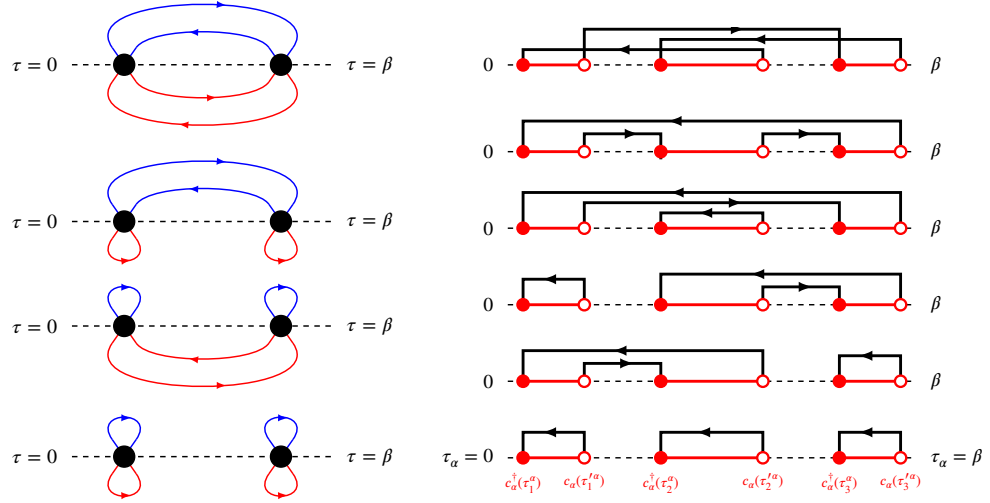
Figure 4.12: Diagrams for CT-INT (left) and CT-HYB (right) that are obtained from determinants of matrices of size 2 (left) and 3 (right). The diagrams contributing to the CT-INT algorithm have already been obtained in 4.5.19. In the segment picture the hybridization line connects creation and annihilation operators. The permutation sign of the segments is $+, -, -, -, +, +$ from bottom to top. For a full discussion see chapter 8.7 [54]

expand the measured Green's function in terms of Legendre polynomials in order to suppress noise and force a correct tail, see also sec. 5.3. The kinetic energy can be measured directly in CT-HYB [54]:

$$
\begin{aligned}
E_{\text{kin}} &= -\sum_\sigma \left\langle \frac{1}{\beta} \sum_{ij} \left[M_\sigma\right]_{ij} \Delta_\sigma(\tau'_j - \tau_i) \right\rangle_{MC} \\
&= -\frac{1}{\beta} \left\langle n_\uparrow + n_\downarrow \right\rangle
\end{aligned}
\tag{4.5.65}
$$

The average perturbation order can be shown to be proportional to the kinetic energy [54]:

$$
\langle n \rangle = -\beta E_{\text{kin}}
\tag{4.5.66}
$$

In fig. 4.13b and fig. 4.13a, the expansion orders for the CT-INT and CT-HYB solvers are shown in comparison. While the latter does need a substantially lower expansion order, there is an overhead due to the computation of the local trace (see segment picture above). The expansion orders are approximately normal distributed (skewness and kurtosis are smaller than 10^{-2} for 2 million samples). In fig. 4.14 a direct comparison between both expansion orders is shown. Both algorithms expansion order scales linearly with β (see for example eq. 4.5.29). Because the convergence speed depends on the temperature, this does not directly translate into overall time complexity. However, assuming the computation of determinant ratios are the dominant performance factor, the scaling can be estimated as β^3 [54].

4.6   PROGRAM FLOW AND EXTENSIONS

Using the DMFT approximation $\Sigma_{\text{loc}}(k, i\omega_n) \approx \Sigma_{\text{imp}}(i\omega)$ and the Dyson equation eq. 4.3.14, we can summarize the program flow for the DMFT self consistency loop. The k independent lattice Green's function should converge against the impurity one by successively tuning the free parameters.

$$G_{\text{imp}\,\sigma}(i\omega_n) \quad \Longrightarrow \quad \int_{\text{BZ}} G_{\sigma}(k, i\omega_n)\, dk$$
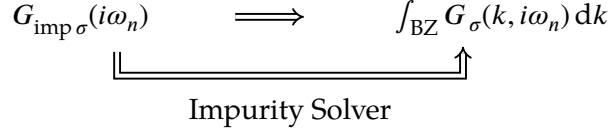
Impurity Solver

The impurity solver will either tune the hybridization function or the Weiss function until convergence is reached.

$$G_{\text{loc},\,\sigma}^{-1}(k, i\omega_n) \approx \int_{\text{BZ}} i\omega_n + \mu - \epsilon_k - \Sigma_{\text{imp}}(i\omega_n)\, dk \tag{4.6.1}$$

$$\Sigma_{\sigma}(k, i\omega_n) = G_{\text{lattice},\,\sigma}^{-1}(k, i\omega_n) - G_{\sigma}^{-1}(k, i\omega_n) \tag{4.6.2}$$

$$\Sigma_{\text{imp}}(i\omega_n) = \mathscr{G}_{0\,\sigma}^{-1}(i\omega_n) - G_{\text{imp},\,\sigma}^{-1}(i\omega_n) \tag{4.6.3}$$

The impurity solver provides us with the impurity Green's function.

> **input**   :Initial guess for Weiss function $\mathscr{G}_{0\,\sigma}(\tau)$, bath dispersion ϵ_k, μ, β, burn-in steps j
>
> **output**:G_{loc}
>
> 1 **while** G_{loc} not converged:
> 2   Solve impurity problem: $G_{\text{imp},\,\sigma}(\tau)\left[\mathscr{G}_{0\,\sigma}(\tau)\right]$
> 3   Fourier transform: $G_{\text{imp},\,\sigma}(\tau) \longrightarrow G_{\text{imp},\,\sigma}(i\omega_n)$
> 4 $\Sigma_{\text{imp},\sigma}(i\omega_n) = \mathscr{G}_{0\,\sigma}^{-1}(i\omega_n) - G_{\text{imp},\,\sigma}^{-1}(i\omega_n)$
> 5   Hilbert transform: $G_{\text{loc},\,\sigma}(i\omega_n) = \int \frac{dk}{\omega_n + \mu - \epsilon_k - \Sigma_{imp}(i\omega_n)} = \int \frac{\rho(\epsilon)}{i\omega_n + \mu - \epsilon - \Sigma(i\omega_n)}\, d\epsilon$
> 6   Update: $\mathscr{G}_{0\,\sigma}^{-1}(i\omega_n) = G_{\text{loc},\,\sigma}^{-1}(i\omega_n) + \Sigma_{\text{imp},\sigma}(i\omega_n)$
> 7   Fourier transform: $\mathscr{G}_{0\,\sigma}(i\omega_n) \to \mathscr{G}_{0\,\sigma}(\tau)$
> 8 **return** G_{loc}

Algorithm 8: DMFT Loop in terms of Weiss Green's function on general lattice
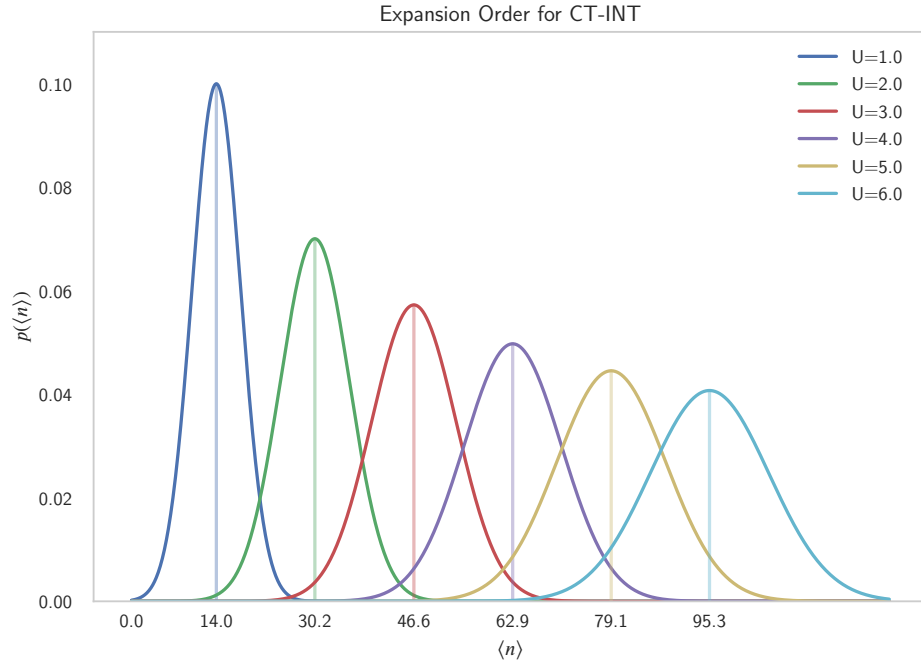
(a) CT-INT expansion order for $\beta = 32$ and $\delta = 0.02$
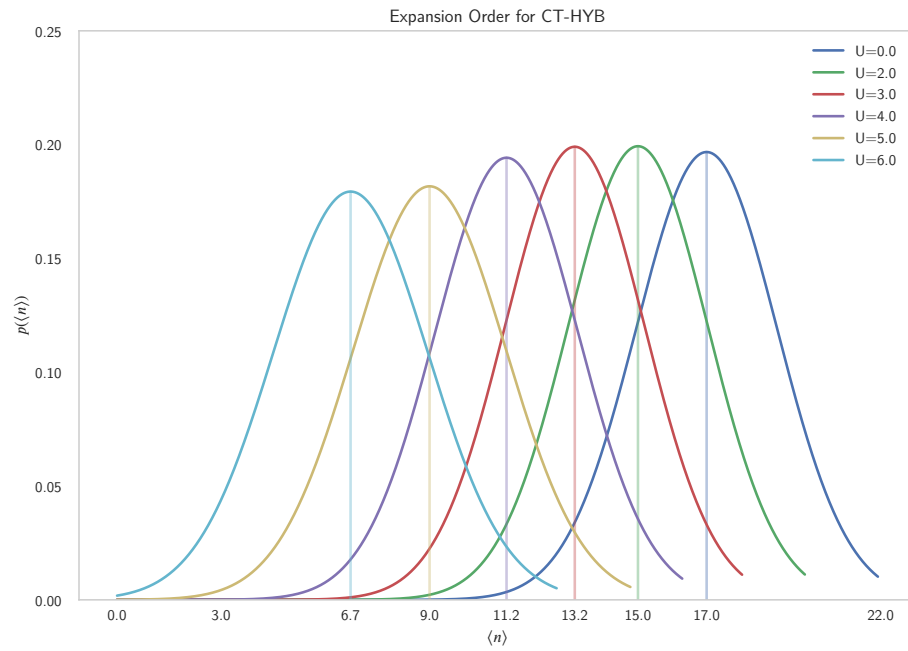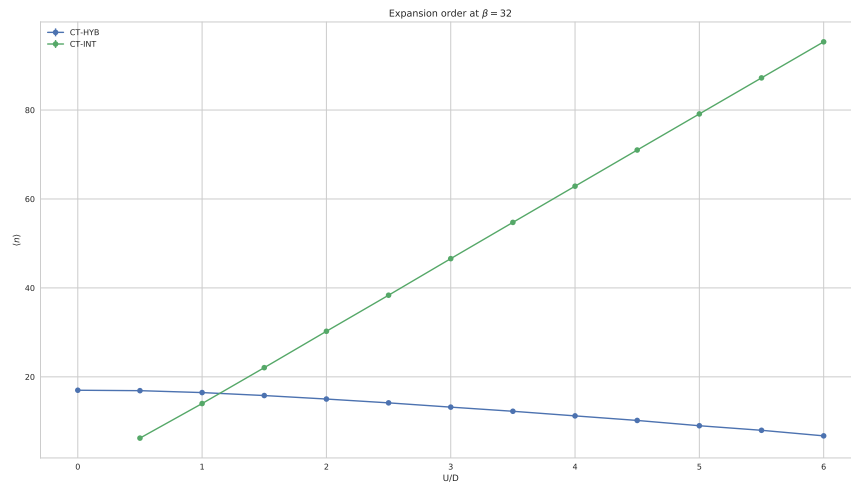

(b) CT-HYB expansion order for $\beta = 32$

Figure 4.14: Comparison of expansion order between CT-INT and CT-HYB. Mott transition occurs between $U/D \approx 2.3$ and $U/D \approx 3$

PROGRAM AND NUMERICAL METHODS

The main goal of this thesis was the development of a DMFT simulation program. Despite a straightforward analytical formulation, especially using the path integral formalism, there were quite a lote of numerical hurdles.

Many of these algorithms are not directly required for the code to work but greatly improve accuracy, reliability or performance. Since the analytic continuation is extremely sensitive to noise of input data, many of these algorithms are actually required in order to obtain more than the simplest of observables. To give some insight that can be used for the development of similar projects, I will give an aggregated overview over the most important methods used and their precise application for DMFT.

5.1 FAST MATRIX UPDATE

This algorithm is essential for the continuous time quantum Monte Carlo methods, because it allows the computation of the determinant ratios in $\mathcal{O}(n^2)$ operations. This is possible since the matrix only changes in k rows and columns (usually $k \leq 2$) on every Metropolis proposal.

The general formula is known as Woodbury matrix identity. The special version in this thesis, is often referred to as Sherman-Morrison formula.

$$M_{(n+1)}^{-1} = \begin{pmatrix} M_{(n)}^{-1} & Q \\ R & S \end{pmatrix} \tag{5.1.1}$$

Q is a $n \times k$ block with entries of the same type as $M_{(n)}^{-1}$ (depending on the sampler $\mathcal{G}_{0\,\sigma}(\tau)$ or $\Delta(\tau)$ or $(e^{\gamma s_j \sigma} - 1)\mathcal{G}_{0\,\sigma}(\tau)$). R and S are $k \times n$ and $k \times k$ sub blocks. We will omit the σ index for this derivation.

$$\frac{\det M_{(n+k)}^{-1}}{\det M_{(n)}^{-1}} = \det \begin{pmatrix} M_{(n)} & 0_{n \times k} \\ 0_{k \times n} & \mathbb{1}_k \end{pmatrix} \det \begin{pmatrix} M_{(n)}^{-1} & Q \\ R & S \end{pmatrix} = \det \begin{pmatrix} \mathbb{1}_{n \times n} & M_{(n)}Q \\ R & S \end{pmatrix}$$

$$= S - R M_{(n)} Q \tag{5.1.2}$$

Writing $M_{(n+k)}$ in terms of sub matrices $\tilde{P}, \tilde{Q}, \tilde{R}, \tilde{S}$, provides 4 equations from which we can construct $M_{(n+K)}$ as functions of $M_{(n)}, R, Q, S$ (these are all stored in memory or can be constructed as seen above) and vice versa.

$$\mathbb{1} = M_{(n+k)} M_{(n+k)}^{-1} = \begin{pmatrix} \tilde{P} & \tilde{Q} \\ \tilde{R} & \tilde{S} \end{pmatrix} \begin{pmatrix} M_{(n)}^{-1} & Q \\ R & S \end{pmatrix}$$

Solving this system of 4 coupled equations yields the 4 necessary equations for insertion of a vertex:

$$\tilde{S} = \left(S - R \left[M_{(n)} Q \right] \right)^{-1} \tag{5.1.3}$$

$$\tilde{Q} = - \left[M_{(n)} Q \right] \tilde{S} \tag{5.1.4}$$

$$\tilde{R} = \tilde{S} \left[R M_{(n)} \right] \tag{5.1.5}$$

$$\tilde{P} = M_{(n)} + \left[M_{(n)} Q \right] \tilde{S} \left[R M_{(n)} \right] \tag{5.1.6}$$

Note that there are only matrix-vector multiplications, some of which are used multiple times. We need 7 multiplications. Each of these takes $\mathcal{O}(n^2)$ multiplications. There are more efficient algorithms available but since $M_{(n)}$ changes often, none of these are applicable. The equations for the removal of a vertex follow as well:

$$\frac{\det M_{(n)}^{-1}}{\det M_{(n+k)}^{-1}} = \tilde{S} \tag{5.1.7}$$

$$M_{(n)} = \tilde{P} - \tilde{Q} \tilde{R} \tilde{S}^{-1} \tag{5.1.8}$$

Sometimes it can be useful to allow for multiple insertions/removals in a single step. This algorithm is still applicable but the matrix-vector multiplications become matrix-matrix ones. The advantage of multiple insertions at once is a faster and more stable exploration of the state space. For the cases considered in this thesis, the expansion order grows monotonic (proportional to the kinetic energy), this is however not guaranteed in general and can therefore lead to the Monte Carlo samplers being "stuck" (or slow down) at a certain expansion order, if only one additional vertex is added at a time[1].

In case of the CT-HYB solver, there are two subtleties to consider. The rows and columns are not added at the border of the matrix and one needs to consider anti-segment insertions and removals (which is a splitting of one segment into two). The first case generally introduces a factor of $(-1)^{i+j}$ because of $\det(PA) = \det(P)\det(A)$, for the insertion/removal at line i and column j. One uses that permutation matrices are orthogonal in order to find the necessary permutations of the inverse matrix:

$$P_\pi M = M_{\pi(i)\pi(j)}$$
$$\Rightarrow \left(P_\pi M \right)^{-1} = M^{-1} P_\pi^T$$
$$= M_{\pi(j)\pi(i)}^{-1}$$

This becomes especially simple in the case of the single orbital model when $i = j$ and $\pi(i) = 1, \cdots i - 1, n, i, \cdots$.

The anti-segment moves can be computed by first removing a row and column and then inserting two new ones for the insertion. For example, removing an anti-segment will have the following determinant ratio associated:

$$\frac{M_{(n-1)}^{-1}}{M_{(n)}^{-1}} = \begin{cases} \dfrac{M_{(n-2)}^{-1}}{M_{(n)}^{-1}} \dfrac{M_{(n-1)}^{-1}}{M_{(n-2)}^{-1}} & \text{if } n \geq 2 \\[2mm] \dfrac{M_{(0)}^{-1}}{M_{(1)}^{-1}} \dfrac{M_{(1)}^{-1}}{M_{(0)}^{-1}} & \text{if } n = 1 \\[2mm] \dfrac{M_{(1)}^{-1}}{M_{(0)}^{-1}} & \text{Empty to full line} \end{cases}$$

For this thesis, I used the permutation matrix modules provided by Eigen3 [55].

---

1 multiple update steps (with $n \pm 2$) had already been considered in the first publication of the CT-INT method but found to be unnecessary for simple applications which will be considered in this thesis [115].

5.2 CONVERGENCE STABILIZATION

Espcially in the coexistence region of the phase diagram, the self consistency cycle stabelizes very slowly or even diverges. There are some established methods to improve convergence in these situations:

The easiest but most costly method is mixing, where only a portion α of the new result is used for the next iteration.

$$G_{\text{loc}}^{(i)} \leftarrow \alpha G_{\text{loc}}^{(i)} + (1 - \alpha) G_{\text{loc}}^{(i-1)} \tag{5.2.1}$$

For the IPT solver the DMFT loop can be carried out quickly enough to disregard the performance impact of mixing but the CTQMC solvers do have a substantial run time atached.

It is therefore advantageous to use more sophisticated methods based on quasi-Newton methods[2] [139, 122]. For this thesis, I implemented two versions of Broyden's method [23, 12].

The action of the solver on the input in iteration n is denoted by:

$$G_{\text{out}}^{(n)} = \mathcal{S}\{G_{\text{in}}^{(n)}\} \tag{5.2.2}$$

The solver is converged under the condition $F_{(n)} \to 0$ with

$$F^{(n)} = G_{\text{out}}^{(n)} - G_{\text{in}}^{(n)} \tag{5.2.3}$$

The usual quasi-newton update method proposes a new imput as:

$$G_{\text{in}}^{(n+1)} = G_{\text{in}}^{(n)} - B^{(n)} F^{(n)} \tag{5.2.4}$$

$B^{(n)}$ is the inverse Jacobian of F. Broyden's method provides an approximation for B. There are two versions with similar accuracy but differing time complexity available. Since the DMFT loop only takes up a very small portion of the total runtime, the fast and less accurate version was only implemented for reference.

Both methods use the fast matrix update formula from the previous section.

$$\Delta G_{(n)} = G_{\text{in}}^{(n)} - G_{\text{in}}^{(n-1)} \tag{5.2.5}$$

$$\Delta F = F^{(n)} - F^{(n-1)} \tag{5.2.6}$$

$$B^{(n)} = B^{(n-1)} + \frac{\Delta G^{(n)} - B^{(n-1)} \Delta F_{(n)}}{\Delta G_{(n)}^{\dagger} B^{(n-1)} \Delta F_{(n)}} \Delta G_{(n)}^{\dagger} B^{(n-1)} \tag{5.2.7}$$

$$\tilde{B}^{(n)} = B^{(n-1)} + \frac{\Delta G_{(n)} - B^{(n-1)} \Delta F_{(n)}}{Y \Delta F_{(n)} Y} \Delta F_{(n)}^{\dagger} \tag{5.2.8}$$

5.3 MONTE CARLO ACCUMULATION AND NOISE REDUCTION

We have seen before that the Green's function can be obtained in Matsubara and imaginary time representation from the expansion matrix M at every step of the sampling process. It is however faster to accumulate a kernel like function $S(\tau)$ first and measure the Green's function after the Monte Carlo sampling [56]. S is approximated by a fine grid so that $S(\tau_k) \equiv S(\tau_l)$ for $\tau_k - \tau_l < \epsilon_S$. The discretization error

---

2 Mixing can be seen as a quasi newton method with an approximation of the Jacobian to $-\frac{1}{\alpha}\mathbb{1}$

introduced here is negligible when set against tail fit and fast Fourier transformation errors.

$$S(\tau) = \sum_{kl} \delta(\tau - \tau_k) M_{kl}^{\sigma} \mathscr{G}_0^{\sigma}(\tau_l) \tag{5.3.1}$$

$$G_{\sigma}(\tau) = \mathscr{G}_{0\,\sigma}(\tau) - \int_0^{\beta} d\tau' \mathscr{G}_{0\,\sigma}(\tau - \tau') \langle S^{\sigma}(\tau') \rangle_{MC} \tag{5.3.2}$$

$$G_{\sigma}(i\omega_n) = \mathscr{G}_{0\,\sigma}(i\omega_n) - \frac{\mathscr{G}_{0\,\sigma}^{-1}(i\omega_n)}{\beta} \left\langle \sum_{kl} e^{i\omega_n(\tau_k - \tau_l)} M_{kl}^{\sigma} \right\rangle_{MC}$$

$$= \mathscr{G}_{0\,\sigma}(i\omega_n) - \mathscr{G}_{0\,\sigma}(i\omega_n) \int_0^{\beta} e^{i\omega_n \tau} \langle S^{\sigma}(\tau') \rangle_{MC} \, d\tau \tag{5.3.3}$$

Using this binning procedure, we can introduce another improvement of the measurement. We first note that S is invariant under shifts of τ_k, τ_l. One can therefore add a random time to both on each update, thereby generating new samples on rejections steps:

$$S_{\sigma}(\tau) \sum_{kl} \delta(\tau - \tau_k + \tau') M_{kl}^{\sigma} \mathscr{G}_0^{\sigma}(\tau_l - \tau') \tag{5.3.4}$$

While this does require additional operations and prevents caching of the Weiss function, it does greatly reduce jitter resulting from high rejection rates, see also fig. 5.1. Another way to reduce noise is expansion into basis functions.
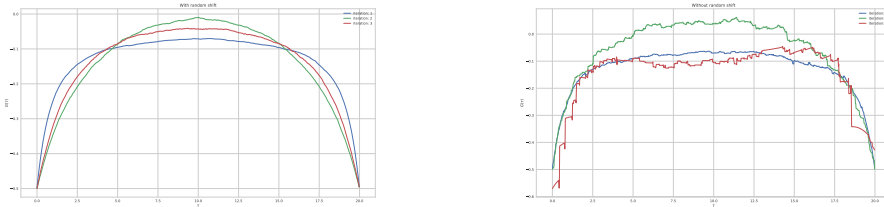

Figure 5.1: Impurity Green's function for three DMFT iterations. Left: random offset for S-bins enabled, right: disabled. The number of Monte Carlo sweeps is intentionally kept low (80000 samples) to make the difference more obvious.

This is especially important for the CT-HYB solver which does not ensure correct tail behavior. One therefore usually expands the solution in terms of Legendre polynomials $P_l(x)$ to enforce the correct tail [21]. The formulas in this section do not directly apply to the other solver types. Fitting the functions proved more time consuming for the CT-INT solver than increasing the number of samples to achieve comparable quality.

$$G(\tau) = \sum l \geq 0 \frac{\sqrt{2l+1}}{\beta} P_l(x(\tau)) G_l \tag{5.3.5}$$

$$G_l = \sqrt{2l+1} \int_0^{\beta} P_l(x(\tau)) G(\tau) \tag{5.3.6}$$

The coefficients c_m for the expansion in Matsubara moments can be obtained analytically as well, see appendix E [21].

$$c_1 = - \sum_{l \geq 0, \text{even}} \frac{2\sqrt{2l+1}}{\beta} G_l \tag{5.3.7}$$

$$c_2 = \sum_{l \geq 0, \text{odd}} \frac{2\sqrt{2l+1}}{\beta^2} l(l+1) G_l \tag{5.3.8}$$

$$\vdots \tag{5.3.9}$$

$$c_n = \frac{1}{\beta^n} \sum_{l \geq 0} t_{n,l} G_l \tag{5.3.10}$$

$$t_{n,l} = \begin{cases} (-1)^n 2\sqrt{2l+1} \frac{(n+l+1)!}{(n-1)!(l-n+1)!} & \text{if } n+l \text{ odd} \\ 0 & \text{else} \end{cases} \tag{5.3.11}$$

The knowledge of the analytic form of the tail coefficients can be used to obtain an analytic expression of the Fourier transformed Legendre coefficients:

$$G(i\omega_n) = \sum_l T_{nl} G_l \tag{5.3.12}$$

$$T_{nl} = (-1)^n i^{l+1} \sqrt{2l+1} j_l\left(\frac{\beta\omega_n}{2}\right) \tag{5.3.13}$$

It is possible to directly measure the impurity Green's function in terms of Legendre coefficients. We absorb the β anti periodic boundary conditions into the definition of the Legendre polynomials by redefining the Legendre polynomials:

$$\widetilde{P}_l(\tau) = \begin{cases} P_l(x(\tau)) & \tau > 0 \\ -P_l(x(\tau+\beta)) & \tau < 0 \end{cases} \tag{5.3.14}$$

with $x(\tau) = \frac{2\tau}{\beta} - 1$.
By using eq. 4.5.64, we immediately obtain the measurement coefficients G_l:

$$G_l = \left\langle - \sum_{ij} \frac{\sqrt{2l+1}}{\beta} \widetilde{P}_l(\tau)(\tau_i - \tau_j') M_{ij} \right\rangle_{\text{MC}} \tag{5.3.15}$$

The two particle Green's functions can be measured similarly for both methods [21].

5.4 FREQUENCY SUMMATION AND TAIL FIT

During the Monte Carlo runs, an array of averages for the Matsubara Green's function at a finite amount of frequencies is computed. Since the overall algorithm requires samples to be drawn from the imaginary time Green's function, but the self energy is extracted from the Matsubara Green's function during the DMFT loop, Fourier transformations are required.

As discussed before, the tail of the real frequency Green's function approaches $1/\omega$, which also applies to the Matsubara frequencies. This fact can be used to construct an explicit analytic tail expansion from relatively few frequencies. Many inaccuracies that are ostensibly the fault of insufficient or biased Monte Carlo sampling, can be traced back to bad treatment of the tail expansion. We will again encounter this

during the discussion of numerical methods for analytic continuation. There are several problems the following algorithm addresses:

precision: Due to the property $G^\star(i\omega_n) = G(-i\omega_n)$ (eq. 3.4.15) we expect the imaginary parts to cancel for the diagonal Green's function at half filling which coincides with eq. 3.4.14. The internal representation of floating point numbers tends to increase the rounding error in this case. Even more so for all sampling algorithms, when the tail values fall below the Nyquist threshold, the Fourier transformation will carry over that error to imaginary time [3].

discontinuity: The normal Fourier transform algorithms are badly suited for the metallic phase because the Matsubara Green's function exhibits a discontinuity at $G(i\omega_{-1}) \leftrightarrow G(i\omega_0)$.

performance: There is a performance drop with increasing number of Matsubara frequencies. Especially the accumulation and inversion of the self energy (not the Monte Carlo sampling itself) suffers, as well as the overall storage requirements. This can have a huge performance impact when the sampled Green's function becomes to large to be stored in fast memory (cache).

sampling: The CT-HYB Monte Carlo algorithm does not recover the correct tail behavior at high frequencies. When this is not the case, the analytic continuation becomes even more unstable. One therefore resorts to expansion in basis functions with the correct tail.

The central problem is the summation over Matsubara frequencies which occurs when transforming to imaginary time or during analytic continuation. We first consider an arbitrary function F of $i\omega_n$ and its Fourier transform $\widetilde{F}$ and expand F in powers of Matsubara frequencies.

$$\widetilde{F}(\tau) = \frac{1}{\beta} \sum_{-\infty}^{\infty} e^{-i\omega_n \tau} F(i\omega_n) \tag{5.4.1}$$

$$= \frac{1}{\beta} \sum_{-\infty}^{\infty} e^{-i\omega_n \tau} \sum_m \frac{c_m}{(i\omega_n)^m} \tag{5.4.2}$$

The naive approximation of only summing over the available samples of $\widetilde{F}$ will exhibit the above problems.

$$\sum_{n=-\infty}^{\infty} \rightarrow \sum_{n=N_{\min}}^{N_{\max}}$$

A better approximation is obtained by fitting a number of coefficients c_m from the available samples, evaluating the full Matsubara sum analytically and then using

---

3 This is an effect of finite lattice spacing in imaginary time. The Nyquist theorem limits the frequency resolution to $\omega_{nq} \geq \frac{\pi}{\Delta\tau}$ for any lattice spacing $\Delta\tau$ even for continuous time sampling.

the coefficients in the resulting series expansion of $\widetilde{F}(\tau)$ (for details of the evaluation see appendix [11]).

$$
\begin{aligned}
F(\tau) = & \frac{1}{\beta} \sum_{n=N_{\text{min}}}^{N_{\text{max}}} e^{-i\omega_n \tau} \left(F(i\omega_n) - \sum_m \frac{c_m}{(i\omega_n)^m} \right) \\
& + \frac{1}{\beta} \sum_{-\infty}^{\infty} e^{-i\omega_n \tau} \sum_m \frac{c_m}{(i\omega_n)^m} \\
\approx & \frac{1}{\beta} \sum_{n=N_{\text{min}}}^{N_{\text{max}}} e^{-i\omega_n \tau} \left(F(i\omega_n) - \frac{c_1}{(i\omega_n)} - \frac{c_2}{(i\omega_n)^2} + \cdots \right) \\
& - \text{sign}(\tau) \frac{c_1}{2} + \frac{c_2}{4}(2\tau - \beta) + \cdots
\end{aligned}
\tag{5.4.3}
$$

Usually few terms are enough to stabilize the Fourier transformation. In fact even the first one proved to be sufficient for most calculations. However, the convergence behavior did suffer from a lower amount of tail coefficients.

The inverse transformation is usually done using a cubic spline interpolation of $G(\tau)$. For the CT-INT sampler it turned out to be sufficient to skip the interpolation and work directly with the data of the first moment (see fig. 5.2 for example)[4]. But for the analytic continuation, to be discussed in the next section, this step is required to smooth out the data. The result, directly written in a usable form for the FFT algorithm (see last section), with N discrete points (see appendix C [16]), is:

$$
\begin{aligned}
G(i\omega) = & \frac{G(0) - \zeta G(\beta)}{i\omega_n} + \frac{S'(0) - \zeta S'(\beta)}{(i\omega_n)^2} + \frac{S''(0) - \zeta S''(\beta)}{(i\omega_n)^3} \\
& + \frac{1 - e^{i\omega_n \beta/N}}{(i\omega_n)^4} e^{i\omega_n \tau_j} \sum_{j=0}^{N-1} e^{i\omega_n \tau_j} S_{j+1}^{(3)}
\end{aligned}
\tag{5.4.4}
$$

with $S_i(\tau)$ being the cubic polynomial in the i-th interval.

While it is possible to measure both imaginary time and Matsubara Green's functions from the impurity solvers directly, we still need eq. 5.4.3 in order to obtain the input for the Monte Carlo impurity solvers from the DMFT loop.

Obtaining the coefficients c_i can be easily done by fitting the tail for example using least squares. In the case of the CT-HYB solver one usually directly accumulates the coefficients of Legendre polynomials [21]. This provides not only a more reliable way to obtain the Fourier transforms, but also smooths out statistical errors. Especially the hybridization and self energy function suffer from statistical error of the measured Weiss function:

$$
\Delta(i\omega_n) = i\omega_n + \mu - \frac{U}{2} - \left[\mathscr{G}_{0\sigma}(i\omega_n) \right]^{-1}
$$

Without a proper tail expansion, $\Delta(i\omega_n)$ and $\Sigma(i\omega_n)$ will be noisy at high frequencies because of a high relative error from the inverse of $\mathscr{G}_{0\sigma}(i\omega_n)$.

---

4 In the coexistence region of the phase diagram non interpolated data restricted the precision of the solver. However, due to time constraints in this thesis (the interpolation does require some performance optimization for this use), I decided not to implement the interpolation.
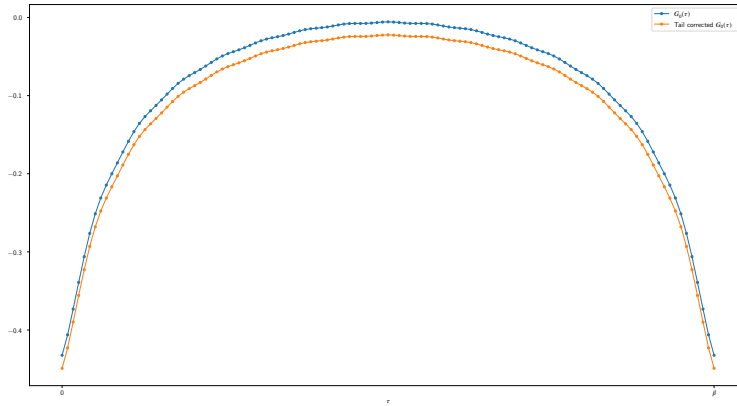
Figure 5.2: Comparison of tail fitted and non fitted impurity Green's function after Fourier transformation to imaginary time.

Expansion of the Weiss function results in the following tail approximation of the hybridization function (see also appendix B.4. [58]):

$$\Delta(i\omega_n) = \frac{\langle \epsilon \rangle^2 - \langle \epsilon^2 \rangle}{i\omega_n} + \mathcal{O}(\frac{1}{(i\omega_n)^2}) \tag{5.4.5}$$

$$\langle \epsilon^k \rangle = \int_{BZ} \epsilon^k \rho(\epsilon)\,d\epsilon \tag{5.4.6}$$

For example on the Bethe lattice with half bandwidth $D = 2t$, the integral can be solved analytically. The same is of course true for the cubic lattice which has a Gaussian DOS as shown in the previous section:

$$\rho_{\text{Bethe}}(\epsilon) = \frac{2}{\pi D}\sqrt{1 - \left(\frac{\epsilon}{D}\right)^2} \tag{5.4.7}$$

$$\langle \epsilon \rangle_{\text{Bethe}} = 0, \qquad \langle \epsilon^2 \rangle_{\text{Bethe}} = \frac{D^2}{4} \tag{5.4.8}$$

This can be confirmed by comparison of eq. 4.4.4 and eq. 4.3.22.

$$G(i\omega_n) = \frac{\Delta(i\omega_n)}{t^2} \tag{5.4.9}$$

The explicit integral for the moments is more controlled than a simple fit, but does offer a less smooth connection between measured data and tail fit.

In the program for this thesis I switched back and forth between both, without noticeable precision differences, see for example fig. 5.3. The most stable solution was obtained by mixing a few analytically obtained tail values into the fit procedure.
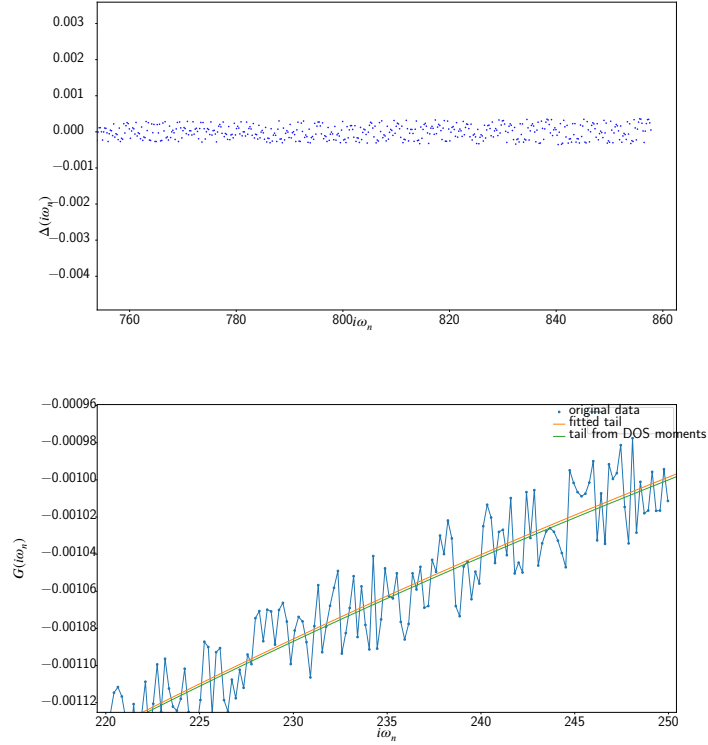
Figure 5.3: Tail fit for sampled Green's function at $\beta = 40$

The tail expansion of the self energy can be obtained as well, the usual particle-hole symmetrization which shifts μ by $\frac{U}{2}$ is assumed:

$$\Sigma_\sigma(i\omega) = \frac{c_{1,G} - c_{1,\mathcal{G}}}{(i\omega)^0} + \frac{c_{1,\mathcal{G}}^2 - c_{1,G}^2 - c_{2,\mathcal{G}} + c_{c,G}}{i\omega} \tag{5.4.10}$$

$$= U\left(\langle n_{\bar{\sigma}} \rangle - \frac{1}{2}\right) + \frac{U^2}{i\omega_n} \langle n_{\bar{\sigma}} \rangle (1 - \langle n_{\bar{\sigma}} \rangle) + \mathcal{O}\left(\frac{1}{(i\omega_n)^2}\right) \tag{5.4.11}$$

$$\overset{\mu=U/2}{=} \frac{U^2}{4i\omega_n} + \mathcal{O}\left(\frac{1}{(i\omega_n)^3}\right) \tag{5.4.12}$$

In practice, the tail coefficients are obtained by solving the following over determined equation:

$$\begin{pmatrix} f_1(x_1) & f_2(x_1) & \cdots & f_n(x_1) \\ \vdots & \vdots & \ddots & \vdots \\ f_1(x_m) & f_2(x_m) & \cdots & f_n(x_m) \end{pmatrix} \cdot \begin{pmatrix} c_1 \\ \vdots \\ c_n \end{pmatrix} = \begin{pmatrix} y_1 \\ \vdots \\ y_m \end{pmatrix} \tag{5.4.13}$$

f_l are the basis functions, i.e. $\frac{1}{(i\omega_n)^l}$ for raw data and Legendre polynomials for the smoothed CT-HYB data. c_l are the coefficients to be determined and y_k the measured data points. One usually specifies a range of tail data to use, depending on the Monte Carlo noise. The self energy and the hybridization function usually require a lower threshold than the impurity Green's function. This system is solved using Cholesky, QR or singular value decomposition which can handle near-singular coefficient matrices better in ascending order but require more computational effort

to do so.

For all calculations at half filling we can use the fact that the Matsubara Green's function is purely imaginary and only the first 4 coefficients have a significant contribution.

$$
\begin{pmatrix}
\frac{1}{i\omega_n} & \frac{1}{i\omega_n \cdot \omega_n^2} \\
\vdots & \vdots \\
\frac{1}{i\omega_m} & \frac{1}{i\omega_m \cdot \omega_m^2}
\end{pmatrix}
\cdot
\begin{pmatrix}
c_1 \\
c_3
\end{pmatrix}
=
\begin{pmatrix}
G(i\omega_n) \\
\vdots \\
G(i\omega_m)
\end{pmatrix}
\tag{5.4.14}
$$

For the inverse transformation the coefficient can be directly obtained form the data using eq. 5.4.3.

When the analytic form of the tail is known (such as $c_1 = \langle \epsilon \rangle^2 - \langle \epsilon^2 \rangle$ for the hybridization function), the right hand side is enlarged by a number of these data points to additionally suppress Monte Carlo noise. As mentioned before, setting the coefficients exactly to the tail values can result in problematic behavior due to the discontinuity between Monte Caro data and exact tail.

In fig. 5.4 and fig. 5.5 the effect of the tail fit after one transformation to imaginary time and back can be seen. Obviously, fitting the first coefficient is enough to supress problematic oscillations. The effect of second coefficient will typically lie below the noise amplitude of the data and can therefore often be set to zero.
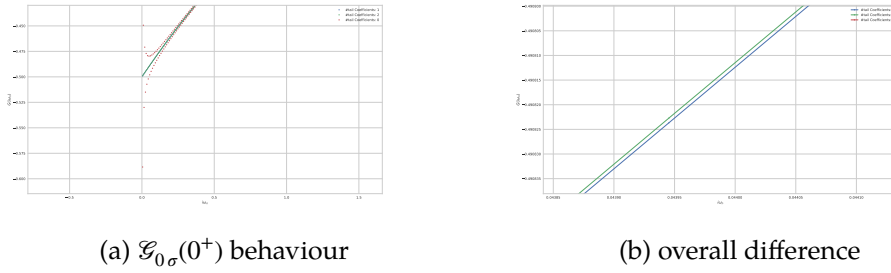

(a) $\mathscr{G}_{0\,\sigma}(0^+)$ behaviour

(b) overall difference

Figure 5.4: Imaginary time dependence on frequency tail fit. Compared are no fit, one and two coefficients for initial guess (no noise)

(a) Frequency tail fit with coarser grid of Matsubara frequencies

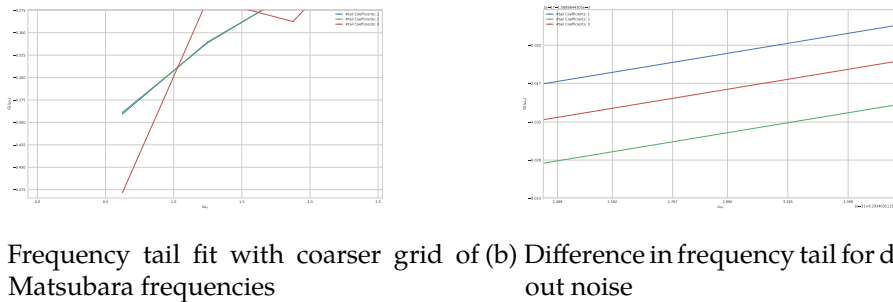(b) Difference in frequency tail for data without noise

Figure 5.5: Effect of tail fit on imaginary time and Matsubara Green's function

5.5   FAST FOURIER TRANSFORMATIONS

The transformation between Matsubara frequencies and imaginary time is closely related to traditional Fourier transforms. Naive transformations algorithms require $\mathcal{O}(n^2)$ operations for input and ouput of equal size n. A family of algorithms called fast fourier transformations (FFT) reduce the computational complexity to $\mathcal{O}(n \log n)$.

We will now look at the basic idea of these algorithms and then consider the transformation to the required input format.

FFT algorithms require equally spaced ($\Delta x = \frac{1}{\Delta f T}$) input points, which are then transformed into an output of equal frequency spacing Δf[5]. Let x_k be an array of n points, sampled in the interval $[0, nT]$. Then the continuous fourier transform reads:

$$f(k) = \int_{-\infty}^{\infty} f(t)\, e^{-ikt}\, \mathrm{d}t \tag{5.5.1}$$

is approximated by the discrete one:

$$f(2\pi k\Delta f) \approx T \sum_{r=0}^{n-1} f(rT)\, e^{\frac{2\pi i k r}{n}} \tag{5.5.2}$$

In the following, the Cooley-Tuckey (radix-2) algorithm is used as an example for a FFT algorithm. This version requires n to be a power of two. In the program I used the fftw3 library [41] which contains a number of different algorithms. The premise of certain input length numbers increasing the overall performance does carry over to the other algorithms (a list of these can be found in the documentation of fftw3).

$$f_k = \sum_{r=0}^{n/2-1} f_{2r} e^{\frac{-2\pi i k 2r}{n}} + \sum_{r=0}^{n/2-1} f_{2r+1} e^{\frac{-2\pi i k (2r+1)}{n}} \tag{5.5.3}$$

$$= \sum_{r=0}^{n/2-1} f_{2r} e^{\frac{-2\pi i k r}{n/2}} + e^{\frac{-2\pi i k}{n}} \sum_{r=0}^{n/2-1} f_{2r+1} e^{\frac{-2\pi i k r}{n/2}} \tag{5.5.4}$$

$$= g_k + e^{\frac{-2\pi i k r}{n/2}} h_k \tag{5.5.5}$$

Due to the periodicity of the Fourier transformation $g_{k+n/2} = g_k$ and $h_k = h_{k+n/2}$, f_k is calculated in $c \times n$ operations from $k/2$ samples of g_k and h_k:

$$f_k = \begin{cases} g_k + e^{\frac{-2\pi i k r}{n/2}} h_k & \text{if } k < n/2 \\ g_{k-n/2} - e^{\frac{-2\pi i k r}{n/2}} h_{k-n/2} & \text{if } k \geq n/2 \end{cases} \tag{5.5.6}$$

The decomposition is applied recursivly. The runtime complexity $T(n)$ is then given as[6]:

$$T(n) = 2T(n/2) + c \cdot n \tag{5.5.7}$$

$$= 2\left(T(n/4) + c(n/2)\right) + c \cdot n \tag{5.5.8}$$

$$= \cdots = c'\frac{n}{2} + cn \log n \tag{5.5.9}$$

$$= \mathcal{O}(n \log n) \tag{5.5.10}$$

In order to use the FFT algorithm we have to transform input and output accordingly. The following transformation has been adapted from the TRIQS package [99]. We define the lowest Matsubara frequency $\omega_0 = \frac{2\pi}{\beta}$ or $\omega_0 = -\frac{2\pi(n_{\min}+1)}{\beta}$ depending

---

5 Equal size of input and output can of course be forced by interpolation or zero padding.
6 Instead of expanding the recursion, one can directly obtain the runtime complexity from the master theorem for divide-and-conquer recurrences.

on storage. The lowest imaginary time[7] $\tau_0 = 0$. The FFT algorithm requires imaginary time and Matsubara Green's functions to be sampled over equally many points $N_\tau = N_\omega$ [8], with spacing $\delta\tau = \frac{\beta}{N_\tau}$ and $\delta\omega = \frac{2\pi}{\beta}$. At half filling one can use the (anti) symmetry to reduce storage cost. This has to be accounted for during transformation. The transformation from imaginary time to Matsubara frequencies, including the tail correction, is carried out as follows:

$$f_r = \left(G(\tau_0 + r\delta\tau) - \mathcal{F}\left[\text{Tail}\right](\tau)\right) e^{i\omega_0(\tau_0 + r\delta\tau)} \tag{5.5.11}$$

Now the FFT operates on f_r and returns f_n, which needs to be transformed before being stored as the Matsubara Green's function. With my choice of $\tau_0 = 0$ the phase factor is equal to 1:

$$G(i\omega_n) = \frac{\beta}{N_\tau} f_n e^{i\tau_0(\omega_n - \omega_0)} + \text{Tail}(i\omega_n) \tag{5.5.12}$$

An expression for the tail was derived in the previous section. The simplest form here is the subtraction of $\frac{c_1}{2}$ and after the FFT transformation, the addition of $\frac{c_1}{i\omega_n}$. The coefficient can be obtained from $G(\tau)$ and its derivatives. For example: $c_1 = G(0) - G(\beta)$, which is at half filling $c_1 = -2 \cdot f_0$.

For the inverse transformation the coefficients are obtained by SVD as explained in the previous section, the FFT and tail preparation read:

$$f_n = \frac{1}{\beta}\left(G(i\omega_n) + \text{Tail}(i\omega_n)\right) e^{-i\tau_0(\omega_0 + n\delta\omega)} \tag{5.5.13}$$

The FFT output is then transformed to obtain the imaginary time representation:

$$G(\tau_r) = \left(f_r\right) e^{-i\omega_0(r\delta\tau - \tau_0)} + \mathcal{F}\left[\text{Tail}\right](\tau) \tag{5.5.14}$$

The most important stability requirement for this transformation is the compliance with the Fourier inversion theorem. This was checked by transforming the free Green's function multiple times between both representations and measuring the overall error.

Starting from $N_\omega = N_\tau = 128$ to 4096 and all tail coefficients except the first one set to zero, the transformations did not introduce an error above 0.1% on each point. However, the lowest Matsubara mode suffers from a bad tail fit. So especially in the coexistence region when the solution slowly stabelize and the lowest Matsubara mode is the most important one for the physical solution, the coefficient number for the tail fit had to be adjusted.

5.6   ANALYTIC CONTINUATION

The nature of computers force us to use discrete quantities in our computations. Fortunately, Matsubara frequencies provide a natural grid for functions during simulations. To obtain observable quantitiesit is necessary to continue these functions

---

7 The choice of τ_0 is important because the tail fit depends on it. I found this choice to be more convenient, since one can enforce the limit $G_\sigma(\tau \to 0^+) = \langle n_\sigma \rangle$.

8 One can use interpolation to obtain these samples from grinds with different numbers of grind points. For this thesis, the grids were small enough to save two equally spaced grids.

back to real frequencies. The class of methods which will be presented here, are generally known as deconvolution algorithms.

$$F^R(i\omega_n) \longrightarrow F(\omega + i\eta)$$

Where the relationship between Matsubara representation and complex frequency is given by the Cauchy integral formula

$$2\pi i F(i\omega_n) = \oint_C \frac{F(z)}{z - i\omega_n} \, dz \qquad (5.6.1)$$

The contour has to be chosen appropriately. Since we know from eq. 3.3.13 that the tail decays as $1/z$, the integration of the real axis can be closed in the usual semi circle with the use of Jordan's lemma.

In order to compare results with experimentally accessible quantities we need to solve eq. 5.6.1 for $F(Z)$, from which we can obtain the retarded Green's function. Subsequently, one can calculate the spectral function by virtue of the Kramers Kronig relations (see eq. 3.3.11). By using the Kramers Kronig relations again and explicitly rewriting the Cauchy integral formula, we obtain the direct relations
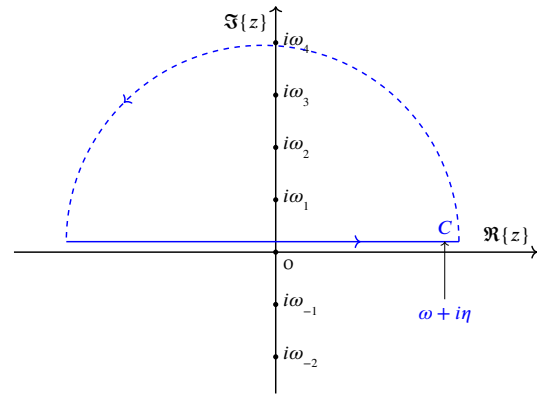
of eq. 5.6.1 for real and imaginary part of the retarded Green's function [11]:

$$G(z) = \frac{1}{\pi} \int_{-\infty}^{\infty} \frac{\Im\{G^R(\omega)\}}{\omega - z} \, dz \qquad (5.6.2)$$

$$= \frac{1}{i\pi} \int_{-\infty}^{\infty} \frac{\Re\{G^R(\omega)\}}{\omega - z} \qquad (5.6.3)$$

This is an inhomogeneous Fredholm equation of the first kind with kernel $K(\omega, z) = \frac{1}{\omega - z}$:

$$g(z) = \int_a^b K(\omega, z) F(\omega) \, d\omega \qquad (5.6.4)$$

Since the kernel only depends on the difference of the arguments (i.e. $K(\omega, z) = K(\omega - z)$) and the integral limits tend to infinity, there exists a formal solution in terms of the Fourier transforms of g and K (for brevity here $\tilde{g}, \tilde{K}$, details can be found in chapter 16 [7]):

$$f(\omega) = \int_{-\infty}^{\infty} \frac{\tilde{g}(x)}{\tilde{K}(x)} e^{2\pi i x \omega} \, dx$$

Instead of using the explicit solution, one may want to include the more general case without transitionally invariant kernel or Fredholm equations of the second

kind. This is also possible with a fairly simple approach: One can discretize the integral and the kernel[9] and obtains a system of equations [11]:

$$\pi G(i\omega_n) = \int_{-\infty}^{\infty} \frac{\Im\{G^R(\omega)\}}{\omega - \omega_n}\, d\omega$$

$$\approx \sum_m \frac{1}{2} \underbrace{\frac{\omega_{m+1} - \omega_m}{\omega_m - i\omega_n}}_{A_{nm}} \Im\{G^R(\omega_m)\}$$

$$\Leftrightarrow -A(\omega) \approx \frac{1}{2}\left[A^{-1} \cdot \left[G(i\omega_n)\right]\right]_m$$

with $\omega_n \subset R$ and $\left[G(i\omega_n)\right]$ denoting a column vector with Matsubara Green's function entries at frequencies $i\omega_n$ at entry n. The direct inversion method does however suffer from extremely poor noise tolerance. In practice one often uses either the Padé approximant of the unknown function or the maximum entropy method. The first one is a stable method for inputs with low signal to noise ratio while the latter greatly improves stability for noisy data such as results from Monte Carlo simulations, at the cost of clearly traceable error.
The Padé approximant of order m, n of a function f is given as:

$$P[f]_{M,N} = \frac{\sum_{i=0}^{M} a_i x^i}{1 + \sum_{i=0}^{N} b_i x^i} \tag{5.6.5}$$

The coefficients can be obtained by solving $f(z) = P[f]_{M,N}(z)$ (there are more efficient algorithms available [107]). One could now smooth out the sampled data, for example by choosing a suitable basis expansion (such as Legendre polynomials) of the functions or using noise reduction filters such as the Wiener filter. The commonly used alternative is however a less noise dependent algorithm called maximum entropy method (MEM), which can subsequently be improved by smoothing as well.
We first rewrite the kernel by transforming to imaginary time, assuming measurement data for which only a finite amount of Matsubara frequencies are available

$$G(\tau) \approx \widetilde{G}(\tau_n)$$

$$\widetilde{G}(\tau_n) = -\int_{-\infty}^{\infty} A(\omega) \sum_{n=n_{\min}}^{n_{\max}} \frac{1}{\beta} \frac{e^{i\omega_n \tau_n}}{\omega - \omega_n}\, d\omega$$

$$= -\int_{-\infty}^{\infty} A(\omega) K(\omega, \tau_n)\, d\omega$$

The sum over the kernel can be carried out explicitly. For the relevant case of this thesis (the particle hole symmetric fermionic one, see also table 3 [85] for other kernels) one obtains:

$$K(\omega, \tau_n) = -\frac{e^{-\tau_n \omega}}{1 + e^{-\omega\beta}}$$

$$K(\omega, \omega_n) = -\frac{\omega_n}{\omega_n^2 + \omega^2}$$

---

9 Here we use the rectangle rule. This method can be seen as a special case of the Nyström method for Fredholm equations of the second kind using the choice of weights acording to sections 19.0 to 19.3 [107].

For large ω the kernel becomes exponentially narrow and $A(\omega)$ therefore depends on minute details of $G(\tau)$. This can also be seen by considering the fact that $G(\tau)$ does not depend on $A(\omega)$ for large ω, which results in an ill conditioned inversion. The MEM takes advantage of two physical properties of the spectral function (see eq. 3.3.12)[10]:

$$\int_{-\infty}^{\infty} \frac{1}{2\pi} A(\omega)\, d\omega = 1 \qquad\qquad \text{Sum Rule} \qquad (5.6.6)$$

$$\begin{array}{ll} \text{Bosons:} & \text{sign}(\omega)A(\omega) \\ \text{Fermions:} & A(\omega) \end{array} \Bigg\} \geq 0 \qquad\qquad \text{Sign} \qquad (5.6.7)$$

We can identify the spectral function as a probability distribution and reformulate the inversion problem in terms of a maximum likelihood estimation, employing Bayes' theorem (eq. 2.1.6):

$$P\Big(A(\omega)|\widetilde{G}(\tau_n)\Big) = \frac{P\Big(\widetilde{G}(\tau_n)|A(\omega)\Big)\, p\,(A(\omega))}{P\Big(\widetilde{G}(\tau_n)\Big)} \qquad (5.6.8)$$

The left hand side is called posterior probability in this context, $p(\widetilde{G}|A)$ is the likelihood, $p(\widetilde{G})$ is the evidence and $p(A)$ is called prior probability. The average over M measurements of $\widetilde{G}(\tau_n)$ will be denoted as $\bar{G}_n$, which allows us to apply the χ^2 goodness of fit under a selected $A(\omega)$.

The likelihood function is assumed to be of Gaussian shape (validity of the CLT is assumed here). We propose some, for now completely randomly selected, trail $A(\omega)$ to compute $\widetilde{G}$:

$$P(\widetilde{G}|A) = e^{-\chi^2/2} \qquad (5.6.9)$$

$$\chi^2 = \sum_{ij} \Big(\widetilde{G}_i - \bar{G}_i\Big) C_{ij}^{-1} \Big(\widetilde{G}_j - \bar{G}_j\Big) \qquad (5.6.10)$$

$$C_{ij} = \text{Cov}[\bar{G}_i, \bar{G}_j] \qquad (5.6.11)$$

If the space of possible $A(\omega)$ is completely unrestricted, one may encounter over fitting (fitting to noise instead of actual features). This is counteracted by using a non-flat prior $P(A)$. In our case we select a so-called default model $m(\omega)$ and punish deviation from it. $S[A]$ is called entropy term.

$$S[A] = -\int \left(A(\omega) - m(\omega) - A(\omega)\ln\left(\frac{A(\omega)}{m(\omega)}\right) \right) d\omega \qquad (5.6.12)$$

$$P(A) = e^{\alpha S} \qquad (5.6.13)$$

S has a maximum when $A \equiv m$. The impact of this regularization term can be adjusted by tuning α.

Computation of the spectral function is done using for example Bryan's method [71]. In order to remove autocorrelation effects between data points and ensure data sufficiency, one has to carefully apply the methods discussed in sec. 2.7 and following. In addition the tails of Green's functions have to be taken care of with methods from

---

10 We do not consider broken time reversal symmetry here (which implies different signs), however there are generalizations available [110]

the previous section.

For this thesis I decided to use Maxent [85] which is part of the ALPSCore library [46]. This program has been demonstrated to work well with results from DMFT on the Hubbard model.

5.7   PROGRAM DESIGN AND ALGORITHMS

In this section I will give a brief overview over design choices and the various algorithms employed in the program for this thesis, including possible extensions over the sometimes naive proof of concept implementations. Some basic algorithms are already implemented in the boost library for `C++`.

The DMFT loop and impurity solvers have been implemented using `C++17`. The 2017 standard allows for more convenient use of templates, which have been used in order to shift as much computational effort as possible to the time of compilation. The use of templates and `constexpr` requires recompilation more often than would be necessary without their use, but greatly improves performance during runtime. This is of course only possible because the code is not supposed to be widely distributed.

The impurity solvers are implemented using the static polymorphism idiom

```
template<class derived>
class ImpuritySolver {};

class CTINT: public ImpuritySolver<CTINT> { ... };

class CTHYB: public ImpuritySolver<CTHYB> { ... };

template<class ImpuritySolver>
DMFT_LOOP(ImpuritySolver solver);
```

This allows for a universal interface of the existing implentations and makes implementation of new solvers easier, since one only needs to implement the interface without touching the DMFT loop itself. At the same time the usual downsides, such as overhead from function pointers and virtual functions, can be omitted.

In many numerical applications and especially for DMFT, the immediate evaluation of mathematical operations is worse than evaluation of a reshaped expression. For example the expression $\Sigma_{\mathrm{Imp}}(i\omega_n) = \mathscr{G}_{0\sigma}^{-1}(i\omega_n) - G^{-1}(i\omega_n)$ should not be evaluated to a final value if it is then immediatly added to the inverse local Green's function $G_{\mathrm{loc}}^{-1}(i\omega_n) + \Sigma_{\mathrm{Imp}}(i\omega_n)$, to avoid cancelation of floating point precision. I have discontinued the use of expression templates throughout the whole program during the development of the code due to time constraints. However, Eigen3 does use this concept internally and therefore most of the performance relevant operation incorporate lazy evaluation. The Green's function class could be updated in the future to support this again.

Most of the code has been documented in a style that can be read by doxygen for autmated generation of a readable pdf documentation. A doxygen config file is included in the project.

Parallelization has been carried out using the message passing interface (MPI), with boost as an intermediate layer for convenience[11]. The MPI threads are subdivided

---

[11] MPI is traditionally used in Fortran and C which do not support many of the high level features of `C++`. Boost provides a wrapper introducing more of these advanced features.

into generators and accumulators. For all test simulations in this thesis one accumulator (rank 0) has been sufficient. The generator processes each start their own Monte Carlo run including burn-in period. Special care has been taken to ensure that the pseudo random number generator produces uncorrelated pseudo random numbers for all processes. This has been done using the leapfrog scheme during startup of the program. The Monte Carlo data from all ranks is accumulated in the `MCAccumulator` class on rank 0. Rank 0 is also responsible for statistical evaluation and IO.

Evaluation of the data and plotting has been done with Python scripts and gnuplot. We expect to obtain very large amount of data sets for all Monte Carlo simulation, which we want to calculated without excessive loss of accuracy. One example is the naive calculation of the Monet Carlo average by summing over all samples of an observable and dividing by the average sign. Even if the total sum does not trigger an overflow (because we only divide by a huge number in the end of the summation), the samples towards the end of the simulation are not taken into account accurately. This is due to the nature of floating point storage on PCs which are stored as $x = \text{sign}\, m * 2^b$ with a total of 16, 32 or 64 bits for the total combined length of sign, mantissa and exponent. The total sum is stored as a normal floating point number with a large exponent and small mantissa, that means large error relative to the total average and expected value of the sample. This effect occurs relatively quickly for fast sampling algorithms like CT-INT and often leads to "false convergence", i.e. the average converges because the total sum does not change anymore when new samples are below the significant bits of the mantissa. Products of very small or large quantities $\prod_i x_i$ are even more unstable, the most prominent of which is is the computation of a likelihood function which is required by the Maximum entropy method. In some cases there is an easy remedy available. One uses the so called log-sum-exp trick:

$$\log \sum_i e^{x_i} = \max(\{x_i\}) + \log \sum_i e^{x_i - \max(\{x_i\})} \tag{5.7.1}$$

The subtraction of the maximum does not only ensure that no overflow can occur, but also that for any underflow, the leading digits are correctly computed. This trick is also occasionally applied to sums by applying the logarithm on both sides.

Another option are one-pass online algorithms for the caluclation of such quantities. We have already seen one such example in fig. 2.12 with a logarithmic binning tree. Popular examples for the improved calculation of mean and variance were developt by P. B. Welford and more recently P. Pébay [131, 102]. Pébay's method allows for the computation of arbitrary moments and covariance. For this thesis I tested Kahan summation and Pébay's rolling mean and variance. The difference in accuracy to the boost Accumulator implementation was not noticable for reasonably long runs. I therefore chose the boost implementation due to a higher level of optimization.

For the segment representation of the hybridization expansion I used a naive implementation of the overlap calculations. This already proved to be a substantial bottleneck. Going beyond the single orbital model increases this problem even more. There is a standard algorithm for this problem available. The segments are stored in a so called interval tree: Interval trees are binary trees with each node containing start and endpoint of the interval $[a, b]$. The ordering can be done using the start point of the intervall, i.e. right child node has $[a_r, b_r]$ with $a_r > a$ stored. We need to

define four operations on this data structure: insertion, removal, search of segments and rebalance. Rebalancing is a standard operation. Insertion and removal should return the change in total overlap or fail if the segment falls inside of another one. Both insertion and removal can be done in $\mathcal{O}(f \log n)$ for f flavors and n segments by traversing the tree. A concrete implementation for the ALPS library [46] has been proposed by E. Gull (chapter 7 [57]).

There are several computationally expensive functions that need be computed repeatedly. The most prominent example being the complex exponential. A usual method for performance improvement is to store values for the function on a fine grid. For the purposes of testing the speedup of such an optimization, I implemented a function memoizer. This class uses the template capabilities of C++14 and newer to build a hash map for function calls, which are not executed on a subsequent calls with the same parameters. Instead, the previously stored return value is returned in $\mathcal{O}(1)$ operations, using hash table lookups. The class takes a callable [12] and stores a hash map with the arguments of the function as lookup keys. There is little to no computational overhead from the function storage[13] itself since no function pointers are used in favor of template matching at compile time. Even though this is slightly less efficient than an explicit storage, this template can be used with almost no additional programming effort, because the Memoizer must only be initialized once with `auto g = Memoizer(f);` and the function can then be used as before.

For the evaluation of the local Green's function an integration routine was implemented[14]. For my tests one the hypercubic lattice I implemented Riemann summation, Gauss-Legendre integration and alg. 9. These provided reasonable performance. For more realistic calculations one can resort to specialized method such as linear tetrahedron [73] or discrete Hilbert transforms. There is a method for discrete Hilbert transformation using fast Fourier transformations available[117]. Using the

---

input : $f(x)$, FFT and IFFT function
output: Hilbert transform of f

1   $\tilde{f}(\omega) = \text{FFT}[f]$
2   $\tilde{r}(\omega) = \text{FFT}[r]$
3   **foreach** ω *on the grid* **do**
4      $\tilde{H}(\omega) = \tilde{f}(\omega) \cdot \tilde{r}(\omega)$
5   **return** iFFT$[\tilde{H}]$

Algorithm 9: Saito's method for discrete Hilbert transforms

definition of the hilbert transform 4.2.12, we let f be the input for the hilbert transformation, then the algorithm for $H(f)(s)$ is given in alg. 9. We need an auxiliary function over the same support as Ω and discretized on an equal grid as f with spacing Δx:

$$r(x) = \frac{1 - \cos\left(\frac{\pi x}{\Delta x}\right)}{\pi x}$$

---

12   due to 14 standard compliance, conecepts could no be used. Therefore a pattern matching template has been used
13   The memory requirements of course depend on the memoized function
14   This module is not needed for computations on the Bethe lattice because of the algebraic equation that conencts impurity and Weiss Green's function.

This results in alg. 9 which has been tested to give results comaprable to the Gauss-Legendre integration.

5.8 LIBRARIES AND SOFTWARE PACKAGES

The solver implemented during this thesis uses a number of libraries and sub programs. following is a list of all major components. Software required to run the

Table 5.1: Software dependencies

Name	Purpose
FFTW [41]	Fast Fourier Transformation
easyloggingpp [83]	Logging
Faddeeva Package [72]	Evaluation of error function
Eigen3 [55]	Vector, Matrix operations and storage, SVD Fitting
GNU scientific library [47]	various mathematical operations
gnuplot [136]	plotting
Gnuplot io [120]	gnuplot interaction
trng [13]	pseudo random number generation
openMPI [45]	parallelization
boost	Filesystem interaction, Statistics, Data accumulation, MPI
ALPSCore [46]	Maxent requirement
Maxent [17]	analytic continuation
doxygen	automated generation of documentation from comments

solver: C++17, the 2017 standard is required due to use of templates, constexpr, type deduction and nested namespaces. Python2.7+ including following packages: NumPy, matplotlib, seaborn, scipy, uncertainties. The Python scripts are required for data evaluation and as glue language to auxilliary software.

RESULTS

6.1 ITERATED PERTURBATION THEORY

There are several analytic approximation for the impurity problem at different energy scales available. Examples are the slave boson method with mean field or non crossing approximation and iterated perturbation theory (IPT) (chapter VI B [51]). I will use IPT due to its simplicity to get a rough overview of the phase diagram for the Hubbard model on the Bethe lattice, before finding more precise results using Monte Carlo methods. Because the solver consists of only a few algebraic equations, this will also demonstrate the correct behavior of the DMFT loop.

IPT is obtained from the weak coupling approximation in powers of U, of the self energy from the Anderson impurity model up to second order. If not otherwise noted U is given in units of the half bandwidth D.

Using eq. 3.6.20 for the self consistency equations on the Bethe lattice with the Weiss function as propagator, we find:

$$\Sigma_\sigma(i\omega_n) \approx \Sigma_\sigma^{(2)}(i\omega_n) = Un + U^2 \int_0^\beta e^{i\omega_n\tau} \big(\mathcal{G}_{0\,\sigma}(\tau)\big) \mathcal{G}_{0\,\bar\sigma}(-\tau)\mathcal{G}_{0\,\bar\sigma}(\tau)\, \mathrm{d}\tau + \mathcal{O}(U^3) \quad (6.1.1)$$

$$\xrightarrow{\mu=\frac{U}{2}} \frac{U}{2} + U^2 \int_0^\beta e^{i\omega_n\tau}\big(\mathcal{G}_{0\,\sigma}(\tau)\big)\, \mathrm{d}\tau + \mathcal{O}(U^3) \qquad (6.1.2)$$

The second line holds for particle hole symmetry in the half-filling case. The IPT scheme above is exact in the atomic limit for which $\mathcal{G}_{0\sigma}^{-1}(i\omega_n) \approx i\omega_n$ (compare eq. 1.3.11, replacing the free Green's function with the Weiss function). There is a more involved scheme which is valid away from half filling and exact in both atomic and non interacting limit [9]:

$$\Sigma(i\omega_n) = U\frac{n}{2} + \frac{A\Sigma^{(2)}(i\omega_n)}{1 - B\Sigma^{(2)}(i\omega_n)} \qquad (6.1.3)$$

$$A = \frac{n(2-n)}{n_0(2-n_0)} \qquad B = \frac{(1 - n/2)U + \mu_0 - \mu}{\frac{n_0}{2}(1 - n_2/2)U^2} \qquad (6.1.4)$$

$$n_0 = 2\mathcal{G}_{0\,\sigma}(\tau \to 0^-) \qquad n = 2G_\sigma(\tau \to 0^-) \qquad (6.1.5)$$

The remaining parameter μ_0 has to be obtained for example by fixing $n_0 = n$ or $\mu = \mu_0$. One can also use the easily obtainable (from CTQMC) double occupancy $D = \langle n_\uparrow n_\downarrow \rangle$ and the relation (see [9] and eq. 4.5.30):

$$D = \frac{1}{\beta U} \sum_n e^{i\omega_n 0^+} \Sigma(i\omega_n)G(i\omega_n) \qquad (6.1.6)$$

The extended IPT scheme was not implemented for this thesis since the normal perturbation scheme is sufficient in order to validate the DMFT loop.

DMFT provides us with the impurity self energy and Green's function as observables, in our case in imaginary frequency and time. In order to find the metal to

insulator phase transition the immediate observable would be the gap Δ_g around the Fermi level in the spectral function.

$$A(x) = 0, x \in \left[-\Delta_g, \Delta_g\right] \tag{6.1.7}$$

However, observables obtained from the analytic continuation are less reliable because the algorithm does not only dependent on the data but also the default model, data error and quality of the tail. Additionally, the scaling of the spectral gap with increasing interaction strength is not immediately obvious while other observables are known to scale (inversely) linear to $|U - U_c|$ in the context of DMFT (see Section D.6 [65]). These are the mass renormalization factor Z, the inverse effective mass, $(m^\star)^{-1}$ and the inverse specific heat coefficient γ^{-1}.

For this reason I found it more reliable to use observables such as double occupancy which can be directly measured during the Monte Carlo runs and the quasi particle weight $Z = \left[1 - \frac{\partial \Re \Sigma(\omega)}{\partial \omega}\Big|_{\omega=0}\right]^{-1}$. Lastly, one can also use the singularity of the imaginary part of the self energy at $\omega = 0$: ρ_2 as associated order parameter for the phase transition [51]

$$\frac{1}{\rho_2} = \int_{-\infty}^{\infty} \frac{\rho(\epsilon)}{\epsilon^2} \, \mathrm{d}\epsilon \tag{6.1.8}$$

The qualitative behavior of the phase transition from low to high U values starts from a single coherent peak in the spectral function, over a triple peak with two incoherent and one coherent band, to the Mott insulating solution with only the incoherent bands remaining. This transition is shown in fig. 6.1 for $\beta = 40$.
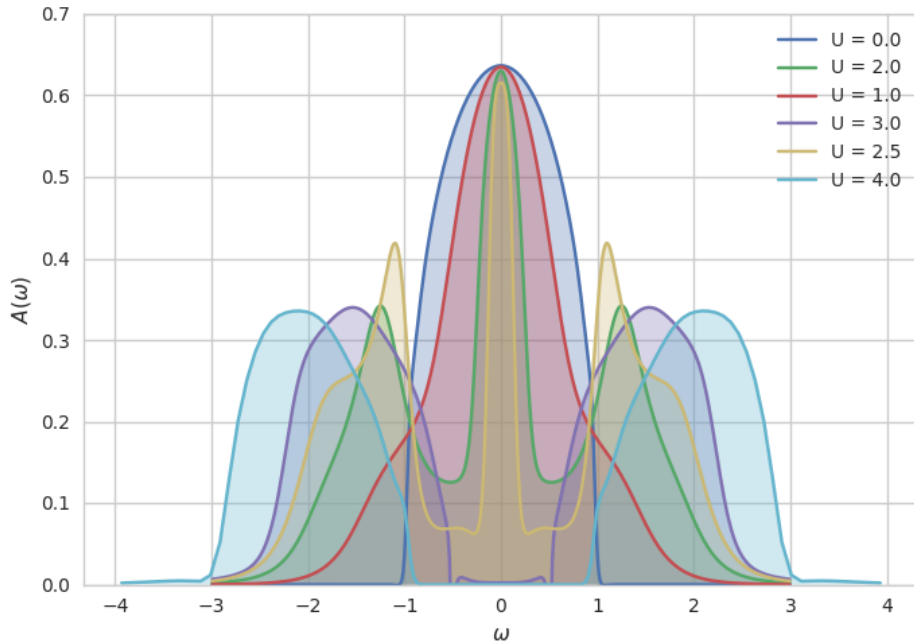

Figure 6.1: Spectral function for $\beta = 40$ with U in units of D. Analytic continuation with Padé approximation.

$$A(\omega = 0) = \rho(0) \tag{6.1.9}$$

While the width of the coherent band shrinks and the Mott gap pre-forms, the height remains the same at low temperatures. This behavior is characteristic for systems that fulfill the Luttinger theorem. In general Luttinger's theorem is only applicable at $T = 0$ and correct values for the effective chemical potential (see [9]). At finite
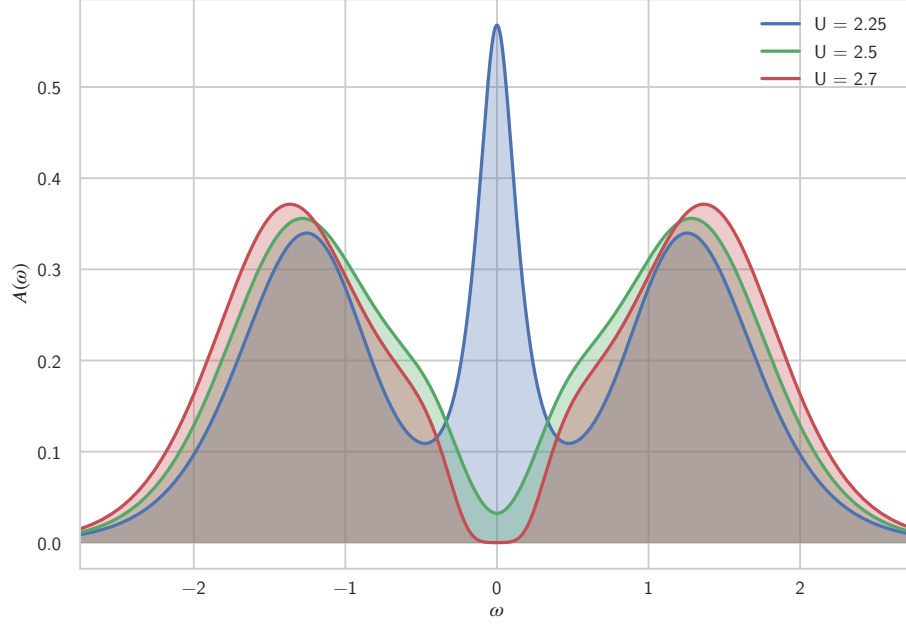

Figure 6.2: Spectral functions for $\beta = 50$, quasi particle peak disappearing before insulating phase is reached.

temperature the Luttinger theorem is not fulfilled and the quasi particle peak does not vanish discontinuously. This means the preformed gab does have some spectral weight left, see fig. 6.2. Especially for Monte Carlo simulations the convergence has to be ensured when obtaining such a result because it is also characteristic for not fully converged solutions. We can also see the preformed gap starting at $U = 2$, the $U = 3$ solution exhibits unphysical weight around the fermi surface originating from the Padé approximation. The Mott transition is known to be of first order with a coexistence region $U_{c1} < U < U_{c2}$ at finite temperature [51, 96]. In the coexistence region there are two allowed solutions, one of which can be continuously connected to the metallic, the other one to the insulating solution at $T = 0$. The coexistence region disappears at temperatures above $\beta_c \approx 10$ [114]. In fig. 6.2 we can observe the breakdown of the Fermi liquid behavior for $U > U_{c2}$ for solutions with initial guesses in the metallic phase. Insulating solutions become metallic for $U < U_{c1}$. This hysteresis is characteristic for first order phase transitions. To find the valid regions for the Fermi liquid behavior, we use eq. 3.7.8. The lowest 6 Matsubara frequencies of the self energy are fitted to a polynomial of degree 4. With it, we can approximate $\Sigma(0)$ and $\partial\Sigma(\omega)/\partial\omega\big|_{\omega=0}$. In the Fermi liquid region both values should be close to 0. The relative noise at low Matsubara frequencies prevented very accurate predictions. In my experience the resulting data was limited to four
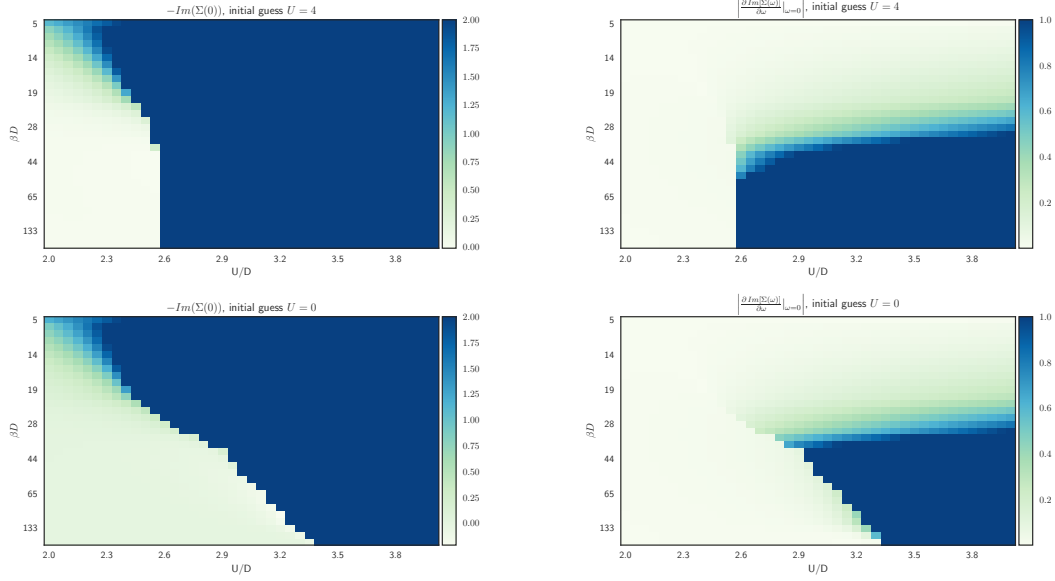
Figure 6.3: Plot of Fermi liquid assumption validity as function of β and U for initial guess in metallic ($U = 0$) and Mott insulating ($U = 4$) phase. Note that the initial guess should not guarantee to stabilize the corresponding solution in the coexistence region. This means there is an additional error in this region of the phase diagram. However, IPT solutions do depend on the initial guess. The values are clipped at 2 for better visualization. U is given in units of half bandwidth D.
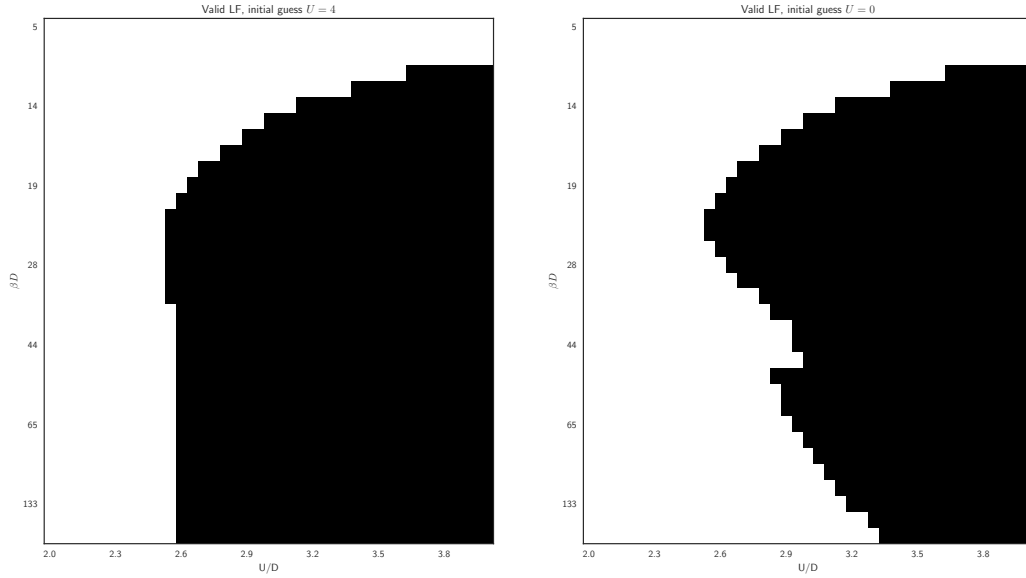
Figure 6.4: White region marks valid Fermi liquid region according to eq. 3.7.8 and fig. 6.3 for each of the two possible solutions.

decimal places by noise when using double precision floating point numbers. However, the resolution is good enough to estimate the valid regions, especially since Z is expected to approach 0 at the phase boundary. The imaginary part of the self energy as well as its derivative are plotted as function of temperature and interactions strength in fig. 6.3. Both are zero for small values of U. There is a sudden jump
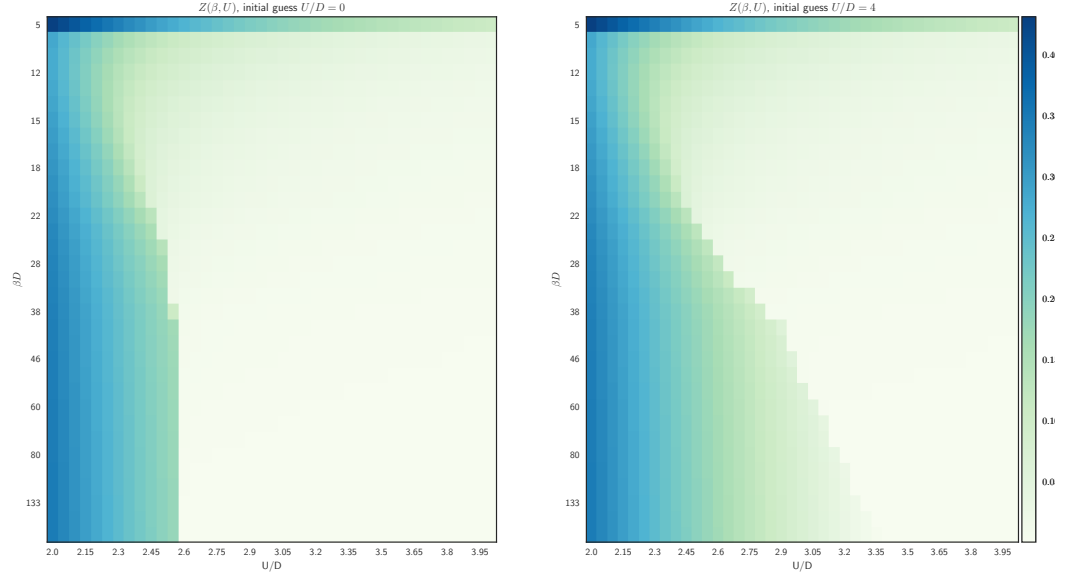
Figure 6.5: Z as function of temperature and interaction strength obtained from iterated perturbation theory, with 80 convergence steps and 200 additional steps to obtain statistics. Initial guesses in the different phases stabilize corresponding solutions in the coexistence region.
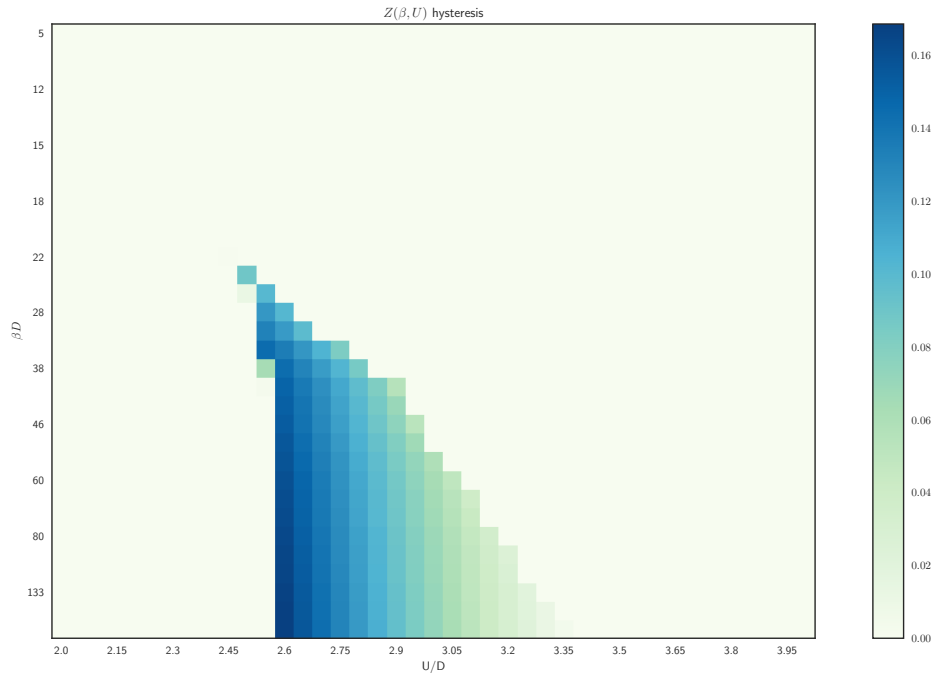

Figure 6.6: Difference between the solutions obtained with initial guesses $U = 0$ and $U/D = 4$: $Z = Z_{U0} - Z_{U4}$.

to finite values for $U > U_c$ at the Mott transition. Even though Z is not an order parameter, we can now use it to distinguish the phases and plot the phase diagram of the Hubbard model at half filling using the IPT solver. This is shown in fig. 6.5 for initial guesses in both phases. One can also see the crossover region in the high temperature regime at $\beta = 1/5$.

A clearer view of the coexistence region is obtained by subtracting both solutions, see fig. 6.6. As previously noted, $Z \sim |U - U_c|$, which we can use to extrapolate the hysteresis to zero temperature. This is shown in fig. 6.7.

The solutions in the coexistence region stabilize slowly in comparison to the rest of the phase diagram. Especially near the critical point, here at $T \approx 0.05$, $U/D \approx 2.5$ the results have a large error attached. Additionally one can run into a two-cycle (the measurement alternates between the two possible solutions). This is a well known phenomenon near quantum phase transitions, called critical slowing down [122]. Stabilization methods are discussed in sec. 5. Both the critical point as well as zero temperature estimates, agree with previous results [51]. From fig. 6.7 we can estimate the critical interactions strengths $U_{c1} = 2.6 \pm 0.05$ and $U_{c2} \approx 3.3 \pm 0.05$. The shape of the coexistence region for finite temperatures fig. 6.6 shows also that $U_{c1}(T)$ has a lower temperature dependence than $U_{c2}(T)$.
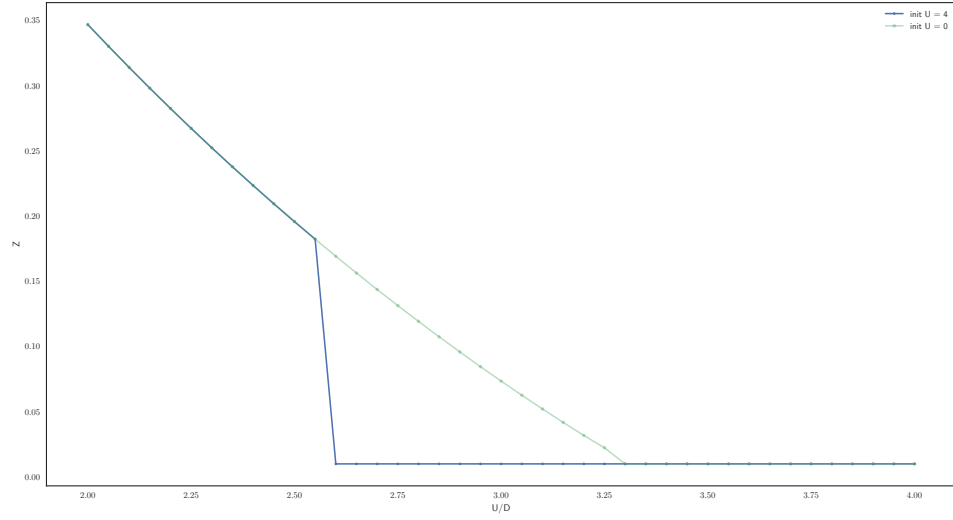
(a) $Z(U)$ with metallic and insulating initial guess.
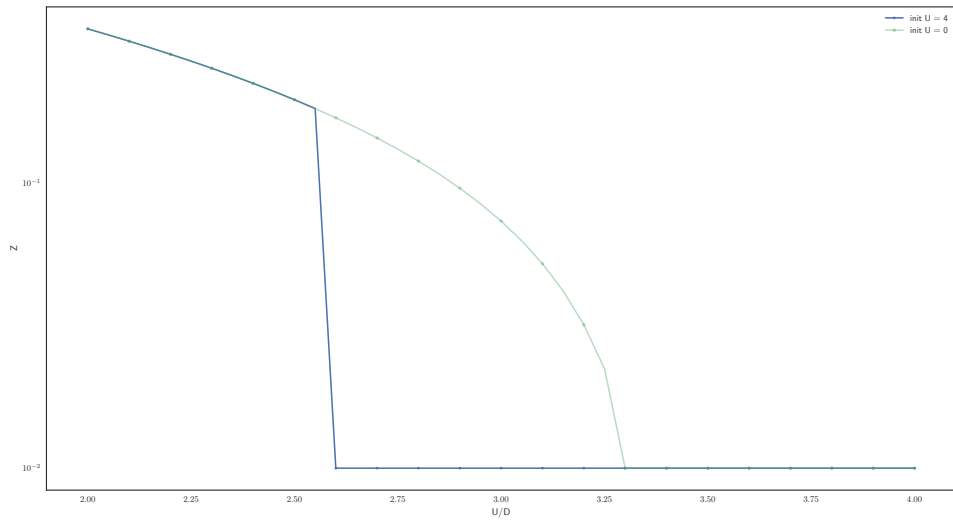
(b) $\log(Z(U))$ with metallic and insulating initial guess.

Figure 6.7: Hysteresis of $Z(U)$. Noise was filtered by clipping values of Z smaller than 10^5.

6.2   MONTE CARLO RESULTS

For Monte Carlo solvers, the quasi particle weight is less useful due to the noise in the element wise inversion needed to obtain the self energy. Instead one can use
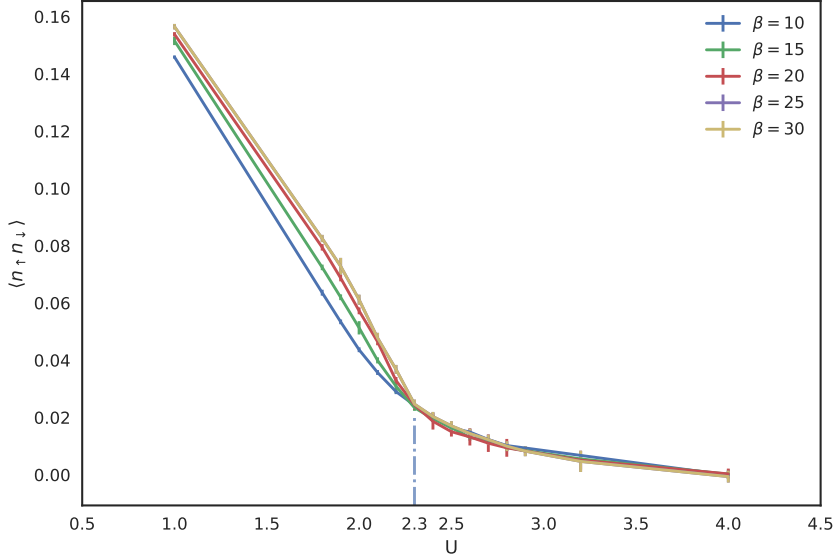
(a) Double occupancy for $T = 1/30$ to $T = 0.1$ (supercritical), onset of crossover at $U/D = 2.4 \pm 0.1$
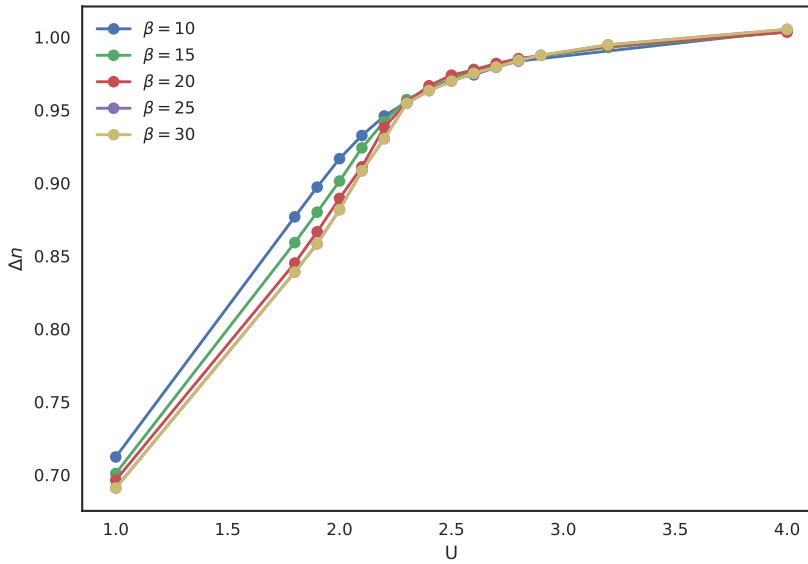
(b) Local moment for $T = 1/30$ to $T = 0.1$

Figure 6.8: local moment and double occupancy for $T = 0.03$ to $T = 0.1$

the expansion order to directly compute the double occupancy and therefore has a high accuracy (see eq. 4.5.29).

$$\langle n_\uparrow n_\downarrow \rangle = \frac{\langle n_\uparrow \rangle + \langle n_\downarrow \rangle}{2} - \frac{\langle n_{\text{MC}} \rangle}{\beta U} - \frac{1}{4} + \epsilon^2 \qquad (6.2.1)$$

At half filling the first term is equal to 1/2 and $\epsilon = 0.5 + 0^+$.

We have seen in chapter 1 (see discussion around fig. 1.3) that the occurrence of the local moment is a good characterization for the Mott insulating phase.

The parameters for the Monte Carlo simulation need to be adapted depending on the temperature and interaction strength. In fig. 6.8 the double occupancy for different supercritical temperatures is shown. In order to decrease autocorrelation times,
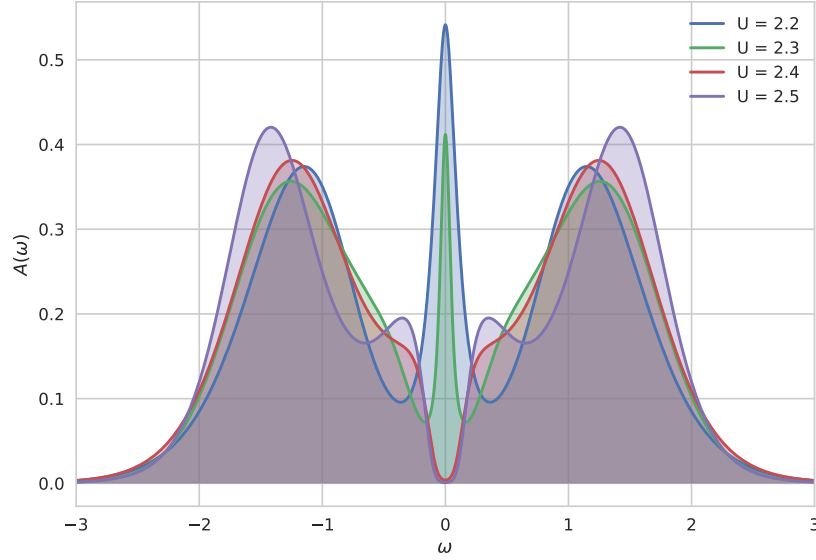

Figure 6.9: Phase transition using CT-INT at $\beta/D = 30$, initial guess $U = 0$. 4×10^7 MC steps, 4096 Matsubara frequencies, no skipping of data points (Measurement after each MC step), Broyden mixing (good), 30 DMFT loops

the impurity Green's function measurement is only done every 30 to 150 Monte Carlo steps, depending on the temperature and proximity to the coexistence region. The number of steps was found to be sufficient at 10^7 to 10^8 samples near the coexistence region. The number of DMFT loop iterations heavily depends on the interaction strength and mixing type. I found anything between 10 and 80 iterations to be sufficient. As expected from the literature the IPT solver overestimates the transition temperature. From fig. 6.9 we already see, that U_c is lies around $U_{c2}/D \approx 2.4 \pm 0.1$ instead of $U_{c2}/D \approx 3.0 \pm 0.1$. However, the temperature of the critical point is also overestimated by IPT. There is no visible hysteresis at $T = 1/30$ but an onset of the transition can be seen at around $U/D \approx 2.3$, see fig. 6.8. In fig. 6.12 the hysteresis of the double occupancy at $T = 0.02$ is shown. This was the highest temperature for which I obtained consistent results. In fig. 6.13 a rough estimation of the phase diagram is shown. All data points were obtained without mixing, $30 \cdot 10^7$ to $50 \cdot 10^7$ Monte Carlo samples and 35 to 60 DMFT iterations. They were obtained on a 4 core PC and took about one to eight hours to converge each. The results are not all converged desirably well due to limited computational recources. Therefore the estimated phase transition lines have an error of $\pm 0.03\, U/D$ attached. Only the mean is plotted here. The phase diagram is nonetheless consistent with previous results [74].
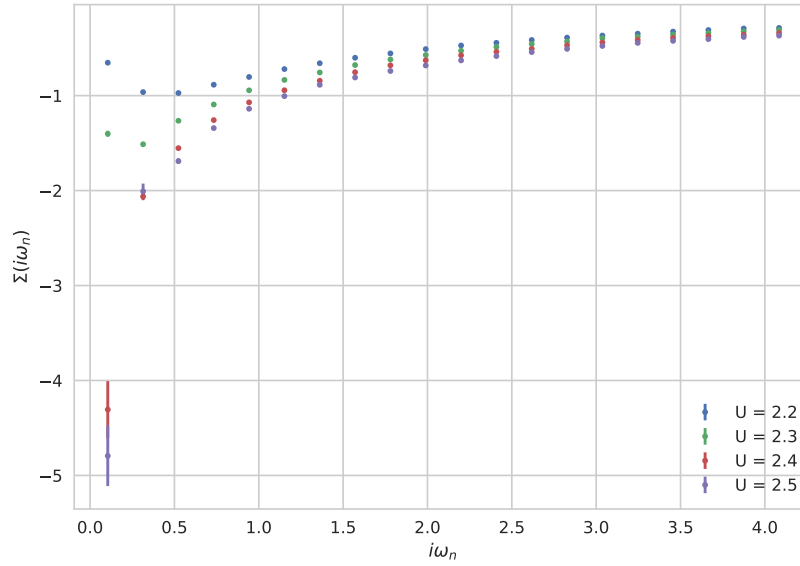
(a) Self energy at $\beta/D = 30$
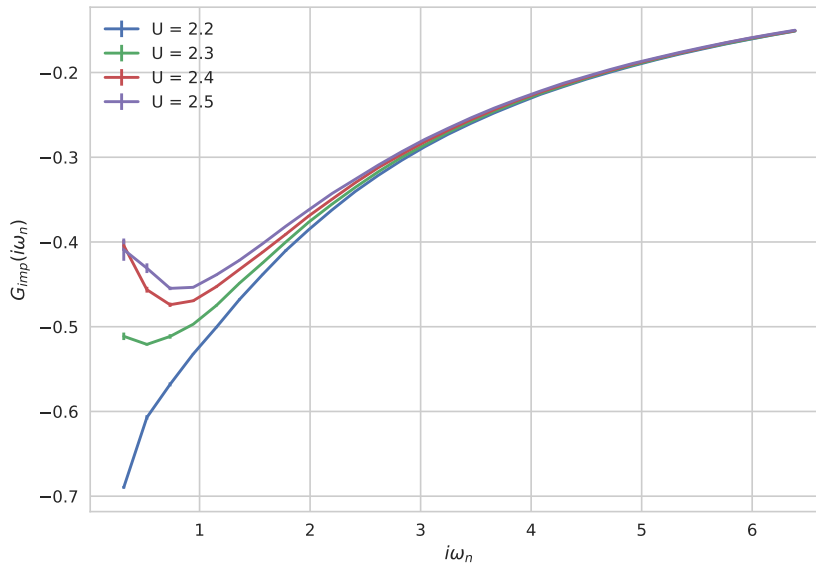
(b) Impurity Green's function at $\beta/D = 30$, note the badly converged lowest Mode of $U = 2.5$. The maximum entropy method accounts for such errors.

Figure 6.10: Self Energy and Impurity Green's function at $\beta/D = 30$

(a) $\beta = 50$, initial guess $U = 0$

(b) $\beta = 50$, initial guess $U = 3.2$

(c) $\beta = 60$, initial guess $U = 0$

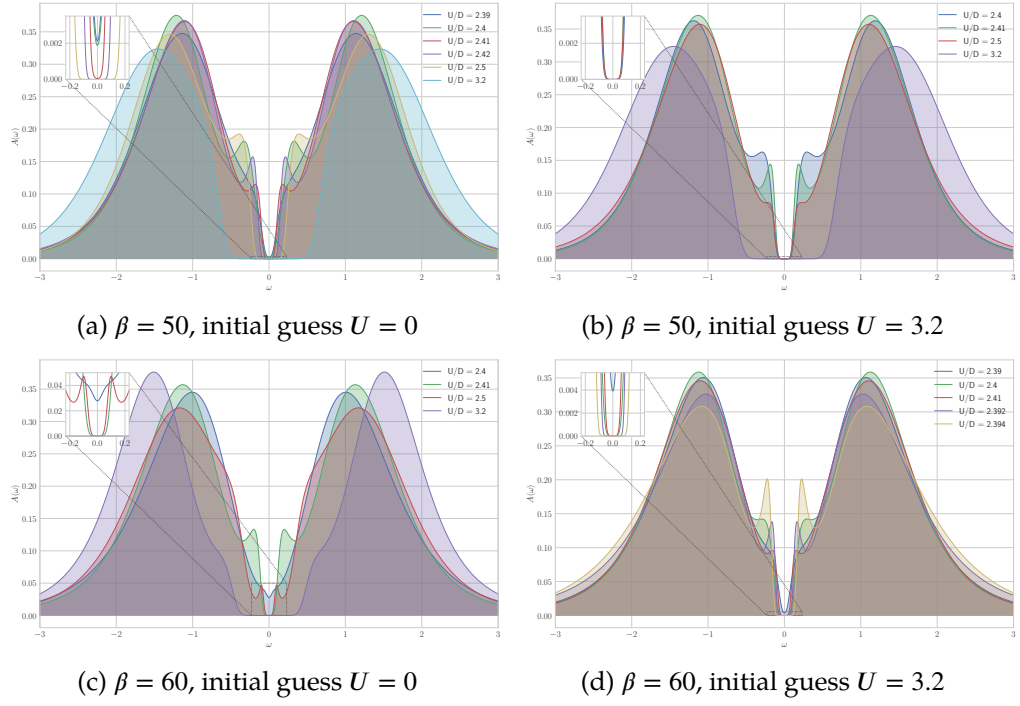(d) $\beta = 60$, initial guess $U = 3.2$

Figure 6.11: $3.5 \cdot 10^7$ samples, skipping of 150 MC steps between measurements, no mixing

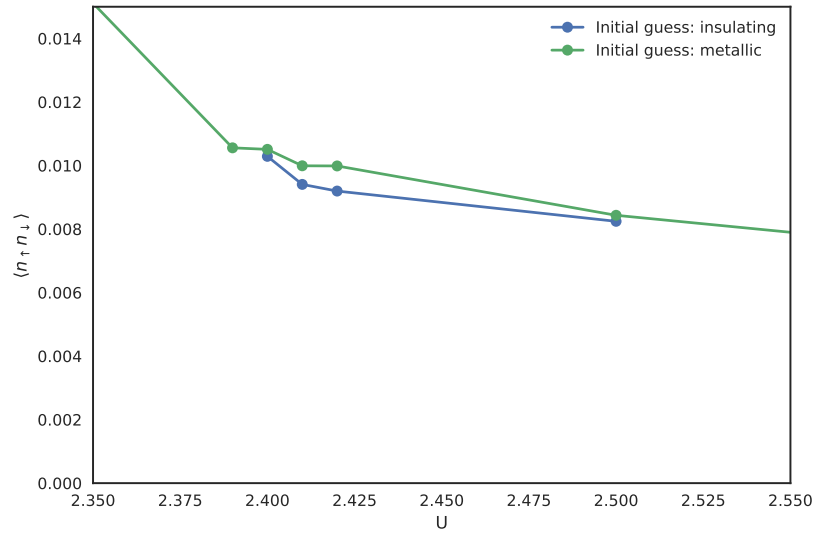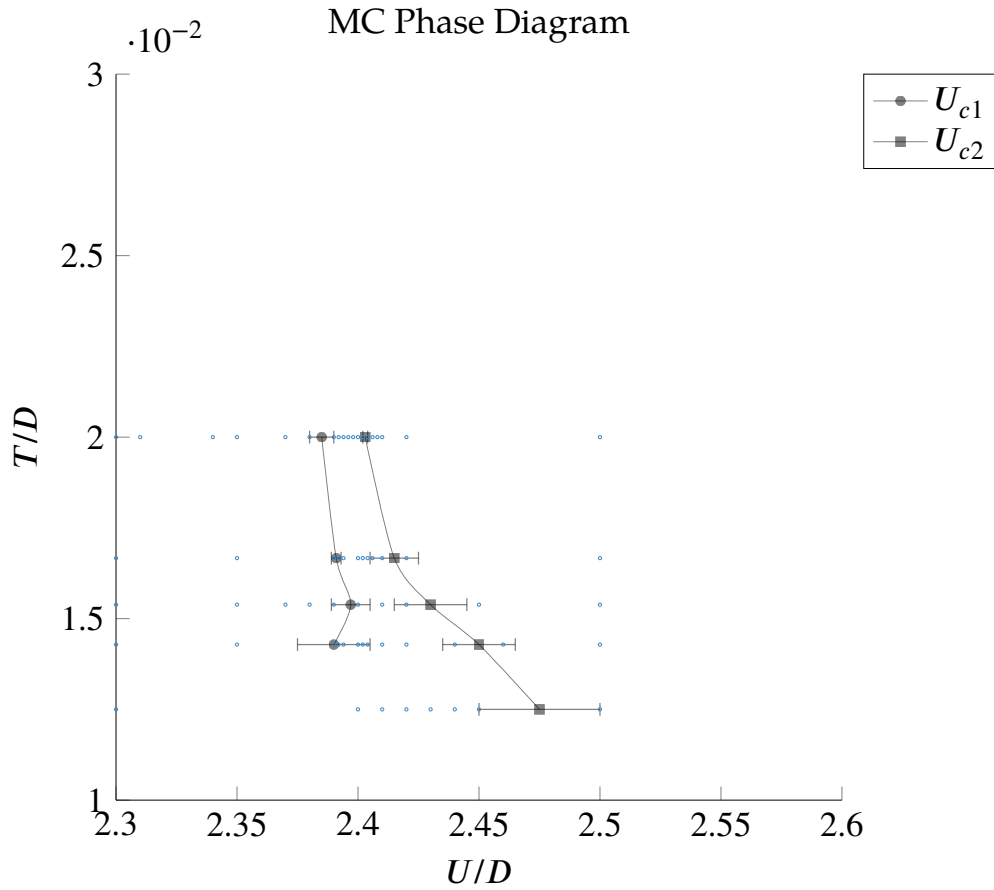Figure 6.12: $\beta = 50$ double occupancy hysteresis

Figure 6.13: Phase diagram obtained from Monte Carlo simulations. Blue dots mark the points for which a solution was obtained. Estimations for the border of the coexistence region are marked with symbols. Phase transition lines are only estimated, since some data points are not well converged. More computational recources and mixing can alleviate that.

CONCLUSION AND OUTLOOK

In this thesis I systematically introduced and implemented all integral parts for the dynamical mean field approximation algorithm and applied the program to the single orbital Hubbard model on the Bethe lattice at half filling. The impurity solver was identified as the central component of the DMFT loop and three commonly used algorithms implemented and tested against known results about the Mott transition on the Bethe lattice.

The first chapter introduced the basic concept of the Hubbard Hamiltonian and used simple approximations to characterize the Mott insulating phase. Furthermore the concept of mean field theories was introduced.

In the second and third chapter the theoretical background for Monte Carlo simulations and Green's function formalism was introduced.

In chapter 4 the core concepts of the dynamical mean field approximation were discussed and the Monte Carlo impurity solvers explained. This included the derivation of the DMFT equations. Having laid the ground work for the full method, we discussed concrete numerical algorithms that are essential for DMFT and Monte Carlo solutions for the impurity problem. Lastly the program was applied to the Hubbard model at half filling, reproducing well known results and demonstrating the usability of the previously discussed algorithms. This was first done using perturbation theory as an impurity solver to test the DMFT loop itself. The properties of the phase diagram were then verified using the more sophisticated continuous time quantum Monte Carlo solver.

Immediate extensions to this solver are the verification away from half filling, different lattice types (investigation of frustrated systems), different model types such as the Hubbard-Holstein or Bose-Hubbard model, multi orbital systems, general interactions and cluster extensions. Multi orbital systems and general interactions can be simulated using the CT-HYB solver, while cluster extensions are better suited for the CT-INT solver [54]. In order to simulate realistic materials, the incorporation of a DFT loop can introduce ab initio results to the Hubbard model. Here the model parameter ϵ_k that was obtained from the lattice in the context of this thesis is substituted for the Kohn-Sham eigenvalues. There are some significant obstacles in the application of this methods because the choice of DFT basis functions influences the DMFT input and more importantly some amount of electronic correlations are treated by both methods. Even though there is continued research interest in finding good approximations and progress has been made for the local density approximation of the exchange correlation potential [60], there is no general solution to this problem known (especially not for more modern approximations such as hybrid functionals).

In order to tackle less localized problems apart from the cluster extensions, it is also possible to use the non-perturbative structure of DMFT (all local diagrams are taken into account) as a basis for more sophisticated re-summations Most prominently the dynamical vertex approximation offers such an option by extending the class of diagrams to non-local ones [48].

8

ACKNOWLEDGEMENTS

I want to express my gratitude to my thesis advisor Prof. Maria-Roser Valentí for giving me the opportunity to write this thesis and her continuous support.
I also thank Prof. Eberhard Engel for kindly agreeing to take on the role of co-referee.
I am grateful for the insightful comments from Dr. Arram Kim and Dr. Steffen Backes.
Lastly I would like to thank Pia, Luke and Marco for proofreading this thesis.

Appendices

CONVERGENCE TO NORMAL DISTRIBUTION

This calculation proofs that the CLT is indeed applicable and the expected value and variance have the form of eq. 4.1.2. We first note according to [95], that

$$\rho_D(\epsilon_k) = \sum_k \delta(\hbar\omega - \epsilon_k)$$

can be understood as the probability density function of finding a certain energy $\epsilon_k = \hbar\omega$.

We then assume a uniform distribution of k vectors:

$$\rho_{k_d}^{[D]}(x) = \begin{cases} a/2\pi & \text{if } x \in [-\frac{\pi}{a}, \frac{\pi}{a}] \\ 0 & \text{else } x \end{cases}$$

We chose the transformation $y = 2t\cos(k_d a)$ which leads to

$$y = \frac{\arccos\left(\frac{y}{2t}\right)}{a}$$

$$\frac{dx}{dy} = -\frac{1}{2t}\frac{a}{\sin(\arccos(y))} = -\frac{a}{2t\sqrt{1 - \frac{y^2}{4t^2}}}$$

$$\Rightarrow \rho_{2t\cos(k_d)}(y) = \sum_{y=2t\cos(k_d)} \rho_{k_d}\left(\frac{1}{a}\arccos\left(\frac{y}{2t}\right)\right)\left|\frac{dx}{dy}\right|$$

$$= \begin{cases} 2\frac{a}{2\pi}\frac{1}{2t\sqrt{1-\frac{y^2}{4t^2}}} & \text{if } \frac{1}{a}\arccos\left(\frac{y}{2t}\right) \in [0, \frac{\pi}{a}] \\ 0 & \text{else} \end{cases}$$

$$= \begin{cases} \frac{a}{\pi}\frac{1}{2t\sqrt{1-\frac{y^2}{4t^2}}} & \text{if } y \in [-2t, 2t] \\ 0 & \text{else} \end{cases}$$

$$\mathbb{E}[y] = \frac{1}{2t}\int_{-2t}^{2t}\frac{a}{\pi}y\left[1 - \frac{y^2}{4t^2}\right]^{-1/2}dy$$

$$= \frac{a}{\pi}\left[-\frac{2t}{2t}\cdot(0 - 0)\right]$$

$$= 0$$

$$\mathbb{E}[y^2] = \frac{1}{2t}\int_{-2t}^{2t}\frac{a}{\pi}y^2\left[1 - \frac{y^2}{4t^2}\right]^{-1/2}dy$$

$$= \frac{t^2}{2t}\frac{a}{\pi}\left[4t\arcsin\left(\frac{y}{2t}\right) - y\sqrt{1 - \frac{y^2}{4t^2}}\right]\Big|_{-2t}^{2t}$$

$$= \frac{t^2 a}{4t\pi}\left[4t(\frac{\pi}{2} + \frac{\pi}{2})\right]$$

$$= 2t^2 a$$

$$\Rightarrow \mathrm{Var}[y] = 2t^2 a$$

$$\Rightarrow \epsilon_k^{[D]} = \frac{1}{D} \sum_{d=1}^{D} D2t \cos\left(k_d\right)$$

$$\longrightarrow \mathcal{N}(0, 2aDt^2)$$

Choosing the renormalized hopping strength and setting $a = 1$ we obtain the Gaussian DOS:

$$\rho^{[D]}(\omega) \longrightarrow \frac{1}{2\sqrt{\pi}t^\star} e^{-\frac{x^2}{4t^{\star 2}}}$$

[1]   A A (Alekseĭ Alekseevich) Abrikosov et al. "Methods of Quantum Field Theory in Statistical Physics". In: 4 (1965), p. 352.

[2]   Charu C Aggarwal, Alexander Hinneburg, and Daniel A Keim. "On the Surprising Behavior of Distance Metrics in High Dimensional Space". In: 2001, pp. 420–434. DOI: 10.1007/3-540-44503-X_27.

[3]   Vinay Ambegaokar and Matthias Troyer. "Estimating errors reliably in Monte Carlo simulations of the Ehrenfest model". In: *American Journal of Physics* 78.2 (Feb. 2010), pp. 150–157. ISSN: 0002-9505. DOI: 10.1119/1.3247985. arXiv: 0906.0943.

[4]   Gidi Amir. *Markov Chains*. Cambridge, 2014.

[5]   H H Andersen et al. "The Multivariate Complex Normal Distribution". In: Springer, New York, NY, 1995, pp. 15–37. DOI: 10.1007/978-1-4612-4240-6_2.

[6]   Stuart L Anderson. "Random Number Generators on Vector Supercomputers and Other Advanced Architectures". In: *SIAM Review* 32.2 (June 1990), pp. 221–251. ISSN: 0036-1445. DOI: 10.1137/1032044.

[7]   George B (George Brown) Arfken. *Mathematical methods for physicists*. Academic Press, 1985, p. 985. ISBN: 0120598108.

[8]   Sanjeev Arora and Boaz Barak. *Computational Complexity: A Modern Approach*. Cambridge University Press, 2009, p. 594. ISBN: 0521424267.

[9]   Louis-François Arsenault, Patrick Sémon, and A.-M S Tremblay. "Benchmark of a modified iterated perturbation theory approach on the fcc lattice at strong coupling". In: *Physical Review B* 86.8 (Aug. 2012), p. 85133. ISSN: 1098-0121. DOI: 10.1103/PhysRevB.86.085133.

[10] F F Assaad and T C Lang. "Diagrammatic determinantal quantum Monte Carlo methods: Projective schemes and applications to the Hubbard-Holstein model". In: *Physical Review B* 76.3 (July 2007), p. 35116. ISSN: 1098-0121. DOI: 10.1103/PhysRevB.76.035116. arXiv: 0702455 [cond-mat].

[11] Steffen Backes. "Density functional theory and dynamical mean-field theory: A way to model strongly correlated systems". PhD thesis. Goethe-Universität Frankfurt, 2017, p. 181.

[12] Andrzej Baran et al. "Broyden's method in nuclear structure calculations". In: *Physical Review C* 78.1 (July 2008), p. 014318. ISSN: 0556-2813. DOI: 10.1103/PhysRevC.78.014318. arXiv: 0805.4446.

[13] Heiko Bauke and Stephan Mertens. "Random numbers for large-scale distributed Monte Carlo simulations". In: *Physical Review E* 75.6 (June 2007), p. 66701. ISSN: 1539-3755. DOI: 10.1103/PhysRevE.75.066701.

[14] Gordon Baym and Leo P Kadanoff. "Conservation Laws and Correlation Functions". In: *Physical Review* 124.2 (Oct. 1961), pp. 287–299. ISSN: 0031-899X. DOI: 10.1103/PhysRev.124.287.

[15]   Mylène Bédard. "Optimal acceptance rates for Metropolis algorithms: Moving beyond 0.234". In: *Stochastic Processes and their Applications* 118.12 (Dec. 2008), pp. 2198–2222. ISSN: 03044149. DOI: 10.1016/j.spa.2007.12.005.

[16]   Dominic Bergeron and A -M. S Tremblay. "Algorithms for optimized maximum entropy and diagnostic tools for analytic continuation". In: (July 2015). DOI: 10.1103/PhysRevE.94.023303. arXiv: 1507.01012.

[17]   Dominic Bergeron and A.-M. S Tremblay. "Algorithms for optimized maximum entropy and diagnostic tools for analytic continuation". In: *Physical Review E* 94.2 (Aug. 2016), p. 023303. ISSN: 2470-0045. DOI: 10.1103/PhysRevE.94.023303.

[18]   H A Bethe. "Statistical Theory of Superlattices". In: *Proceedings of the Royal Society A: Mathematical, Physical and Engineering Sciences* 150.871 (July 1935), pp. 552–575. ISSN: 1364-5021. DOI: 10.1098/rspa.1935.0122.

[19]   H. Bethe. "Zur Theorie der Metalle". In: *Zeitschrift fuer Physik* 71.3-4 (Mar. 1931), pp. 205–226. ISSN: 1434-6001. DOI: 10.1007/BF01341708.

[20]   Adel Bilal. *Advanced Quantum Field Theory : Renormalization, Non-Abelian Gauge Theories and Anomalies*. Brussels, 2014.

[21]   Lewin Boehnke et al. "Orthogonal polynomial representation of imaginary-time Green's functions". In: *Physical Review B* 84.7 (Aug. 2011), p. 075145. ISSN: 1098-0121. DOI: 10.1103/PhysRevB.84.075145. arXiv: 1104.3215v3.

[22]   B. Böttcher et al. "Feynman formulas and path integrals for some evolution semigroups related to τ-quantization". In: *Russian Journal of Mathematical Physics* 18.4 (Dec. 2011), pp. 387–399. ISSN: 1061-9208. DOI: 10.1134/S1061920811040017.

[23]   C. G. Broyden. "A class of methods for solving nonlinear simultaneous equations". In: *Mathematics of Computation* 19.92 (1965), pp. 577–577. ISSN: 0025-5718. DOI: 10.1090/S0025-5718-1965-0198670-6.

[24]   Henrik Bruus and Karsten Flensberg. *Many-Body Quantum Theory in Condensed Matter Physics: An Introduction*. Oxford Univ Press, 2004, p. 352. ISBN: 978-0198566335.

[25]   R Bulla. "Zero Temperature Metal-Insulator Transition in the Infinite-Dimensional Hubbard Model". In: *Physical Review Letters* 83.1 (July 1999), pp. 136–139. ISSN: 0031-9007. DOI: 10.1103/PhysRevLett.83.136. arXiv: 9902290 [cond-mat].

[26]   David M Burton. *Elementary number theory*. McGraw-Hill, 2011, p. 436. ISBN: 0073383147.

[27]   R H Cameron. "A Family of Integrals Serving to Connect the Wiener and Feynman Integrals". In: *Journal of Mathematics and Physics* 39.1-4 (Apr. 1960), pp. 126–140. ISSN: 00971421. DOI: 10.1002/sapm1960391126.

[28]   K Capelle et al. "Density-Functional Theory for the Hubbard Model: Numerical Results for the Luttinger Liquid and the Mott Insulator". In: 2003, pp. 145–168. DOI: 10.1007/978-94-017-0409-0_12. arXiv: 0209245 [cond-mat].

[29]   Shailesh Chandrasekharan and Uwe-Jens Wiese. "Meron-Cluster Solution of Fermion Sign Problems". In: *Physical Review Letters* 83.16 (Oct. 1999), pp. 3116–3119. ISSN: 0031-9007. DOI: 10.1103/PhysRevLett.83.3116. arXiv: 9902128 [cond-mat].

[30]   Michele Cini and Gianluca Stefanucci. "Antiferromagnetism of the two-dimensional Hubbard model at half-filling: the analytic ground state for weak coupling". In: *Journal of Physics: Condensed Matter* 13.6 (Feb. 2001), pp. 1279–1294. ISSN: 0953-8984. DOI: 10.1088/0953-8984/13/6/308. arXiv: 0009058 [cond-mat].

[31]   Matteo Cococcioni. "4 The LDA+U Approach: A Simple Hubbard Correction for Correlated Ground States". In: *Correlated Electrons: From Models to Materials, Modeling and Simulation, Vol. 2*. Jülich: Autumn School on Correlated Electrons: From Models to Materials, 2012. Chap. 4. ISBN: 978-3-89336-796-2.

[32]   Mathias Drton, Christopher Fox, and Y Samuel Wang. "Computation of maximum likelihood estimates in cyclic structural equation models". In: (Oct. 2016). arXiv: 1610.03434.

[33]   R. M. (Richard M.) (Richard M.) Dudley. *Real Analysis and Probability*. Cambridge University Press, 2002, p. 568. ISBN: 0521007542.

[34]   Martin Eckstein et al. "Hopping on the Bethe lattice: Exact results for densities of states and dynamical mean-field theory". In: *Physical Review B* 71.23 (June 2005), p. 235119. ISSN: 1098-0121. DOI: 10.1103/PhysRevB.71.235119. arXiv: 0409730 [cond-mat].

[35]   E. N. Economou. *Green's functions in quantum physics*. Springer, 2010, p. 477. ISBN: 9783642066917.

[36]   Bradley Efron and Robert J. Tibshirani. *An Introduction to the Bootstrap*. Boston, MA: Springer US, 1993. ISBN: 978-0-412-04231-7. DOI: 10.1007/978-1-4899-4541-9.

[37]   M EICHLER. "A new proof of the Baker-Campbell-Hausdorff formula". In: *Journal of the Mathematical Society of Japan* 20.1-2 (Apr. 1968), pp. 23–25. ISSN: 0025-5645. DOI: 10.2969/jmsj/02010023.

[38]   Jan Eriksson, Esa Ollila, and Visa Koivunen. "Statistics for complex random variables revisited". In: *ICASSP, IEEE International Conference on Acoustics, Speech and Signal Processing - Proceedings* April (2009), pp. 3565–3568. ISSN: 15206149. DOI: 10.1109/ICASSP.2009.4960396.

[39]   F H L Essler et al. *The one-dimensional Hubbard model*. Cambridge University Press, 2003, p. 692. ISBN: 978-0-521-80262-8.

[40]   Uwe Franz and Nicolas Privault. *Probability on Real Lie Algebras*. Cambridge: Cambridge University Press, 2016. ISBN: 9781316415054. DOI: 10.1017/CBO9781316415054.

[41]   M. Frigo and S.G. Johnson. "The Design and Implementation of FFTW3". In: *Proceedings of the IEEE* 93.2 (Feb. 2005), pp. 216–231. ISSN: 0018-9219. DOI: 10.1109/JPROC.2004.840301.

[42]   Bert Fristedt and Lawrence Gray. *A Modern Approach to Probability Theory*. Boston, MA: Birkhäuser Boston, 1997, p. 775. ISBN: 978-1-4899-2839-9. DOI: 10.1007/978-1-4899-2837-5.

[43]   S. Frullani and J. Mougey. "Single Particle Properties of Nuclei Through (e, e′ p) Reactions". In: *Adv.Nucl.Phys.* 14 (1984), pp. 1–283.

[44]   Peter Fulde. *Electron Correlations in Molecules and Solids*. Vol. 100. Springer Series in Solid-State Sciences. Berlin, Heidelberg: Springer Berlin Heidelberg, 1995, p. 499. ISBN: 978-3-540-59364-5. DOI: 10.1007/978-3-642-57809-0.

[45]   Edgar Gabriel et al. "Open MPI: Goals, Concept, and Design of a Next Generation MPI Implementation". In: *Proceedings, 11th European PVM/MPI Users' Group Meeting*. Budapest, Hungary, Sept. 2004, pp. 97–104.

[46]   A. Gaenko et al. "Updated core libraries of the ALPS project". In: *Computer Physics Communications* 213 (Apr. 2017), pp. 235–251. ISSN: 00104655. DOI: 10.1016/j.cpc.2016.12.009.

[47]   M. Galassi. *GNU Scientific Library Reference Manual*. 3rd ed. Network Theory Ltd., 2009, p. 592. ISBN: 0954612078.

[48]   Anna Galler et al. "Ab initio dynamical vertex approximation". In: *Physical Review B* 95.11 (Mar. 2017), p. 115107. ISSN: 2469-9950. DOI: 10.1103/PhysRevB.95.115107. arXiv: 1610.02998.

[49]   Christof Gattringer and Christian B. Lang. *Quantum Chromodynamics on the Lattice*. Vol. 788. Lecture Notes in Physics. Berlin, Heidelberg: Springer Berlin Heidelberg, 2010. ISBN: 978-3-642-01849-7. DOI: 10.1007/978-3-642-01850-3.

[50]   Florian Gebhard. *The mott metal-insulator transition : models and methods*. Springer, 1997, p. 317. ISBN: 9783642082634.

[51]   Antoine Georges et al. "Dynamical mean-field theory of strongly correlated fermion systems and the limit of infinite dimensions". In: *Reviews of Modern Physics* 68.1 (Jan. 1996), pp. 13–125. ISSN: 0034-6861. DOI: 10.1103/RevModPhys.68.13.

[52]   James. Glimm and Arthur Jaffe. *James Glimm, Arthur Jaffe Quantum physics a functional integral point of view*. 1987.

[53]   Dieter. Gollmann. *Computer security*. Wiley, 2011, p. 436. ISBN: 0470741155.

[54]   James Gubernatis, Naoki Kawashima, and Philipp Werner. *Quantum Monte Carlo Methods: Algorithms for Lattice Models*. 1st ed. Cambridge University Press, 2016, p. 512. ISBN: 9781107006423.

[55]   Gael Guennebaud and Jacob Benoit. "Eigen v3". In: (2010).

[56]   Emanuel Gull. "Continuous-Time Quantum Monte Carlo Algorithms for Fermions". In: 18124 (2008), p. 161. DOI: 10.3929.

[57]   Emanuel Gull. "Continuous-Time Quantum Monte Carlo Algorithms for Fermions". PhD thesis. ETH Zuerich, Mar. 2008. DOI: 10.3929/ethz-a-005722583Rights.

[58]   Emanuel Gull et al. "Continuous-time Monte Carlo methods for quantum impurity models". In: *Reviews of Modern Physics* 83.2 (2011), pp. 349–404. ISSN: 00346861. DOI: 10.1103/RevModPhys.83.349. arXiv: 1012.4474.

[59]   E Gull et al. "Continuous-time auxiliary-field Monte Carlo for quantum impurity models". In: *EPL (Europhysics Letters)* 82.5 (June 2008), p. 57003. ISSN: 0295-5075. DOI: 10.1209/0295-5075/82/57003.

[60]   Kristjan Haule. "Exact Double Counting in Combining the Dynamical Mean Field Theory and the Density Functional Theory". In: *Physical Review Letters* 115.19 (Nov. 2015), p. 196403. ISSN: 0031-9007. DOI: 10.1103/PhysRevLett.115.196403.

[61]   Michiel. Hazewinkel. *Encyclopaedia of mathematics*. 2002.

[62] Peter M Heffernan. "Unbiased Estimation of Central Moments by using U-statistics". In: *Journal of the Royal Statistical Society: Series B (Statistical Methodology)* 59.4 (Nov. 1997), pp. 861–863. ISSN: 1369-7412. DOI: 10.1111/1467-9868.00102.

[63] P Hellekalek. "Good random number generators are (not so) easy to find". In: *Mathematics and Computers in Simulation* 46.5-6 (June 1998), pp. 485–505. ISSN: 03784754. DOI: 10.1016/S0378-4754(98)00078-0.

[64] J E Hirsch. "Discrete Hubbard-Stratonovich transformation for fermion lattice models". In: *Physical Review B* 28.7 (Oct. 1983), pp. 4059–4061. ISSN: 0163-1829. DOI: 10.1103/PhysRevB.28.4059.

[65] Masatoshi Imada, Atsushi Fujimori, and Yoshinori Tokura. "Metal-insulator transitions". In: *Reviews of Modern Physics* 70.4 (Oct. 1998), pp. 1039–1263. ISSN: 0034-6861. DOI: 10.1103/RevModPhys.70.1039.

[66] Russell Impagliazzo. "A personal view of average-case complexity". In: *Proceedings of Structure in Complexity Theory. Tenth Annual IEEE Conference*. UC, San Diego: IEEE Comput. Soc. Press, 1995, pp. 134–147. ISBN: 0-8186-7052-5. DOI: 10.1109/SCT.1995.514853.

[67] L. ISSERLIS. "ON A FORMULA FOR THE PRODUCT-MOMENT COEFFICIENT OF ANY ORDER OF A NORMAL FREQUENCY DISTRIBUTION IN ANY NUMBER OF VARIABLES". In: *Biometrika* 12.1-2 (Nov. 1918), pp. 134–139. ISSN: 0006-3444. DOI: 10.1093/biomet/12.1-2.134.

[68] Kiyosi Itô. "Proceedings of the Berkeley Symposium on Mathematical Statistics and Probability." In: *Berkeley Symposium on Mathematical Statistics and Probability*. University of California Press, 1967.

[69] Fusayoshi J. Ohkawa. "Electron Correlation in the Hubbard Model in d =∞ Dimension". In: *Journal of the Physical Society of Japan* 60.10 (Oct. 1991), pp. 3218–3221. ISSN: 0031-9015. DOI: 10.1143/JPSJ.60.3218. arXiv: JPSJ.60.3218 [10.1143].

[70] J.W. Negele and H.O. Orland. *Quantum Many-Particle Systems*. Perseus Books, 1998, p. 459. ISBN: 0738200522.

[71] Mark Jarrell and J.E. Gubernatis. "Bayesian inference and the analytic continuation of imaginary-time quantum Monte Carlo data". In: *Physics Reports* 269.3 (May 1996), pp. 133–195. ISSN: 03701573. DOI: 10.1016/0370-1573(95)00074-7.

[72] Steven G. Johnson. *Faddeeva Package*.

[73] Mitsuaki Kawamura, Yoshihiro Gohda, and Shinji Tsuneyuki. "Improved tetrahedron method for the Brillouin-zone integration applicable to response functions". In: *Physical Review B* 89.9 (Mar. 2014), p. 094515. ISSN: 1098-0121. DOI: 10.1103/PhysRevB.89.094515.

[74] Aaram J. Kim, M. Y. Choi, and Gun Sang Jeon. "Estimate of the phase transition line in the infinite-dimensional Hubbard model". In: *Journal of the Korean Physical Society* 64.2 (Jan. 2014), pp. 268–276. ISSN: 0374-4884. DOI: 10.3938/jkps.64.268.

[75] Frederick W. King. *Hilbert transforms*. Cambridge University Press, 2009. ISBN: 0521887623.

[76]   Michael Wolfgang Kinza. "Single Impurity Anderson Model and Dynamical Mean Field Theory". PhD thesis. RWTH Aachen, 2013, p. 122.

[77]   John R Klauder. "The Feynman Path Integral: An Historical Slice". In: (Mar. 2003). DOI: 10.1142/9789812795106_0005. arXiv: 0303034 [quant-ph].

[78]   H Kleinert. *Path Integrals in Quantum Mechanics, Statics, Polymer Physics and Financial Markets*. 5 edition. World Scientific, 2004, p. 1579. ISBN: 978-9814273565.

[79]   Donald Ervin Knuth. *The art of computer programming*. Addison-Wesley Pub. Co, 1973. ISBN: 0201896842.

[80]   Peter Kopietz. *Vielteilchetheory*. 2014.

[81]   G Kotliar et al. "Electronic structure calculations with dynamical mean-field theory". In: *Reviews of Modern Physics* 78.3 (Aug. 2006), pp. 865–951. ISSN: 0034-6861. DOI: 10.1103/RevModPhys.78.865.

[82]   Pierre L'Ecuyer and Richard Simard. "TestU01". In: *ACM Transactions on Mathematical Software* 33.4 (Aug. 2007), 22–es. ISSN: 00983500. DOI: 10.1145/1268776.1268777.

[83]   Muflihun Labs. *easyloggingpp*. 2018.

[84]   E. L. (Erich Leo) (Erich Leo) Lehmann and George Casella. *Theory of point estimation*. 2nd ed. Springer, 1998, p. 589. ISBN: 0387985026.

[85]   Ryan Levy, J.P.F. LeBlanc, and Emanuel Gull. "Implementation of the maximum entropy method for analytic continuation". In: *Computer Physics Communications* 215 (June 2017), pp. 149–155. ISSN: 00104655. DOI: 10.1016/j.cpc.2017.01.018.

[86]   Elliott H Lieb and F Y Wu. "Absence of Mott Transition in an Exact Solution of the Short-Range, One-Band Model in One Dimension". In: *Physical Review Letters* 20.25 (June 1968), pp. 1445–1448. ISSN: 0031-9007. DOI: 10.1103/PhysRevLett.20.1445.

[87]   Yi-Wen Liu. "Hilbert Transform and Applications". In: *Fourier Transform Applications*. InTech, Apr. 2012. DOI: 10.5772/37727.

[88]   E Y Loh et al. "Sign problem in the numerical simulation of many-electron systems". In: *Physical Review B* 41.13 (May 1990), pp. 9301–9307. ISSN: 0163-1829. DOI: 10.1103/PhysRevB.41.9301.

[89]   J M Luttinger and J C Ward. "Ground-State Energy of a Many-Fermion System. II". In: *Physical Review* 118.5 (June 1960), pp. 1417–1427. ISSN: 0031-899X. DOI: 10.1103/PhysRev.118.1417.

[90]   Gerald D. Mahan. *Many-particle physics*. Kluwer Academic/Plenum Publishers, 2000, p. 785. ISBN: 0306463385.

[91]   Ferdinando Mancini, Evgeny Plekhanov, and Gerardo Sica. "Exact solution of the 1D Hubbard model with NN and NNN interactions in the narrow-band limit". In: *The European Physical Journal B* 86.10 (Aug. 2013), p. 408. ISSN: 1434-6028. DOI: 10.1140/epjb/e2013-40527-y. arXiv: 1308.5196.

[92]   Alan G. (Alan George) Marshall. *Fourier, Hadamard, and Hilbert transforms in chemistry*. Plenum Press, 1982, p. 562. ISBN: 9780306409042.

[93]   Avery McIntosh. "The Jackknife Estimation Method". In: (June 2016). arXiv: 1606.00497.

[94] Walter Metzner. "Variational theory for correlated lattice fermions in high dimensions". In: *Z. Phys. B -Condensed Matter* 77 (1989), pp. 253–266.

[95] Walter Metzner and Dieter Vollhardt. "Correlated Lattice Fermions in d = oo Dimensions". In: 62.3 (1989). DOI: `https://doi.org/10.1103/PhysRevLett.62.324`.

[96] E Miiller-Hartmann. "Condensed Zeitschrift Matter for Physik B Correlated fermions on a lattice in high dimensions". In: *Z. Phys. B -Condensed Matter* 74 (1989), pp. 507–512. DOI: `10.1007/BF01312686`.

[97] Wolfgang Nolting and Anupuru. Ramakanth. *Quantum Theory of Magnetism*. Springer, 2009. ISBN: 9783540854159.

[98] Mariana M Odashima, Beatriz G Prado, and E Vernek. "Pedagogical introduction to equilibrium Green's functions: condensed-matter examples with numerical implementations". In: *Revista Brasileira de Ensino de Física* 39.1 (Apr. 2017). ISSN: 1806-1117. DOI: `10.1590/1806-9126-RBEF-2016-0087`. arXiv: `1604.02499`.

[99] Olivier Parcollet et al. "TRIQS: A toolbox for research on interacting quantum systems". In: *Computer Physics Communications* 196 (Nov. 2015), pp. 398–415. ISSN: 00104655. DOI: `10.1016/j.cpc.2015.04.023`. arXiv: `1504.01952`.

[100] Eva Pavarini et al. *DMFT at 25: Infinite Dimensions*. Forschungszentrum Jülich GmbH Institute for Advanced Simulation, 2014, p. 459. ISBN: 978-3-89336-953-9.

[101] Eva Pavarini et al. *Quantum Materials: Experiments and Theory*. Vol. Volume 6. Forschungszentrum Jülich GmbH Institute for Advanced Simulation, 2016, p. 420. ISBN: 978-3-95806-159-0.

[102] Philippe Pebay. *Formulas for Robust, One-Pass Parallel Computation of Covariances and Arbitrary-Order Statistical Moments*. Tech. rep. Sandia National Laboratories, 2008, p. 18.

[103] John P. Perdew. "Density functional theory and the band gap problem". In: *International Journal of Quantum Chemistry* 28.S19 (June 1985), pp. 497–523. ISSN: 00207608. DOI: `10.1002/qua.560280846`.

[104] Michael Edward Peskin and Daniel V. Schroeder. *An Introduction To Quantum Field Theory*. Westview Press, 1995, p. 864. ISBN: 0201503972.

[105] Michael Potthoff. "Non-perturbative construction of the Luttinger-Ward functional". In: (June 2004). arXiv: `0406671 [cond-mat]`.

[106] Michael Potthoff. *Strongly Correlated Systems*. Ed. by Adolfo Avella and Ferdinando Mancini. Vol. 171. Springer Series in Solid-State Sciences. Berlin, Heidelberg: Springer Berlin Heidelberg, Aug. 2012. ISBN: 978-3-642-21830-9. DOI: `10.1007/978-3-642-21831-6`. arXiv: `1108.2183`.

[107] William H. Press et al. *Numerical Recipes 3rd Edition: The Art of Scientific Computing*. 3rd. Cambridge University Press, 2007, p. 1256. ISBN: 0521880688.

[108] M Radici et al. "Many-body effects in 16O(e,e'p)". In: *Physical Review C* 50.6 (Aug. 1994), pp. 3010–3017. ISSN: 0556-2813. DOI: `10.1103/PhysRevC.50.3010`. arXiv: `9408015 [nucl-th]`.

[109]   J. F. Rentrop, V. Meden, and S. G. Jakobs. "Renormalization group flow of the Luttinger-Ward functional: Conserving approximations and application to the Anderson impurity model". In: *Physical Review B* 93.19 (May 2016), p. 195160. ISSN: 2469-9950. DOI: 10.1103/PhysRevB.93.195160. arXiv: 1602.06120.

[110]   A. Reymbaut, D. Bergeron, and A. -M. S. Tremblay. "Maximum Entropy Analytic Continuation for Spectral Functions with Non-Positive Spectral Weight". In: *Physical Review B* 92.6 (July 2015), p. 060509. ISSN: 1098-0121. DOI: 10.1103/PhysRevB.92.060509. arXiv: 1507.01956.

[111]   Lorenzo Rimoldini. "Weighted skewness and kurtosis unbiased by sample size and Gaussian uncertainties". In: *Astronomy and Computing* 5 (July 2014), pp. 1–8. ISSN: 22131337. DOI: 10.1016/j.ascom.2014.02.001. arXiv: 1304.6564.

[112]   Robert G. Brown. *Diehard Test*.

[113]   Christian P Robert. "The Metropolis-Hastings algorithm". In: (Apr. 2015). arXiv: 1504.01896.

[114]   M J Rozenberg, G Kotliar, and X Y Zhang. "Mott-Hubbard transition in infinite dimensions. II". In: *Physical Review B* 49.15 (Apr. 1994), pp. 10181–10193. ISSN: 0163-1829. DOI: 10.1103/PhysRevB.49.10181.

[115]   A N Rubtsov, V V Savkin, and A I Lichtenstein. "Continuous Time Quantum Monte Carlo method for fermions". In: *Physical Review B* 72.3 (Nov. 2004), p. 35122. ISSN: 1098-0121. DOI: 10.1103/PhysRevB.72.035122. arXiv: 0411344 [cond-mat].

[116]   Lewis H. Ryder. *Quantum field theory*. Cambridge University Press, 1996, p. 487. ISBN: 0521478146.

[117]   Masanori Saito. "Hilbert transforms for sampled data." In: *Journal of Physics of the Earth* 22.3 (1974), pp. 313–324. ISSN: 1884-2305. DOI: 10.4294/jpe1952.22.313.

[118]   L. J. Sham and M. Schlüter. "Density-Functional Theory of the Energy Gap". In: *Physical Review Letters* 51.20 (Nov. 1983), pp. 1888–1891. DOI: 10.1103/PhysRevLett.51.1888. arXiv: /dx.doi.org/10.1103/PhysRevLett.51.1888 [http:].

[119]   P J C Spreij. *Measure Theoretic Probability*. Tech. rep. 2016, p. 168.

[120]   Daniel Stahkle. *gnuplot-io*. 2013.

[121]   Julian Stobbe. *https://github.com/Atomtomate/MSC_Thesis*.

[122]   Hugo U. R. Strand et al. "The Dynamical Mean Field Theory phase space extension and critical properties of the finite temperature Mott transition". In: *Physical Review B* 83.20 (May 2010), p. 205136. ISSN: 1098-0121. DOI: 10.1103/PhysRevB.83.205136. arXiv: 1012.3829.

[123]   H F Trotter. "On the Product of Semi-Groups of Operators". In: *Proceedings of the American Mathematical Society* 10.4 (Aug. 1959), p. 545. ISSN: 00029939. DOI: 10.2307/2033649.

[124]   P G J Van Dongen, F Gebhard, and D Vollhardt. "Variational evaluation of correlation functions for lattice electrons in high dimensions". In: *Z. Phys. B -Condensed Matter* 76 (1989), pp. 199–210.

[125]   Dieter Vollhardt. "CORRELATED ELECTRON SYSTEMS". In: *Correlated Electron Systems*. Ed. by V. J. Emery. WORLD SCIENTIFIC, Aug. 1993, p. 57. ISBN: 978-981-02-1232-2. DOI: 10.1142/9789814536363.

[126]   Dieter Vollhardt. "Dynamical Mean-Field Theory of Electronic Correlations in Models and Materials". In: (Apr. 2010). DOI: 10.1063/1.3518901. arXiv: 1004.5069.

[127]   Anton Wakolbinger and Götz Kersting. *Stochastische Prozesse*. 1st ed. Birkhäuser Basel, 2014, p. 155. ISBN: 978-3-7643-8432-6. DOI: 10.1007/978-3-7643-8433-3.

[128]   Peter Walters et al. *An Introduction to Ergodic Theory undergraduate texts in mathematics*. Springer-Verlag, Mar. 2000, p. 250. ISBN: 9780387951522. DOI: 10.1103/PhysRevA.87.043613. arXiv: 1303.2213.

[129]   Steven Weinberg. *The quantum theory of fields*. Cambridge University Press, 1995, p. 609. ISBN: 0521670535.

[130]   Pierre Weiss. "L'hypothèse du champ moléculaire et la propriété ferromagnétique". In: *Journal de Physique Théorique et Appliquée* 6.1 (1907), pp. 661–690. ISSN: 0368-3893. DOI: 10.1051/jphystap:019070060066100.

[131]   B. P. Welford. "Note on a Method for Calculating Corrected Sums of Squares and Products". In: *Technometrics* 4.3 (Aug. 1962), pp. 419–420. ISSN: 0040-1706. DOI: 10.1080/00401706.1962.10490022.

[132]   Philipp Werner et al. "Continuous-time solver for quantum impurity models". In: *Physical Review Letters* 97.7 (Aug. 2006), pp. 4–7. ISSN: 00319007. DOI: 10.1103/PhysRevLett.97.076405. arXiv: 0512727 [cond-mat].

[133]   D H D West. "Updating mean and variance estimates: an improved method". In: *Communications of the ACM* 22.9 (Sept. 1979), pp. 532–535. ISSN: 00010782. DOI: 10.1145/359146.359153.

[134]   Kate A Whittaker et al. "The Hilbert transform: Applications to atomic spectra". In: (Nov. 2014). DOI: 10.1103/PhysRevA.91.032513. arXiv: 1411.6420.

[135]   G C Wick. "The Evaluation of the Collision Matrix". In: *Physical Review* 80.2 (Oct. 1950), pp. 268–272. ISSN: 0031-899X. DOI: 10.1103/PhysRev.80.268.

[136]   Thomas Williams, Colin Kelley, and Many others. *Gnuplot 4.6: an interactive plotting program*. \urlhttp://gnuplot.sourceforge.net/. Apr. 2013.

[137]   J. (James) (James) Yeh. "Real Analysis - Theory of Measure and Integration". In: 3rd ed. World Scientific, 2005, p. 834. ISBN: 9814578533.

[138]   Alexandre Zagoskin. *Quantum Theory of Many-Body Systems*. Graduate Texts in Physics. Cham: Springer International Publishing, 2014. ISBN: 978-3-319-07048-3. DOI: 10.1007/978-3-319-07049-0.

[139]   Rok Žitko. "Convergence acceleration and stabilization of dynamical mean-field theory calculations". In: *Physical Review B - Condensed Matter and Materials Physics* 80.12 (Sept. 2009), p. 125125. ISSN: 10980121. DOI: 10.1103/PhysRevB.80.125125. arXiv: 0908.0613.